TECHNISCHE UNIVERSITÄT MÜNCHEN

Lehrstuhl für Numerische Mechanik

Computational modeling, clinical comprehension and improvement of aortic manipulation

Michael Hamman de Vaal

Vollständiger Abdruck der von der Fakultät für Maschinenwesen der Technischen Universität München zur Erlangung des akademischen Grades eines

Doktor-Ingenieurs (Dr.-Ing.)

genehmigten Dissertation.

Vorsitzender: Univ.-Prof. Phaedon-Stelios Koutsourelakis, Ph.D.

Prüfer der Dissertation:

1. Univ.-Prof. Dr.-Ing. Wolfgang A. Wall

2. Univ.-Prof. Dr. med. Ulrich A. Stock
   Johann Wolfgang Goethe-Universität Frankfurt am Main

3. Univ.-Prof. Dr.-Ing. Michael W. Gee

Die Dissertation wurde am 25. Juni 2014 bei der Technischen Universität München eingereicht und durch die Fakultät für Maschinenwesen am 25. Januar 2015 angenommen.

Abstract

Of the approximately two million open-heart cardiac surgeries performed world-wide annually, up to 5.4% end in stroke, while less severe neurological deficits occur in an even more substantial amount of cases. Clinical experience, procedure development, experimental findings and technological advances have all contributed to significantly improve not only myocardial, but also neurological outcome. However, the latter remains persistent and becomes especially critical in the majority of patients requiring cardiac intervention, i.e. older patients with multiple co-morbidities.

An extensive literature overview of aortic manipulation, yielded a comprehensive definition which includes any surgical maneuver responsible for structural impact to the aortic wall (large deformations or lacerations) as well as disruption of the physiological hemodynamics. Such maneuvers have repeatedly been shown to increase the likelihood of embologenesis, especially in the presence of atherosclerosis, as well as cerebral malperfusion. Consequently, aortic manipulation have been implicated to be one of the main, if not *the* main, contributor to the stated poor neurological outcomes. Such manipulation maneuvers do not only occur in best-practice cardiac surgery, but in state-of-the-art cardiac interventions in general, including percutaneous interventions.

Aortic manipulation presents complex, multi-factorial risks – some of which are often left unaccounted for or unavoidable in standard clinical practice. While prior advances have been able to substantially improve the safety of aspects external to the patient, e.g. improved cardiopulmonary bypass (CPB) components, or in terms of global patient homeostasis, e.g. blood pressure, acid-base levels etc., the variation in outcome becomes dictated by local patient-specific aspects directly influenced by manipulation. Since many specifics about the exact mechanisms responsible for adverse outcomes cannot be evaluated clinically or experimentally, the mechanical nature of aortic manipulation offers the unique opportunity for more advanced computational analysis.

Hence, a computational study was performed to evaluate two of the arguably most dangerous aortic manipulation maneuvers. A structural investigation was performed of aortic occlusion, i.e. cross-clamping and endo-aortic balloon occlusion (EABO), and fluid investigation of arterial cannular flow, i.e. the local effects of the high velocity jet formed with arterial return during CPB. State-of-the-art computational methods and material models allowed for approximating physiologically relevant effects.

The formulation of functional requirements that describe a safe, efficient and reliable aortic occluder enabled previously unappreciated detail and scope in comparing structural occluder performance in the context of an idealized aorta. The occluders compared included different cross-clamps, endo-aortic balloon occlusion (EABO), as well as a novel occluder design, namely constrained EABO (CEABO). The overall results indicated performance trade-offs, reflected that the current clinical trend of preferably using cross-clamps is dictated by its simplicity, stability and cost – not its high potential danger. But it is also further motivated by the insufficiently poor performance of EABO, also reflected in these results. Furthermore, it also demonstrated the superior performance of CEABO, which included its ability to yield the same potential of occluding the vessel as cross-clamps, but at approximately half the increase in tensile strain in the vessel wall ($\sim$30%). Furthermore, it did not cause pinching of the wall as cross-clamps do and it solved the problem of the positional instability associated with EABO. Perhaps most importantly, it was shown to also possess the scope for addressing the main shortcoming of currently available occluders: the reliable prediction of the load required to achieve occlusion. Its uncertainty is the reason why more (unwanted) load is practically always applied to the aorta than what is necessary to occlude it.

Occluding a mildly calcified patient-specific ascending aorta was also considered, by applying standard DeBakey cross-clamps and EABO at different occluder configurations, i.e. positions and/or orientations. The results revealed a complex loading state of the aorta, responsible for significant increases in strain at different calcification lesions. In the clinical setting, such patient-specific peculiarities would be difficult to predict intuitively and to accurately execute – contrary to what has been suggested in literature.

Functional requirements were also formulated for optimal proximal cannular flow effects, i.e. flow aspects prior to entering the aortic arch. Considering an idealized aortic lumen, previously unevaluated detail was obtained from different clinically available cannulas, as well as different cannula configurations of a straight end-hole cannula, i.e. cannula orientation and insertion depth. Additionally, a new cannula tip design, was also considered, not clinically available nor previously evaluated, i.e. a shielded (end-hole) cannula. Considering only 50% of CPB flow rate, results displayed unexpected design trade-offs, substantial cannula tip design inefficiencies and also dangers. All available tips that yielded a relatively satisfactory flow profile entering the aortic arch, relied predominantly on the jet landing directly on the vessel for its dissipation. This an undesirable feature, but not only observed for these cannulas. Every cannula evaluated resulted in a region approximately half of the size of a 1-Euro-cent coin that will cause endothelial erosion on a healthy aortic wall, not even to speak of a diseased wall. Furthermore, a high sensitivity to the cannula configuration was also shown, i.e. cannula performance is also dependent on its immediate orientation and tip-to-opposite wall in the cannulated vessel. Finally, the shielded cannula tip's overall good comparative performance came at a cost of a high pressure drop.

The cross-clamped (highly deformed) patient-specific geometries from the above-mentioned structural study were also used to evaluate the proximal flow effects of arterial cannular flow. Considering a straight end-hole cannula, the resulting functional performance yielded significant variability in the resulting flow patterns when simply changing the orientation by which the vessel was cross-clamped.

The original contributions presented in this investigation, include the following: (1) A comprehensive oversight of aortic manipulation in terms of the multi-factorial risks it poses in terms of peri-operative cerebral vascular accidents (CVAs), bringing together vascular injury (structural) and perfusion disruption (fluid), in a way not previously considered; (2) The use of computational models for previously unattainable insights into the mechanical consequences of certain clinically performed manipulation maneuvers. Therein, certain design trade-offs, design inefficiencies and potential mechanisms by which manipulation maneuvers can (hazardously) interact, were described for the first time; (3) A novel method of aortic occlusion was proposed and an untested cannula tip design were evaluated with the aim to make these maneuvers safer. Both yielded very promising results; and (4) The computational analyses of patient-specific models demonstrated the immense variability that will be encountered clinically when performing aortic manipulation, and its sensitivity to subtle changes in surgical technique.

Two fundamental aspects currently lacking from clinical practice, as identified in this investigation, are occluding techniques that allow for a clinically determinable level of occlusion and arterial cannula performance data that incorporate aspects of vessel-induced variations. Conceivably, the main reason why many previous procedural and technological attempts to lessen the impact or to avoid aortic manipulation have had limited or inconclusive benefits, is the lack of understanding/consideration of the complex mechanisms and outcomes as a whole. To this end, the presented computational analyses are expected to be of invaluable benefit. Consequently, the development of safer *and* more robust strategies for aortic manipulation are needed in order to reduce potentially detrimental consequences within the context of high clinical variability.

Acknowledgments

It takes a village to raise a child.

— African proverb

The work in this dissertation was completed from 2009 to 2014 during my time as a research associate at the Institute of Computational Mechanics at the Technische Universität München (TUM). During this time, I was of course accompanied by a number of people who ultimately contributed to its successful completion, whom I would like to thank here.

First of all, thank you very much to my supervisor, Prof. Dr.-Ing. Wolfgang A. Wall, and co-supervisor, Prof. Dr.-Ing. Michael W. Gee, for taking the chance on this specific applicant from a distant university. What I have learnt and experienced because of this opportunity, both topical and in general, has been great and grandiose. I am also very grateful for what both of you have invested in me professionally.

In terms of medical advice, I would like to express my gratitude to Prof. Dr.-med. Ulrich A. Stock for the initial idea and assisting in supervision, to Prof. Dr.-med. Stephen M. Wildhirt for great discussions, and to Assc.-Prof. Thomas Franz for an informative research stay at the University of Cape Town.

In terms of financial support, I would like to thank the Munich Centre of Advanced Computing (MAC Project B8) under administration of the International Graduate School of Science and Engineering (IGSSE) for support from 2009 to 2013, and Prof. Dr.-Ing. Wolfgang A. Wall for support from 2013 to 2014.

In terms of colleagues, I would like to particularly thank Keijo Nissen for not just having a less-spoken language in common, but sharing in a lengthy and arduous journey with much coffee, loud conversations in the institute kitchen, long runs, introductory and advanced German culture tips and friendship. To my office mates, Rui Fang, Manuel Hahn, but especially Markus Gitterle – I could not have asked for more real, fun and smart people to share an office with and to bombard with questions. Thank you also to my other "co-supervisors": Mahmoud Ismail, Andreas Maier, Florian Henke, Kei Müller, Shadan Shahmiri, Caroline Danowski, Susanna Tinkl, Andreas Nagler and Heinrich Küttler. Of course, also to all my other colleagues for always having an open door. Thank you also to Ms. Ingrid Nagl and Ms. Annette Reinecke, whose wonderful secretarial support lightened my administrative load significantly.

In terms of other friends, I would like to thank all my friends and "family" at the Jesus-the-Way Christian community church, for your unwavering support, meals and simply special times together, especially to Helmut and Veda Schneider, Dietmar and Jeanette Beyer and Hermann and Petra Sorg – and many others, of course. I owe thanks also to friends in South Africa, who frequently provided encouragement – thank you Coos Diener, Albert Viljoen and Niël van der Merwe and many more.

To my parents, whose selfless sacrifice and investment in me from day one, took and guided me on a path which has enabled me to take on great challenges and stand firm under pressure that would have otherwise overwhelmed me. My debt of gratitude also extends to my siblings, Bernard, Alma and Sarita, for your lives and love have also been intertwined with this whole process of "raising the child".

Thank you to my wife, Mirelle, for if someone's love for another can be measured by what they sacrificed for them, then I do not know of numbers that can express your love for me – and in the same breath, my love for you. But not only in your sacrifice, but also for believing in me, sharing in this whole adventure and making it a lot more fun!

And last but definitely not least: thank you Jesus! My relationship with Him was where everyday worries and frustrations was taken, where I was carried through in difficult times and where this journey of the last five years was sprinkled with the miraculous, the guarding of my heart from thoughts of giving up and the existence and upkeep of wonderful relationships and opportunities. He truly did equip me with everything I needed to complete this, and I believe, with that which comes next.

Munich, November 2015   M. Hamman de Vaal

Contents

Contents

Contents

Nomenclature

Abbreviations

AAA	Abdominal aortic aneurysm
AMG	Algebraic multigrid
BVP	Boundary value problem
CABG	Coronary artery bypass grafting
CBF	Cerebral blood flow
CC	Cross-clamping
CG	Conjugate gradient
CPB	Cardiopulmonary bypass
CST	Conventional sternotomy
CVA	Cerebrovascular accidents
CEABO	Constrained endo-aortic balloon occlusion
DNS	Direct numerical simulation
ECC	Extracorporeal circulation
ECG	electro cardiogram
ECMO	Extra-corporeal membrane oxygenation
ECM	extra-cellular matrix
EVAR	Endo-vascular aortic repair
EAB	Endo-aortic balloon
EABO	Endo-aortic balloon occlusion
FE	Finite element
GMG	Geometric multigrid
GMRES	Generalized minimal residual
HLFB	hypothermic low-flow bypass
IABC	Intra-aortic balloon counterpulsation
IAF	Intra-aortic filter
IMA	Internal mammary artery
ID	Inverse design
ILU	Incomplete LU factorization
LDPE	Low-density polyethylene
MAP	Mean arterial pressure
MIS	Minimally invasive surgery
MIVS	Minimally invasive valve surgery
MVOF	Minimum vascular occlusion force
NP	Neurophysiological (impairment)
OPCAB	Off-pump coronary artery bypass (grafting)
PC-MRI	Phase-contrast magnetic resonance imaging
PCI	Percutaneous coronary intervention
PHCA	Profound hypothermic circulatory arrest
PVW	Principal of virtual work
RCTs	Randomized controlled trials

ROIs	Regions of interest
SCAD	Small capillary arteriolar dilations
SEF	Strain energy function
SMCs	smooth muscle cells
TCD	Transcranial Doppler (ultrasound)
TECAB	Totally endoscopic coronary artery bypass
TEVAR	Thoracic endo-vascular aortic repair
TEE	Transesophageal echocardiography
VAD	Ventricular assist device
WS	Watershed (areas in the brain/infarction)
WSS	Wall shear stress

Terminology

Aortic manipulation	Any surgical intervention disturbing the physiological state of the aorta, whether related structurally to the wall or in terms of the flow within
Cannula	Here specifically the arterial cannula, used to feed/return blood from the heart-lung-machine to the systemic (high pressure) circulation of the patient
Cannula tip	The part of the cannula that is inserted into the aorta, usually limited in depth by a type of flange. The tip has the narrowest diameter through which the blood has to flow
Cannula tip conduit	The conduit of the tip
Cannula conduit	The part of the cannula preceding the tip that is *not* inserted into the cannula
Cannula configuration	The orientation of the cannula and its relative insertion depth (tip-to-opposite-wall distance)
Luer lock	$\sim$2 cm from the inflow side, is a transverse opening to the cannula conduit that can easily be opened or closed to allow e.g. flushing of air, administration of pharmacological agents, etc.
Occluder	Any instrument that is used to occlude a vessel – here, the aorta. Examples include cross-clamps and endo-aortic balloon occlusion (EABO)
Occlusion site	The axial position of the vessel where the occluder is/will be applied
Occluder configuration	The position and/or the orientation of the occluder at the Occlusion site
Occluder loading configuration	The different mode in which an occluder applies a load on the vessel
Occluding load	The load applied by the occluder, not implying that the vessel is or has already been occluded
Occlusion potential	a scalar value that describes the potential of the current occluding load to yield an occluded state of the vessel, cf. Section 7.4.1

Operators, symbols and superscripts

$(\cdot)^{\mathsf{T}}$	Transpose of a tensor
$(\cdot)^{-1}$	Inverse of a tensor or mapping
$(\cdot)^{-\mathsf{T}}$	Transpose of the inverse of a tensor
$\dot{(\cdot)}$	First time derivative

$\hat{(\cdot)}$	Prescribed quantity
$\tilde{(\cdot)}$	Modified or transformed quantity
$(\cdot)^{(e)}$	Element
$(\cdot)^{(1)}, (\cdot)^{(2)}$	Slave/Master
$\mathbf{0}$	Zero tensor
$\mathbf{1}$	Identity tensor
$\delta(\cdot)$	Virtual quantity
$\Delta(\cdot)$	Increment
$\otimes$	Dyadic product
det	Determinant
Div, $\nabla\cdot$	Material divergence operator
Grad, ∇	Material gradient operator
Lin	Linearization operator
tr	Trace operator

Nonlinear structural and contact continuum mechanics

A, a	Area in the reference/current configuration
$\boldsymbol{a}_0$	Directional vector describing directional dependence of fiber-reinforced, anisotropic material in the reference configuration
$\boldsymbol{C}, \boldsymbol{b}$	Right/left Cauchy-Green deformation tensor
$\mathbb{C}$	Material tangent or constitutive tensor for linear elasticity
$\boldsymbol{E}, \boldsymbol{e}$	Green-Lagrange/Euler-Almansi strain tensor
$\bar{E}_i$	Green-Lagrange strain-like term (for n-fiber families)
$\mathcal{E}_{\mathsf{int}}$	Internal energy
$\boldsymbol{f}$	Force vector
$\boldsymbol{F}$	Deformation gradient
g	Gap function
Γ_0	Boundary in reference configuration
$\Gamma_{0,u}$	Dirichlet partition of boundary in reference configuration
$\Gamma_{0,\sigma}$	Neumann partition of boundary in reference configuration
$\Gamma_{0,c}, \Gamma_c$	Potential contact partition of boundary in the reference/current configuration
$I_j, \bar{I}_j$	j^{th} principal invariant/j^{th} modified invariant
J	Jacobian determinant, determinant of $\boldsymbol{F}$
$\boldsymbol{\lambda}, \lambda_n, \boldsymbol{\lambda}_\tau$	Lagrange multiplier vector: all/normal/tangential component
$\lambda_{\mathsf{fib}}, \lambda_{\mathsf{fib}}^{zz}, \lambda_{\mathsf{fib}}^{\theta\theta}$	Stretch in fiber direction: total/longitudinal/circumferential
$\lambda_1, \lambda_2, \lambda_3$	Principal stretches
$\boldsymbol{M}_1, \boldsymbol{M}_2, \boldsymbol{M}_3$	Principal direction basis vectors in the reference configuration
$\boldsymbol{m}_1, \boldsymbol{m}_2, \boldsymbol{m}_3$	Principal direction basis vectors in the current configuration
$\boldsymbol{N}, \boldsymbol{n}$	Unit normal vector in the reference/current configuration
Ω_0, Ω	Reference/current configuration
$\partial\Omega_0, \partial\Omega$	Boundary in reference/current configuration

p	Lagrange multiplier (for enforcing of compressibility constraint)
p_n	Normal contact traction (contact pressure)
P	Contact mapping from slave to master surface
$\boldsymbol{P}$	First Piola-Kirchhoff stress tensor
ϕ	Coulomb limit
$\Psi, \bar{\Psi}, \Psi_{\text{vol}}$	Strain energy function: total/isochoric/volumetric components
$\boldsymbol{Q}$	Orthogonal rotational tensor
$\boldsymbol{R}$	Rotation tensor
$\boldsymbol{S}$	Second Piola-Kirchhoff stress tensor
$\boldsymbol{\sigma}$	Cauchy stress tensor
$\boldsymbol{t}_0, \boldsymbol{t}$	Traction vector in reference/current configuration
$\boldsymbol{t}_c, \boldsymbol{t}_\tau$	Contact traction vector: total/tangential
$\boldsymbol{u}$	Displacement vector
$\boldsymbol{U}, \boldsymbol{V}$	Material stretch/spatial stretch tensor
$\boldsymbol{v}_{\tau,\text{rel}}$	Relative tangential velocity vector
V, v	Volume in the reference/current configuration
$\boldsymbol{w}$	Weighting function vector
$\delta W, \delta W_{\text{int}}, \delta W_{\text{ext}}$	Virtual work: total/internal/external
$\boldsymbol{X}, \boldsymbol{x}$	Position in reference/current configuration
χ	Mapping between reference and current configuration

Physical structural quantities

α_{fib}	Fiber-family orientation with respect to the circumferential direction
α_{HU}	HU-dependent material parameter
c, c_1, c_2, c_3	Material parameter (isotropic)
E	Young's modulus
HU	Radio-density attenuation coefficient (Houndsfield unit)
k_1, k_2	Stress-like material/dimensionless parameter for exponential anisotropic constitutive models
λ, μ	Lamé parameters
μ_τ	Friction coefficient
ν	Poisson's ratio
κ	Bulk modulus
κ_d	Fiber dispersion parameter
κ_{calc}	Bulk modulus for calcification

Discretized quantities

$\boldsymbol{d}, \boldsymbol{D}$	Element-wise/global nodal displacement vector
$\boldsymbol{f}_{\text{int}}, \boldsymbol{f}_{\text{ext}}$	Element force vectors: internal/external contributions
$\boldsymbol{F}_{\text{int}}, \boldsymbol{F}_{\text{ext}}$	Global force vectors: internal/external contributions
n_{ele}	Number of elements
$\boldsymbol{R}$	Global residual vector
$\boldsymbol{K}_T$	Tangential stiffness matrix

Occlusion-related quantities (structural simulations)

$A_c^{\mathrm{adv}}, A_c^{\mathrm{int}}$	Contact area: adventitial/intimal
$|A_{\mathrm{cl}}^{\mathrm{lumen}}|$	Clamped luminal area, normalized to the unoccluded luminal area
α_{CC}	Relative angle of axial rotation (of the cross-clamps)
α_{rot}	Angle between plane in which clamp-arms are hinged longitudinal direction of clamp-surfaces
BB	Bounding box used in capturing $\mathcal{S}_c^{\mathrm{closed}}$
$\mathcal{C}$	A set of all possible contour lines of a certain property
$D_{\mathrm{i}}, D_{\mathrm{o}}$	Inner/outer diameter
$\varepsilon_1, \varepsilon_2, \varepsilon_3$	principal strain components
$\varepsilon_{\mathrm{EA}}$	Euler-Almansi strain
$\varepsilon_{\tau,\max}$	Maximum shear strain
$\varepsilon_{\mathrm{VM}}$	Von Mises strain
$F^{\mathrm{cl}}, F_n^{\mathrm{cl}}, F_\tau^{\mathrm{cl}}$	Applied clamp force: total/normal/tangential
$\boldsymbol{F}_n, \boldsymbol{F}_\tau$	Contact force vectors: normal/tangential
$F^{\mathrm{migr}}, F_n^{\mathrm{migr}}, F_\tau^{\mathrm{migr}}$	Migration resistance force of the occluder: total/normal/tangential components
$h_{\mathrm{x}}^{\mathrm{closed}}, h_{\mathrm{y}}^{\mathrm{closed}}$	Relaxation distances to reduce the BB to sufficiently capture $\mathcal{S}_c^{\mathrm{closed}}$
$L_{\mathrm{a}}, L_{\mathrm{a}}^{\mathrm{occl/cann}}, L_{\mathrm{a}}^{\mathrm{constr/EABO}}$	Axial (centerline) length/Occlusion site to cannula distance (measured along centerline)/Offset between constrainer and EABO
L_{rot}	Length of the hinged, rotating arm, i.e. hinge to start of clamp surface
L_{w}	Clamp surface width
$\boldsymbol{n}^{\mathrm{cl}}$	Clamp surface normal
$\boldsymbol{n}^{\mathrm{vess}}$	Direction of the vessel axis, current configuration
$n_{\mathrm{ele}}, n_{\mathrm{ele}}^{\mathrm{ROI}}$	Number of elements/elements within the ROI
$n_{\mathrm{nd}}^{\mathrm{occl}}$	Nodes on the vessel surface making contact with the occluder
p_n, p_n^{int}	Normal contact traction or contact pressure/contact pressure on the intima
p_n^{occl}	Occlusion potential – highest value of contact pressure in $\mathcal{P}^{closed}$
$\mathcal{P}^{closed}$	A set of contact pressure values corresponding to each contour line in $\mathcal{S}_c^{\mathrm{closed}}$
$|P_{\mathrm{EAB}}|$	EAB pressure, normalized to the maximum EAB pressure considered
$\mathcal{Q}_c, \mathcal{Q}_{c,i}$	The set/subset of all possible points on the curves of $\mathcal{S}_c$
q, q_x, q_y	Cartesian coordinates of points in some subset of $\mathcal{Q}_{c,i}$, x-coordinate only, y-coordinate only
$R_i^{\mathrm{v}}, R_{\mathrm{EAB}}$	Inner radius of vessel/EAB, reference configuration
$\mathcal{S}_c$	A subset of $\mathcal{C}$ formed by the contact pressure p_n on the to-be-occluded surface
$\mathcal{S}_c^{\mathrm{closed}}$	A subset of $\mathcal{S}_c$ that form closed lines on the to-be-occluded surface, i.e. *valid lines along which occlusion can occur*
$\mathcal{S}_c^{\mathrm{open}}$	A subset of $\mathcal{S}_c$ that does not include $\mathcal{S}_c^{\mathrm{closed}}$
T_{w}	Wall thickness
$V_h^{\mathrm{aCalc}}, V_h^{\mathrm{pCalc}}$	Discretized calcification volume: all and pure calcification only
$|V_{\mathrm{EAB}}|$	EAB volume, normalized to the maximum EAB volume considered when only considering the EAB

Fluid mechanics

$\boldsymbol{u}$	Fluid velocity
$\bar{p}, p$	Hydrostatic/kinematic fluid pressure
μ_{f}	Dynamic viscosity
μ_{∞}	Maximum shear thinning dynamic viscosity
ν_{f}	Kinematic viscosity
$\boldsymbol{\varepsilon}$	Strain rate tensor
ρ_{f}	Fluid density

Arterial cannular flow-related quantities (fluid simulations)

A_{danger}	Danger-zone area
A_{slice}	Slice surface area (through fluid domain)
A_i^{v}	Surface area element (of the vessel surface)
β_{tip}	Tip angle, relative to axial direction of preceding cannula conduit
$D_i^{\mathrm{v}}, d_i^{\mathrm{c}}$	Inner diameter of vessel/cannula
$h_{\mathrm{b}}, h_{\mathrm{f}}$	Base-level/first element discretization size
$L_a^{\mathrm{v}}, L_a^{\mathrm{c}}$	Axial length (centerline distance) of vessel/cannula, also referred to as tip conduit length
$L_{\mathrm{a}}, L_a^{\mathrm{cann/out}}, L_a^{\mathrm{occl/cann}}$	Axial (centerline) length/cannula to outflow length (measured along centerline)/occlusion site to cannula distance (measured along centerline)
L_{depth}	Relative insertion depth of cannula tip into vessel
$\mathrm{n}_{\mathrm{ele}}$	Number of elements
$\mathrm{n}_{\mathrm{nd},i}, \mathrm{n}_{\mathrm{nd},i}^{\mathrm{danger}}$	Nodes belonging to a specific A_i^{v}/nodes belonging to a specific A_i^{v} above a endothelium erosion threshold (danger threshold)
$\boldsymbol{n}^{\mathrm{slice}}$	Outward normal of a slice through the fluid domain
$\boldsymbol{n}^{\mathrm{vel}}$	Normalized nodal velocity
ΔP	Pressure drop
P_{slice}	Nodal values of pressure in a slice through the fluid domain
P_{out}	Nodal values of pressure at the outflow surface
Q, Q_{in}	Flow rate, inflow flow rate
R_{center}	Centerline radius of main cannula curvature
Re	Reynolds number
$\boldsymbol{v}, \boldsymbol{v}_{\mathrm{in}}$	Flow velocity/inflow velocity
v_{exit}	Exit velocity
y_n	Direction orthogonal to the wall, considering the calculation of WSS

Simulation abbreviations (structural)

$CC_{\parallel}$	Cross-clamps, parallel
CC_{std}	Cross-clamps, standard (DeBakey)
CC_{crab}	Cross-clamps, crab pincher-like (Cosgrove/Chitwood)
$CEABO_{\mathrm{n,i}}$	Constrained EABO, narrow constrainer, offset with EAB of i mm
$CEABO_{\mathrm{w}}$	Constrained EABO, wide constrainer, offset with EAB of 0 mm
$CEABO_{\mathrm{p,i}}$	Constrained EABO, profiled constrainer, offset with EAB of i mm
$CC_{\theta}^{\mathrm{Calc},i}$	Cross-clamps, standard (DeBakey), patient-specific aorta *with* calcifications, at relative axial rotation θ and position i
$CC_{\theta}^{\mathrm{noCalc},i}$	Cross-clamps, standard (DeBakey), patient-specific aorta *without* calcifications, at relative axial rotation θ and position i
$EABO_{\mathrm{pure}}$	Endo-aortic balloon occlusion (EABO)

Simulation abbreviations (fluid)

$Endh_{\theta_{\mathrm{trans}},\theta_{\mathrm{long}}}$	End-hole cannula, straight, at different transverse θ_{trans} and longitudinal θ_{long} orientations
$Endh_{\mathrm{d},i}$	End-hole cannula, straight, at different insertion depths i relative to flange-determined depth
$Endh_{\mathrm{str}}$	$\equiv Endh_{0°,0°} \equiv Endh_{\mathrm{d},0}$
$Endh_{\mathrm{curv}}$	End-hole cannula, curved, forward-facing (downstream-pointing)
$Endh_{\mathrm{curv}}^{\mathrm{sh}}$	End-hole cannula, curved, shielded, backward-facing
$Endh_{\mathrm{ic}}$	End-hole cannula, straight, in an incompletely clamped artery
$Endh_{\mathrm{CC},\theta}$	End-hole cannula, straight, in a patient-specific, incompletely cross-clamped artery corresponding to $CC_{\theta}^{\mathrm{Calc},1}$
$Side_{\mathrm{str}}$	Side-hole cannula, straight
$Side_{\mathrm{curv}}$	Side-hole cannula, curved, forward-facing
$Hybr_{\mathrm{str}}$	Hybrid cannula, straight
$Hybrid_{\mathrm{curv}}$	Hybrid cannula, curved, forward-facing

1. Introduction

(...since) the world's first successful open heart procedure...aortic manipulation and post-operative neurological complications have co-existed.

— Lange et al. [206]

1.1. Background

1.1.1. Cardiac surgery outcomes: scale, impact and importance

Numerous review articles and books have covered the best practices for cardiac surgery, especially with regards to preventing or minimizing neurological injury due to emboli or hypoperfusion, as well as the management of systemic inflammatory response, ischemia in other end-organs, aortic dissections, etc. [5, 31, 89, 121, 139, 162, 192, 206, 221, 257, 267, 291, 311, 318, 327]. Such a review of best practice cardiac surgery is usually compiled by considering a multitude of different equipment, patient and procedural-related risk factors, as well as pre-, peri- and post-operative screening, monitoring, procedural options and optimal clinical management. Since the inception of open-heart surgery in the 1950's, pharmacological, technological and procedural advances and the subsequently gained experience are continually enabling increased access to previously inoperable patients that form part of an ever increasing population requiring such interventions, whilst keeping complication rates relatively low, as shown in Figure 1.1. Although cardiac surgical procedures are expected to decrease due to improved preventative measures and percutaneous interventions, even considering a constant decline in incidence still constitutes a substantial amount of procedures required, as indicated in Figure 1.1c.

Nevertheless, the complication rate remains significant and needs to be further addressed due to the immense impact these complications have on patient morbidity and mortality, as well as the strain on health-care systems [296, 318]. Further aspects to be considered in this regard include the sheer number of open-heart procedures performed worldwide – approximately 2 million annually [121, 279], the fact that the worldwide occurrence of cardiovascular disease is one of the major causes of death and is still on the increase [360], that the complication rates are becoming higher as the procedure increases in complexity [192, 257] and that the aging patient-population requiring these interventions presents more co-morbidities, especially cerebrovascular disease and atheromatous disease, that can aggravate complications even further [64, 107, 221].

1.1.2. Cardiac surgery-related cerebrovascular accidents (CVAs)

Although exceptional advances have been made in myocardial protection during cardiac surgery, limited progress have been achieved in protecting the brain [221]. As such, apart from procedural failure, probably the most devastating complications associated with cardiac surgery are cerebrovascular accidents (CVA), which can range from transient cognitive impairment to stroke and death. Patient age also increases the likelihood of neurological deficit, which is not necessarily the case with outcomes such as myocardial infarction or low cardiac output state [64, 221], cf. Figure 1.1b. CVAs are typically classified clinically as
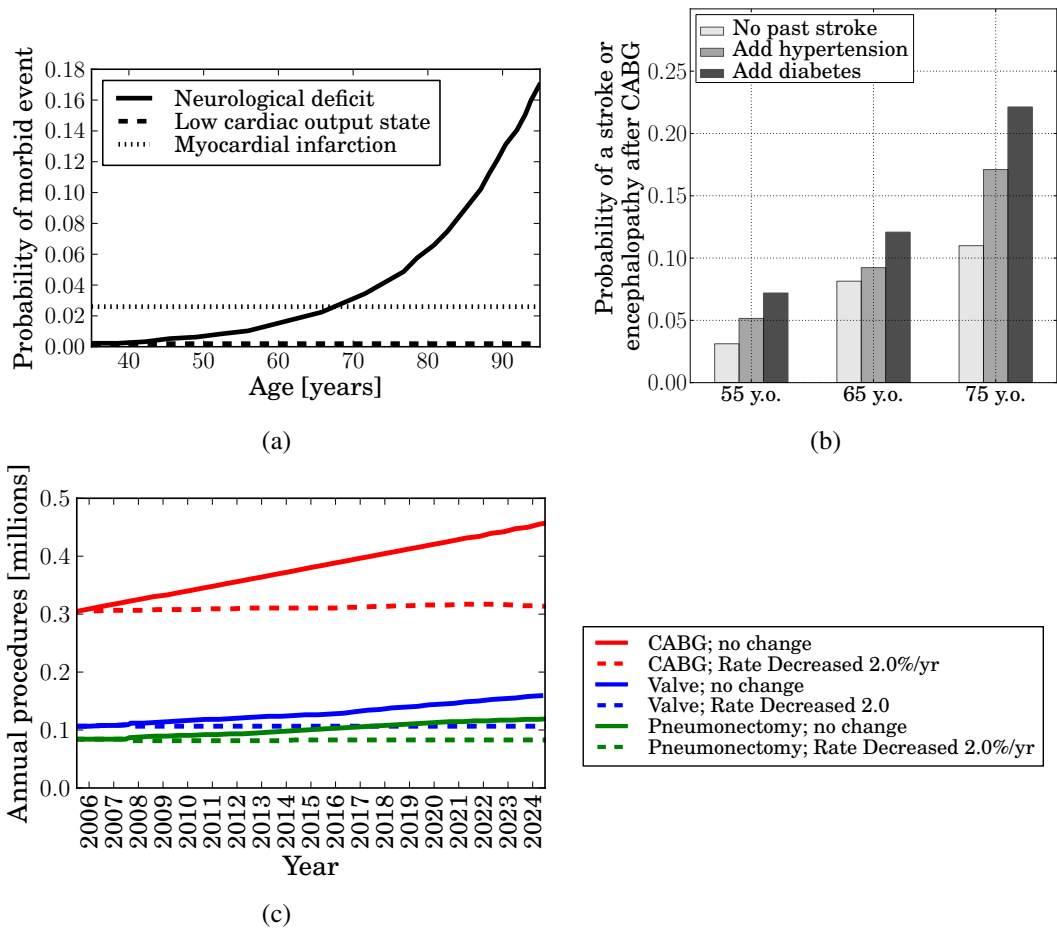
Figure 1.1.: Cardiac surgery outcomes, relative to age, co-morbidities and number of procedures per annum, showing (a) probabilities of main outcomes vs. age, adapted from [339], (b) probabilities of outcomes vs. age and co-morbidities, adapted from [235] and (c) projected number of annual cardiac procedures in the USA, showing scenarios of a constant incidence and constant decline, adapted from [101].

Type I (most severe, clinically apparent), Type II (less severe, easily assessable post-operatively) and neurophysiological (NP) impairment (least severe, sophisticated post-operative neuropsychometric testing required) [296]. Citing a current review on neurological protection during cardiac surgery [291], Type I and Type II deficits normally vary between 0.9% and 5.4% and between 3.0% and 10%, respectively. NP impairment varies even more, with incidence rates ranging between 28% and 79% being reported for the period immediately post-operative and between 19% and 57% of persisting NP impairment at six months follow-up. These variations are dependent on the type of procedure performed, as well as patient-related risk factors. Although some limitations with regards to correctly and consistently diagnosing Type II injury and NP impairment do exist, including laborious testing and learning curve dependent diagnoses [37, 299], the weight of consequences associated with CVAs during cardiac surgery is clearly evident. Not only patient-related consequences are to be noted, but also the financial implications thereof. Based on a landmark report in the mid-1990's [296], it was calculated that at that stage, only considering cerebral injury from cardiac surgery, costed the US approximately $2–$4 billion annually, which included in-hospital, out-of-hospital and rehabilitation services. Another study found that only the direct cost of

stroke after coronary artery bypass grafting (CABG) already amounts to between $90,000 and $228,000 per patient lifetime, which excludes indirect costs such as loss of productivity [95].

The major cardiac surgery-related ischemic CVA etiologies include particulate and gaseous embolic events, cerebral hypoperfusion and a generalized inflammatory reaction. Other etiologies are also known, including focal vaso-motor spasm, cerebral reperfusion injury, as well as toxic and metabolic effects [121, 139, 151]. Of these, the release of emboli into the systemic circulation and hypoperfusion of the brain are considered the most common etiologies of CVAs and are the focal point etiologies considered in this investigation.

1.1.2.1. CVA etiology: Emboli

Emboli are gaseous or particulate matter suspended in the blood and originate from either equipment-, procedural- or patient-related factors. It can consist of air, tube fragments generated by the pump, glove powder, silicone anti-foam, chylomicrons, remnants of damaged cells, lipids from the surgical field, debris from the disruption of atherosclerotic plaques and/or calcifications, etc. [327]. The danger of these emboli is that they could potentially occlude an artery/arteriole, leading to tissue ischemia distal to such an occlusion site when no sufficient co-lateral perfusion pathway(s) exist.

Of all the etiologies of emboli that can potentially lead to CVAs, the most notable has been identified as the presence of atherosclerosis in the ascending aorta and aortic arch. Atherosclerotic lesions can potentially be disturbed by aortic manipulation during cardiac surgery, giving rise to atherosclerotic/atheromatic emboli entering the systemic circulation and potentially contributing to neurological and other end-organ ischemia [26, 36, 38, 42, 44–46, 89, 113, 151, 186, 220, 326, 343, 344]. Probably the most definitive demonstration that such lesions are disturbed and cause a substantial release of emboli into the arterial circulation was in a number of studies investigating the use of an intra-aortic filter inserted distal to the cross-clamping site during cardiopulmonary bypass (CPB) procedures, cf. Section 4.2.2.1. These studies found that the overwhelming majority of particulate emboli physically captured with such a filter were atheromatic in origin.

Furthermore, although equipment- and procedural-related factors responsible for emboli generation can be controlled/minimized to a large extent – enabled especially by technological advancements, surgical technique-related improvements and evidence-based algorithms – the patient-related factors, especially the presence of atherosclerosis, cannot. Atherosclerosis among the patient population requiring cardiac surgery remains prevalent and will increase in future as the world population ages and increases [107, 221], cf. Figure 1.1c. Prevalence of atherosclerosis in patients was already demonstrated in a study using data from the 1980's: In a large cohort of patients (n=1735, mean age=68.9 yrs) undergoing coronary artery bypass surgery, 4.5%, 2.2% and 2.0% presented with mild, moderate and severe atherosclerosis of the ascending aorta, respectively [241]. Since then, such prevalence has repeatedly been reported, as shown in Figure 1.2.

All of these reviewed factors concerning the danger of disrupting an atherosclerotic lesion are clearly evident from the following guidelines set by the American Heart Association (AHA) regarding the principle factors affecting cardiac surgery patient outcome, as taken from Slaughter et al. [318]:

- Post-operative stroke is the second most common cause of operative mortality;

- The surgeon's identification of an atherosclerotic ascending aorta is the single most significant marker for an adverse cerebral outcome after coronary bypass operations;

- Atherosclerosis plays a role in at least two-thirds of adverse events after coronary bypass;

- Significant atherosclerosis of the ascending aorta mandates a surgical approach that will minimize the possibility of atherosclerotic emboli;
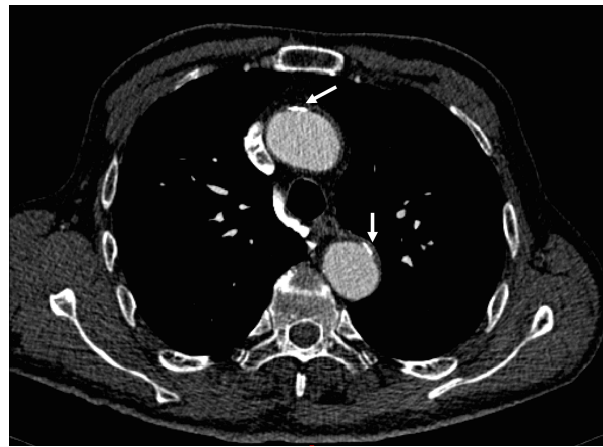
(a)
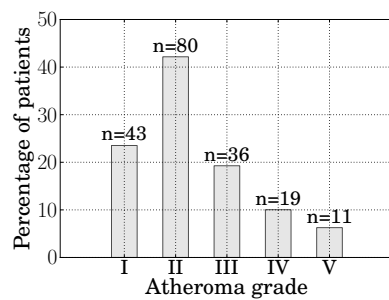
(b) Distribution of atheroma grades (n=189)
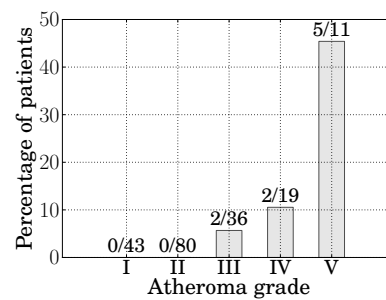
(c) One week stroke rate as a function of
atheroma grade (n=189)

Figure 1.2.: Common manifestations of atherosclerosis, showing (a) an axial sliced CT-scan from a typical patient requiring surgical intervention, where substantial calcific lesions in the ascending aorta (top) and descending thoracic aorta (bottom) are indicated by white arrows and showing (b) the grades of atheroma confronted clinically and patient outcomes, in a patient population undergoing multi-vessel on-pump coronary artery revascularization (n=248), adapted from [155] and (c) the resulting stroke rates, adapted from [155].

- Peri-operative athero-emboli from aortic arch plaques to be the culprit in one out of three strokes following coronary artery revascularization;

- Patients who are actually receiving cardiac surgery are older than in the past. Atherosclerosis plays a role in two-thirds of all adverse events after revascularization.

1.1.2.2. CVA etiologies: Hypoperfusion

Hypoperfusion refers to insufficient or less than normally required, homeostatic circulatory supply of oxygenated blood to the entire brain or parts thereof. It is widely accepted that permanent ischemic brain injury due to circulatory arrest typically sets in after approximately four minutes. However, the extent of permanent ischemic brain injury when oxygen supply to the brain is still present, but less than required, varies due to a number of factors, which is especially important for any surgical intervention disrupting normal physiological hemodynamics, such as cardiac surgery.

As stated in a recent review by Grocott [140], due to the mechanism of permanent ischemic brain injury described above, the first mechanism of perioperative CVAs that enjoyed intensive clinical consideration was that of hypoperfusion during CPB. The main parameter considered in this context was the mean arterial pressure (MAP) that was maintained during CPB. Animal studies revealed that healthy auto-regulatory mechanisms were responsible for preventing increases in cerebral blood flow (CBF) above a MAP of 50 mmHg. Above this threshold, CBF basically plateaued. Clinically, MAP is usually maintained between 50 mmHg and 100 mmHg, although patients with chronic hypertension or anemia benefit from an increased lower threshold of MAP during CPB. Adequate MAP during cardiac surgery can be maintained through different means, including increasing flow from the CPB, procedural alterations, anesthetic management and inducing cerebral hypothermia. The latter reduces the metabolic requirements and therefore also the oxygen demand. Thereby, the likelihood and risk of hypoperfusion is reduced and is generally seen as neuroprotective. Although the induction of hypothermia is a widely considered topic, it is outside the scope of this investigation and can be reviewed elsewhere [151]. These findings are of equal importance to off-pump cardiac surgeries, since although no CPB is required, the MAP is also significantly altered during such a procedure.

1.1.2.3. CVA etiologies: Synergy between emboli and hypoperfusion

An oversimplified, yet often considered assumption of the combined effects of these two etiologies, is to consider them in isolation: emboli are distributed proportionally to blood flow, and therefore less perfusion would mean less embolic risk, but increased hypoperfusion risk and *vice versa*.

A very telling indication that cardiac surgical-related adverse neurological consequences occur due to a complex combination of embolic and hypoperfusion etiologies, comes from investigations of the pathophysiology of watershed (WS) infarctions in patients with internal carotid artery disease, as reviewed by Momjian-Mayor and Baron [249], considered in the following.

A WS infarction can be defined as an infarct occurring in the junction between two distal perfusion fields, i.e. after many bifurcation generations, down to the levels of arterioles and capillaries, of two non-anastomosing arterial systems. Such infarctions are in contrast to localized "wedge-shaped" and/or deep striato-capsular infarcts. A number of studies investigating the origins of such WS infarctions have propagated the notion that either severe hypotension or emboli are responsible for watershed infarctions – causing considerable controversy. Hypoperfusion has been attributed as the main cause of WS infarctions based on the supposition that perfusion pressure is the lowest at these distal perfusion fields, thereby causing WS infarction upon repeated episodes of hypotension. This interpretation has also been supported by radiological studies indicating that WS infarctions in these diseased conditions are more likely with a non-competent circle of Willis, i.e. where co-lateral perfusion has been impaired. Other aspects such as vessel stenosis, frequently associated with internal carotid artery disease, have also been implicated on the same grounds. On the other hand, emboli have been attributed to cause WS infarctions based on emboli found in post-mortem evaluations, especially microemboli that preferentially occlude small vessels in these WS areas due to their distinctly small size.

Inconsistencies in findings that prefer the one etiology over the other have lead some investigators to propose a synergism of these two etiologies based on the following: Patients where areas of marginal perfusion exists, e.g. in WS areas, may be more susceptible to embolic events due to the already exhausted vascular reserve and a reduced clearance/wash out of microemboli would be possible. Of course, the etiology of hypoperfusion cannot be identified as easily as an embolic event etiology, especially in post-mortem investigations. Although a seemingly probable etiology, at the time of this review, a hypothesis of the synergistic effect between hypoperfusion and emboli at causing neurological injury has not been unequivocally demonstrated to be true, or not. Notwithstanding, a more recent review considering the role

of hypotension in perioperative stroke could still not uncover the exact mechanism, due to the complex nature of such a multifactorial problem and the inability to clearly pinpoint the exact etiology/ies [33].

However, certain recent findings provide further evidence for and more clarity on this phenomenon, particularly in relation to cardiac surgery outcomes. Initial support of such a synergistic relationship between these two etiologies came from a study demonstrating that patients at higher risk for embolic stroke due to severe atheroma were more likely to have adverse neurological outcomes following cardiac surgery when a lower MAP was maintained compared with a higher MAP [155]. Furthermore, many research groups have found a positive correlation between the number of emboli entering the CBF and neurological outcome [70, 175, 220, 287, 341], also clearly evident from findings from animal studies and pathological findings in humans [160, 231, 251]. However, such a positive correlation does not imply a linearly proportional relationship [326] and non-correlating findings remain [27, 213]. One of the best examples demonstrating contradictory findings and the complex synergy of etiologies responsible for adverse neurological outcome are studies comparing on-pump and off-pump coronary artery revascularization. On the one hand, a number of trans-cranial Doppler (TCD) studies have clearly shown a significant reduction of emboli entering the cerebral circulation, as reviewed by Dittrich and Ringelstein [88]. On the other hand, a very recent special report considering retrospective non-randomized, prospective randomized, and meta-analyses trials comparing these two surgical approaches states that off-pump procedures have failed to show a reduction in adverse neurological outcomes [208], despite the expected lower embolic load entering the cerebral circulation.

These conflicting results can be attributed to the fact that only considering one etiology in isolation within such a correlation, is a coarse assumption of a complex occurrence made with non-specific data. The brain is a complex non-homogeneous organ with a delicate, yet robust perfusion system, which substantiates the above statement based on the following: Firstly, monitoring emboli entering the cerebral circulation with TCD cannot as of yet unequivocally distinguish between gaseous and particulate matter, nor the nature of the particle, and is limited in resolution [88]. TCD studies are thus far the only intraoperative method of determining embolic load entering the cerebral circulation. Secondly, the complexity of embolic stroke comes in part from the uncertainty about the nature, size and number of emboli, the potential conglomeration of emboli, as well as the possible perfusion paths and whether collateral paths exist [27, 36, 42, 292, 326]. Thirdly, the severity of an embolic occlusion also varies based on the quality of the brain parenchyma and vascular reserve capacity [27, 64], i.e. generally, elder patients with more co-morbidities might be affected more by embolic occlusion than younger, healthier patients. Although not elucidated upon in these investigations, the latter aspect might conceivably be equally applicable to considerations of cerebral hypoperfusion.

Without even considering other potential etiologies of perioperative stroke, such as systemic inflammatory response, it is clear that the relationship between the embolic and hypoperfusion etiologies are complex, multifactorial in nature, still incompletely understood and thus deserves further investigation.

1.1.3. Aortic manipulation: definition and significance

Studies investigating surgical-related aortic dissections have repeatedly demonstrated the occurrence of vascular injury due to some sort of manipulation of the aorta [61, 98, 149, 217, 324, 330], although injury has also been demonstrated when no dissection occurred [341], as shown in Figure 1.3a. The consequences of such vascular injuries that have repeatedly been attributed to cause or exaggerate perioperative CVAs, especially in the presence of atherosclerotic lesions, as reviewed in Section 1.1.2.1. Transcranial Doppler ultrasound (TCD) studies intraoperatively monitoring emboli entering the cerebral circulation have repeatedly shown how the embolic load relates to certain specific aortic manipulation maneuvers, i.e. surgical interventions. Moreover, manipulation of the aorta (or the heart) has also been shown to influence cerebral perfusion characteristics, also associated with causing or exaggerating peri-
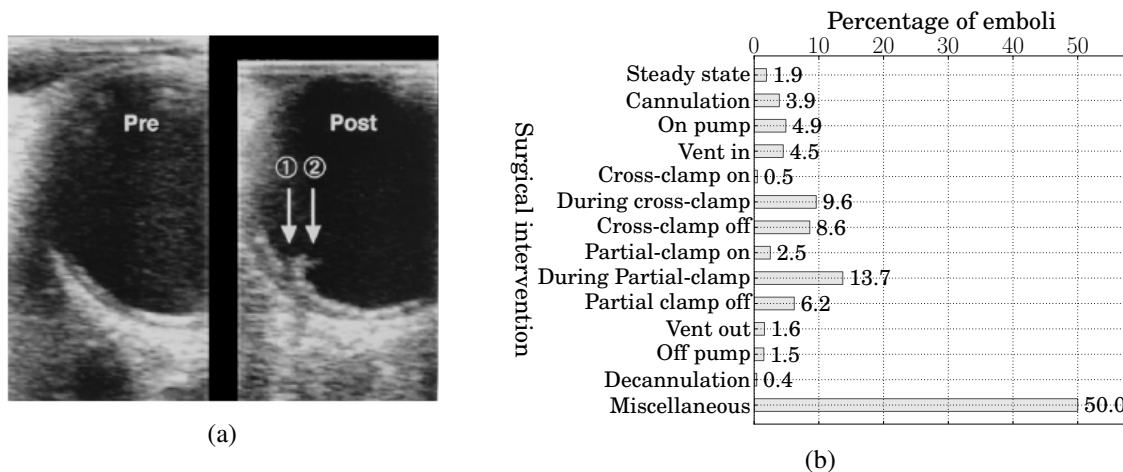
Figure 1.3.: (a) Epiaortic echocardiography demonstrating manipulation related injuries, adapted from [341] with permission, showing a new intimal tear (arrow 1) and a new mobile lesion (arrow 2), plausibly caused by manipulation and (b) a typical TCD study investigating emboli entering the cerebral perfusion during cardiopulmonary bypass (CPB), adapted from [326]

operative CVAs, as reviewed in Section 1.1.2.2. However, demonstration of which mechanism should be attributed for a subsequent CVAs remains difficult. From the studies reviewed in Section 1.1.2.3, it seems plausible to assert that there may be multiple mechanisms, that some or all interact and can have a variable influence. Current knowledge about these mechanisms of CVAs are unfortunately lacking. Nevertheless, it clearly becomes important to better understand the consequences of aortic manipulation and how these can be lessened.

With this background, a general definition for aortic manipulation can thus be given as any (mechanical) surgical intervention/maneuver responsible for a disturbance of the normo-physiological function and/or state of the aorta at any level along the arterial tree. For the purposes of this investigation, the main focus here will remain on the ascending aorta and the aortic arch. These manipulation maneuvers include surgical interventions that damage, deform, abrade or puncture the aortic wall, and also those that disturb physiological hemodynamics of the aorta. Inclusion of the latter into this definition has not always been implied when considering aortic manipulation. However, as will be made clear from this investigation, it is pivotal that the definition explicitly includes hemodynamical consequences of handling the aorta. Aortic manipulation maneuvers include, but are not limited to, aortic occlusion, partial-clamping, digital palpation, arterial cannulation, antegrade cardioplegia cannulation, grafting/anastomosing onto the aorta, arterial cannular jet flow, antegrade cardioplegia cannular jet flow, intra-aortic filters or catheterization, etc.

With the foregoing background of aortic manipulation in mind, the motivation for the investigation presented in this dissertation is formulated and expounded upon in the following section.

1.2. Motivation and research objective

Most manipulation maneuvers are an unavoidable part of many types of surgical treatments, which under given circumstances imply the least overall risk to the patient. If no procedures or technologies exist that can avoid manipulation, it must be reduced to an absolute minimum. In order to know how to avoid or reduce it, the manifold problems associated with aortic manipulation *in its entirety* must be better

understood. Although certain aspects of aortic manipulation have been well researched, a comprehensive investigation to elucidate upon the current clinical understanding, the mechanisms of injury, its potential far-reaching consequences, recent technological and procedural advances and novel ideas to lessen its impact, has not been undertaken in literature.

Consequently, the research objective of this dissertation is four-fold: (1) To consider the multi-factorial problem of aortic manipulation during cardiac surgery as it is currently understood in clinical terms, with special emphasis on the mechanical aspects of emboli and cerebral hypoperfusion associated with CVAs; (2) to evaluate the most critical aortic manipulation maneuvers in detail, using complex, state-of-the-art computational models not yet done before; (3) to propose novel ideas whereby the impact of these critical manipulation maneuvers can be lessened, using the same computational tools; and finally (4) to supply comprehensive up-to-date insights into the risks of aortic manipulation during cardiac surgery as a whole, in order to aid in clinical decision-making and facilitate the future directions of research that this investigation precedes.

With this dissertation, it is the aim of the author to address both a clinical and a technical audience. Thereby, it should firstly convey sufficient comprehension to clinicians who wish to better understand the impact and risks associated with aortic manipulation and to those involved in new procedural developments. Furthermore, with the help of the computational investigation, it is aimed to provide better understanding of aortic manipulation mechanisms responsible for increased risk to patient outcome, to aid clinical decision-making, but also to act as design input for improved technologies.

The main emphasis and volume of work presented will focus on the structural mechanical considerations, followed by fluid mechanical considerations. Specifically, focus will be placed on manipulation-related etiologies responsible for CVAs or other surgical complications associated with either emboli or hypoperfusion. The conveyance of clinical comprehension is approached from the perspective of understanding the problem in such a way that not only more complex analyses of these problems are realizable, i.e. enabling correctly formulated computational evaluations, but also allow requirement formulation for engineering improved solutions.

1.3. Outline

The above-stated research objectives are achieved in this dissertation in two parts.

Part I consists of an in-depth literature review investigating the current clinical comprehension of the aortic manipulation in cardiac surgery, as obtained from clinical and experimental research. It is performed for the three main categories, namely: large deformation manipulation by external equipment with the intention of occlusion, partially clamping or manual palpating, **Chapter 2**; disrupted hemodynamics during on-pump and off-pump procedures, **Chapter 3**; and direct laceration of the aorta by puncture and intra-aortic abrasion, **Chapter 4**. This part is brought to an end by a concluding discussion about the current clinical comprehension as a whole and future perspectives in **Chapter 5**. For improved clarity, relevant computational investigations from literature are only considered within the next part.

Part II considers the computational investigations performed as part of this investigation and is split from the first part for improved clarity. After presenting the computational analyses used to evaluate aortic manipulation in **Chapter 6**, the structural consequences of aortic occlusion in the context of an idealized aortic wall is investigated in **Chapter 7**. **Chapter 8** considers proximal cannular flow effects in the context of an idealized aortic lumen. Thereafter, patient-specific variability is respectively incorporated into the preceding structural and fluid investigations in **Chapter 9**.

Finally, a summary and an outlook is given, considering all the overall findings presented in **Part I** and **Part II**.

Part I.

Current clinical comprehension of aortic manipulation

2. Large deformation manipulation

Questions without answers must be asked very slowly.

— Anne Michaels

Many modern cardiac surgical procedures require the surgeon to largely deform the aorta without which the procedure would be impossible. Such maneuvers include occlusion of the aorta to prevent blood from entering the cardiac environment either by cross-clamping or by endo-aortic balloon occlusion (EABO), but also the partial occlusion of the aorta in order to perform a proximal graft anastomosis or to introduce a cannula, i.e. side-clamping. Although often considered as a side issue and part of a much more involved and complex procedure, it can have dire consequences with regards to patient outcome. Large deformation will induce supra-physiological strains on the different components of the aortic wall, especially the delicate intimal layer of the aorta. Additionally, in most cases such large deformations will also lead to additional compressive and shearing forces on the intimal layer when it is brought into contact either with itself, e.g. during cross-clamping or partial-clamping, or with an intra-luminal occluder, e.g. EABO.

The induced supra-physiological loading can lead to damage and is compounded by the presence of vascular pathologies, especially atherosclerotic lesions. The principal danger of these maneuvers is its potential to release significant amounts of embolic material into the arterial circulation. This has repeatedly been shown in transcranial Doppler (TCD) ultrasound studies to occur in all of these large deformation maneuvers during its application and subsequent removal, i.e. cross-clamping [26, 27, 213, 230, 255, 307, 326, 329, 332, 342], EABO [230, 307] and partial-clamping [26, 213, 255, 326, 332], and also depicted in Figure 1.3b.

The main focus in this chapter is the structural consequences brought on by large deformation aortic manipulation. Here, the background and mechanisms of injury of all aortic manipulation maneuvers responsible for large deformation are considered, followed by an in-depth review of experimental and clinical studies elucidating upon their risks to patient outcome. Particular emphasis is placed on the comparison of occluding techniques, due to the many advantages and disadvantages of both that are difficult to directly compare. For every maneuver considered, technological and potential procedural advancements will also be considered. Many findings and conclusions applicable to one maneuver are clearly of equal importance to another maneuver and will therefore not be repeated. Main consideration will be given to cross-clamping, EABO and partial-clamping, but also briefly considering digital palpation.

2.1. Aortic occlusion by cross-clamping

2.1.1. Fundamentals

Cross-clamping, also known as *trans-thoracic clamping*, *trans-aortic clamping* or *external aortic clamping*, refers to the occlusion of a vessel using a clamp positioned transversely across the whole vessel with the intention to temporarily occlude the blood flow. Its use can be traced back to the 16th century, when Ambroise Paré started to ligate arteries and devise occluding forceps instead of (largely uncontrolled) cauterization [199]. From the first scissor-like clamps used, the design and the concept of cross-clamping remain largely the same today, cf. angular DeBakey vascular clamp. The most commonly used clamp for

(a)   (b)
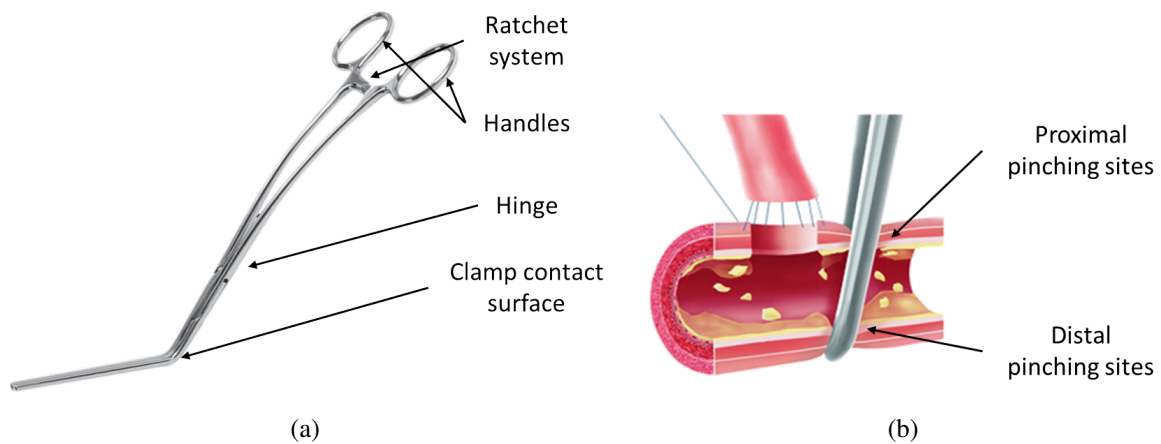
Figure 2.1.: A typical angular DeBakey cross-clamp, showing (a) the different parts of the clamp. An example of clamp application for a certain procedural variation of performing proximal anastomosis is shown in (b), adapted from [99] with permission.

this procedure is a variation of an angular vascular clamp, e.g. an angular DeBakey cross-clamp, which significantly deforms the aorta, as shown in Figure 2.1.

The main advantages of occluding the vessel with a cross-clamp are its stability, ease-of-use and the low direct costs involved [234, 294, 350], due to its reusability.

The three main disadvantages are the following: Firstly, it induces significant vascular injury [18, 39, 71, 94, 102, 157, 225, 226]. The main reason for this injury is simply due to the inherent configuration of cross-clamps which will inadvertently pinch the aorta, as further expanded upon below. Furthermore, whether or not a cross-clamped vessel has been occluded is unknown intra-operatively, unless a leak can be physically observed, which is a highly undesirable condition. Therefore, it implies that to ensure complete and stable occlusion, the vessel is always over-occluded, i.e. more force is applied to the vessel than what is needed to occlude it. Over-occlusion is further compounded by the fact that current cross-clamp design only allows the application of a discrete clamping force at relatively large intervals, as necessitated by the ratchet system designed to hold the cross-clamp arms in the clamped position. Currently, typical cross-clamp design for occlusion of large vessels has converged to a breadth of 4–5 mm and has ratchet notches that advance the clamp surfaces 0.8–1.0 mm (own measurements), due to space-saving, dexterity and practicality requirements. These dimensions have become standard despite the fact that a broader cross-clamp surface will better distribute the applied force in order to occlude the artery [157] and despite these relatively coarse notch intervals needed to occlude a large vessel with a typical wall thickness of between 1.0–2.5 mm. Secondly, it clutters the surgical field, which can become a significant hindrance, especially, but not limited to, minimally invasive procedures. Thirdly, upon clamping, the surrounding vessel geometry becomes largely deformed. This is problematic when considering surgeries like valve replacement or repair, where sewing/fixing a valve to a clamped (and therefore distorted) vessel, will inherently cause potential distortion of the valve after the clamps have been released. This is true to a lesser extent when performing proximal graft anastomosis on the aorta.

The mechanism by which iatrogenic injury of cross-clamping occurs has been widely studied. The most visible site of injury are a result of pinching of the vessel, due to the scissor-like/hinged configuration of a cross-clamp. This injury is most severe in the intima, followed by the media and then the adventitia [18, 157, 226]. An evaluation of cross-clamping-inflicted damage in an animal study is shown in Figure 2.2. Whereas most experimental studies only considered the subsequent injured vessel after cross-clamping

(a)

(b)
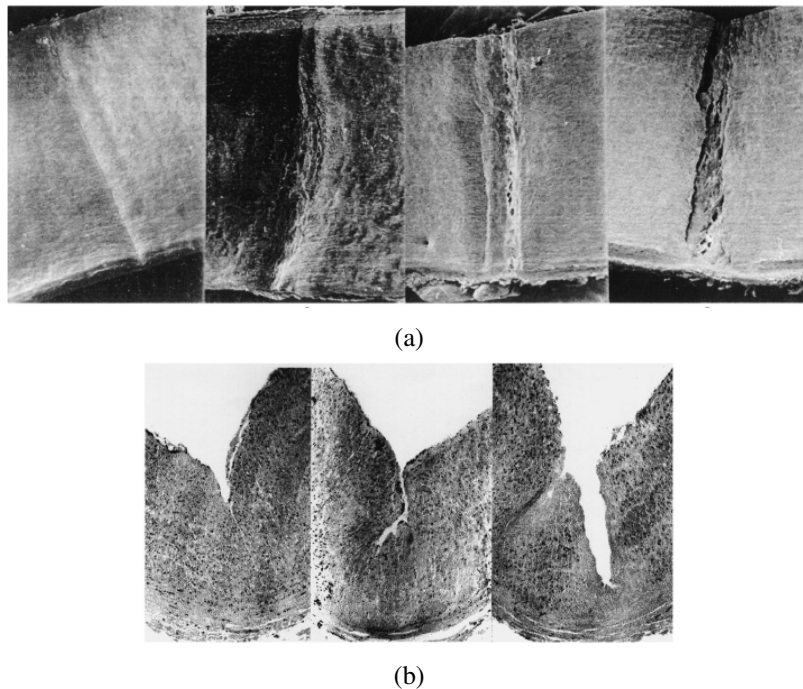
Figure 2.2.: Vascular injury due to cross-clamping, showing the laceration caused at the pinching site upon cross-clamping for (a) various notch levels $(3, 4, 5, 6)$ of a standard, surgically used cross-clamp evaluated by electron microscopy and (b) various grades of injury (mild, moderate and severe) evaluated by light microscopy – adapted from [226] with permission.

and mostly only qualitatively due to experimental limitations, the process by which such an injury actually progresses during cross-clamping is not completely understood.

2.1.2. Clinical considerations

Cross-clamping is considered a high risk procedure for both healthy and diseased arteries [71, 337]. The traumatic effect of cross-clamping increases the risk of emboli release in that it can cause intimal tears and flaps, as well as disrupt atherosclerotic lesions which carry the risk of becoming dislodged as emboli, as has been discussed in Chapter 1. It is considered to be particularly dangerous to cross-clamp an atherosclerotic lesion directly. However, even if a detected lesion is not directly cross-clamped, the risk of emboli occurring becomes higher for patients with a higher global atheroma burden, since it affects the global aortic wall material properties [224, 320]. The reason for this is that the aortic quality in terms of atherosclerosis in general has been correlated to the occurrence of CVAs [71] and because detection methods are neither perfect nor faultless, leading to a consistent proportion of bad aortas only discovered intra-operatively [369]. Furthermore, cross-clamping the most atherosclerotic-free part of the aorta is not always practically possible or could add additional, unnecessary or even dangerous procedural complexity. Additionally, subsequent mild or severe vascular injury due to cross-clamping has also been shown to increase platelet uptake in healthy animals [225]. It has also been shown that fibrous plaques will develop at these sites of injury or even an atheromatic plaque in patients with hypercholestrolemia [157]. Injury to the atherosclerotic lesion may also expose lipid-laden, pro-thrombotic material that could potentially contribute to post-operative thrombus formation [165], and have been associated with an increased risk of delayed post-operative stroke [341]. Even just the presence and extent of atherosclerosis have been

positively correlated with delayed stroke after cardiac surgery [344]. Thus, a number of aspects need to be considered prior to cross-clamping, as expanded upon in the following.

Repeated clamping   have been shown to cause a significant release of embolic material in a cadaver model [39], and therefore should be kept at a minimum. With regards to patient-outcome, the large debate between single- and multiple-clamping techniques during coronary artery bypass grafting (CABG), cf. Section 2.4.3, has also shown the danger of repeated clamping. For example, Kapetanakis et al. [183] showed in a series of 7272 patients from one institution that those who have had their aorta cross-clamped and partial-clamped had a 1.8 times higher risk to have a stroke compared to patients where the aorta was not touched. Furthermore, those patients receiving both cross-clamping and partial-clamping also had a 1.7 times higher risk to have a stroke compared to those patients whose arteries were only partial-clamped.

Duration and pressure   In terms of vascular injury, the intimal and the medial layers of the aortic wall are particularly sensitive. Under controlled experimental conditions, it was found that the measure of intimal injury is proportional to the duration of clamping – up to ∼30 minutes, after which the degree of damage plateaus [18]. This implies that this plateaued level of injury will always be reached during practically all cardiac surgical procedures involving cross-clamping. Additionally, the same study showed that neither the duration nor the occluding pressure can be regulated to completely prevent vascular injury. Despite the observed injury described above, the mechanical function of an artery has been found to be unaffected, although persistent morphological changes have been found at the clamp-sites [90]. Unavoidable injury to the aortic wall due to cross-clamping has been shown to occur experimentally despite moderate clamp application pressure [226], when only cross-clamped for a single minute [18] or even at a cross-clamping force defined as the minimum vascular occlusion force (MVOF) using a specialized laboratory setup [94]. Different clinically used clamps have also been tested and shown to all cause some level of trauma to the vessel [157], even though some cause relatively less than others. As mentioned above, vascular injury due to cross-clamping has also been ascribed as being responsible for aortic dissection. Therefore, the popular notion of "atraumatic" clamps or clamp-inserts, i.e. clamping without causing vascular trauma, is (still) a misnomer.

Clamp-site and orientation   Current clinical knowledge dictates that prior to cross-clamping, the surgeon must consider avoiding as much of the atherosclerotic lesion as possible. He/she should take into consideration where the pinching sites will be with respect to the atherosclerotic lesion [271, 293]. Although these authors do not completely qualify or demonstrate the effectiveness of their recommendation, it most probably stems from the fact that experimental work has shown that the maximum amount of damage occurs at the pinching sites, as mentioned above, especially the proximal pinching site, due to the scissor-like/hinged design of cross-clamps, cf. Section 2.1.1 and 7.5. Furthermore, such a recommendation is seen exemplified in the following: Using 24 cadavers, Boivie et al. [41] found that the distribution of aortic plaque in the ascending aorta was the most prolific on the anterior wall, and that in 83% of cases where plaque was present on the anterior wall, concomitant plaques were also found on the posterior wall. A prospective study by van der Linden et al. [344] also found an elevated occurrence of atheromatic lesions in specific regions in a large cohort of patients referred for coronary revascularization (n = 611), by using epiaortic echocardiographic ultrasound. Considering those patients that had atherosclerosis of the ascending aorta (36.2% of total cohort), the highest prevalence of atherosclerosis was found in the distal anterior and posterior segments. Therefore, the conventional orientation and site of cross-clamp application are dangerous by default, due to the statistically averaged location where these lesions are found. Furthermore, when relating the risk of stroke over a 5-year period with the location of atherosclerosis in the ascending aorta, the presence of atherosclerosis in the distal and middle segments, i.e. the inner curvature of the ascending aorta towards the innominate artery branch, carried the highest risk of stroke. As such, a modification of the cross-clamp orientation seems to be absolutely necessary, as further considered in Section 9.1.

2.1.3. Technological advances

The technological development to significantly reduce the trauma induced by cross-clamping has been limited, while cross-clamps suitable for minimally invasive procedures have received more attention. In the following, a space-saving design has also been included in the discussion, since the inclusion of this space-saving hinge configuration can potentially aggravate trauma to the vessel, as expanded upon below.

Reduction of trauma   In an attempt to reduce the trauma of cross-clamping, MVOF threshold was formulated [94] and expanded upon [337] since over-occlusion always occurs, i.e. more force is applied to the vessel than what is needed to occlude it, as mentioned above. Even though the MVOF threshold has been shown to exist in experimental studies, this simplified analytical model to predict MVOF has still not been successfully translated into everyday clinical practice. The most probable reason is a combination of the complexity of the problem, the technical requirements and the inter-patient variability of the parameters needed to determine MVOF, including the required accuracy of force applied by the clamps, as well as determining the geometry and spatially varying material properties.

More recent attempts to reduce such trauma is to include "atraumatic" or padded inserts to existing clamps surfaces [121, 137, 324], as shown in Figure 2.3. These are expected to distribute the clamping force slightly better compared to not using inserts, increase the stability/grip of the clamps and cause less damage to the adventitia. However, the extent to which vascular trauma is subsequently decreased has not yet been elucidated upon in literature, and as such, cross-clamping without inserts are still frequently performed. Even balloon-type inserts have been proposed [76], although its clinical practicality and efficacy is questionable, since no further investigation, advancement or commercialization of this type of cross-clamp could be found.
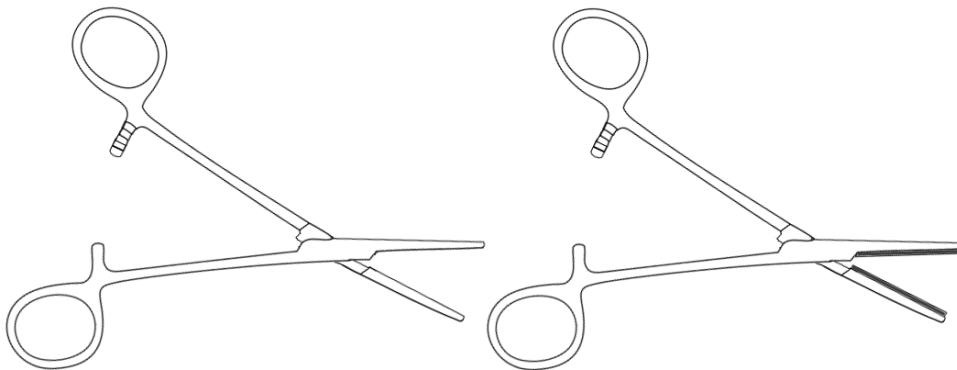
Figure 2.3.: "Atraumatic" inserts are simply a soft material extrusion attached to clamping surfaces, showing without (left) and with (right) inserts.

Other novel attempts to reduce vascular trauma upon cross-clamping have been to use shape memory alloys in the clamp arm itself to limit clamping pressures [218]. Notwithstanding, such a shape memory alloy will be limited to a single range of pressure and will subsequently be unable to sufficiently and safely limit the pressure when geometrical and material vessel parameters vary, which is clinically required. Another related novel proposal has been the external occlusion of the aorta with an inflatable belt [356]. However, this still does not negate the large deformation induced or the pinching/crushing brought about by aortic cross-clamps. Consequently, none of these proposed solutions have enjoyed clinical adoption, since they do not fulfill clinical requirements for safe, efficient and stable aortic occlusion, as put forth in cf. Section 7.2.

Space-saving Recent advances yielded many design variations in order to use less space in the surgical field – specifically to enable cross-clamping during minimally invasive procedures. The three main such commercially available, fundamentally different designs, are considered here: the Chitwood-DeBakey clamp (Scanlan International Inc., Minneapolis, MN), the Cosgrove Flex clamp (Edwards Lifesciences LCC, Irvine, CA) and the Portaclamp (Cardio Life Research, S.a., Belgium), shown in Figure 2.4.

(a)   (b)   (c)
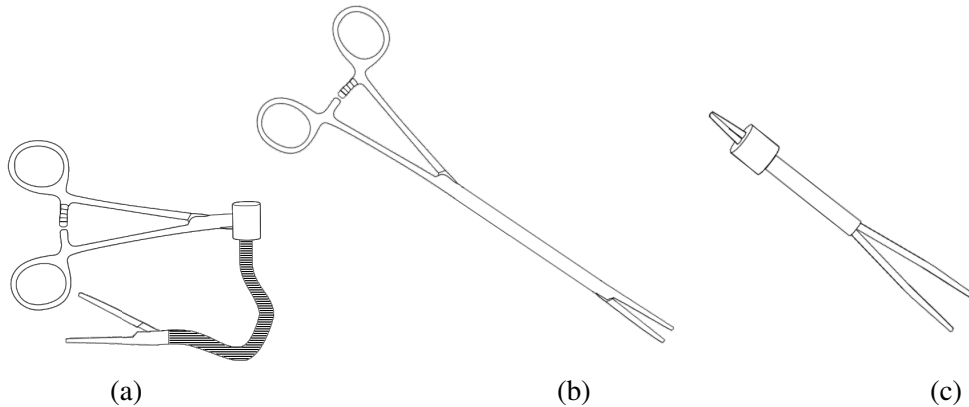
Figure 2.4.: Example diagrams of space-saving cross-clamps: (a) Cosgrove Flex clamps (Edwards Lifesciences LCC, Irvine, CA), (b) The Chitwood-DeBakey clamp (Scanlan International Inc., Minneapolis, MN) and (c) The Portaclamp (Cardio Life Research, S.a., Belgium).

The Chitwood-DeBakey clamp features a unique clamping mechanism where the clamp body and the one clamp arm are continuous and maintains its rod-like form during clamping. Moving the clamp handles therefore only moves a single clamp arm. It is a simple design that can be inserted in a small port (stab-wound) in the intercostal space in order to cross-clamp the ascending aorta during minimally invasive surgery [66]. Even though this extra port is required, it is justified by the other complexities that it avoids and is frequently utilized in minimally invasive procedures. The Cosgrove Flex clamps feature clamping arms similar to the Chitwood-DeBakey, but has a flexible body, perfect for hard-to-reach angles of clamping and enabling port-access. Notably, this clamp can be used without the need for an additional port [174], as opposed to the Chitwood-DeBakey clamps. The Portaclamp is another space saving cross-clamp technology, but has a different clamping mechanism to the cross-clamps described above. The Portaclamp is inserted by first passing a guide wire around the vessel to be clamped. Two thin, inextensible, but bendable clamp arms are inserted along the two sides of the guide wire, after which a unique system is used to fix the two clamp arms at the nearest end. Thereby the two clamping surfaces are brought together to occlude the vessel. Clinical use of this product has been limited, but reported in a favorable light by its inventors [78] and their collaborators [106].

The importance of presenting these cross-clamps with space-saving functionality in terms of potential vascular trauma lies in the fact that all three these designs possess a so-called "crab-pincher" clamp design. This means that the hinge of these clamps is far closer to the clamping surfaces than a standard angled vascular cross-clamp, cf. Figure 2.1. This results in an even greater non-uniformity of force exerted on the vessel and therefore also increased trauma necessary to achieve occlusion, especially at the proximal pinching site. Even though the Portaclamp is not hinged, the configuration in which the clamping surfaces are brought together creates an equivalently (poorly) distributed force as the so-called "crab-pincher" designs. Therefore, the space-saving functionality comes at a cost of increased trauma. How much more trauma has never before been elucidated upon in literature, but is further considered in Section 7.5.
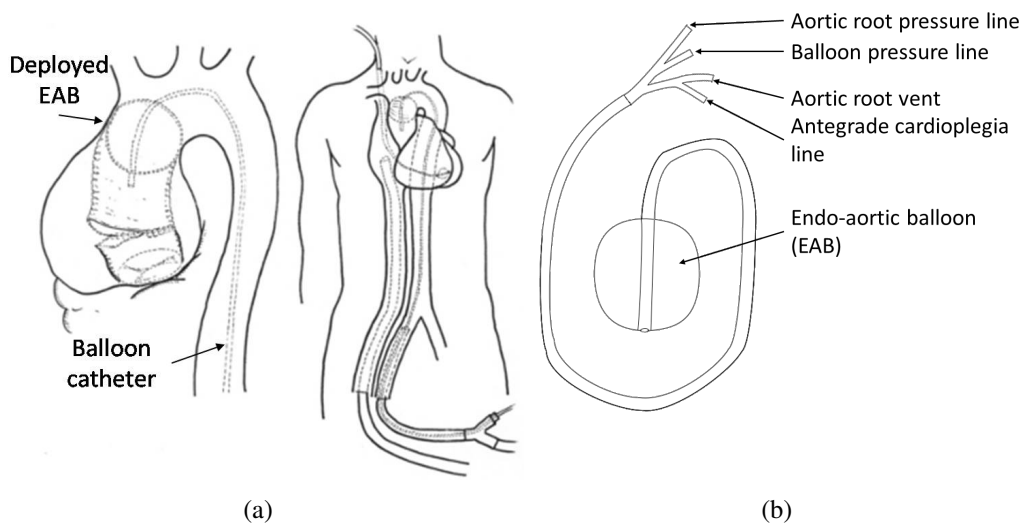
Figure 2.5.: Endo-aortic balloon occlusion (EABO), showing a) a schematic of its clinical application, adapted from [229] with permission, using it in the context of an ascending aortic aneurysm, and b) a typical EABO system with all of its components, adapted from a brochure of Model EC1001, Edwards Lifesciences Irvine, CA, USA.

2.2. Aortic occlusion by endo-aortic balloon occlusion (EABO)

2.2.1. Fundamentals

EABO is the intravascular occlusion of the aorta with an endo-aortic balloon (EAB). It has been marketed as the *Endoclamp* system but is also known as *endo-vascular balloon occlusion*, *endo-vascular aortic clamp* or *intra-aortic balloon occlusion*, etc. EABO has exactly the same purpose as cross-clamps, i.e. to provide surgeons with a bloodless cardiac environment by occluding the concomitant artery – mostly the ascending aorta. Figure 2.5 shows a typical EABO system and a schematic of its application. The EAB catheter is inserted into the femoral artery and then guided to the desired occlusion site. EABO systems also exist that can be inserted into the axillary artery or centrally in the ascending aorta.

EABO was first proposed in the 1980's [100] and even though the number of surgeries using EABO is small compared to the total number of surgeries performed annually [318], its frequency of use is steadily increasing [59, 134, 177, 214], despite certain groups abandoning it completely [16, 234, 247, 275, 294]. This increase in use stems from one of its main advantages: its multiple functionalities make it particularly well-suited for a number of minimally/less-invasive/port-access cardiac procedures [134, 318]. In this context, it is worth mentioning that these types of procedures are becoming of increased importance and are being performed more frequently, due to its potential to yield similar operative mortality, shorter hospital stay, shorter ICU stay, fewer blood transfusions, better cosmetic results and higher rates of mitral valve repair compared to conventional sternotomy procedures [65, 118, 136]. A recent review that considered only minimally invasive mitral valve surgeries (n=28,143 cases), reported a significant increase in the percentage of total number of these procedures: 11.9% in 2004 increased to 20.1% in 2008 [118].

The functionalities which give a typical EABO system its main advantage for use are the following: It does not only provide vascular occlusion which is percutaneously insertable (usually through the femoral artery), but it can also deliver antegrade cardioplegia, enable venting of the aortic root and enable the monitoring of aortic root pressure – an all-in-one system. This makes the need for an extra antegrade cardioplegia cannula redundant, thereby further reducing vascular trauma, de-cluttering the surgical field

and winning the time and cost required by the additional procedure [59, 134]. Furthermore, EABO has the advantage that it does not pinch/crush the vessel upon occlusion, as compared with cross-clamping – cf. Section 7.5.

The main disadvantages of EABO are: Firstly, the initial positioning, EAB inflation and monitoring of its position, as well as potential repositioning during the procedure are complex and delicate. Multiple factors influence the safety and efficiency of EABO in a non-trivial way, including the interplay with the patient-specific aorta geometry and material properties, the difference in pressure on either side of the EAB upon occlusion and interplay with the (inner) EAB pressure and balloon volume [346]. Secondly, as with cross-clamping, it is also associated with the release of emboli and with the occurrence of aortic dissections, as considered in more detail below. Thirdly, EABO can also be responsible for unwanted vessel deformation, although to a lesser extent than with cross-clamping. Finally, as with cross-clamping, the occluded state of the aorta is unknown intra-operatively, and therefore the vessel is always over-occluded.

Since EABO is a much more recent developed method of occlusion, fundamental research on the mechanisms of iatrogenic injury caused by EABO has mainly been done in the context of comparing it with cross-clamping, as considered in Section 2.3.1.

2.2.2. Clinical considerations

As mentioned above, a very pertinent danger associated with EABO is the release of emboli during occluding and de-occluding. Furthermore, some pertinent technical difficulties with the clinical use of EABO have been reported. The unstable position of the EAB can cause its migration [135, 308], requiring repositioning or potentially abandonment of the procedure. The migration of the EAB can also change the geometry of a valve, thereby complicating the valve repair/replacement [144]. Furthermore, EAB migration can also lead to occlusion of the innominate artery, inferior myocardial protection, ventricular distension or aortic valve injury [245]. A previously proposed method of preventing EAB migration requires additional aortic root manipulation and potentially unwanted fixation of the catheter [300]. The entry site of the EAB catheter also needs to be carefully considered. An axillary or femorally inserted catheter can avoid cannulation of a severely calcified ascending aorta, cf. Section 4.1, but will be more prone to EAB migration. Contrary to this, a centrally inserted catheter will negate the risks of peripheral cannulation and has been found to stabilize EAB movement [134, 144, 308], but requires more invasive vascular access. Peripheral cannulation/catheterization risks include arterial calcification or restricted access simply due to patient size [59, 350]. Other consequences associated with the use of EABO are the occurrence of aortic dissection [117, 246] and EAB rupture [92, 247].

2.2.3. Technological advances

Since EABO is a relatively newer and a less frequently used occlusion technique, compared to cross-clamps, relatively few improvements have been reported.

Although a higher chance of aortic dissection was initially reported during the use of EABO, it has become safer with increased experience, better techniques and improved technologies for EABO [117, 240, 245]. Furthermore, as mentioned above, EABO systems have been designed that do not only have the functionality of aortic occlusion, but have multiple functionalities which reduce the requirement for other systems and the subsequent procedures.

EABO is currently receiving an increased amount of attention from academia in aiming to understand the factors that influence the EAB stability [346]. Although novel ways have been developed to clinically determine whether the EAB has occluded the innominate artery [308], a current research focus is directed at full intra-operative visualization systems to aid in the positioning and monitoring of the EAB [116]. Re-

cently, a specialized cannula designed to facilitate the insertion of an intra-aortic filter, cf. Section 4.2.2.1 was used to insert the EAB into the lumen instead, providing a very stable EAB position and not requiring additional aortic puncture for the EAB catheter [6], but has been associated with unwanted cannulation site leakage.

2.3. Comparison of aortic occlusion techniques

2.3.1. Experimental comparisons

As far as the author could determine, only two such relevant qualitative experimental studies have been performed. Farhat et al. [106] occluded the descending aorta (shunted at the occlusion site) in three groups of five pigs each for one hour, each group with a different occlusion technique. They found that EABO was responsible for more severe lesions of the intima and endothelial disturbance at the occlusion site, when compared with the Chitwood-DeBakey and the Portaclamp cross-clamps, respectively. For all three types of occlusion techniques, spongy lesions in the external third of the media and moderate inflammatory lesions in the adventitia were observed. Anzai et al. [8] occluded the ascending aorta, while performing CPB, on two groups of twelve dogs each for three hours, comparing a non-specified type of cross-clamp with EABO. From histological results, both cross-clamping and EABO caused detachment of endothelial cells, mild degeneration and necrosis of parts of the intima, as well as loosening of connective tissue of the media. For cross-clamping, some necrotic smooth muscle cells were also found in the media, which were not observed for the EABO.

These two studies have the same significant shortcomings with respect to assessing their value to determine the clinically safest overall occlusion technique. Firstly, only the EAB pressures were prescribed and reported in these studies, while no indication of the clamping force, applied pressure, notch-level or vessel thickness was given. Therefore no comparable state of occlusion could be evaluated. Whether or not the vessel was actually occluded was not reported. Secondly, the experiments were performed under different blood pressure conditions – the former under a pulsatile physiological pressure with a shunted occlusion site, while the latter considered a constant perfusion pressure with a pressure difference over the occlusion site. The influence on the iatrogenic injury due to these different pressure conditions is unknown. Finally and probably most significantly, all these experiments were performed on healthy animals. These animals will have significantly different arterial wall responses compared to the pathological state of the arteries of elderly patients in which these procedures are most often performed – cf. studies on cross-clamping of fresh cadavaric aortas [39, 40], as well as the large-scale improvements achieved by performing epiaortic or transesophageal echocardiography (TEE) prior to aortic occlusion [89, 343]. A deeper understanding of the influence of occlusion technique-related injuries on arteries with atherosclerotic lesions or pathological layer delamination as a precursor for both embologenesis and dissections simply cannot be sufficiently evaluated from these experiments.

2.3.2. Clinical comparisons

Clinically realizable visualization of these two occlusion techniques are shown in Figure 2.6. Despite some previous comparative remarks, a summary of literature reporting the clinical results of cardiac valve procedures that specifically report the use of the two different occlusion techniques is presented in Table 2.1. This sub-field of cardiac surgery has been particularly interesting for such comparisons, due to the increased use of minimally invasive valve procedures, for which EABO is particularly well-suited. Studies were identified by searching electronic databases and scanning reference lists of articles for terms related to aortic occlusion on human subjects reported in the English language. Only studies that distinctively differentiated between the two occlusion techniques and showing the associated surgical aspects,

complications and post-operative results were included in the comparison. Furthermore, only cardiac valve procedures were considered, due to the relative irregularity of other types of procedures performed with both types of occluders.
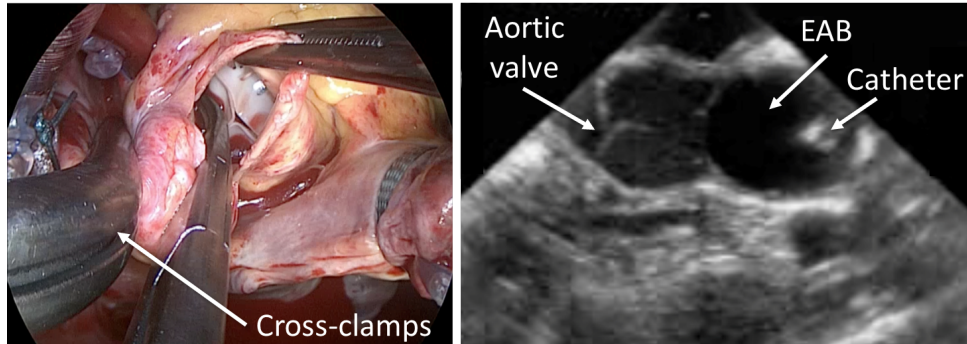
Figure 2.6.: Typical intraoperative visualization of the two types of aortic occluders, namely endoscopic view of the cross-clamps (left) and echocardiographic view of EABO (right). *Images courtesy of Prof. Stephen Wildhirt.*

The studies considered in Table 2.1 were divided into two groups: Group A are those comparing the use of conventional sternotomy (CST) with cross-clamping to minimally invasive valve surgery (MIVS) with EABO and Group B are those comparing MIVS with cross-clamping to MIVS with EABO, although the latter group of studies were not necessarily exclusively aimed at comparing the occlusion technique only. From this comparative summary presented, further comment is warranted, as expanded upon below.

Learning curve when using EABO is higher than for cross-clamps [59, 117, 234, 346]. Table 2.1 also gives an indication of how the experience level of these groups has increased overall, considering better outcomes as a function of published data of each study.

CPB and aortic occlusion durations are generally reported to be higher for EABO, but not always and not necessarily significantly. The aortic occlusion durations (commonly referred to as *cross-clamp time*) are of particular importance, because it refers to the time in which the heart is in an ischemic state, i.e. myocardial ischemic time. The disparities presented can be attributed to different concomitant procedures/steps required by each method of occlusion. Nevertheless, differences in procedural times did not have a clear impact on the outcomes, as shown in Table 2.1, as also confirmed in a recent review by Loforte et al. [214].

Occlusion technique as isolated factor for outcome The studies compared here entail an array of different equipment, procedural and patient factors, that were not all included to match the different patient groups, making conclusive comparison challenging, especially for the indicated Group A studies. In probably the largest review to date comparing cardiac valve surgery using CST to MIVS, Cheng et al. [65] also performed a sub-analysis of their data to shed light on the safety and efficiency of the occlusion technique. Of the 35 studies included in their analysis, only the six listed in Group A reported findings that specifically separated the treated patients in groups that exclusively received either cross-clamping or EABO. Considering the limitations associated with sub-analysis of retrospective data, no difference was found in the all-cause mortality between the two occlusion techniques. Regarding neurological outcomes, a trend of increased stroke, albeit not significantly higher, was found when using EABO exclusively, but was significantly worse when using a mixture of occlusion techniques in a single series of procedures. These trends of stroke and in-hospital mortality are also observable for the studies of Group B. In another recent review which considered the MIVS recorded in the The Society of Thoracic Surgeons

Table 2.1.: A comparative review of clinical studies on aortic and/or mitral valve procedures comparing the two existing techniques of vascular occlusion. One technique was only considered better or safer than the other when a significance of $p \leq 0.05$ was reported. Blank entries indicate that no data was reported.

Authors of study	Patients per occlusion technique [n]		Surgical aspects				Complications								Postoperative		
	CCI	EABO	Operative time	CPB time	Aortic occlusion time	Ventilation time	Stroke	Cerebral embolic events	Aortic dissections	Reoperation for bleeding	Other complications †	Transfusion requirements / blood loss	New onset of atrial fibrillation	Renal insufficiency	Mortality rates (in-hospital)	ICU stay	Length of hospital stay
Group A: MIVS with EABO vs. CST with CCI																	
Glower et al. (1998)	20	21	EABO	EABO	=	=					=	=					=
Schneider et al. (2000)	14	21	=	CCI	=	=		=							=	=	=
Grossi et al. (2001)	88	109	=	CCI							EABO	EABO			=		EABO
Onnasch et al. (2002)	226	209	=	=	=	=	CCI	=	=	=			=	=	=	=	=
Dogan et al. (2005)*	20	20	=	=	=	=	=	=	=		=		=	=	=	=	=
Ryan et al. (2010)	177	177		=	CCI	EABO	=		=	EABO		=	=		=	EABO	EABO
Group B: MIVS with EABO vs. MIVS with CCI																	
Aybek et al. (2000)	35	23	CCI	CCI	CCI	=			=	=	=	CCI	=		=	=	=
Reichenspurner et al. (2005)	60	60	=	=	=	=			=	=	=	=		=	=	=	=
Maselli et al. (2006)	16	20	=	=	=			EABO	=						=		
Ius et al. (2006)	93	29	CCI	CCI	CCI	CCI	=		=	CCI	=	CCI	=	=	=	CCI	CCI
Modi et al. (2009)	573	479	=	CCI	CCI	=	=		=	=	=	=	=	=	=		CCI
Glower et al. (2010)	235	436	EABO	EABO	EABO		=		=	=	=		=	=	=	=	
Loforte et al. (2010)	93	45	=	=	=	=	=	EABO	=	=	=	=	=	=	=	=	=
Krapf et al. (2013)	460	307	CCI	EABO	EABO	=	=		=	=	=	=	=	=	=	=	=
Mazine et al. (2013)	103	140	CCI	CCI	CCI	=	=		=	=	=	CCI	=	=	=	=	=

CCI   Cross-clamping performed significantly better than EABO (p ≤ 0.5)
EABO   EABO performed significantly better than cross-clamping (p ≤ 0.5)
=   Differences obtained did not reach significance (p ≤ 0.5)
*   Prospectively randomized
†   Including wound problems, femoral artery reconstructions, etc.

Adult Cardiac Surgical Database, Gammie et al. [118] also found that the occlusion technique was not an independent predictor of a higher stroke rate.

Monitoring of occluder performance   Considering the importance and etiology of emboli release during CPB in terms of the occlusion technique, only three of these studies made use of transcranial Doppler (TCD) ultrasound to monitor the embolic load entering the cerebral circulation, which is an essential parameter when considering the nature of this comparison. The only other markers of cerebral injury that were reported otherwise were stroke and in-hospital mortality. Persistent neurophysiological impairment was never considered. Schneider et al. [307] did not find any significant difference in the number of emboli detected between the two groups and detected the most emboli after release of the occluders. Here, only low-risk patients were considered, i.e. those with no calcified lesions or vessel stenosis (<50% stenosis) at any vascular level. Maselli et al. [230] not only found that the application *and* the release of the occluder caused a significant increase in brain embolic event rate, but also that cross-clamping resulted in a significantly increased number of emboli compared to EABO. This was also while considering a low-risk patient population. Loforte et al. [214] included a slightly higher risk profile of patients, but matched the risk between the two groups based on pre-operative variables, and also found that cross-clamping was responsible for a comparatively higher number of emboli detected than EABO.

Power of comparison   Infrequently occurring events such as stroke, aortic dissection and mortality need to be evaluated with caution. On the one hand, the number of occurrences were mostly found to be very low. Combined with the relatively small study populations, the power of the comparison was not particularly strong. However, statistically, there were no differences between the two occlusion techniques. On the other hand, these complications are of such severity, that it is understandable that only a small difference, even if not significant, influences the clinicians' conclusions about which occlusion technique is safer.

Costs   The differences in direct costs were often mentioned in the studies considered, but not in enough detail to allow comparison. Grossi et al. [147] found that total hospital and blood costs were significantly lower when performing MIVS with EABO, compared to CST with cross-clamping. Reichenspurner et al. [294] compared the costs of MIVS with cross-clamping and MIVS with EABO to valve surgery with CST and found that the per-patient equipment costs were $200 and $3000 higher, respectively. Of course, such a comparison does not take into consideration the added value and benefit to the patient and health-care system in terms of operating theater time, post-operative complications, length of hospital stay, etc. and as such, a more comprehensive cost-analysis is required. Owing to institutional and regional differences in costing, a more comprehensive cost-analysis is warranted to clarify the actual overall costs involved.

Indications of use   Few investigations have elucidated on which occlusion technique is indicated and contra-indicated under which circumstances. EABO has been described to be successful for limited cases in the vascular occlusion of severely calcified ascending aortas, for which cross-clamping is contra-indicated [212, 351], since it does not require pinching/crushing of the aorta [134]. Zingone et al. [369] presented results contrary to these findings. However, the study design of the latter does not allow relating adverse outcomes of performing EABO on a severely calcified aorta to the occlusion technique, but rather reflects the influence of aortic pathology on the outcome and the technical problems to be surmounted. Furthermore, EABO has been described as an ideal occlusion technique for redo-operations, due to the difficulty and potential risks of cross-clamping during these procedures. This is because the placement of a cross-clamp during redo-operations can be difficult and potentially dangerous due to the higher complication risk of these patients [174]. A final aspect in this regard is that EABO is proving to be a very useful method of aortic occlusion in robotic cardiac surgery, including totally endoscopic coronary artery bypass (TECAB) procedures [205, 209, 263], not otherwise achievable with a cross-clamping approach.

In summary, from the above comparison it is evident that no conclusive clinical outcome-related evidence exists to show that one occlusion technique is overall safer, better and more efficient than the other. However, the simplicity, low direct costs, potentially shorter procedural times, more stable occlusion, no

need for peripheral vascular access or retrograde perfusion, as well as comparable outcomes, have put cross-clamps in a generally more favorable light with many clinicians – as reflected in a number of recent reviews of MIVS [65, 118, 245, 350]. This, despite the fact that compared to cross-clamping, EABO results in less emboli entering the cerebral circulation, a similar amount of adverse consequences, causes less cluttering of the surgical field, provides more functionality, requires no additional port creation during MIVS, requires less aortic manipulation, e.g. no antegrade cardioplegia cannulation needed, and its use has been shown to be favorable in cases where cross-clamping is contra-indicated.

2.4. Partial-clamping

2.4.1. Fundamentals

Partial- (or side-)clamping of the aorta, also referred to as *tangential occlusion clamping*, *side-clamping* or *side-biting*, consists of temporarily occluding only a part of the aorta, in order to allow perfusion past the partially clamped site and thereby creating a stabilized, pressure-isolated section of the aorta onto which a graft can be anastomosed.

Some of the first partial-clamps used in modern cardiac surgery were already patented in the late 1950's [319] and this is currently a standard method for performing graft anastomosis in cardiac surgery. A typical partial-clamp is shown in Figure 2.7 and is frequently used in both on-pump and off-pump coronary artery bypass grafting (CABG) procedures. In conventional on-pump CABG, after CPB has been established, the ascending aorta is first cross-clamped prior to performing the distal anastomosis. Thereafter, the cross-clamps are removed and the partial-clamped site allows for the performing of the proximal anastomosis, while simultaneously allowing oxygenated blood from the heart-lung machine to perfuse the heart – also known as the multiple-clamp technique, cf. Section 2.4.3. In off-pump CABG (OPCAB), the pulsating aorta is only partially occluded when the proximal anastomosis needs to be performed – no other occlusion of the aorta is performed. Ironically, off-pump procedures using partial-clamps are often erroneously referred to as clampless, although they are technically only clampless if neither cross-clamps nor partial-clamps are used. This convention probably stems from the fact that in clinical language, clampless seem to indicate no myocardial ischemic time. However, in this context, it should actually refer to when no clamps are applied to the aorta in any way – also known as the no-touch technique, expanded upon in Section 2.4.3.

As with cross-clamping, the advantages of using partial-clamps are its stability, its ease-of-use and the low direct costs due to reusability. Accordingly, the disadvantages are also the fact that clamping causes vascular injury and potentially disrupting atheromatic lesions, further aggravated by over-clamping due to the intra-operative unknown state of the (partial) occlusion. As much as the release and the application of a cross-clamp contribute to the release of embolic load, so too does partial-clamping, as were found in the TCD studies referred to in the introduction of this chapter. The comparative similarities are exemplified by Barbut et al. [26], showing that while 34% of the TCD embolic signals were due to the release of the cross-clamps, 24% were due to release of the partial-clamps. This can be ascribed the fact that partial-clamping involves large deformation of the aorta on a similar scale and configuration as cross-clamping, i.e. it also induces a greater impacted proximal and a lesser impacted distal pinching site at a clinically unknown state of occlusion. Therefore, all the same advantages and disadvantages described above for cross-clamping are applicable here. The only real difference is that the partial-clamps cover a larger area along the length axis of the aorta. Furthermore, a partial-clamp clutters up the surgical field and although it allows for perfusion past the partially occluded site, it significantly influences the hemodynamics, especially during off-pump (beating heart) procedures. The latter is considered in more detail in Section 3.2.2.2.
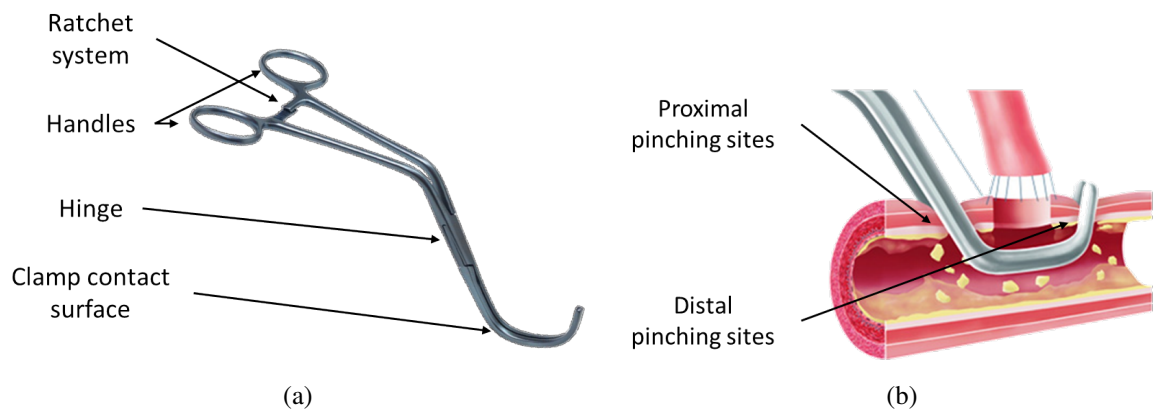
Figure 2.7.: A typical partial-clamp, showing the different parts of the clamp. An example of clamp application for a certain procedural variation of performing proximal anastomosis (as taken from [99] with permission).

2.4.2. Clinical considerations

There are two main groups of clinical investigations which provide valuable insights into the problems associated with partial-clamping. The first group comprise of comparisons between on-pump and off-pump coronary artery bypass grafting (CABG) and the second group of the occurrence of cardiac surgery-associated iatrogenic aortic dissections, as expanded upon below.

Theoretically, less manipulation should imply less post-operative complications and therefore, off-pump procedures should be more beneficial to the patient than on-pump procedures. This has indeed been shown in a number of observational studies. However, this is a simplistic comparison of highly complex problems. Without reviewing the whole, much contested debate in its entirety, it is worth considering a recent in-depth review on randomized controlled trials (RCTs) and meta-analyses comparing cerebral outcome between on- and off-pump CABG procedures by Alston [5]. It was shown that when considering all of the results from the stated studies, there were no differences in outcome in terms of either stroke or cognition 6 months postoperatively. This excluded observational studies, due to being subject to bias. In this context, it is important to realize that no differences in outcome should be regarded in terms of the vastly different state to which a patient's physiology is subjected during these treatments. Only considering manipulation-related differences, on-pump procedures necessitate the puncture of the aorta for arterial and cardioplegic cannulation and the associated non-pulsatile perfusion, aortic occlusion, the potential use of partial-clamps, hemodilution, etc. On the other hand, off-pump procedures require either the application of partial-clamps or an automatic graft connector on an aorta under pulsatile loading and increased dislocation of the heart, which in turn also significantly influence the cerebral perfusion. Furthermore, the surgeon also has to anastomose in a non-stationary cardiac environment, often leading to incomplete revascularization. Additionally, TCD studies have revealed that the embolic load entering the cerebral circulation was significantly reduced in off-pump procedures compared to on-pump. However, owing to the similar long-term neurological outcomes, it is clear that the nature of these multi-factorial influences on patient outcome is an insufficiently understood phenomenon and as such, partial clamping in itself cannot be seen in isolation of the other important factors. These include insights into the structural impact of partial clamping of the aorta, as reviewed extensively in this chapter, as well as hemodynamical consequences of such a procedure, as considered in detail in Section 3.2.2.2.

Iatrogenic aortic dissections during or after cardiac surgery are an infrequently occurring, but devastating consequence linked to damage caused by aortic manipulation, which involves partial-clamping specifically [61, 98, 149, 207, 217, 324, 330, 359]. Cases have also been presented where using an automatic graft connector device was responsible for dissection [274]. The quality of the aortas that are manipulated has also been implicated as a compounding factor for the occurrence of aortic dissections, which include calcifications, cystic medial change, Marfan syndrome, collagen vascular disorders, hypertension, as well as thin and dilated aortas, but also aspects like femoral cannulation and Asian race. Cardiac surgery-related dissections under these surgical conditions have also been found to occur in aortas perceived to be normal [170, 262, 324]. The hypothesis that uncontrolled pulsatile pressure can further aggravate such an injury is further considered in Section 3.2.2.2.

2.4.3. Technological and procedural advances

Technological advances of the partial-clamps have primarily only consisted of added inserts to clamping surface and ensuring a clamp configuration which maintains as parallel as possible clamp surface configuration near the occluded clamping state, similar to standard cross-clamps. Otherwise, any advances in this context have been focused on technological and procedural adjustments focusing on avoiding partial-clamping of the aorta completely, some even focused on avoiding any type of aortic manipulation completely. To achieve this end, five different procedures/techniques have been developed and investigated, as expanded upon below.

Single-clamp technique is used during on-pump procedures, but differs from the conventional multiple-clamp technique in that the anastomosis/es are performed without partial-clamping, but while the aorta is completely occluded (cross-clamped), proximal to the occlusion site. This is possible because the anastomotic site is depressurized and stabilized by the occluder. The downside of this method is that it inadvertently increases the cross-clamping time, which implies a longer myocardial ischemic time and hence the procedural risk – cross-clamp time has frequently been shown to be an independent predictor of increased mortality following cardiac surgery [91, 272]. Nevertheless, this method has been shown to be safe and effective, reaching outcomes comparable (and sometimes even superior) to both off-pump with partial-clamping as well as on-pump with the multiple-clamp technique [9, 12, 52, 150, 208, 338].

No-touch technique comprises of taking either only the left internal mammary artery (IMA), or both the left and right IMAs, and grafting the distal end of the artery/ies directly onto the desired coronary artery for revascularization, i.e. Y- or T-graft constructions. With this technique, no proximal graft anastomosis onto the aorta is required, since the coronary vasculature is perfused directly by the arterial perfusion. Furthermore, these arteries have been shown to have superior long-term patency compared to commonly used saphenous vein grafts [109]. Such a procedure can safely be performed during both on- and off-pump CABG procedures. The benefit of its use is limited by the quality and length of the native left and right IMAs, and should more than two graft vessels be required, an additional graft is necessary and requires subsequent proximal anastomosis onto the aorta. Disadvantages include increased sternal wound infection rates [145, 159], respiratory dysfunction [43] and potential insufficient perfusion through the IMA for revascularization [179, 276]. However, apart from excellent long-term patency rates of using these autologous arteries, the main advantage of using the no-touch technique exclusively in terms of manipulation, is that combining it with off-pump CABG, the aorta does not have to be manipulated at all [210, 227]. Clinical results by several groups have found a reduced rate of stroke, ascribed to the avoidance of CPB, as well as aortic manipulation, as recently reviewed by Abu-Omar and Taggart [2]. It must be noted that performing off-pump CABG using an automatic graft connector (see below) is sometimes erroneously referred to as the no-touch technique, since the aorta is actually manipulated through puncturing of the aorta.

Profound hypothermic circulatory arrest (PHCA) consists of cooling down a patient to lower tissue metabolic requirements, enabling the heart to be arrested safely for a short period of time and thereby allowing the performance of the required surgical procedures [132, 198, 260]. If aortic regurgitation is not present, the heart can be operated on without requiring aortic occlusion. This procedure has been modified to include low perfusion from CPB and is known as hypothermic low-flow bypass (HLFB) [266]. Consensus has not yet been reached on optimal temperatures, management of inflammation, duration of arrest, cooling/rewarming rates and the use of neuroprotective medication for this type of procedure. Due to the limited time and neurological safety concerns, this procedure is only performed as an alternative in the rare event when contra-indications or complex procedural requirements (e.g. aortic arch replacement) do not support the use of standard on- or off-pump procedures [132, 310].

Automatic graft connectors have been developed that only entail an aortotomy and graft suturing at the site of proximal anastomosis, thereby only requiring puncturing the aorta and not largely deforming it, suitable for use in both on- and off-pump anastomoses. As such, while partial-clamping of the aorta is completely avoided, the inadvertent puncture of the aorta for achieving proximal anastomosis is still needed, which carries certain manipulation-related complexities and consequences [148].

Simplified insertion of the arterial cannula The standard method of introducing cannulas involves suturing one or two purse string sutures around the desired cannulation site, then partial-clamping the site to enable aortotomy for cannulation insertion [211]. Although this method is still used, a more recent method of inserting an arterial cannula consists also of these purse-string sutures, but instead of using a partial-clamp, the adventitia at the aortotomy site is dissected away as a flap, after which the media is incised until the intima can be identified – usually a blue-ish transparent color. Thereafter, a gentle application of pressure on the cannula tip can be used to gain access to the lumen, after which the purse-strings are immediately tightened around the cannula [122]. Alternatively, a cannula can also be inserted by a specialized introducer tool for inserting cannulas without the need for partial clamping [293].

2.5. Digital palpation of the aorta

The most rudimentary form of evaluating the aorta for increased calcified atherosclerotic lesions is to simply digitally palpate it, with the purpose of manually feeling calcifications. However, the increased use of intra-operative TEE and epiaortic ultrasound scanning, as well as studies showing the comparative insensitivity of palpation to detect lesions, especially soft atheromatic lesions, and the danger of disrupting a lesion by palpation [77], have significantly diminished the use of palpation in standard care.

3. Disrupted physiological hemodynamics

Our knowledge can only be finite, while our ignorance must necessarily be infinite.

— Karl Popper

Physiological hemodynamics is inadvertently disturbed by most cardiac surgical interventions, most notably, during a cardiopulmonary bypass (CPB) procedure, but also during beating heart procedures. These two procedures are also referred to as on-pump and off-pump procedures, respectively. The former, due to the need to induce cardiac arrest and using a heart-lung-machine to return oxygenated blood to the systemic circulation, while the latter requires substantial cardiac handling and manipulation of the aorta, thereby impairing cardiac output. This disruption of hemodynamics not only runs the risk of causing hypoperfusion to end-organs, especially the brain, but can also lead to embologenesis. Regardless of the cause of the disrupted hemodynamics, an immense volume of research has been dedicated to better understanding and improving patient-outcome since the advent of cardiac surgery in the 1950's, especially with regards to hemodynamics and neuroprotection during cardiac surgery.

What follows in this chapter is an in-depth review of the dangers of disrupted physiological hemodynamics during cardiac surgery with regards to increasing the incidence of both hypoperfusion and embologenesis. The complete pathophysiological response due to disrupted hemodynamics are not considered here, as it has been excellently reviewed elsewhere [129, 257]. The two main topics of this chapter consider surgical procedures requiring extracorporeal circulation (ECC), specifically referring to CPB procedures and those performed on the beating heart, respectively. For each topic, its fundamentals are considered, followed by the myriad of clinical considerations intertwined with recent technological advances.

3.1. Arterial return hemodynamics

3.1.1. Fundamentals

In CPB procedures, deoxygenated blood is taken from the venous circulation, oxygenated, filtered and returned into the arterial circulation by a heart-lung-machine. Oxygenated blood delivered through an arterial cannula to the arterial circulation system is known as *arterial return*, whereas *arterial cannular flow* specifically refers to the jet of blood delivered through the arterial cannula. To initiate CPB, the arterial cannula must first be introduced into an artery, typically the ascending aorta. To achieve safe arterial cannula access to the (still) pressurized artery, prior to arresting the heart, purse-string sutures are inserted into the cannulation site which can be tightened around the inserted cannula after its introduction.

The first successful open heart surgery with the help of a heart-lung-machine in 1953 in Philadelphia, PA, USA, by John H. Gibbon, Jr, MD, was preceded by many key developments of such a procedure that are now taken for granted, including how to best drain blood from the circulation, how to safely pump it, oxygenate it, prevent coagulation, clear the heart from air and, of course, safely return the blood to the arterial circulation [72]. Since then, major advances have been made clinically, e.g. improved diagnostics, preoperative preparation, uniform anti-coagulation, improved postoperative care, training of perfusionists,

etc. and also technologically, e.g. improved cannulas, heart-lung-machine pumps and oxygenators, arterial line filtration design, etc. [236, 260].

The main advantage and reason for performing a CPB procedure, is that it affords the surgeon a stable, bloodless cardiac environment for extended periods of time. The disadvantage thereof, however, is that it comes at a price of disrupting normal homeostasis. During CPB, (1) blood makes contact with the artificial surfaces of the extracorporeal circuit causing blood damage and mediator activation, treated with substantial anti-coagulation; (2) physiological hemodynamics are disrupted by generally continuous arterial cannular flow; (3) different grades hypothermia are used to reduce tissue metabolic requirements and therefore also oxygen demand, especially the brain, but also the myocardium; (4) a reduced hematocrit is the consequence of the large volume of priming fluid required in the CPB circuit at procedural start, reducing the total oxygen-carrying ability that blood can supply to tissue; (5) some degree of renal dysfunction and changes in intestinal permeability may also occur; (6) pulmonary function is impaired, although its severity has dramatically improved; (7) acid-base and glucose levels need to be actively maintained due to their subsequent disruption and (8) as mentioned above, neurological damage and neurophysiological impairment are important potential consequences [151, 172].

Of main interest in the following sections are the disrupted hemodynamics due to CPB and its potential for adverse neurological outcomes. Contrary to the previous chapter on large deformation manipulation maneuvers, technological and procedural advances are incorporated in the clinical considerations below.

3.1.2. Clinical considerations

In order to better understand the degree by which physiological hemodynamics are disrupted during CPB, consider the following: The required flow rate that a heart-lung machine must deliver has been calculated to be between 2.2 and 2.8 l/min/m^2 (liters/minute/body surface area), which translates to a required flow in most adult patients of more than 4 l/min, on average 5 l/min [50]. During a CPB procedure, such a flow rate is generally delivered through a cannula with an inside diameter of typically 6 mm (28.3 mm^2) [180, 347] inserted at an angle perpendicular to the main flow direction, with limited placement along a short length of the aorta, or limited sites into which it can be inserted. Physiologically, approximately the same flow rate is delivered through the ascending aorta which has a typical inner diameter of 30 mm (706.9 mm^2) [216] under pulsatile flow conditions, exhibiting a natural, preferential, helically rotating flow pattern through the ascending aorta and subsequent branches.

Since flow rate through a pipe is inversely proportional to its cross-sectional area, flow through the arterial cannula entering the arterial circulation results in a high-velocity jet. Since it is desirable to keep the outer cannula diameter as small as possible to ensure the smallest aortotomy (incision into the aorta) required for cannulation, design variations to mitigate the detrimental consequences of the jet have focused on the cannula-tip. Existing tip-designs either deflect the jet, disperse the jet, or do both. Tip-designs can be classified into two categories, namely end-hole and side-hole cannulas, while some hybrid cannula tip-designs exist that have properties of both. The main difference is, as the names imply, the end-hole cannula which is simply a pipe with an open end, where the tip can be of arbitrary design, e.g. straight or curved end-hole cannulas. The side-hole cannula has a closed end with holes on the side of the cannula close to the pipe end. The main trade-offs in cannula tip-design are the strength by which the jet hits the arterial wall, the dispersion of blood flow entering the aortic arch and the pressure gradient over the entire cannula. The range of all the main, clinically available cannula tip-designs are shown in Figure 3.1. Cannulas frequently evaluated include straight-tip and curved-tip end-hole cannulas (manufactured by various companies), SoftFlow side-hole cannula (Sarns, Ann Arbor, MI, USA), Dispersion side-hole cannula (e.g. Research Medical Inc., Midvale, UT, USA), Stöckert hybrid cannula (Stöckert Instrumente, Munich, Germany), Medos end-hole with stator cannula (Medos Medizintechnik, Stolberg, Germany).
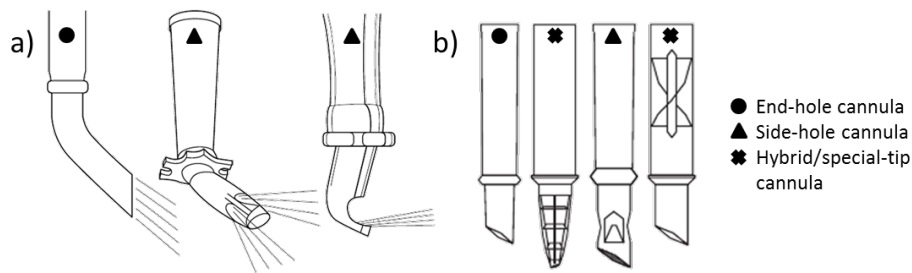
Figure 3.1.: Current cannula tip-designs, showing examples of different designs of end-hole, side-hole and hybrid/special-tip cannulas, as reported (and extracted from) by a) Joubert-Huebner et al. [180] and b) Scharfschwerdt et al. [305]. All figures used with permission.

Many experimental and clinical studies have investigated the arterial cannular flow characteristics of different tip designs under various laboratory conditions [7, 50, 141, 143, 180, 244, 258, 305, 347, 357]. Testing conditions vary in terms of working fluid used, i.e. water, glycerin-water and bovine blood while using different setups, i.e. in vitro closed-circuit in a straight tube, in vitro closed-circuit in a mock aorta, in vitro closed-circuit, in vivo or some variation thereof and using different means and standards of quantifying the danger of the jet, including peak velocities, jet force/back pressure, jet dissipation, pressure drop over cannulas and wall shear stresses induced. All of these are not always evaluated in every study. If the experimental setup allowed, circulation patterns in the aortic arch were also analyzed, where some mock-up aortas were made of glass, others of silicone, some with simple outflow boundaries, others with more sophisticated boundaries that mimic a type of naturally occurring Windkessel effect. Although variations in results exist due to different conditions, many different aspects about the jets yielded by different cannula designs are evident, although some consequences are not.

The main detrimental consequences of this high-velocity jet in general are: (1) its potential for dislodging particulate matter from the vessel wall into the arterial circulation, i.e. embologenesis; (2) the degree of hemolysis that can occur due to pressure gradients induced by different cannula tip-designs; (3) its influence on perfusion, especially cerebral perfusion, due to its tip-design, orientation and location of origin, i.e. cannulation site; (4) responsible for "washing" a majority embolic matter along a consequent dominant perfusion path, e.g. only the left cerebral hemisphere; (5) its variable effect when considering continuous and pulsatile heart-lung-machine perfusion; (6) its disturbance of the natural helicity of flow in the aortic arch; and (7) its variability when considering different cannulation sites, i.e. central vs. peripheral cannulation. These seven aspects are considered in the following section.

Although not explicitly considered in the following, extra-corporeal membrane oxygenation (ECMO), especially veno-arterial ECMO, as described by Kohler et al. [201], and the arterial return of ventricular assist devices (VAD), as described by Yang et al. [365] disrupt physiological hemodynamics in a similar manner as CPB, and should also be considered when reviewing the risks to patient outcome considered in the following.

3.1.2.1. Sandblasting effect of different cannula tips

When a jet of blood hits the arterial wall, it causes a sharp increase in the wall shear stress[1] (WSS) on the intimal layer of the artery, and as such has been commonly referred to as the sandblasting-effect[2] and has been repeatedly inferred from clinical observations as being the cause of subsequent intimal damage [114, 186, 328, 341]. Furthermore, Brown et al. [51] also demonstrated that a 90% increase in embolic load occurred for every additional hour that a patient was kept on CPB. Such sharp increases in the WSS do not only occur where the jet from the arterial cannula hits the arterial wall, i.e. primary landing-site, but also at subsequent landing-sites. Such danger is also not only limited to flow from the arterial cannula, but also from the antegrade cardioplegia cannula [215], although flow rates required for the latter are considerably lower.

Recognizing the potential danger of the jet that could lead to embolization by "sandblasting" lead to the development of different cannula tip designs aimed at better distributing the jet into the aorta. The main parameter considered to deduce that one cannula is safer than another has been to measure the peak velocity of the working fluid and/or the velocity at various distances from cannula tip. Of the standard tips considered at comparable flow rates, the peak velocity measured was the lowest for the Dispersion (side-hole) cannula, increasing with the SoftFlow (side-hole) and bent-tip (end-hole) cannulas, with the highest peak velocity measured for the straigth-tip (end-hole) cannulas [143, 180, 244, 357]. Specialized cannulas such as the Stöckert (hybrid) cannula performed better than the Medos (end-hole with stator) which in turn performed better than the SoftFlow [305]. The typical shape of the jets produced by these different cannula designs are shown in Figure 3.2, although these are not exactly the submerged shapes. Other indices considered to quantify the impact of the jet have been the jet force or so called "back-pressure", i.e. the pressure measured at a close and specified distance from the tip [130, 258, 305], jet force derived by integrating the jet velocity over the (assumed circular) jet area [347] and the velocity attenuation over a distance from the tip [143, 258, 347]. Once again, considering these measured quantities, the Dispersion cannula performed the best, followed by the SoftFlow, curved-tip and finally straight-tip cannulas.

The fluid dynamical requirements summarized from the above-mentioned investigations for the "safest" jet are: the jet strength must be as low as possible upon exiting the cannula and reduced as much as possible over the shortest possible distance. Considered in these terms, although not always thoroughly evaluated for all of these factors, the safest jet is delivered by the Dispersion cannula, since the jet hits the closed end of the cannula that causes energy dissipation, and is then freely dispersed in a fan-like pattern through the open side-hole. The SoftFlow also reduces the jet strength quickly over a short distance, albeit to a lesser extent, by dividing the main jet into four smaller jets. A smaller (in radius) jet of a viscous fluid will dissipate faster than a larger one. The curved-tip cannulas also performed better than equivalently sized straight-tip cannulas, attributed to the energy loss experienced when the fluid hits the bend in these cannulas, thereby reducing the effective jet velocity.

While these indices above do give important insight into the danger of the jet, the actual tangential traction, or WSS, that is induced by the jet on the aortic wall is of course the final defining parameter to evaluate in this regard. A study by Fry [111] demonstrated experimentally that endothelial cell erosion already occurs at a WSS of 40 Pa in a time scale ranging from minutes to hours, as is the case during CPB. As far as the author could determine, only a single experimental study investigated the comparable influence of the jet in terms of the risk of sandblasting-released atheroemboli. White et al. [357] compared various cannulas in a straight, rigid tube with a sheet of charcoal granules adhered to the inner surface of the tube. Considering similar flow rates at similar durations, they measured the weight of particles released

---

[1]This is the measure used most often in literature, but the mechanically correct indication for this is actually wall shear *traction*.

[2]As rightly pointed out by Verdonck et al. [347], sandblasting is technically large particles suspended in a fluid brought to a high velocity which erode the surface it comes into contact with by shearing. In blood, the only particles are microscopic blood components which would not yield a true sandblasting effect.

(a) straight-tip (end-hole) [130]   (b) curved-tip (end-hole) [244]   (c) SoftFlow (side-hole) [244]

(d) Dispersion (side-hole) [244]   (e) Medos X-flow (end-hole with sta-   (f) Stöckert (hybrid) [305]
                                          tor) [130]
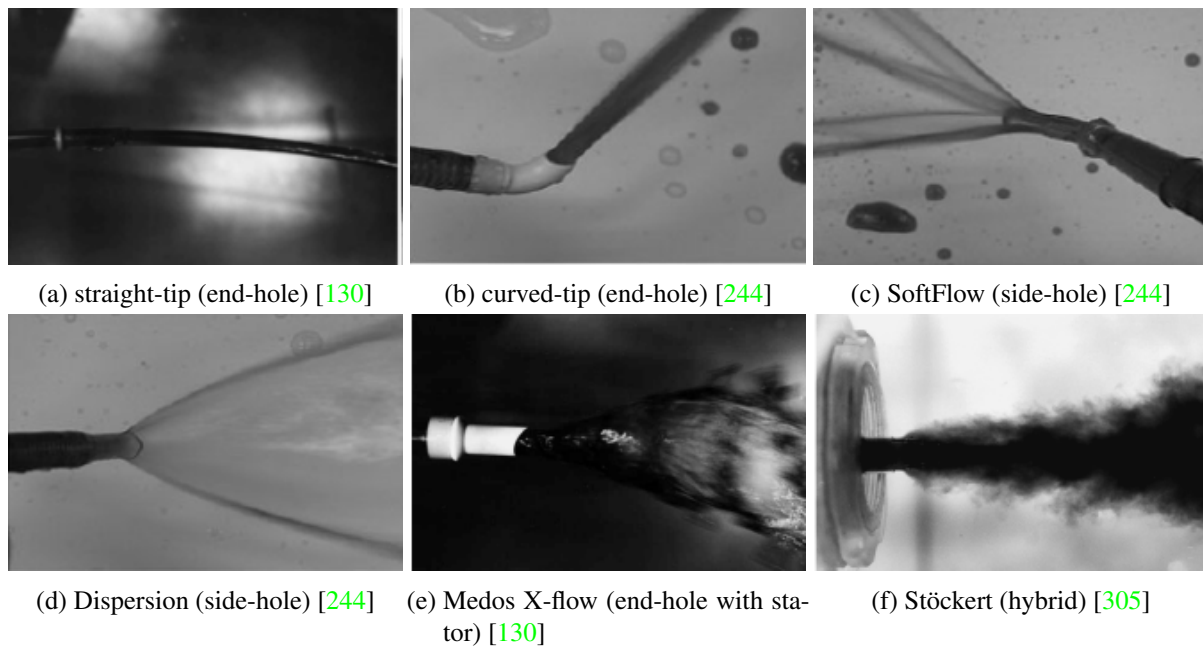
Figure 3.2.: Visualization of arterial cannular jets showing different cannula tip designs, as extracted from
             the cited references. All figures used with permission.

from the adhesive surface. Such an evaluation is, however, trivial in its design and practically not useful, since as rightly pointed out many years prior [141], the angle of attack of the jet combined with the jet strength will determine the magnitude of this sandblasting effect. Here the angle of attack was arbitrarily allowed to differ according to the tip design, i.e. a jet pointed parallel to the opposing wall would perform better than the same jet pointed straight at the opposing wall. Furthermore, such a tip orientation cannot be maintained or guaranteed in vivo and non-primary landing sites cannot be evaluated in a straight tube.

A proposed cannula tip design that is worth mentioning in this regard is a conically expanding diffuser-like tip [7, 238, 357]. This tip has been designed to expand by an angle smaller than 15° to prevent flow separation, thereby ensuring uniform expansion of the jet to optimally reduce velocity and increase pressure – and showed very good performance in terms of peak velocity, jet attenuation and pressure gradient (see next section). Although conically expanding diffusers are common in many industrial applications, the problem with applying it to cannula tip design, is that the maximum tip diameter is limited to the aortotomy size required to insert the cannula. Therefore, if one would increase the aortotomy size, one would naturally simply select a larger nominal cannula size – not opting for a smaller nominal cannula size with such a specialized tip. Although White et al. [357] suggested that a self-expanding tip made of shape memory alloys might be a solution to this problem, the subsequent cost-and-complexity-to-benefit ratio becomes highly questionable. Furthermore, the performance of the diffusive tip is dependent on the flow rate, diffusive cone angle and tip length [238], which limits the full efficiency exploitation of this velocity reducing feature, since flow often needs to be adjusted during CPB. Another issue is the large size needed, with an effective tip length for use in a neonatal application being 10 mm – which would practically be too big. Not surprisingly, such a cannula design is not currently found on the market.

Menon et al. [238] also proposed a further novel design extension to their diffusive cannula tip, namely a four-lobe swirler inducer. It forms part of the cannula conduit prior to its tip and consists of four lobes/channels that helically swirls the conduit of the cannula in order to passively cause a more coherent flow structure of the jet. Combined with the diffusive tip, the onset of turbulence by the jet was

efficiently delayed, improving the non-turbulent dissipation of energy in the jet. However, will this benefit be clinically observed due to the jet hitting the aortic wall before any of these jet effects have a chance of developing? Furthermore, its clinical acceptance is questioned, simply due to its size that will clutter the surgical field – for cannula diameter D, the swirler introducer will have a diameter $4.25D$, which then sits in the surgical field directly at the cannulation site.

Another novel development in cannula design worth mentioning is the Cobra catheter (Cardeon Corp., Cupertino, CA, USA) [73, 317] designed for dual-temperature management during CPB. It consists of a long, double lumen cannula with two main outflows, one for the cold perfusiate (three orifices) to the cerebral circulation and one for warm perfusiate to the rest of the body. It is positioned in the arch, and also has an inflatable baffle to secure its position and to segment (not occlude) the greater and lesser curvatures of the aortic arch, thereby also redirecting most particulate emboli originating in the aortic root, ascending aorta or aortic arch into the descending aorta. Although the jets' risks produced were never studied experimentally as far as the author could determine, it is expected that jets of cold perfusiate directed and intended to the cerebral circulation will be much weaker than the jets considered above, due to only having a portion of the total flow passing through it, i.e. only the portion of flow intended for the cerebral circulation. However, the main expected drawback is that these orifices are fixed and cannot be altered to suit patient-specific needs. As such, even though these jets are relatively weak, they may very likely not be directed straight into the branching vessel orifice and might hit the adjacent aortic wall directly from a very close proximity. Furthermore, atherosclerotic lesions that are often found at branching orifices are at an elevated risk than when considering other cannula tip designs. Finally, the inflation of the baffle also has the potential of causing abrasion against a large surface area of the aortic arch, cf. Section 4.2. Regardless of the performance of this cannula in terms of jetting effects, a randomized clinical study revealed no conclusive evidence that it provides better results than standard treatments [191].

All of the cannula tip modifications to better disperse the high velocity jet in order to amplify its attenuation, as described here, come at the cost of usually inducing a higher pressure gradient (or pressure drop) over the cannula, which carries its own risks, as described in the following section.

3.1.2.2. Pressure gradient over different cannula tips

Apart from the length and diameter of the conduits from the heart-lung-machine and the arterial cannula conduit, which often includes a narrowing taper proximal to the tip, the main variable contributor to pressure gradients experienced by extracorporeally circulated blood is across the cannula tip itself. As mentioned in the preceding section, cannula tips that better disperse the dangerous jets usually come at a cost of inducing a larger pressure gradient on the blood. In fact, any tip more complex than the straight end-hole cannula causes an increased pressure gradient over the tip. Such a high pressure gradients are highly undesirable, because it can lead to hemolysis and plasma denaturation above a clinically accepted pressure gradient threshold 100 mmHg [50, 171, 280]. Hemolysis in itself does not only diminish the oxygen-carrying capacity of the circulating blood by destroying red blood cells (erythrocytes), but it also complements activation and unfavorable changes in the mechanical properties of erythrocytes, promotes the activation of platelets and leukocytes, and increases concentrations of inflammatory mediators [181, 362]. Consequently, it will also further contribute to the embolic load in the arterial circulation.

In terms of the pressure drop, the tip performance of each cannula was not simply inversely related to its corresponding jet strength, jet velocity or a direct relationship with its jet attenuation characteristics. Joubert-Huebner et al. [180] described the simple expected progression of performance, i.e. of the standard cannula tips, the curved tip (end-hole) performed the best, followed by the SoftFlow (side-hole) and lastly the Dispersion (side-hole) cannulas. Contrary to this finding, although not evaluating the Dispersion cannula, Muehrcke et al. [258] found that these cannulas all had similar pressure drops, while Verdonck et al. [347] found that SoftFlow performed better than any end-hole cannulas. White et al. [357] found

that the SoftFlow yielded the best performance, followed by the Dispersion, 45° curved tip and finally the 80° curved tip. These findings also indicate the influence of the tip curved angle on the pressure drop. Furthermore, the influence of the smoothness of such a bend might also play a role. Of the specialized tips, Scharfschwerdt et al. [305] found that the Medos X-flow and the Stöckert cannulas both performed better than the SoftFlow, and in turn better than the curved tip cannula. These observations confirm in part the trade-offs existing between the different jet attenuation abilities, but it clearly shows that an optimum has not been reached.

All these findings have one overriding limitation, namely the correct measurement of pressure gradients over the cannula tip. The pressure gradient over a cannula is usually measured between the Luer-lock of the cannula, i.e. close to the cannula inlet, and somewhere in the reservoir into which the jet is blown. Four main problems arise from this evaluation: Firstly, the main conduit of the cannula, i.e. prior to the tip, is inherently included in the measurement. This is problematic, since the conduit of some cannulas taper down to a minimum diameter is reached at the tip, while others do not taper at all or at different taper geometries. Furthermore, the conduit length of a cannula is by no means standard. Therefore, the pressure gradient conventionally measured is actually the pressure drop over the entire cannula (at least from the Luer-lock), i.e. a combination of the cannula tube and the tip. Only the study by Verdonck et al. [347] actually considered this discrepancy and accordingly reported on the superior performance of the SoftFlow over straight and curved end-hole cannulas in terms of pressure gradient. Their findings revealed a complex relationship between the pressure drop over the tip and the preceding conduit, which can have a significant impact on the pressure drop over the whole cannula, as further expanded upon in Section 8.7.3.1. Secondly, an additional complexity often overlooked when trying to measure or avoid high pressure gradients is that arterial cannulas are sized according to their *outer* diameter, but can have significantly varying inner diameters [7, 180, 347]. Notwithstanding, only some of the studies considered reported on the inner diameters. Andersen et al. [7] found that even the outer diameter of the cannula, where it enters the aorta, varies significantly between different cannulas. A cannula of a certain material, e.g. soft polymer, hard polymer, metal etc., can also inadvertently influence the inner diameter, because the type and hardness of the material will ultimately determine the manufactured wall thickness. And since cannulas are rated by their outside diameter, the wall thickness will determine the inner diameter [29]. Thirdly, blood as a testing fluid was seldomly considered, not to even mention hematocrit and temperature varying influence on the viscosity of the testing fluid, or comparative values as would be present clinically. Mostly either water or a 60%-40% water-glycerin mixture at room temperature. Furthermore, it must also be considered that although not significantly contributing to stroke, a standard CPB circuit is primed with 2–3 L colloid or crystalloid solution and mixed with typically 5 L of blood circulating throughout the procedure, significantly diluting the blood [82]. Nevertheless, despite limitations in inter-study comparison, many studies report pressure gradients over arterial cannulas currently used clinically that exceed this 100 mmHg pressure gradient threshold for hemolysis [50, 180, 258]. All of these varying aspects negatively influence the absolute, but also comparative value of these reports in general. Therefore, the pressing need exists to perform such comparative studies evaluating different clinically used and new cannulas, comprehensively considering all of the discussed factors and clinical requirements.

The difficulty to compare different cannulas as a whole is not new, as seen in the development [250] and testing [83] of a dimensionless number for cannula performance based on the Reynolds number of flow through cannulas, the so-called *M-number*, to account for the pressure/flow characteristics of cannulas of different lengths and tip designs. The M-number of straight cannulas can be determined analytically, whereas it must be determined experimentally for more complex geometries. However, this measure does not include temperature dependency or hemodilution/hematocrit, which can alter the value of such a measure significantly [197]. Accordingly, this M-number has not enjoyed standard clinical adoption as far as the author could determine. Although such an absolute value for a pressure gradient threshold is important to know, suppliers generally only present clinicians with flow-pressure data for different cannulas
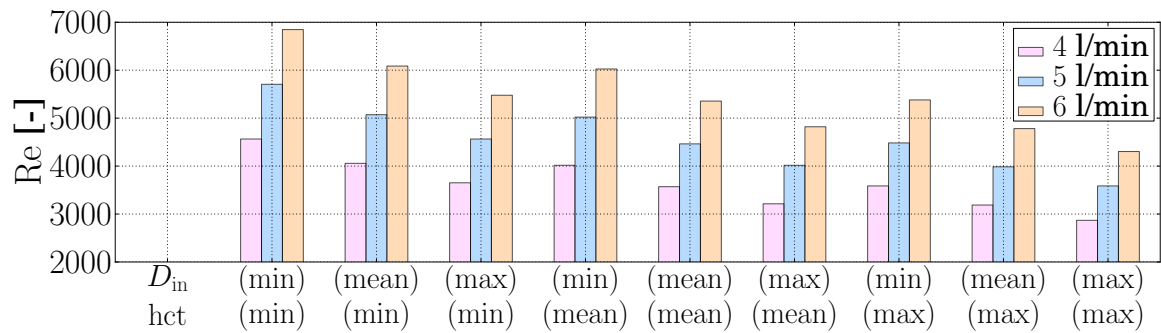
Figure 3.3.: The Reynolds number Re at the tip of a straight end-hole cannula resulting from clinically reported variability in the cannula tip diameters d_{in} (all rated as 24 Fr) and hematocrit levels hct cannula. Three different relevant flow rates are considered. See text for details.

using water at room temperature [29]. Therefore, clinicians can only assess the relative performance of a cannula from supplier information, possibly only between cannulas from a single supplier, but not its absolute performance in terms of hemolysis risk, not even to speak of the risks yielded by the concomitant jet. Additionally, as discussed in this section, not even the comparative studies presented here can necessarily be compared with one another.

All of these aspects are infrequently considered in the clinical setting, although it can have a significant effect on the resulting cannula performance – and should therefore also be included in the cannula selection process. Figure 3.3 presents a simple analysis effectively demonstrating the significant influence that a subtle, yet clinically relevant change to the inner diameter of the tip and hematocrit-dependent viscosity will have on the cannula performance. By considering the minimum, mean and maximum of a range of reported cannula tip inner diameters, i.e. $D_{\mathrm{inner}} = [5.6, 7.0]$ [7], and a range of operative hematocrit levels, i.e. hct $= [0.19, 0.25]$ [82], resulting Reynolds numbers ($Re = \frac{\rho Q D_{\mathrm{inner}}}{\mu A_{\mathrm{inner}}}$) are plotted for three different flow rates ($Q = [4, 5, 6]$ l/min) of flow through a simple pipe, as shown in Figure 3.3. The mean dynamic viscosity μ and density of blood ρ was chosen as 0.004 and 0.00106 g/mm^3, respectively according to normal physiological parameters [196]. Blood was considered here to yield a predominantly Newtonian character (cf. Section 6.4.2). Furthermore, variation of viscosity due to change in the hematocrit hct was calculated simply as 4% for every percentage increase or decrease in hct, which is an acceptable assumption at medium to high flow shear rates [28]. As is clear from this figure, parameter variation, and especially combination of extremes can result in Reynolds number that are almost doubled that of the opposite extreme. Naturally, the pressure drop will be proportional to the Reynolds number for laminar flow, and although not linear for transitional to turbulent flow, will follow the same trend. This relatively simple consideration did not even consider the effect of temperature, but emphasizes the variability encountered clinically, but also cautions of analyses concluding about an optimal level of one singe such a parameter, as have also been previously reported [96]. These conclusions will be questionable if no consideration was given to rigorously and explicitly maintain the constancy of the other parameters referenced here.

Finally, in this regard, the recent novel backward suction cannula design used in an animal experiment should also be mentioned, as reported by Shani et al. [312]. The cannula consists of a regular curved-tip end-hole cannula, with an additional port located on the posterior surface of the curved-tip, i.e. facing proximally. Through this additional port, the authors demonstrated that a high percentage of osseous particles injected in the proximal aorta can be effectively sucked out of the circulation. Thereby, the authors propose to eliminate dangerous emboli originating proximal to the cannulation site from the systemic circulation. Three major concerns to this cannula design arise in the context of all the effects considered

here: (1) Even higher cannular flowrates will be required to compensate for the suction flowrate. This can be compensated by either requiring a larger bore cannula (undesirable) or allowing an even higher pressure gradient over the cannula (undesirable). (2) If the effect of the curved end-hole cannula on distal (and cerebral) perfusion is in fact bad, cf. next subsection, then this design leaves the problem of poor distal perfusion unaddressed. (3) As with the intra-aortic filter, cf. Section 4.2.2.1, only the particulate matter that originate proximal to the cannulation site, and only when suction is switched on, have the *potential* of being captured. Should this design finally be tested in humans, it is the opinion of the author that such a study should also aim to thoroughly report the cannula location and direction. Clinical outcomes using this device would be interesting, however, it is the opinion of the author that outcomes might possible be inconclusive, as it was for other novel designs addressing only a single consequence of aortic manipulation, e.g. intra-aortic filter (Section 4.2.2.1), cobra cannula (Section 3.1.2.1) etc.

Apart from trying to evaluate or determine a cannula tip design which possesses the optimal trade-off between lowest peak velocity, shortest jet attenuation distance and pressure gradient, there are also the further consequences of the resulting patterns of flow occurring in the patient. These patterns are not only influenced by the jet strength, but also by the cannulation site, cannula orientation and patient-specific aortic geometry, as expanded upon in the section below.

3.1.2.3. Distal flow disturbances due to continuous arterial cannular flow

Under healthy physiological flow conditions, typically 14% of the total flow ejected by the heart that enters the aortic arch is perfused into the first three branches, i.e. brachiocephalic, left common carotid and left subclavian arteries, all of which supply different cerebral arteries with typically 750 ml/min of oxygenated blood, accounting for approximately 20% of the total body oxygen consumption. However, during hypothermic CPB with an alpha-stat acid-base-management strategy, the brain only receives approximately 5–7% of the cardiac output. Autoregulatory mechanisms are responsible for mainting a cerebral blood flow (CBF) of approximately 45–60 ml/100 g of brain tissue [291]. These flow quantities and patterns of physiological flows in the aorta have been studied extensively in various imaging studies, especially phase-contrast magnetic resonance imaging (PC-MRI) studies, as reviewed and summarized by Morbiducci et al. [253]. They also comprehensively listed the reasons for the complex flow patterns arising in the aortic arch. These include the complex geometry of the aortic arch, e.g. non-planar curvatures, branches at the superior part of the arch, a distensible and tapering vessel structure, a degree of dynamic movement of the aortic root, structures protruding into the flow field and the complex ventricular twisting and torsional movement during contraction. Consequently, the pulsatile feed of blood into the aortic arch gives rise to a complex, net forward, helically rotating flow pattern which mostly has laminar to laminar-turbulent transitional properties.

Although the ratios of blood entering the different cerebral vessels may slightly vary between healthy subjects, various homeostatic auto-regulation capabilities of the body work to maintain these levels of perfusion [140]. However, various downstream pathologies or surgical conditions might alter perfusion to the brain or other end-organs, e.g. carotid stenosis, aortic coarctation, impaired auto-regulation due to global anaesthesia and of course continuous arterial cannular flow, of which the latter is expanded upon below in detail.

General flow pattern in aortic arch due to arterial cannular flow Many experimental studies have considered flow patterns in a mock aorta due to arterial cannular flow from different cannula tip designs with 2D [141] and 3D flow visualization techniques [242, 244], some changing the cannula orientation [112], while others also considered cerebral perfusion pressure [180]. All describe regions of elevated WSS and unphysiological vortices and flow concentrations forming for the different cannula tip designs. Joubert-Huebner et al. [180] also reported significant pressure and cerebral flow variations in the three branches that exit the aortic arch dependent on cannula tip used and cannula orientation. Even

though these studies only considered flow conditions for certain cannulas fixed at a certain predetermined cannulation site, all of them also speculate that the perfusion patterns, as well as regions of elevated WSS will vary if the cannulation site, cannula orientation, or if a cannula tip other than what was investigated, was used.

Robust peak velocity reduction A more robust attempt at obtaining a more uniform flow with low peak velocity entering the aortic arch has been to point the most sufficiently dispersed jet, e.g. as produced by the Dispersion cannula, towards the aortic valve. This was shown to be effective in smaller clinical studies [142, 363], of which this effect has also been confirmed experimentally [112]. However, its widespread clinical adoptation has not been found because of the scarcity of literature on the matter. This can be attributed to the fact that the trade-off for obtaining such a uniform flow with a low peak velocity is that the jet has to be dissipated by the aortic valve and aortic root itself. The common occurrence of atherosclerotic lesions in the aortic root, potential aortic valvular disease or insufficiency and a shorter distance over which the jet can be attenuated (compared to pointing the jet into the aortic arch), would actually cause increased embolic risk brought about by such a maneuver, due to the sandblasting effect.

Diverting the problem downstream It has been suggested to advance a centrally placed cannula further distally along the aortic arch (also referred to as a long cannula) such that the cannular jet points down into the descending aorta, thereby causing retrograde perfusion of the cerebral vessels and presumably preventing atherosclerotic lesions in the ascending aorta and aortic arch to be embolized by the jet and also washing the majority of the embolic load into the descending aorta [45, 146, 193], as also shown by monitoring the embolic signals of flow entering the cerebral arteries [259]. The latter advantage was also advocated by the investigators of the Cobra catheter, which also aims to deflect embolic material from entering the cerebral arteries, cf. Section 3.1.2.1. Other attempts following the same guiding principle have spurred the developement of the Embrella Embolic Deflector (Embrella Cardiovascular Inc, Wayne, Pa) or the EmBlocker (Neurosonix Ltd). The former is a percutaneously insertable filter device to cover the aortic arch orifices supplying cerebral perfusion. Its efficacy to deflect the majority of emboli downstream and the concomitant pressure drop over the filter have been shown to be satisfactory in an animal model [58] and a pilot clinical study [270]. However, such an intra-luminal device once again increases the risk of embolic release due to abrasion, cf. intra-aortic filter, Section 4.2.2.1. The latter is an ultrasound probe positioned directly adjacent to the aortic arch to deflect emboli downstream. One pilot clinical study has demonstrated its ability to reduce the embolic signals entering the cerebral circulation by half compared to a control group [304]. Unfortunately, this intervention comes at a price of a local increase of temperature and can therefore only be applied for intermittant periods of time. Both of these interventions, however, also only (partly) divert the embolic risk, but do not prevent it.

Dominant particle path The disturbance caused by the continuous arterial cannular jet has also been attributed to cause a dominant particle path, i.e. the concentration of the high velocity jet transports most of the embolic material entering/generated in the aortic arch along a preferential perfusion path. In a non-randomized prospective study of 2217 consecutive patients undergoing CABG surgery, Weinstein [353] deduced that curved tip end-hole cannulas are dangerous and that side-hole cannulas should be used instead, since the former, causing an unattenuated jet, "washes" the bulk of the embolic load into the more distal of the cerebral arteries branching out of the aortic arch, i.e. the left common carotid artery. This was based on their results showing that strokes in the left hemisphere were 3 times more likely to occur than in the right hemisphere. Although making some conclusions only considering different manipulation maneuvers in isolation of each other, they make a valid point, as also observed elsewhere [38, 259].

Disturbed helicity Another often infrequently considered disruption caused by the continuous arterial cannular flow, is the disruption of the physiologically occurring helical flow pattern in the aortic arch. Such helical flow patterns have repeatedly been described *in vivo* in healthy volunteers [194, 253, 321]. It has been hypothesized [57, 252, 325] and supported with evidence from PC-MRI studies [253] that these helical flow patterns develop during growth as a natural optimization of perfusion in order to reduce en-

ergy dissipation in the aortic arch. This is based on the fact that non-zero helical flow have been shown to reduce energy dissipation by inhibiting energy flux from larger to smaller vorticity scales [333]. The first investigation describing the difference between rotational flow patterns comparing patients under physiological conditions, as well as when receiving CPB, was performed by Koh et al. [200]. Using TEE in vivo, and verifying with MRI in an experimental setup *in vitro*, they demonstrated that aortic geometries imposed a handedness to flow in the aortic arch and descending aorta, i.e. a patient-specific preferential rotational direction, either clockwise or anti-clockwise. Arterial cannular flow was shown to nullify this preference and could either maintain the handedness or change it. Based on these findings, they suggested that the disturbance of the natural occurring helical flow caused by arterial cannular flow may have embolization and hypoperfusion risks. Embolization, since certain lesions have experienced a preferential direction and variation of WSS over a duration of time, which can be disturbed by a change in helicity. Hypoperfusion, since the natural helicity has developmentally been adapted to provide optimal perfusion which becomes disrupted by arterial cannular flow. However, this mechanism for cardiac surgery-related stroke is difficult to isolate and has very seldomly been considered clinically [288].

Inadequately testable outcomes Limitations of the experimental results are that the dynamic response of the distensible aortic wall and the Windkessel type outflow conditions are simplified. Furthermore, in all of these, mostly water, but also water-glycerin mixtures at room temperature, were used as working fluid. The main reason why no clinical studies could be found evaluating these disturbed flow patters can be ascribed to the fact that very limited flow visualization capabilities exist during surgery. The only intra-operative imaging available is transesophagoeal echocardiagraphy (TEE) and epiaortic echocardiography, both of which cannot completely visualize the arch due to certain, at present insurmountable artifacts and that only a single plane of measurement is available. Additionally, whether clinical or experimental, the results from all of these studies are subject to patient-specific variability. Ultimately, all these studies do deliver an important, albeit only qualitative, result, namely: that continuous arterial cannular perfusion strongly influences flow patterns in the aortic arch and increases the potential of cerebral hypoperfusion and arterial cannular jet-related embolic risks. The extent of such potential dangers might be refinable in a general sense, but would ultimately need to be determined for every patient-specific case. However, it seems reasonable to infer, as has been done in many of these studies, that this increased potential danger due to arterial cannular flow is significant and needs to be addressed.

The following section considers solutions aimed at alternatives to central cannulation with continuous arterial cannular flow.

3.1.2.4. Non-cannula adjustments influencing distal flow

While central cannulation with continuous arterial cannular flow is considered standard when performing conventional CPB, alternatives have been suggested to surmount associated complications, although not necessarily complications in the context of altered hemodynamics. These two strategies consider pulsatile arterial cannular flow and peripheral cannular access sites, expanded upon below, and are considered mainly in terms of its influence on the hemodynamical factors previously considered, i.e. their risks of hypoperfusion and embolization.

Continuous vs. pulsatile arterial cannular flow It has been argued that extra corporeal circulation should completely mimic the physiological conditions of a patient as closely as possible, and therefore pulsatile perfusion needs to be used during these procedures. However, only comparing the cannular flow characteristics of a range of clinically used cannulas, it was found that arterial cannular jet peak velocities averaged 45% higher when considering pulsatile to continuous flow. More specifically, for the same set of cannulas evaluated, continuous and pulsatile flow yielded peak jet velocities of 3-9.5 times and 6-17 times that of normal aortic flow velocity (80 cm/s), respectively [141]. Considering the above reviewed aspects of arterial cannular flow, this automatically implies a more dangerous jet and higher

pressure gradients over the cannula. Furthermore, as pointed out in a recent review, conventional pulsatile pump systems actually only deliver sinusoidal pulsatility, which is not physiological [140]. Therefore, since the cannulation position and cannula orientation influenced distal flow in an unintuitive way, it is not clear at all whether adding pulsatility to the cannular flow will enhance replication of physiological hemodynamics in the aortic arch.

Although limited clinical studies have been done to elucidate on the benefits of pulsatile perfusion, a systematic review by Alghamdi and Latter [4] found that the evidence from the available clinical studies was conflicting and insufficient to argue for or against a particular perfusion strategy to reduce stroke and myocardial infarction. This conclusion was drawn despite the expectation that pulsatile perfusion improves micro-circulatory flow, myocardial perfusion, oxygenation, and indices of contractility. Additionally, this conclusion was drawn even despite the fact that pulsatile perfusion has been demonstrated to decrease fluid retention in the lungs and reduce the frequently observed rise in systemic vascular resistance during CPB by being able to maintain normal levels of aldosterone, catecholamines and plasma angiotensin. As pointed out by Murkin [261], regardless of the fact that such comparative studies need to be better designed and controlled, pulsatile perfusion may be beneficial to a certain patient profile due to some promising results. Nevertheless, the standard of care remains continuous perfusion due to technical difficulties in achieving pulsatile flow [5], as well as the unproven benefit and the hemodynamical aspects considered here.

Peripheral cannular flow Multiple reasons exist why it may be unsuitable or undesirable to cannulate a patient centrally, i.e. in the ascending aorta, but rather cannulate peripherally. Such reasons predominantly include severe atherosclerosis of the ascending aorta [318] or as required for performing a minimally invasive procedure [65]. The aorta or any of its branches can be cannulated at any level, even through the apex of the left ventricle, provided safe access exists, no pathologies detrimental to cannulation exist in this region and that the aorta is of sufficient size to allow insertion of a cannula that can provide the perfusion required. The main alternative cannulation sites, apart from central cannulation, is axillary and femoral cannulation, considered below. Although the reason for changing cannulation site might not be hemodynamical considerations, it will definitely result in flow patterns significantly different than with central cannulation.

As excellently summarized by Fukuda et al. [113], the femoral artery has classically been the alternative cannulation site of choice, mainly due to its easy access and sufficient size to allow an adequately sized cannula. However, the femoral and iliac arteries can be severely damaged by cannulation, show significant infection rates, can yield distal limb ischemia, are frequently affected by atherosclerosis, especially in elderly patients and are more prone to complications in patients with peripheral vascular disease, including aortic dissection. The potential for lower extremity ischemia also exist during long-term perfusion. Furthermore, since a femoral cannula is only advanced a couple of centimeters into the artery, all arteries proximal to the cannulation site receive circulation in a retrograde fashion. As such, retrograde femoral artery perfusion has been associated with perioperative risk in certain procedures, e.g. redo mitral valve. Despite risks associated with femoral cannulation, it has been demonstrated that meticulous screening of the affected area and taking all necessary precautions can keep the risk of associated stroke at an acceptable level.

As far as the author could determine, studies of flow patterns created by retrograde perfusion have not been done experimentally or clinically. However, due to the size of the femoral arteries, smaller cannulas are generally used, but since atherosclerotic lesions can occur at any arterial level, such a high velocity jet also poses a risk of perioperative CVAs. This becomes dangerous when considering that continuous retrograde perfusion will definitely cause WSS on atherosclerotic lesions from another direction in a different loading regime compared to what it receives physiologically. Such a change in loading regime has been pointed out as being a potential mechanism of perioperative CVA due to disrupted helical flow, cf. Section 3.1.2.3. Furthermore, as also pointed out in Section 3.1.2.3, the likelihood of atherosclerotic

lesions existing in the descending aorta when severe atherosclerosis exists in the ascending aorta is high. Therefore, the very reason for choosing femoral cannulation due to atherosclerosis of the ascending aorta or aortic arch may in fact be paradoxical.

Concerning the other main alternative, axillary artery perfusion, Fukuda et al. [113] continued: Axillary cannulation can either be achieved directly or by anastomosing the cannula graft onto the artery, the latter yielding the best comparative outcome. As with femoral cannulation, peripheral vascular disease, size and atherosclerosis of the axillary artery also play an important role as to allowing its use, although atherosclerosis of the axillary artery occurs less frequently. Complications of this perfusion strategy include hyperperfusion of the ipsilateral arm, brachial plexus injury, compartment syndrome of the arm, thrombosis of the artery and the rare occurrence of local or diffuse dissection of the axillary artery. Nevertheless, complications associated with axillary perfusion have been low. Axillary perfusion has the advantage over femoral retrograde perfusion, that at least antegrade perfusion can be delivered to the right carotid system and can also be used for selective cerebral perfusion during major aortic procedures. Only one experimental study considered the flow patterns caused by axillary perfusion in a glass model of the aortic arch using water [243] and noted that flow entering the aortic arch was particularly rapid. Consequently, it was suggested that special care be taken in patients with fragile atherosclerotic lesions around the arch vessels or the lesser curvature of the aortic arch when performing such perfusion. Altered cerebral flow was not considered.

Other variations of the cannulation site perfusion strategies that have been successfully attempted include the brachiocephalic and carotid arteries, as well as transapical cannulation of the left ventricle. The frequency at which these have been performed clinically is low and therefore their clinically efficacy unclear. Although many studies have compared smaller cohorts of patients comparing all of the cannulation site perfusion strategies considered here, no randomized studies have been performed to elucidate which site-specific perfusion strategy is optimal for patient outcome [113]. Furthermore, there also exists a lack of homogeneity among patient cohorts compared in the available studies, and studies of altered hemodynamics are lacking. Nevertheless, relatively safe alternative cannulation site perfusion strategies exist that can be used when another is contra-indicated or not preferred.

3.2. Beating-heart (off-pump) procedure hemodynamics

3.2.1. Fundamentals

Off-pump beating-heart procedures refers to cardiac surgical procedures where no CPB is used, also commonly referred to as *off-pump* procedures. The most common procedure is coronary revascularization, and also the main focus of this section, which requires additional external instrumentation to stabilize the local region on the heart where the distal anastomosis will be made.

Although some of the first coronary revascularization procedures were performed on a beating heart [21], the mid-1970's brought the safety standardization of CPB. The technical challenges of operating on a bloodless and stationary field and growing concerns for increasing the risk of myocardial injury while performing temporary coronary occlusion in the beating heart, lead most surgeons to abandon such procedures [23]. However, during the 1980's off-pump surgery resurged in resource-limited centers, due to advantages posed by this procedure [60]. Evidence from these centers and a growing interest in performing minimally invasive procedures lead to a global resurgence of off-pump procedures in the late 1990's. The Society of Thoracic Surgeons' database reported that in 2001, already 18.6% of all coronary revascularization procedures were performed off-pump [219].

Although much has already been said concerning its main advantages, disadvantages and outcomes compared to on-pump procedures, these were mostly done in relation to the dangers of partial-occluding

involved in many of these procedures, cf. Section 2.4. It is therefore the purpose here to concisely consider maneuvers responsible for temporary disruption of the physiological hemodynamics, specifically with regards to coronary revascularization procedures, owing to the large volume of research on this topic. Finally, although not considered pure cardiac surgery, the endo-vascular repair of the thoracic aorta disrupts the CBF in a similar manner as during off-pump coronary revascularization, and is considered here for completeness sake.

3.2.2. Clinical considerations

The two manipulation maneuvers which can significantly alter the physiological hemodynamic state is the dislocation of the heart and the partial-occluding used when performing the proximal anastomosis. Although the latter can be avoided and the former is technically not aortic manipulation *per se*, both of these are used and can alter hemodynamics in the aorta in such a way as to hold risks of procedural-related CVAs.

3.2.2.1. Cardiac handling

The physiology and anesthetic management of off-pump coronary artery bypass have been extensively reviewed by Chassot et al. [60] and will be used as a guideline for considering the following hemodynamic consequences of this procedure. The three main aspects that influence physiological hemodynamics considered in this review are obtaining adequate exposure to the distal anastomotic site on the heart, restraining the motion of this site and disrupting coronary flow during distal anastomosis on the heart. Although critically important to myocardial outcome, the latter falls outside the context of perioperative CVAs and will therefore not be considered here.

The exposure of the distal anastomotic site(s) and the stabilization thereof have been shown to significantly increase the atrial pressure and causing a marked decrease of cardiac output (<2 liter/min/m^2). These consequences are attributed to the displacement of the heart and compression (or restriction of movement) of the ventricular wall. Different maneuvers performed during such a procedure will have different hemodynamical consequences, of which the main maneuvers are considered here. Firstly, the heart is tilted vertically with the apex pointing upward. As such, blood has to flow upward (against gravity), into the ventricles. This increases the filling pressures that need to be achieved by the atria. Secondly, the stabilizer device pushes against the walls of the heart, thereby restricting its local movement and its ventricular distensibility. Especially critical is when the movements of the anterior and lateral walls of a ventricle are blocked, because these contribute the most to stroke volume. Thirdly, the vertical position, as well as twisting involved to gain better access to anastomotic sites, cause distortion of the mitral and bicuspid valve annuli and can lead to not only severe regurgitation, but also a temporary induced valvular stenosis. Such consequences have also been reported for the aortic valve. The severity of the hemodynamic disturbance is mostly linked with the site of anastomosis, i.e. more cardiac tilting, twisting and compression of the ventricular walls are required to gain access to the circumflex artery on the lateral side of the left ventricle, compared to the left anterior descending artery on the anterior of the left ventricle. Finally, in an attempt to decrease the left ventricular preload, the patient is positioned in the Trendelenberg position (tilted longitudinally downwards towards the head between 15–30°). This can alter central venous pressure even more and thus has to be carefully considered/monitored.

These hemodynamic disturbances can be managed with rigorous pressure adjustments by specialized anesthetic strategies, aiming to perform such impacting maneuvers as quickly as possible and even by strategies such as leg elevation to help increase cardiac output. However, the hemodynamical alterations are not without certain risks. Since cerebral perfusion pressure depends on the difference between mean arterial and central venous pressures, a decrease in the former (due to decrease cardiac output) or an in-

crease in the latter (due to increased atrial pressure) can also be a potential mechanism of hypoperfusion. Although distal anastomoses are performed in both on-pump and off-pump procedures, such hypoperfusion is much more prevalent during off-pump procedures due to the dislocation of the heart, as confirmed in a comparative study estimating cerebral hypoperfusion by considering jugular bulb oxyhaemoglobin saturation of less than 50% between the two types of procedures [86].

3.2.2.2. Temporary stenosis by partial-clamping

Not considered in the above-mentioned review on hemodynamical disturbances during off-pump CABG [60] is the potential hemodynamical influence of a partially occluded ascending aorta. Although partially occluding the aorta to achieve proximal anastomosis can be avoided by a "no touch strategy" or using an automatic graft connector, cf. Section 2.4.3, there are still indications for the use of off-pump CABG: mainly its stability, simplicity and low cost. Such a partial occlusion does not merely cause structural damage, but also temporarily constricts the aorta at the proximal anastomotic site. Such a constriction implies the manipulation of the aorta under pulsatile, inadequately controlled pressure conditions, which causes an increase in afterload for the heart, i.e. pressure that the heart must overcome to expel blood from the ventricle.

Pulsation against the partially clamped aorta An incompletely understood phenomenon is the manipulation of the pressurized aorta, especially under inadequately controlled pulsatile conditions during off-pump procedures. This fact is highlighted in a group of studies investigating cardiac surgery-related aortic dissection, also referred to in Section 2.4.2. When considering the origin of an aortic dissection, it is clear that some tear in the intimal wall at a certain pressure will force layers of the aorta apart. Consequently, hypertension is considered a risk factor for aortic dissection, also reflected in the fact that perfusion pressure during on-pump procedures is, typically, specifically maintained at no higher than 60 mmHg during manipulation procedures in consideration of the dissection risk, among other reasons. Furthermore, uncontrolled hypertension has also been identified as a major risk factor in the occurrence of aortic clamp trauma [324].

Chavanon et al. [61] found a more frequent occurrence of dissections after off-pump procedures than on-pump procedures. Despite the low number of these cases, they and others [149, 313, 330] have hypothesized that pulsation aggravates the laceration caused by the fixation of a partial clamp onto a portion of the aorta, which partly limits its distensibility. Such is the case during partial-clamping in off-pump procedures, but potentially also the case for any manipulation of the aorta, e.g. fixation of a part of the aortic wall by an automatic graft connectors [274]. In on-pump procedures, the perfusion pressure is generally non-pulsatile and more controllable. This hypothesis is further supported by outcomes from a recent analysis of The Society of Thoracic Surgeons database from 2004–2007 considering the occurrence of all cardiac surgical-related aortic dissections. Although not explicitly distinguishing between on-pump and off-pump coronary revascularization procedures, the analysis revealed that of the 0.06% rate of aortic dissection associated with coronary revascularization, two-thirds of these dissections occurred during off-pump procedures [359]. Furthermore, in a recent review following a case-presentation of aortic dissection during off-pump surgery [330], it was suggested that the frequency of dissections during off-pump procedures is underestimated. This is because it has been found that intra-operative dissections occur more frequently during on-pump procedures, whereas early post-operative dissections occur more frequently with off-pump procedures, which are usually hard to detect, diagnose correctly or determine its origin.

However, although there is compelling evidence to support such a hypothesis, more focused investigations are required to elucidate on the proposed increased severity of laceration and increased risk of perioperative dissections associated with the partial-clamping of the aorta under uncontrolled, pulsatile pressure conditions.

Ascending aortic temporary quasi-stenosis As far as the author could determine, very little has been reported regarding the influence of proximal anastomosis on hemodynamic stability. This aspect was not even mentioned in the comprehensive review on the hemodynamical influences of off-pump surgery [60]. Furthermore, the paucity of available literature on this topic was emphasized in a recent case study by Santos et al. [302].

These authors presented two cases of off-pump coronary revascularization where hemodynamic instabilities were recorded that were associated with the partial occlusion of the aorta. In the first case presented, the patient had a small ascending aorta luminal diameter (28 mm), which lead them to deduce that the decreased luminal diameter due to partial occlusion increased the afterload to such an extent as to affect ventricular function and thereby also causing an increase in pulmonary artery pressure. This was observed immediately after partial-clamp application, as recorded by the pulmonary artery catheter. In the second case, a patient with preoperative left ventricular dysfunction remained hemodynamically stable until the partial clamp was applied, attributed to the same effect, as also monitored by the pulmonary artery catheter.

Such an effect can be explained relatively simply by considering the fluid dynamical effects of a converging nozzle directly coupled with a diverging nozzle, which is effectively what the partial clamping produces. The decrease in cross-sectional area of the converging nozzle will cause a reduction in pressure but an increase in velocity, whereas the opposite will occur in the diverging part. However, this converging-diverging nozzle created by partially clamping the aorta is expected to significantly alter the perfusion, as was observed in stenosis flow and indexing studies [120, 281, 345]: Firstly, pressure losses will be significant since the converging and diverging profiles are steep. Large variations of cross-sectional diameter are also induced and the pulsatility of flow will continually yield transient flow patterns dissipating energy. Additionally, this "nozzle"-structure is partly distensible and will therefore further dissipate energy compared to a rigid walled structure. Secondly, such a constriction so close to the heart will also yield an increased pressure experienced by left ventricle, i.e. an increased afterload, as observed in the above-mentioned case-studies. Such an increase in afterload comes in addition to the other causes described by Santos et al. [302].

3.2.2.3. Temporary aortic occlusion by TEVAR

For completeness sake, although outside of the scope of this dissertation, the following is briefly considered.

In beating-heart vascular (non-cardiac) surgical procedures, the aorta is only occluded distally to the main branches supplying the brain with oxygenated blood. Within certain time limits, this can be done without the need of additional CPB, e.g. during open repair of abdominal aortic aneurysms (AAA). Such disturbances to physiological hemodynamics due to aortic occlusion are significant on all organ systems, since it results in increased systematic vascular resistance, increased impedance to aortic flow, increased afterload, redistribution of blood volume caused by collapse and constriction of venous vasculature distal to the occlusion site with a subsequent increase in preload. Such changes in hemodynamics also result in the release of many different mediators that may reduce or increase the harmful effects caused by not only occlusion, but also occluder release, i.e. reperfusion injury. All of these factors depend further on the level at which the aorta was occluded and the duration of occlusion. For a detailed review of the mechanisms and consequences involved, the interested reader is referred to Gelman [129].

The only exception where the aorta is temporarily occluded proximal to the cerebral perfusion supplying branches in a beating-heart procedure is during total or hybrid endo-vascular aortic repair (EVAR) of the thoracic aorta, also referred to as thoracic endo-vascular aortic repair (TEVAR). In such procedures, deployment of the stent-graft requires an EAB to expand in order to sufficiently plastically deform the stent material to hold the stent-graft in place. Such deployment by an EAB causes temporary occlusion

of the aorta. Strokes associated with EVAR are generally considered to be of embolic origin as demonstrated by TCD studies, but the hemodynamical disturbances must also be considered. Although limited reporting of the concomitant hemodynamical consequences exists, it has been reported that during balloon inflation/molding, the cerebral blood flow in the middle cerebral arteries, as measured by TCD, was significantly altered [35]. Additional consequences include significantly altered hemodynamics due to existing patient-specific stenosis or incomplete circle of Willis [237], while the stent-graft may also cut off certain crucial branches relying on other colateral perfusion pathways. Sometimes such flow is not sufficient and requires revascularization thereof to reduce procedural-related strokes or other end-organ ischemia, e.g. stent-graft covering the left subclavian artery [140, 286].

4. Direct laceration of the aortic wall

Seek first to understand, then to be understood.

— Stephen Covey

From the preceding two chapters, it is abundantly clear that large deformation of the aorta and a multitude of procedural maneuvers influencing hemodynamics can be initiators of various embolic or hypoperfusion events during cardiac surgery. However, apart from all of these, there is another group of maneuvers performed during cardiac surgery not covered by the above-mentioned, which specifically holds risks of embolization. Such a group involves maneuvers where the artery is directly lacerated, and of critical importance is the laceration to the intimal layer of the artery. These maneuvers include the puncture of the arteries and intra-arterial abrasion. Of prime interest is, of course, cardiac surgery-related maneuvers responsible for direct laceration of the aorta, but certain interventional cardiological procedures that can lead to similar direct lacerations are also briefly considered. As will be shown in this chapter, such manipulation maneuvers induce similar types of injuries as have already been considered, and therefore, a more concise overview suffices in order to emphasize the gravity of the associated risks. Here the terms "artery" will be used to indicate the general risks associated with direct lacerations without loss of applicability to aorta-specific manipulation maneuvers.

The chapter will begin by considering arterial puncture, followed by considering an array of different maneuvers responsible for intra-aortic abrasion produced by both surgical and interventional cardiological interventions.

4.1. Arterial puncture

4.1.1. Fundamentals

Arterial puncture, also referred to as *aortic perforation*, can be defined as a continuous laceration stretching through the complete thickness of the aortic wall, which is broader than the term *aortotomy*, because it includes puncturing of the wall by suture. Maneuvers performed during cardiac surgeries responsible for arterial puncture include the introduction of an arterial cannula or a catheter [122, 211, 293] – cf. Section 2.4.3 – anastomosis onto/into an artery and possible concomitant removal of a diseased portion of artery [48, 282], access to debride an artery of some lesion [113], or due to any type of suture reaching the intima [324, 340].

4.1.2. Clinical considerations

Regardless of the maneuver responsible for aortic puncture, the consequences are similar: Firstly, puncture exposes atmospheric pressure and potential air trapped in the cannula tip to the luminal blood pressure, thereby increasing the risk of air entering the arterial circulation as gaseous emboli, as seen experimentally [30] and in TCD studies correlating maneuvers to number of emboli entering the cerebral circulation during cannulation and decannulation, cf. TCD studies considering all CPB manipulation maneuvers, Figure 1.3. Secondly, a tear in a pressurized conduit is at risk of tearing further in patients with connective tissue disorders such as Ehlers-Danlos type IV syndrome [69]. Thirdly, the media and adventitia

are exposed to the luminal blood pressure which increases the risk of aortic dissection, especially when the purse-string sutures are fixed around the cannula leading to luminal blood pressure directly on these layers, cf. discussions on iatrogenic aortic dissections in Section 2.4.2 and 3.2.2.2. Fourthly, an intimal lesion is created that can increase the chances of atheromatic lesion formation, as seen in animal studies investigating cross-clamping-related damage, cf. Section 2.1.2. Finally, puncturing the artery poses the risk of dislodging embolic material into the arterial circulation, especially at fragile lesions of the artery, as emphasized in experimental studies [38, 40], studies promoting echo-guided cannula placement [137] and in the TCD studies investigating all manipulation maneuvers, mentioned above.

Specific risk factors for arterial puncture have always been discussed in terms clinical risk factors relating to the above-mentioned consequences, but not identified explicitly in literature, as far as the author could determine. However, based on the literature reviewed in the preceding chapters, it seems reasonable to assume that the size of the puncture, its location in terms of existing atherosclerotic lesions, existing patient vascular pathologies, and luminal pressure magnitude and character (continuous or pulsatile) during and after such maneuvers will influence the risk posed to patient outcome.

4.2. Luminal abrasion

4.2.1. Fundamentals

Luminal abrasion refers to any manipulation maneuver responsible for direct laceration inflicted from within the lumen to the aortic wall, ranging from superficial intimal laceration or scraping to lacerations stretching through to the adventitia, but not complete puncture. Indirect laceration are those caused by an external manipulation, such as cross-clamping, cf. Figure 2.2. Similar to the risks involved in aortic puncture, described above, luminal abrasion increases the risk of particulate embologenesis as well as the risk of aortic dissection. Various inter-vascular devices can have such consequences, as expanded upon below.

4.2.2. Clinical perspectives

4.2.2.1. Intra-aortic filter

An excellent example of intra-aortic abrasion is the use of an intra-aortic filter (IAF).Recognizing the danger of embologenesis during the application and the concomitant release of the cross-clamps, especially in the presence of atherosclerotic lesions, a system was developed to capture such particulate emboli. The only commercially available IAF, as part of the Embol-X Glide protection system (Edwards Lifesciences, Irvine, CA), basically consists of inserting a filter covering the aortic lumen through a port in the cannula, negating additional puncture of the aorta. The IAF is inserted distal to the cross-clamping site and proximal to the arterial cannula. IAFs have been shown to capture life-threatening particulate emboli originating from surgical interventions [25, 153], mainly consisting of fibrous atheroma and platelets/fibrin, but also calcified particles. However, the first randomized study investigating the usefulness of IAFs could only demonstrate a significant positive effect on the occurrence of renal-failure, but could not demonstrate improved neurological outcome [25]. The low potential for improving neurological outcome and/or difficulties in application of IAFs might explain its relatively poor clinical acceptance [31].

Among many other reasons that can be put forth to explain the clinical failure of such a device, in terms of manipulation-related CVAs, is the subsequent intra-aortic abrasion inflicted by an IAF. Whether or not an IAF consistently covers the entire luminal area to be able to capture all of the particulate proximally emboli originating is unknown clinically. Consequently, the filter will always be expanded more than what is necessary to cover the luminal area and will therefore press harder against the aortic wall than necessary

– analogous to why a vessel is practically always over-occluded, because clinically the state of occlusion is indeterminable, yet essential, cf. Section 2.1.1. Furthermore, movement of the fine-wired filter in its deployed state cannot be completely restricted and will therefore be prone to shear against the intimal wall. Such luminal abrasion injuries that release particles additional to those captured by the IAF have been shown experimentally in a cadaver model [40] and clinically [25]. No further investigations into the extent of the injury, increased risk of embolization and neurological outcome associated with the use of an IAF is foreseen due to its clinical failure to show efficacy.

Within this context, it is worth considering a recent development following the same guiding principle which yielded the IAF, namely the CardioGard cannula (BEL Bioengineering Laboratories, Italy). This arterial cannula has a standard bent-tip end-hole cannula design that must be pointed distally, but possesses an additional lumen pointing proximally. By simultaneously sucking blood through the additional lumen while conventional arterial cannular flow continues through the primary lumen, its intention is to remove embolic material released from the manipulation sites proximal to the arterial cannulation site, and to subsequently filter the removed blood and introduce it back into the available blood reservoir. Thereby, additional manipulation with an IAF is avoided. In an animal study, it has been successfully demonstrated to have an embolic retrieval rate of 77%, with no significant changes in hemodynamical or blood parameters [312]. However, two limitations can be pointed out here in hindsight of what has been reviewed in Section 3.1.2: Firstly, by removing more blood from the arterial system, more blood need to be returned. As such, the required increase in flow rates for concomitant removal of blood to maintain adequate cerebral perfusion will need to be closely considered in a clinical setting, as it could become dangerously high. Reduced flow regimes, as described in this study, can of course only be maintained for short periods of time, but adds to the risk of cerebral hypoperfusion. Secondly, this solution does not address the embolic and hypoperfusion risks associated with cannular flow through an end-hole cannula.

4.2.2.2. Cardiac catheterization

Whether performing coronary angiography, percutaneous coronary intervention (PCI), some kind of catheterized carotid intervention or endo-vascular aortic repair, a catheter will not only have to puncture an artery, but will be advanced a certain length to the desired state of application. Therein lies the risk of catheter scraping/direct laceration being responsible for embologenesis, but also aortic dissection. Unfortunately, patients with more severe coronary artery disease (CAD) requiring a PCI due to certain clinical risk factors that contra-indicate open surgical repair, more frequently present with more severe cases of atheroma and are consequently at a higher risk of atheromatic disruption and therefore stroke [176]. This was confirmed in a recent meta-analysis of comparing outcome between PCI and on-pump CABG treatment of multivessel CAD [315]. This study revealed that in such a patient-population, only a trend of more strokes occurred in patients receiving on-pump CABG, compared to PCI, i.e. not a significant difference. Such a result is impressive considering the amount of manipulation that is avoided in PCI compared to on-pump CABG, as reviewed in this report. However, PCI is more advantageous in terms of stroke risks when considering a broader patient population in terms of CAD severity, also considering a recent systematic review [47].

Although much has been said on the topic, the following considers information supplied by a recent clinical perspective of periprocedural stroke occurring during cardiac catheterization by Hamon et al. [152]. Periprocedural stroke associated with cardiac catheterization is low, 0.2–0.4%, of which clinical risk factors include hypertension, diabetes mellitus, prior stroke, renal failure, previous catheterization, previous IABP, or emergency procedures (where less care is taken). The main mechanism by which strokes occur is considered to be embolic in nature, as confirmed by TCD studies during such procedures. The main sources include air, thrombus formation on the catheter surface, as well as aortic atherosclerosis. One study reported that such aortic plaques/lesions are scraped in >50% of PCI cases. Since antegrade

perfusion is maintained during these catheterization procedures, the ascending aorta and aortic arch have been identified as the sources of embolic material. Understandably, atheroma in the aortic arch have been identified as an independent risk factor for recurrent stroke – as already comprehensively presented in Section 1.1.2.1.

Apart from the laceration danger posed by the catheterization itself, the angioplasty or stenting carries its own risks. Both are principally performed to treat an artery stenosed by some sort of atheromatic plaque build-up. This is achieved by inserting a balloon catheter into the stenotic region and inflating it to literally break open the stenosis. Stenting differs from angioplasty in that a metal mesh structure is crimped over the deflated balloon. Therefore, the balloon expansion causes permanent plastic deformation of the stent to approximately the diameter of the inflated balloon, thereby mechanically supporting the broken open stenosis and ensuring lumen patency. Stenting was developed in reaction to the limited therapeutic benefit of angioplasty, since without stenting, restenosis and often complete occlusion frequently sets in, especially in coronary interventions [314], although stenting does not completely eliminate these risks [202]. Despite excellent successes achieved with stenting and limited success angioplasty, its inherent requirement to break open the stenotic region, is still associated with embolization in the case of carotid [34] and coronary procedures [22]. Of course, due to the comparatively larger size of carotid stenosed lesions and being part of the main arteries supplying cerebral perfusion, embolization carries a much higher risk of periprocedural CVAs compared to coronary treatments, whereas the latter increases the risk of embolic-related myocardial ischemia.

Finally, it should also be noted that due to the thromboembolic risks involved during cardiac catheterization, even when the instrumentation is heparinized, there has been a tendency to employ increasingly aggressive antithrombotic treatments during these interventions. Such strategies have been found to increase the risk of cerebral hemorrhages [152].

4.2.2.3. Endovascular aortic repair (EVAR)

Apart from the risk presented by aortic puncture and the catheterization when performing endovascular aortic repair (EVAR), the scraping/laceration of the wall during stent-graft deployment will further add to this risk. Embolic events have been attributed as being the main cause of stroke following EVAR procedures as demonstrated in TCD studies [35, 334], although malperfusion risks do also exist, cf. Section 3.2.2.3.

Of particular significance to periprocedural embolic events responsible for CVAs is thoracic EVAR, or TEVAR. Although TEVAR treatments initially yielded more embolic signals entering the cerebral circulation compared to conventional open repair [334], procedural and technological advances have lead to lower mortality and morbidity compared to open repair, although some series still recorded stroke rates of up to 6% [204]. Proximal landing site and grade of atherosclerosis in the aortic arch have been attributed as significant and independent predictors of periprocedural strokes [204, 237]. Although some debate existed whether the proximal landing site during TEVAR played a role in predicting stroke [35], it has been proposed that landing zones distal to the left subclavian artery actually hold a similar risk, simply due to the fact that the guide wires involved mostly also need to enter the aortic arch [204].

4.2.2.4. Balloon occlusion and counterpulsation

Apart from the EAB used in PCI, carotid artery interventions, or those used to expand stent-grafts during EVAR, the two other applications of EAB hold the potential of lacerating the intimal wall by shearing, namely endo-aortic balloon occlusion (EABO) and intra-aortic balloon counterpulsation (IABC), as considered below.

Although EABO has been considered here in detail, it has mostly been considered in a comparative context in relation to aortic cross-clamping, cf. Section 2.2 and 2.3. However, as inferred from studies reviewed in these preceding sections, the balloon expansion upon occlusion as well as axial movement of the EAB catheter will be responsible for increased WSS against the intima, thereby potentially causing direct intimal laceration by shearing. Such damage was also implicated in an increased incidence of aortic dissections during the initial use of this type of occlusion [117].

IABC is a percutaneous therapeutic device typically positioned in the descending aorta and counterpulsates relative to the heart. Thereby, diastolic pressure is increased in order to subsequently increase coronary arterial perfusion, which has been found especially useful in cases of cardiogenic shock as a result of acute myocardial infarction. Despite the fact that indications for the use of IABC remain controversial, its use under certain indications have been demonstrated to prevent early infarct extension and ventricular remodeling [265, 316]. However, despite this primary functionality, a recent systematic review and meta-analysis by Sjauw et al. [316] showed that the use of IABC lead to a significant increase of stroke of 2% higher than the control groups. Mechanisms for such stroke has mostly been attributed to intra-aortic abrasion, especially in the presence of severe atheromatic lesions [164, 184], although hemodynamical disturbances in terms of CBF were not considered, as far as the author could determine.

4.2.2.5. Debridement by endarterectomy

Endarterectomy is the process by which an atherosclerotic lesion is removed surgically by scraping, bluntly dissecting or aspirating (with an ultrasonic aspirator) the lesion from the wall. Its can be performed at different arterial sites, of which the most common application is in carotid endarterectomies. Currently, a large and important debate surrounding the use of either endarterectomy or stenting/angioplasty when treating carotid stenosis exists for different patient risk profiles in literate [1]. Different indications favor different treatments, although both have their validity within vascular surgical treatments. Confining endarterectomy to cardiac surgical procedures presents a different picture, as expanded upon below.

The debridement by endarterectomy of the ascending aorta or aortic arch is a technically feasible procedure and is sometimes still suggested as potential treatment of patients with severe grades of atheroma undergoing cardiac surgery procedures, as shown in some single center studies [10, 331]. However, one earlier single-center study revealed the contra-indication for such treatment in considering a subgroup of 268 out of 3404 patients (8%) undergoing cardiac surgery who presented with a severe grade of aortic arch atheroma ($\geq$5 mm) [323]. Of this subgroup, 43 patients received an aortic arch endarterectomy in conjunction to their cardiac surgical procedure in an attempt to prevent perioperative stroke. Although the average stroke rate for the entire subgroup was high (15.3%), the stroke rate for those patients receiving concomitant endarterectomy was three times as high. In this entire series, only age and aortic arch endarterectomy was identified as independent predictors of intraoperative stroke.

As stated in a current review [206], adverse outcomes after aortic arch endarterectomy could be attributed to the disruption of the intimal surface, resulting in new thrombus formation that can become dislodged. Another potential mechanism could simply be debris left over after the procedure. Such conflicting data in literature and the lack of large RCTs have caused surgeons to rather opt for more conservative alternative of surgical technique, compared to a rather aggressive maneuver, such as aortic arch endarterectomy. Alternatives include change of occlusion technique or location, cannulation site, cannula tip design, etc., as considered thoroughly in this dissertation. The reason why carotid endarterectomy yields comparatively more favourable outcomes than aortic arch endarterectomy has not been elucidated in literature, but is expected to be related to the size of the lesion debrided, the post-procedural WSS induced on the debrided site, the technique of debridement, irrigation strategies, the composition of the atherosclerotic lesion as well as concomitant thrombotic factors.

5. Conclusions and future perspectives

*If the brain was simple enough to understand, we would
be too simple to understand it!*

— Arrowsmith and Ganugapenta [11]

Aortic manipulation maneuvers either cause large deformation of the aorta, disturbance of flow patterns in the aorta, direct laceration to the aorta or even a combination thereof. As reviewed extensively in the preceding chapters, an array of aortic manipulation maneuvers exist in cardiac surgery which can cause disruption or damage to the aorta and cause subsequent embolization, especially in the presence of atherosclerotic lesions, although other sources of emboli do also exist. Concomitantly, many such maneuvers disrupt the normo-physiological perfusion volume and patterns, predominantly to the brain – some, on top of also increasing the risk of embolization. As also briefly considered due to its importance in this context, interventional cardiological treatments can also lead to such consequences.

Although other mechanisms have been identified, emboli and hypoperfusion constitute the main aortic manipulation-related etiologies responsible for perioperative CVAs. Notwithstanding that many procedural and technological advances have yielded increased safety in terms of perioperative CVAs associated with these manipulation maneuvers, it remains a very pertinent risk with far-reaching consequences, not even mentioning other potential consequences such as non-cerebral end-organ ischemia and aortic dissections.

5.1. Current clinical thinking about aortic manipulation

As derived from the reviewed literature, it is evident that current clinical comprehension of aortic manipulation has been focused on a policy of *prevention is better than cure*. This is also emphasized in a review by Grocott [140] stating that non-pharmacological solutions have been attributed to yielding greater success in terms of overall clinical outcome than pharmacological solutions.

Prevention by inter-procedural changes in manipulation strategies include e.g. echo-guided change of manipulation site to prevent embolization of atherosclerotic lesion, choosing a more dispersion cannula tip, preventing partial-clamping by utilizing a single-clamp technique, limiting large cardiac distortions, using automatic graft connectors instead of partial-clamping, using the internal mammary arteries to revascularize the myocardium instead of performing a proximal anastomosis etc. *Prevention* by intra-procedural factors include performing off-pump instead of on-pump CABG, performing PCI instead of CABG surgery etc.

Unfortunately, as stated before, some aortic manipulation maneuvers are inadvertent and as a whole yield the least overall risk to patient-outcome. As such, some *cure*-focused strategies also exist to diminish the consequences of manipulation maneuvers, such as using soft clamp-inserts, dispersion cannula tips maintaining safe pressure gradients, the use of intra-aortic filters, diverting emboli released in the ascending aorta and aortic arch into the descending aorta etc. Although not considered here, other *cure*-focused strategies with significant benefit are anesthetic strategies, such as maintaining glucose and pH-levels, temperature management and administering certain pharmacological agents.

Interestingly, as also seen in the preceding chapters, both *preventative-* and *cure*-based strategies have often not yielded the desired results, in spite of being implemented based on good theoretical premises. Some of which deserve more consideration, as expanded upon below.

5.2. Well-intended advancement, marginal or no improvement

As found relatively frequently in literature, a new surgical tool or procedural alteration is proposed to either prevent or lessen the impact and/or consequences of aortic manipulation. Most are based on in-depth understanding from clinical and experimental experience, while others seem to be based only on limited conclusions from previous studies. Many such suggested improvements consequently suffer one of the following fates:

- Nothing happens. Investigation does not extend beyond the experimental, computational or clinical-case studies due to limited or no demonstration of clinical benefit or unnecessary increase in complexity, e.g. balloon-type clamp inserts to reduce trauma, shape memory alloy clamp arms (Section 2.1.3).

- Some benefit is demonstrated in prospective animal and clinical observational studies, but its marginal improvement and/or implied complexity did not (yet) yield sufficient momentum to facilitate further investigation, e.g. Portaclamp (Figure 2.4), Medos X-flow cannula tip (Section 3.1), pointing a dispersion cannula at the aortic valve for better distributed flow in the aortic arch (Section 3.1.2.3).

- Benefit is demonstrated in prospective animal and clinical observational studies and held enough potential to be the focus of a prospective RCT, but then yielded no clear demonstrable benefits to patient-outcome, e.g. Embol-X intra-aortic filter system (Section 4.2.2.1), Cobra catheter (Section 3.1.2.1).

- Benefit is demonstrated in prospective animal and clinical observational studies, although yielding some clear disadvantages. The scale of its benefits and disadvantages did not justify performing a RCT. However, it enjoys some clinical adoption due its potential for enabling/simplifying other procedural aspects, e.g. EABO enabling totally endoscopic or minimally invasive valve surgery procedures (Section 2.3.2), automatic graft connectors (Section 2.4.3).

- No, or little benefit is demonstrated or supposed, yet its apparent and marketable benefit and seamless integration into current clinical setting allows for clinical adoption, e.g. "atraumatic" inserts (Section 2.1.3), change of cross-clamp orientation (Section 2.1.2).

- Much benefit is demonstrated in prospective animal and large clinical observational studies, followed by a favourable RCT findings. However, paradoxical outcomes consequently trigger more RCTs, some finding benefit, others not. As a result, its benefit becomes controversial and/or limited to certain indications, e.g. off-pump CABG over on-pump CABG (Section 1.1.2.3 and 2.4.2) and even PCI as an alternative to on-pump CABG [315][1].

The progression seen here is evident, showing in fact that preventative strategies are better than cure strategies, although both are needed. Furthermore, its not that these procedural or technological advancements do not bring about any benefits, but rather that they only lead to similar outcomes, failing to demonstrate significant improvement over a general patient-population. However, all such improvements have

---

[1]These are arguable two of the current most contested discussions in the cardiac surgery/interventional cardiology field. The author does not claim to have reviewed these in full, although the cited references yield very strong conclusions stating that the one type of treatment is not unequivocally better than the other.

not been made in vain, when considering that some of these alternative procedures and technologies are in fact better when the conventional has been contra-indicated or some alternatives have had other secondary benefits like reducing operating field clutter, costs, concomitant treatments etc.

The reason why these advancements have not been able to provide significant improvements to patient outcomes could be attributed to the fact that they are aimed at addressing a single or a limited amount of consequences of maneuvers that pose a non-trivial, multifactorial, definite amount of risk to patient-outcome. Additionally, the current wealth of medical and technological knowledge and experience have enabled the optimization of cardiac surgical conditions to a level that such isolated considerations of manipulation-related etiologies and consequences, as well as an incomplete understanding of these consequences, will no longer suffice to enable significant procedural or technological improvements in patient-outcome.

Therefore, the success of future advancement will hinge on an increased understanding of the extent of complications caused by aortic manipulation, multi-factorial influences and also a comprehensive understanding of clinical adoption involved. Furthermore, it will be required that any new future advancement be scrutinized by these criteria. All of this is further considered below.

5.3. Open issues for future consideration

5.3.1. Extent of complications

Determining the extent of complications resulting from aortic manipulation is a multifactorial problem and needs attention on different levels, even when considering only CVAs, as expanded upon below.

A more specific understanding of the basic mechanical conditions coupled with the biochemical and molecular conditions responsible/indicative of cerebral injury. Although the latter is an actively research topic, as reviewed by Weiss and Baumgartner [355], certain open questions remain with regards to patient-specific translation in terms of hypoperfusion and embolic risks, e.g. what influences the properties of an atherosclerotic lesion and how prone to disruption is it upon manipulation? How does the perfusion pressure distribution in the brain vary among patients? How sensitive is such a distribution to hypoperfusion and emboli and by which extent? To which extent will a specific manipulation maneuvers contribute to the increase extent of an etiology? etc.

A feasible clinical implementation of these basics are also required, supplemented by means to obtain predictive, pre-operative and peri-operative measures required to better facilitate clinical decision-making. This includes understanding which global patient-specific risk factors will aggravate the extent of the presence of these etiologies brought about by aortic manipulation, as well as a standardized, comprehensive patient-specific assessment of these risks with a sufficiently detailed system of classification. Furthermore, clarity is also required as to conditions which contra-indicate specific manipulation maneuvers. Finally, improved intra-operative cerebral and aortic arch monitoring will aid in assessing risk, potential mechanisms of injury but also allow potential intervention to reduce the severity of the complications.

Currently, as reviewed in the preceding chapters, the only basic measures of the extent of the presence of these etiologies due to manipulation are mostly limited to qualitative results from in vitro, animal and cadaver experiments, as well as some TCD studies. Many more clinical monitoring devices exist to aid in assessing risk and incidence of cardiac surgery related CVAs, both preoperatively and perioperatively, including aspects relating to emboli, hypoperfusion, but also brain function, as excellently reviewed by Arrowsmith and Ganugapenta [11]. However, as these authors point out, despite the clinical availability of such monitors it adoptation has largely been confined to specialist centers, researchers and enthusiasts. Furthermore, it principally only provides global measures which could be used to indicate intervention. The failure of large-scale clinical adoption is most significantly attributed to a lack of incontestable evidence of outcome benefit. Clinical patient-specific risk factors predicting adverse neurological outcome

have been more comprehensively considered and include age, proximal aortic atheroma, diabetes, hypertension, use of IABC, unstable angina, pulmonary disease, excessive alcohol intake, baseline intellectual function, baseline functional status [291]. However, these risk factors are not directly linked to a specific manipulation maneuver, with the indirect exception of proximal aortic atheroma. Thereby, the chain of events of pathology-manipulation-disruption-CVA is incomplete and remains unclear. Finally, patient-specific pre-operative classification to reduce the extent of manipulation-related complications basically only consists of gradation of the extent of atherosclerosis using a global classification system principally based intimal thickening and lesion thickness protruding into the lumen, cf. [186]. Such pre-operative screening strategies to detect, but not necessarily classify such risks are only now starting to become widely adopted in the clinical setting.

It is therefore clear that the extent of the complications related to aortic manipulation and its clinically translatable potential has much left to be desired, and need significant attention in future studies.

5.3.2. Multi-factorial influences

As already presented in Section 1.1.2.3, clinical evidence seems to suggest certain synergistic effects between emboli and hypoperfusion exist which will aggravate CVAs, not to even mention other etiologies. Such interdependencies between these two etiologies, in turn depend on multifactorial aspects related in part to aortic manipulation, some more apparent, some less apparent, as considered in the following.

Firstly, one manipulation maneuver could pose multiple risks in terms of these etiologies, of which probably the best example is the arterial cannula choice. Not only are pressure gradients influenced by the cannula length, tapering factor and tip design that could lead to hemolysis, but the risk of sandblasting, malperfusion of the cerebral arteries, disturbance of the natural pulsatile character and helical flow is also implicated. This consideration does not even consider the influence of cannulation, cannulation site and cannula orientation, all of which potentially contribute to both embolization and hypoperfusion, cf. Section 3.1.2.

Secondly, multiple manipulation maneuvers at the same time could compounded the risks in terms of these etiologies. For example, interplay between partial-clamping and the aortic cannula has been suggested to be a compounding factor [324], but never considered further. A further important example is that shown in Figure 1.3. Consider the fact that both cross-clamp application and removal only last for a couple of seconds and both are performed while CPB is on, i.e. during arterial cannular flow. For this short time a significant portion of the total embolic load entering the cerebral circulation is generated. Additionally, ~50% of the embolic signals are not associated with a particular maneuver, but is CPB still on in this time? Such a figure falsely creates the impression that these maneuvers are performed independent from each other. Such compounding interplay between the cross-clamped aorta and arterial cannular flow has also been mentioned before and recommended that pump flow be reduced prior to cross-clamping, but was never considered further [324].

Thirdly, the timing and duration of manipulation maneuvers could also compound the risks in terms of these etiologies. Classically, for example, cross-clamp (or occlusion) duration and CPB duration is associated with myocardial ischemia time and systemic inflammatory response syndrome time. However, a lot of other factors will also ultimately influence patient outcome, including patient-specific risk factors, perioperative difficulties, surgical and anesthetical skills, postoperative care etc. [272]. However, manipulation related influences were not mentioned in this context and could very well also play a role. For example, one study demonstrated a 90% increase in embolic load occurred for every additional hour that a patient was kept on CPB [51]. Furthermore, as found experimentally, cross-clamping time also increases the damage that occurs, although the level plateaus after approximately 30 minutes, cf. Section 2.1.2. Therefore, it seems reasonable that manipulation-related effects can at least partly help explain findings that relate these procedural times to of adverse events.

Fourthly, certain clinical patient-specific risk factors could also compound the risk in terms of these etiologies. As already mentioned, patient-specific risk factors can cause a further compounding effect with regards to cerebral outcome, for example, based on the quality of the brain parenchyma and vascular reserve capacity, cf. Section 1.1.2.3.

Finally, a less apparent interplay is that a single embolic bolus is not necessarily limited to only have occlusive consequences. As reviewed by Hammon and Stump [151], of the three main constituents of emboli entering the cerebral circulation are air, atherosclerotic debris and fat – all of which can be caused by manipulation. A massive air embolism can cause not only ischemic injury, but its gaseous nature may also directly damage the endothelium. Furthermore, recent identification of small capillary arteriolar dilations (SCAD) raises questions whether fat might not only cause vessel occlusion, but also release cytotoxic free radicals which may significantly increase damage to lipid-rich neurons.

The main challenge to prevent the manifestation of manipulation-related etiologies, as is evident from the preceding chapters, is how to diminish risks by considering the entire multifactorial nature of aortic manipulation in the risk that it would pose to patient outcome, as brought about by a variety of different patient, procedural and technological aspects. The multifactorial aspects considered above are only an indication of the interdependencies that have been shown to exist. Further study is needed to elucidate on these and other unknown interdependencies responsible for aggravated CVAs. Finally, new procedures and technologies aiming at reducing manipulation-related CVAs have to be rigorously tested against as many as possible of these known factors.

5.3.3. (Hampered) clinical adoption

Although no comprehensive study on the clinical adoption of new procedures and technologies has been performed, some remarks are warranted here.

In order to conclusively evaluate a new procedure or technology and thereby substantiate its place in standard clinical practice, the current gold standard is to perform a prospective RCT. However, its not that straight-forward. Substantial funding and effort is required to reach the stage of a RCT evaluation, as well as the RCT itself. Furthermore, to perform a RCT (or RCTs) to test a single new procedure or device on reducing cardiac surgery-related CVAs on an fairly progressed optimized clinical setting would most probably require an infeasibly large patient cohort to provide sufficiently powered outcomes [5]. Therefore, as already mentioned, new procedures or technologies have to be aimed at addressing a multitude of these factors for a likelihood of improved outcome.

Another noteworthy aspect is with regards to costs. When testing a new procedure or product, cost is seldomly mentioned, unless it significantly justifies a its use or its rejection. Then costs are usually described in terms of direct material costs or length of hospital stay, e.g. Reichenspurner et al. [294] comparing direct material costs of using EABO compared to cross-clamps and Slaughter et al. [318] relating the number of emboli entering the cerebral circulation detected intra-operatively related to length of hospital stay. Otherwise, broad economic indices such as direct and indirect costs are made on a global scale, cf. Section 1.1.2. Although these are relevant numbers, even only direct costs in terms of material and hospitalization specifics are not systematically reported and therefore, cannot be compared when evaluating a new therapy. Furthermore, a very relevant index would be to consider the direct and indirect costs arising from a specific grade of CVA.

Finally, although not considered here, marketing aspects as well as surgeon preferences play a very important, albeit sometimes unintuitive, role in clinical adoption of new therapies. A good example is the persistence of advocates for one therapy over another even though the former has been shown to be less effective [208].

5.4. Limitations

In the presented evaluation of the current clinical comprehension of aortic manipulation, some limitations are present and considered here.

With regards to emboli, the distinction between micro- and macro-emboli has often been made. However, as stated in a recent review by Bhudia et al. [32], this distinction is arbitrarily set at 200 μm, based on its ability to occlude a vessel of this size. More useful classification of emboli are actually in terms of its nature, i.e. gaseous or particulate, and if particulate, its constitution, i.e. biological or non-biological. Limitations still exist in determining the nature and constitution, as mentioned above, but foreknowledge could aid in identifying the sources and concomitant strategies to reduce its occurrence. Furthermore, focus was placed mostly on particulate emboli from an atheromatic origin, although as stated in a review by [151], apart from atherosclerotic debris, the main types of emboli responsible for brain injury in clinical practice are air and fat. Both of these have their clinical relevance, but were not considered for brevity sake.

Two aspects omitted here for the sake of brevity, is the potentially significant permanent disruption of hemodynamics as a result of aortic arch repair, e.g. [48, 282], as well as the timing that CVAs occur post-operatively. Considering the latter, a recent review by [355] discussed that early-onset CVAs are most likely attributable to hypoperfusion, emboli and systemic inflammation, whereas late-onset CVAs to the preoperative neurological state of the patient and certain cardiovascular risk factors.

Finally, as set in the research objectives, the main focus of the reviewed literature was to extract the multifactorial aortic manipulation influences responsible emboli generation and cerebral hypoperfusion. Although briefly mentioned but not considered in detail in the preceding chapters, other non-pharmacological as well as pharmacological strategies have played a paramount role in the reduction in the rate of perioperative CVAs. The important non-pharmacological strategies include temperature, blood-gas, acid-base, hematocrit and glucose management [140, 291]. The available pharmacological strategies are too numerous to mention – the interested reader is referred to Harrington et al. [154]. The interdependencies of these aspects with aortic manipulation were not considered.

5.5. The need for more sophisticated analyses

As made abundantly clear from the reviewed material, is that aortic manipulation maneuvers cannot be considered in independent of each other when evaluating the concomitant adverse neurological outcomes. With that being said, there is also a need for previously unachieved detailed evaluations of the impact of every aspect of each manipulation maneuver. All of which should work together to not only aid clinical decision-making, but also the development of new procedures and technologies for either avoiding manipulation or making the needed manipulation safer.

The advent of computational models not only yielded the potential of providing local detail about an aspect of one maneuver, but also when considering a multitude of aspects for multiple maneuvers. In this context, and as investigated in the second part of this dissertation, computational mechanical models will be used to elucidate on some of these aspects which hold risks relating to aortic manipulation.

Part II.

Computational evaluation of aortic manipulation

6. Computational modeling

> *The ships hung in the sky in much the same way that*
> *bricks don't.*
>
> — Douglas Adams

The following chapter provides the basis upon which further computational consideration of selected aortic manipulation maneuvers is build. It includes an overview of the tools required for the computational modeling of (structural) solid and fluid mechanics, respectively. This includes the consideration of the necessary continuum mechanical principals and considerations, the incorporation of experimental information into relevant constitutive relations and aspects on numerical solution strategies that can be applied to appropriate models for simulating the desired aortic manipulation maneuvers. Following the solid and the fluid mechanics sections, respectively, detailed information is given as to how the models for each selected maneuvers were constructed, which includes its geometry, computational mesh generation, selection of appropriate material models and parameters, followed by the presentation of further maneuver-specific details.

In terms of the continuum mechanics problem formulation, each type of mechanical phenomenon is modeled as a continuum body/domain in three-dimensional Euclidian space and naturally lends itself to a preferred formulation in terms of a reference system. Structural solid mechanics often need to account for large deformations and is therefore particularly suited to a Lagrangean or material formulation. Such a formulation uses the material frame as a reference system, where the movement of a point in the continuum body is followed during deformation. Conversely, fluid mechanics often need to account for large fluxes, and is therefore more suited to an Eularian or spatial formulation. Such a formulation uses a fixed spatial frame as a reference system, where the flux through the borders of a control volume in the continuum domain are considered. In the present work, structural solid and fluid continuum mechanical principals are considered independently of each other, as it relates to the selected aortic manipulation maneuvers.

6.1. Solid mechanics

6.1.1. Kinematics

Commonly used deformation measures for solid structural bodies using a material formulation are briefly presented in the following section, guided by the detailed formulations considered in Holzapfel [166] and Humphrey [169].

Consider an undeformed, stress-free body, which is by definition in the *reference* (*undeformed, material, initial*) configuration Ω_0. The position of an arbitrary point on this body in the reference configuration is given by the vector $\boldsymbol{X}$. Any deformation of the body places it in the *current* (*deformed, spatial*) configuration and the previous position of the chosen arbitrary point is now described by the vector $\boldsymbol{x}$ in the same orthogonal Cartesian coordinate system. Thus, the deformation of such a point can be described by a mapping function χ transforming the body from Ω_0 to Ω, as follows,

$$\chi : \begin{cases} \Omega_0 \to \Omega \\ \boldsymbol{X} \mapsto \boldsymbol{x} \end{cases} \tag{6.1}$$

Mapping a quantity from the reference to the current configuration is referred to as a push-forward operation, while mapping from the current to the reference configuration is known as a pull-back operation.

Throughout this dissertation, the notational convention used by Holzapfel [166] will be followed to indicate quantities in the reference configuration Ω_0 by capital lettered symbols and possibly also a subscript 0, while quantities in the current configurations Ω either by lower-case lettered symbols. The bold-faced letters will indicate vector or second-order tensor quantities depending on the variable, as is also clear from Eq. (6.1). The deformed or current position $\boldsymbol{x}$ can therefore be described in terms of the reference position $\boldsymbol{X}$ and the absolute displacement $\boldsymbol{u}$ as,

$$\boldsymbol{x} = \boldsymbol{X} + \boldsymbol{u} \tag{6.2}$$

In the finite elasticity problem under consideration, cf. Section 6.1.3, the reference point position $\boldsymbol{X}$ is considered the known independent variable, whereas the deformation map χ or the material displacement $\boldsymbol{u}$ are the unknown(s) to be solved for. An exception occurs in an aspect of the cardiovascular problems considered, where the current configuration is known and the reference configuration needs to be solved for, as further considered in Section 6.1.4.2.

A fundamental kinematic measure is the *deformation gradient $\boldsymbol{F}$*, defined as,

$$\boldsymbol{F} = \mathrm{Grad}(\boldsymbol{x}) = \frac{\partial \boldsymbol{x}}{\partial \boldsymbol{X}} = \boldsymbol{1} + \frac{\partial \boldsymbol{u}}{\partial \boldsymbol{X}} \tag{6.3}$$

where $\boldsymbol{F}$ for the considered problems is constrained to $J = \det \boldsymbol{F} > 0$ in order to guarantee affine mappings. Here, J is the Jacobian determinant, which represents the transformation of an infintesimal volume element between the current and the reference configuration,

$$\mathrm{d}v = \det \boldsymbol{F} \, \mathrm{d}V = J \, \mathrm{d}V \,. \tag{6.4}$$

Analogously, the transformation of an infintesimal area (Nanson's formula) and line element is given respectively as,

$$\mathrm{d}a = J \, \boldsymbol{F}^{-\mathsf{T}} \cdot \mathrm{d}A \tag{6.5}$$

$$\mathrm{d}\boldsymbol{x} = \boldsymbol{F}\mathrm{d}\boldsymbol{X} \,. \tag{6.6}$$

Using the polar decomposition theorem, cf. [166], Eq. (2.93), the volume preserving rigid body motion and the volume non-preserving stretch that a body undergoes can be obtained separately by the splitting of $\boldsymbol{F}$,

$$\boldsymbol{F} = \boldsymbol{R}\boldsymbol{U} = \boldsymbol{v}\boldsymbol{R} \,. \tag{6.7}$$

Here, $\boldsymbol{R}$ is the orthonormal rotation tensor, while $\boldsymbol{U}$ and $\boldsymbol{v}$ are the material (right) and spatial (left) stretch tensor, respectively. The latter two tensors are positive definite and symmetric. By considering the eigenvalue problem of the right $\boldsymbol{U}$ and left $\boldsymbol{v}$ stretch tensors, respectively, i.e.

$$\boldsymbol{U}\boldsymbol{M_i} = \lambda_i \boldsymbol{M_i}, \quad \text{for } i = 1, 2, 3 \tag{6.8}$$

$$\boldsymbol{v}\boldsymbol{m_i} = \lambda_i \boldsymbol{m_i}, \quad \text{for } i = 1, 2, 3 \tag{6.9}$$

the normalized eigenvectors $\boldsymbol{M_1}$, $\boldsymbol{M_2}$ and $\boldsymbol{M_3}$ and the corresponding eigenvalues λ_1, λ_2 and λ_3 of $\boldsymbol{U}$, as well as the normalized eigenvectors $\boldsymbol{m_1}$, $\boldsymbol{m_2}$ and $\boldsymbol{m_3}$ and the corresponding eigenvalues λ_1, λ_2 and λ_3 of $\boldsymbol{v}$ can be obtained. The eigenvectors $\boldsymbol{M_i}$ can be interpreted as the principal axes in terms of the reference configuration, with the eigenvalues λ_i being the corresponding principal stretches. Similarly, the eigenvectors $\boldsymbol{m_i}$ can be interpreted as the principal axes in terms of the current configuration, sharing the

same corresponding eigenvalues principal stretches, λ_i of the previous vector. The spectral decomposition of these tensors yield,

$$\boldsymbol{U} = \sum_{i=1}^{3} \lambda_i \boldsymbol{M_i} \otimes \boldsymbol{M_i} \,, \tag{6.10}$$

$$\boldsymbol{v} = \sum_{i=1}^{3} \lambda_i \boldsymbol{m_i} \otimes \boldsymbol{m_i} \tag{6.11}$$

where $\otimes$ indicates a dyadic product.

Utilizing the orthogonality of the rotation tensors obtained from 6.7, the *right Cauchy-Green deformation tensor* is defined as,

$$\boldsymbol{C} = \boldsymbol{F}^{\mathsf{T}} \boldsymbol{F} = \boldsymbol{U}^{\mathsf{T}} \boldsymbol{R}^{\mathsf{T}} \boldsymbol{R} \boldsymbol{U} = \boldsymbol{U}^{\mathsf{T}} \boldsymbol{U} = \boldsymbol{U}^2 \,. \tag{6.12}$$

As a fundamental measure of deformation, $\boldsymbol{C}$ has the advantage over $\boldsymbol{F}$ that it is defined only with respect to the reference configuration, whereas $\boldsymbol{F}$ is a two-point tensor, i.e. it refers to both reference and current configurations. Furthermore, $\boldsymbol{C}$ is an objective measure of deformation, since it does not change due to any imposed rigid body motion, whereas $\boldsymbol{F}$ is not objective. The eigenvalues of $\boldsymbol{C}$ are λ_i^2 for $i = 1, 2, 3$. These properties make $\boldsymbol{C}$ an ideal basis to formulate suitable finite strain measures upon. Thereby, the *Green-Lagrange strain tensor* is defined as,

$$\boldsymbol{E} = \frac{1}{2}(\boldsymbol{C} - \boldsymbol{1}) \tag{6.13}$$

which ensures a consistent definition of a zero strain state in the reference configuration. The spatial counterpart of $\boldsymbol{C}$ and $\boldsymbol{E}$ are the left Cauchy-Green deformation $\boldsymbol{b}$ and Euler-Almansi strain $\boldsymbol{e}$ tensors, respectively, defined as,

$$\boldsymbol{b} = \boldsymbol{F} \boldsymbol{F}^{\mathsf{T}} = \boldsymbol{v}^2 \,, \tag{6.14}$$

$$\boldsymbol{e} = \frac{1}{2}(\boldsymbol{1} - \boldsymbol{b}^{-1}) \,. \tag{6.15}$$

Analogous to their counterparts in the reference configuration, $\boldsymbol{b}$ and $\boldsymbol{v}$ have the same eigenvectors, while the eigenvalues of $\boldsymbol{b}$ are λ_i^2 for $i = 1, 2, 3$.

Although many other strain measures exist, the above-mentioned measures are exclusively considered, due to their frequent use owing from the favorable properties discussed. Various concomitant stress measures have also been developed, as considered in the next section.

6.1.2. Stress concept and governing equations

In general, stress can be defined as a measure of force acting on an area. Different stress measures are mainly distinguished by whether the force and the area of its application, respectively, is taken in the reference or current configuration. To derive an adequate stress measure describing the internal stress state of an elastic body, it is helpful to consider the traction vector $\boldsymbol{t}$ acting on an arbitrarily cut section of the body, defined as,

$$\boldsymbol{t} = \lim_{\Delta a \to 0} \frac{\Delta \boldsymbol{f}}{\Delta a} = \frac{d\boldsymbol{f}}{da} \,. \tag{6.16}$$

As shown in this equation, the resultant force $\Delta \boldsymbol{f}$ originating from the part of the body that has been cut away, acting on the cut section Δa, both in the current configuration, yields the traction stress vector $\boldsymbol{t}$ in

the zero limit. Whereas t is dependent on the orientation of the cut surface, the Cauchy stress tensor $\boldsymbol{\sigma}$ is independent of this orientation and can be derived using the Cauchy theorem as follows,

$$t = \boldsymbol{\sigma} n \tag{6.17}$$

showing that $\boldsymbol{\sigma}$ can be projected by the normal of the arbitrarily cut body n to yield the traction vector t. Considering a state of equilibrium in the absence of body forces or any transient effects requires that the integral of the total traction acting upon the boundary of a body $\partial\Omega$ must be equal to zero,

$$\int_{\partial\Omega} t \, da = \int_{\partial\Omega} \boldsymbol{\sigma} n \, da = \mathbf{0} \, . \tag{6.18}$$

Applying Gauss' divergence theorem and integration by parts allows the preceding relation to be expressed in terms of the current configuration body domain Ω as, which, when considering only an infinitesimal body domain, yields the static point-wise balance equation,

$$\text{div}(\boldsymbol{\sigma}) = \mathbf{0} \tag{6.19}$$

where the divergence operator $\text{div}(\cdot)$ acts on Ω. While $\boldsymbol{\sigma}$ is symmetric and represents the true internal stress state of the body, it is *a priori* unknown in the current configuration.

Additional stress measures include the *first Piola-Kirchhoff stress tensor* $\boldsymbol{P}$ that can be obtained by using Nanson's formula, Eq. (6.5) and Eq. (6.17) to obtain,

$$\boldsymbol{P} = J\boldsymbol{\sigma} \cdot \boldsymbol{F}^{-\mathsf{T}} \, . \tag{6.20}$$

$\boldsymbol{P}$ is an unsymmetric, two-point tensor, which is useful under experimental conditions, since it can be physically interpreted as the force acting on the body in the current configuration, while considering the corresponding area in the reference configuration. A stress measure purely defined in the reference configuration, the second Piola-Kirchhof stress tensor $\boldsymbol{S}$ can be obtained by a pull-back operation performed on $\boldsymbol{P}$,

$$\boldsymbol{S} = \boldsymbol{F}^{-1}\boldsymbol{P} = J\boldsymbol{F}^{-1}\boldsymbol{\sigma}\boldsymbol{F}^{-\mathsf{T}} \, . \tag{6.21}$$

$\boldsymbol{S}$ is a symmetric stress tensor that becomes helpful in the boundary value problem discussed below, but is difficult to interpret physically. This is owing to the fact that it represents the actual force pulled back into the reference configuration acting on the area in the same configuration. In summary, the different stress measures considered here are,

$$\boldsymbol{P} = J\boldsymbol{\sigma}\boldsymbol{F}^{-\mathsf{T}} = \boldsymbol{F}\boldsymbol{S} \tag{6.22}$$

$$\boldsymbol{S} = J\boldsymbol{F}^{-1}\boldsymbol{\sigma}\boldsymbol{F}^{-\mathsf{T}} = \boldsymbol{F}^{-1}\boldsymbol{P} \tag{6.23}$$

$$\boldsymbol{\sigma} = J^{-1}\boldsymbol{P}\boldsymbol{F}^{\mathsf{T}} = J^{-1}\boldsymbol{F}\boldsymbol{S}\boldsymbol{F}^{\mathsf{T}} \, . \tag{6.24}$$

The boundary value problem (BVP) of the quasi-static nonlinear solid structural mechanics in absence of body forces described above consist of a coupled set of second-order partial differential equations that has to satisfy equilibrium and a set of boundary conditions. Appropriate boundary conditions can be applied by decomposing the boundary domain $\partial\Omega_0 = \Gamma_0$ into a complementary set of boundaries, where $\Gamma_{0,u}$ represents the Dirichlet boundary with displacements prescribed as $\hat{\boldsymbol{u}}$, while $\Gamma_{0,\sigma}$ represents the natural or Neumann boundary with tractions given as $\hat{\boldsymbol{t}}$. These boundaries are disjoint sets and can therefore be written as,

$$\Gamma_{0,u} \cup \Gamma_{0,\sigma} = \Gamma_0 \, , \qquad \Gamma_{0,u} \cap \Gamma_{0,\sigma} = \emptyset \, . \tag{6.25}$$

By considering these boundaries and the static point-wise equilibrium stated in Eq. (6.19), the entire BVP in the reference configuration is formulated as,

$$\text{Div}\, \boldsymbol{P} = 0 \qquad \text{in } \Omega_0 \tag{6.26}$$

$$\boldsymbol{u} = \hat{\boldsymbol{u}} \qquad \text{on } \Gamma_{0,u} \tag{6.27}$$

$$\boldsymbol{P} \cdot \boldsymbol{N} = \hat{\boldsymbol{t}}_0 \qquad \text{on } \Gamma_{0,\sigma} \tag{6.28}$$

The BVP is also generally referred to as the *strong form* of the nonlinear mechanics, which in itself is *a priori* statically indeterminate, since Equations (6.26) to (6.28) are formulated for each point in the continuum Ω_0. This well-posed set of partial differential allow for the existence of a unique solution. Reformulating the BVP in the so-called *weak form* of the nonlinear mechanics, forms the basis for which numerical discretization can be performed to find an approximate solution to the BVP, such as the Finite Element method, considered below in Section 6.1.4.

6.1.3. Constitutive modeling

Having established appropriate measures for strains and stresses needed for the problem under consideration, constitutive (or material) models are necessary to link the kinematics and the response of the material. All of the structural solid constitutive models in this investigation only considers continuum bodies undergoing purely elastic, isothermal deformation, implying that no internal dissipation occurs. Such hyperelastic material properties allow a *Helmholtz free-energy function* Ψ to be postulated, defined per unit reference *volume*. The above-mentioned assumptions imply that this free-energy function is only dependent on the $\boldsymbol{F}$, i.e. $\Psi = \Psi(\boldsymbol{F})$ – also referred to as a *strain energy function (SEF)*. In other words, under these assumptions, the stored energy Ψ is only dependent on the current strain state of the body and is derivable from the SEF. Similarly, the stress state can also be derived from the SEF when the strain state of the body. Accordingly, the specific strain measure used to derive stress via the SEF will naturally yield its so-called energy conjugated stress. The equivalence of such energy-conjugate pairs are demonstrated below in terms of the total internal energy of a body,

$$\mathcal{E}_{\text{int}} = \int_{\Omega} \boldsymbol{\sigma}(\boldsymbol{F}^{-\mathsf{T}} \boldsymbol{E} \boldsymbol{F}^{-1})\, \mathrm{d}\Omega = \int_{\Omega_0} \boldsymbol{P}\boldsymbol{F}\, \mathrm{d}\Omega = \int_{\Omega_0} \boldsymbol{S}\boldsymbol{E}\, \mathrm{d}\Omega \tag{6.29}$$

where the deformation tensor $\boldsymbol{F}^{-\mathsf{T}} \boldsymbol{E} \boldsymbol{F}^{-1}$ simply represents the push-forward of $\boldsymbol{E}$, which itself is in the reference configuration. From this equivalence, it can be seen that the energy vanishes under purely rigid body motions, due the intentional formulation of $\boldsymbol{E}$ and $\boldsymbol{F}$.

Using this information, for example, the first Piola-Kirchhoff stress tensor $\boldsymbol{P}$ can be derived from its energy-conjugated strain type tensor, the deformation gradient $\boldsymbol{F}$, and the SEF, as follows,

$$\boldsymbol{P} = \frac{\partial \Psi}{\partial \boldsymbol{F}} \tag{6.30}$$

In the event that incompressibility needs to be enforced, a volumetric constraint can be added to the constitutive equation Eq. (6.30) yielding,

$$\boldsymbol{P} = \frac{\partial \Psi}{\partial \boldsymbol{F}} - p\boldsymbol{F}^{-1}, \; J = 1 \tag{6.31}$$

where p is a Lagrangian multiplier that enforces incompressibility of the material and $J = 1$ is the incompressibility condition stating that the volume remains constant, cf. Eq. (6.4).

Another useful constitutive equation can be found in an analogous manner, namely the second Piola-Kirchhoff stress tensor $\boldsymbol{P}$ with its energy-conjugated Green-Lagrange strain tensor $\boldsymbol{E}$,

$$\boldsymbol{S} = \frac{\partial \Psi}{\partial \boldsymbol{E}} = 2\frac{\partial \Psi}{\partial \boldsymbol{C}} \tag{6.32}$$

Here, the constitutive equation is also written in relation to the right Cauchy-Green strain tensor $\boldsymbol{C}$ due to its formulation enabling straight-forward incorporation into the Finite Element method. Since the relationship between $\boldsymbol{S}$ and $\boldsymbol{E}$ is generally nonlinear, the *material tangent fourth-order tensor* $\mathbb{C}$ in the reference configuration is required, calculated as,

$$\mathbb{C} = \frac{\partial^2 \Psi}{\partial \boldsymbol{E}^2} = 4\frac{\partial^2 \Psi}{\partial \boldsymbol{C}^2} \,. \tag{6.33}$$

Such a measure is basically the linearization of this relationship at a specific strain state and is especially important in the context of the linearization-based solution strategies of the boundary value problem, cf. Section 6.1.4.1.

Requirements of any suitable SEF include that the free energy yielded by the SEF must vanish in the residual stress-free reference configuration, described by,

$$\Psi(\boldsymbol{F} = \boldsymbol{1}) = 0 \tag{6.34}$$

as already eluded to in Eq. (6.29). It must be noted, however, that a body is not necessarily stress-free in the reference configuration, despite the absence of external loads, due to the potential existence of residual stresses.

Furthermore, a suitable SEF must be objective, i.e. the stored energy must be independent of rigid body motions. Considering that the deformation gradient $\boldsymbol{F}$ is independent of rigid body translation, the following considers only rigid body rotations: the subsequent objectivity requirement is,

$$\Psi(\boldsymbol{F}) = \Psi(\boldsymbol{Q}\boldsymbol{F}) \tag{6.35}$$

where $\boldsymbol{Q}$ is an arbitrary orthogonal rotational tensor. Therefore, choosing $\boldsymbol{Q} = \boldsymbol{R}^{\mathsf{T}}$, Eq. (6.7), the objectivity requirement can also be written as,

$$\Psi(\boldsymbol{F}) = \Psi(\boldsymbol{U}) \tag{6.36}$$

implying that the SEF is objective if it only depends on the stretch contribution $\boldsymbol{U}$. Since a SEF can also be written in terms of $\boldsymbol{E}$, $\boldsymbol{C}$, or their invariants (see below), such SEFs will also be *a priori* objective.

Finally, a suitable SEF should fulfill convexity or polyconvexity requirements to ensure stability in numerical applications, depending on the type of SEF. For a detailed consideration, the reader is referred to Holzapfel [166] and Balzani [24].

In terms of the directionality that a hyperelastic SEF can describe, distinction is most commonly made between isotropic and anisotropic material responses. A material is isotropic relative to its reference configuration if the strain energy remains equal for any rigid body motion, as imposed by an arbitrary chosen orthogonal tensor $\boldsymbol{Q}$, that is,

$$\Psi(\boldsymbol{F}) = \Psi(\boldsymbol{F}\boldsymbol{Q}^{\mathsf{T}}) \,. \tag{6.37}$$

As soon as Eq. (6.37) is not satisfied, the SEF is said to be anisotropic. Although the basic physical requirements state that a SEF must be objective during rigid body motions, cf. Eq. (6.35), it is fundamentally different to that which is stated here in Eq. (6.37). The latter equation simply states a material-dependent requirement that may or may not be satisfied, whereas the former states a property that needs to be fulfilled by all SEFs.

In the formulation of constitutive models, it is especially helpful to consider the principal invariants of the $\boldsymbol{C}$ and $\boldsymbol{b}$,

$$I_1 = I_1(\boldsymbol{C}) = I_1(\boldsymbol{b}) = \text{tr}\boldsymbol{C} = \lambda_1^2 + \lambda_2^2 + \lambda_3^2 \tag{6.38}$$

$$I_2 = I_2(\boldsymbol{C}) = I_2(\boldsymbol{b}) = \frac{1}{2}[(\text{tr}\boldsymbol{C})^2 - \text{tr}(\boldsymbol{C})^{\mathbf{2}}] = \lambda_1^2\lambda_2^2 + \lambda_1^2\lambda_3^2 + \lambda_2^2\lambda_3^2 \tag{6.39}$$

$$I_3 = I_3(\boldsymbol{C}) = I_3(\boldsymbol{b}) = det\boldsymbol{C} = \lambda_1^2\lambda_2^2\lambda_3^2 = J \tag{6.40}$$

where the last equation basically describes the Jacobian determinant, mapping a volume element from the reference to the current configuration, cf. Eq. (6.4).

Invariance of the scalar-valued tensor function Ψ under rotation allows it to be expressed in terms of the principal invariants of its argument (e.g. $\boldsymbol{C}$ or $\boldsymbol{b}$), cf. Holzapfel [166], p. 215. Thereby, an isotropic hyperelastic material can alternatively be formulated as,

$$\Psi = \Psi(\boldsymbol{C}) = \Psi(I_1(\boldsymbol{C}), I_2(\boldsymbol{C}), I_3(\boldsymbol{C})) \,. \tag{6.41}$$

Due to numerical difficulties of modeling perfectly incompressible materials, but also due to real materials not exhibiting perfect incompressibility, it is often desired to model such materials as nearly-incompressible, i.e. to allow a limited, reasonable amount of material compression. Assuming compressibility, $\boldsymbol{F}$ can multiplicatively be decoupled into an isochoric (distortional, volume preserving) and a volumetric (dilatational, volume changing) component, as first proposed by Flory [110],

$$\boldsymbol{F} = I_3(\boldsymbol{C})^{\frac{1}{3}}\bar{\boldsymbol{F}} = J^{\frac{1}{3}}\bar{\boldsymbol{F}} \,. \tag{6.42}$$

When the material is perfectly incompressible, then $J = 1$ and consequently the isochoric deformation gradient $\bar{\boldsymbol{F}}$ will revert back to the original $\boldsymbol{F}$. In the context of the soft biological tissues considered in this dissertation, it is assumed that the materials allow for an additive split of the SEF into according parts,

$$\Psi(\boldsymbol{F}) = \bar{\Psi}(\bar{\boldsymbol{F}}) + \Psi_{\text{vol}}(J) \tag{6.43}$$

where the isochoric strain contribution to the strain energy simply being dependent on the modified strain measure. For example, modified counterparts for selected measures given as,

$$\bar{\boldsymbol{C}} = J^{-\frac{2}{3}}\boldsymbol{C} \,, \quad \bar{I}_1 = \bar{I}_1(\bar{\boldsymbol{C}}) = J^{-\frac{2}{3}}I_1 \,, \quad \bar{I}_2 = \bar{I}_2(\bar{\boldsymbol{C}}) = J^{-\frac{4}{3}}I_2 \,, \quad \bar{I}_3 = \bar{I}_3(\bar{\boldsymbol{C}}) = \det\bar{\boldsymbol{C}} = 1 \,. \tag{6.44}$$

A multitude of different isotropic hyperelastic constitutive models exist that can be used to model the nonlinear behavior of hyperelastic materials. For example, the Neo-Hookean model, written in the isochoric-volumetric split (or decoupled) form in terms of its first invariant, looks as follows,

$$\Psi^{\text{NH}} = c(\bar{I}_1(\bar{\boldsymbol{C}}) - 3) + \Psi_{\text{vol}}(J) \tag{6.45}$$

with $c = \frac{\mu}{2}$ related to the shear modulus μ. The first and second terms describe the SEF contributions due to isochoric and volumetric deformations, respectively. This model is also frequently extended to include higher order terms, such as the Yeoh-model,

$$\Psi^{\text{Yeoh}} = c_1(\bar{I}_1(\bar{\boldsymbol{C}}) - 3) + c_2(\bar{I}_1(\bar{\boldsymbol{C}}) - 3)^2 + c_3(\bar{I}_1(\bar{\boldsymbol{C}}) - 3)^3 + \Psi_{\text{vol}}(J) \tag{6.46}$$

Different suitable volumetric SEFs exist by which the contribution of the volumetric deformation to the total SEF can be calculated, including the one by Ogden [273],

$$\Psi_{\text{vol}}^{\text{OG}} = \frac{\kappa}{\beta^2}\left(J^{-\frac{\beta}{2}} + \beta\ln J^{\frac{1}{2}} - 1\right) \tag{6.47}$$

$$\overset{\beta=2}{=} \frac{\kappa}{4}\left(J - \ln J - 1\right) \,. \tag{6.48}$$

Another common isotropic, hyperelastic constitutive model is the St.-Venant-Kirchhoff model considered here, formulated below in its coupled form, i.e. no isochoric-volumetric split,

$$\Psi^{\mathrm{SVK}} = \frac{\lambda}{2}(\mathrm{tr}\boldsymbol{E})^2 + \mu\boldsymbol{E} : \boldsymbol{E} \tag{6.49}$$

where λ and μ are the Lamé parameters, which can be written in terms of the Poisson's ratio ν and the Young's modulus E,

$$\mu = \frac{E}{2(1+\nu)}\,, \quad \lambda = \frac{E\nu}{(1+\nu)(1-2\nu)}\,. \tag{6.50}$$

The fundamental difference between the neo-Hookean and the St.-Venant-Kirchhoff models are that substituting Eq. (6.49) and (6.45) into (6.32) and (6.33), respectively, shows that a linear relationship between $\boldsymbol{S}$ and $\boldsymbol{E}$ exists for the St.-Venant-Kirchhoff model, while a nonlinear relationship exists for the Neo-Hookean model.

Of particular relevance in modeling biological soft tissue, is to consider fiber-reinforced material models. These consist of a combination of a ground substance and one or more families of fibers, and resulting in a composite, heterogeneous, hyperelastic, anisotropic constitutive model. Its main advantage, especially in terms of arterial modeling, stems from how it corresponds to the two main mechanically relevant physiological constituents of an arterial wall, namely elastin (ground substance or matrix material) and collagen (family of fibers). Conversely, its biggest drawback is the increased computational cost compared with conventional isotropic materials, e.g. Eq. 6.49 and 6.45, and also limited knowledge about how to practically combine these different types of materials. Nevertheless, such models have attained wide acceptance in literature. For an in-depth consideration of these aspects, the reader is referred to [55, 166, 167]. In general, such a composite anisotropic constitutive models is given as,

$$\Psi = \Psi(\boldsymbol{C}, \boldsymbol{a}_0 \otimes \boldsymbol{a}_0) \tag{6.51}$$

with the directional dependence direction $\boldsymbol{a}_0$ not present in the formulation of an isotropic material model.

Performing a multiplicative split of the deformation gradient $\boldsymbol{F}$ (Eq. 6.44) allows for the decoupled additive split of the anisotropic SEF of the form,

$$\Psi_{\mathrm{aniso}} = \bar{\Psi}_{\mathrm{matr}}(\bar{\boldsymbol{C}}) + \bar{\Psi}_{\mathrm{fib}}(\bar{\boldsymbol{C}}) + \Psi_{\mathrm{vol}}(J) \tag{6.52}$$

representing the different individual contributors to the strain energy, namely the isochoric part of the matrix material $\bar{\Psi}_{\mathrm{matr}}(\bar{\boldsymbol{C}})$ and each family of fibers $\bar{\Psi}_{\mathrm{fib}_i}(\bar{\boldsymbol{C}})$, respectively, as well as the volumetric part $\Psi_{\mathrm{vol}}(J)$. Here, it is once again helpful to formulate specifics of these constitutive relations in terms of invariants, referred to as pseudo-invariants in terms of $\boldsymbol{C}$ and $\boldsymbol{a}_0 \otimes \boldsymbol{a}_0$,

$$I_4 = \boldsymbol{C} : (\boldsymbol{a}_0 \otimes \boldsymbol{a}_0) = (\boldsymbol{F} \cdot \boldsymbol{a}_0)^2 = \lambda_{\mathrm{fib}}^2 \tag{6.53}$$

where $\boldsymbol{a}_0 \otimes \boldsymbol{a}_0$ represents a second order tensor, build up from the directional dependence direction in the reference configuration $\boldsymbol{a}_0$ in the case of anisotropy, see Eq. (6.51). This preferential direction in this case is the orientation direction ascribed to a family of fibers. Additional pseudo-invariants can be defined in this regard, but can be neglected due to it either being constant or for simply restricting the number material parameters. In the biomedical application considered here, cylindrical type geometries are often considered, making it useful to define a circumferential direction $\theta\theta$ and an axial direction zz. Eq. (6.53) also indicates that I_4 represents the squared stretch in the fiber direction λ_{fib}, such that it can also be written as,

$$I_4 = \lambda_{\mathrm{fib}}^2 = (\lambda_{\mathrm{fib}}^{\theta\theta})^2\cos^2\alpha_{\mathrm{fib}} + (\lambda_{\mathrm{fib}}^{zz})^2\sin^2\alpha_{\mathrm{fib}} \tag{6.54}$$

where the λ_{fib} is simply split into components relating the fiber direction to a certain angle α_{fib} relative to the circumferential direction $\theta\theta$, not the axial direction zz. The concomitant isochoric-volumetric split of these pseudo-invariants, similar to what was done in Eq. (6.44), are,

$$\bar{I}_4 = J^{-\frac{2}{3}} I_4 \,. \tag{6.55}$$

This pseudo-invariant, together with the three principal invariants, are sufficient to describe material anisotropy in the special case of a single family of fibers, i.e. transverse isotropy. For more than one such preferential directions, additional invariants are required to relay the relationship of the interaction between these different preferential directions. Other invariants are omitted for the sake of brevity. The interested reader is referred to Holzapfel [166].

Based on the constitutive relations and models presented here, appropriate models and associated parameter choices for all simulated structural solid bodies are considered below. Specifically, the modeling of the aortic wall (Section 6.2.2), calcifications that occur within the aortic wall (Section 6.2.3), as well as the different materials used to model the occluders are presented (Section 6.2.4).

6.1.4. Numerical solution

This section briefly reviews key aspects of numerically solving the stated BVP, including the Finite Element (FE) formulation, prestressing of the vessel obtained from medical data, suitable FE element technology employed, specialized boundary conditions used, frictional contact considerations, and efficient solvers for the models presented.

6.1.4.1. Finite Element method for solid structures

As mentioned in Section 6.1.2, the solution to the BVP can be approximated numerically by considering the weak form of the BVP. The numerical solution strategy employed in this dissertation is the FE method. For full details into the background, detailed derivations, variations and limitations of the FE method, the reader is referred to Zienkiewicz and Taylor [367] and Wriggers [361]. In the following, only a brief summary of components of the method is given, which is needed for clarification of specific considerations in subsequent sections. Only the required BVP is considered, formulated as a quasi-static relation of a hyperelastic 3D solid structure domain in the absence of body forces in the reference configuration.

The FE method utilizes the weak form of the BVP, which is obtained by applying the method of weighted residuals to the equilibrium equations, defined by the balance of static equilibrium in Eq. (6.26) and the traction boundary condition in Eq. (6.28). The multiplication of these equations with a weighting (or test) function $\boldsymbol{w}$ yields the weak form,

$$\int_{\Omega_0} \text{Div}\boldsymbol{P} \cdot \boldsymbol{w} \, \mathrm{d}\Omega + \int_{\Gamma_0} \left[\hat{\boldsymbol{t}}_0 - \boldsymbol{P}\boldsymbol{N} \right] \cdot \boldsymbol{w} \, \mathrm{d}\Gamma = 0 \tag{6.56}$$

By identifying the arbitrary test function as a variation of the displacement field (or virtual displacement) $\delta\boldsymbol{u}$ leads to the variational *principal of virtual work* (PVW), which states that the external work on the body by boundary tractions and internal work by the stress field of the body have to be in equilibrium. After performing integration by parts followed by Gauss' divergence theorem, the relation reads,

$$\delta W = \delta W_{\text{int}} - \delta W_{\text{ext}} = 0 \tag{6.57}$$

$$\int_{\Omega_0} \delta\boldsymbol{F} : \boldsymbol{P} \, \mathrm{d}\Omega - \int_{\Gamma_0} \delta\boldsymbol{u} \cdot \hat{\boldsymbol{t}}_0 \, \mathrm{d}\Gamma = 0 \,. \tag{6.58}$$

Inserting Eq. (6.22) into the relation and utilizing the symmetry of $\boldsymbol{S}$ gives,

$$\int_{\Omega_0} \delta \boldsymbol{E} : \boldsymbol{S} \, \mathrm{d}\Omega - \int_{\Gamma_0} \delta \boldsymbol{u} \cdot \hat{\boldsymbol{t}}_0 \, \mathrm{d}\Gamma = 0 \,. \tag{6.59}$$

This PVW relation describes the displacement based equilibrium in the reference configuration. It also holds when certain additional aspect causing additional internal loads, e.g. body forces, external loads etc. are consistently brought into the BVP and subsequently weighted as described above. As is evident here, the BVP is formulated using the initial (reference) configuration as reference, also referred to as the Total Lagrange Formulation.

The relation of PVW can now be solved numerically by discretizing the 3D continuum domain into a finite number of subdomains $\Omega_0^{(e)}$, namely finite elements. The approximate total virtual work obtained from the discretized problem, by element-wise integration and summation over the whole body can be written as,

$$\delta W \approx \delta W^{(e)} = \sum_{e=1}^{\mathrm{n_{ele}}} \left[\int_{\Omega_0^{(e)}} \delta \boldsymbol{E} : \boldsymbol{S} \, \mathrm{d}\Omega - \int_{\Gamma_0^{(e)}} \delta \boldsymbol{u} \cdot \hat{\boldsymbol{t}}_0 \, \mathrm{d}\Gamma \right]^{(e)} = 0 \tag{6.60}$$

From this point it is possible to approximate the displacements and virtual displacements by $\boldsymbol{u}^{(e)} = \boldsymbol{N}^{(e)}(\boldsymbol{X})\boldsymbol{d}$ and $\delta \boldsymbol{u}^{(e)} = \boldsymbol{N}^{(e)}(\boldsymbol{X})\delta \boldsymbol{d}$, respectively, with the nodal displacement values $\boldsymbol{d}^{(e)}$ and the so-called shape functions $\boldsymbol{N}^{(e)}$. For the remainder of this work, a Bubnov-Galerkin approach will be employed in the context of structural FE, implying that the test function $\delta \boldsymbol{d}$ and the unknown $\boldsymbol{d}$ are interpolated in the same way, namely by piecewise-linear polynomial functions, unless otherwise stated. Omitting details about the linearization for brevity sake, the linearization obtained after inserting the approximate displacements into the preceding relation results in,

$$\delta W^{(e)} = \sum_{e=1}^{\mathrm{n_{ele}}} \left[\delta \boldsymbol{d} \Big\{ \int_{\Omega_0^{(e)}} \frac{\partial \boldsymbol{E}(\boldsymbol{d})}{\partial \boldsymbol{d}} : \boldsymbol{S}(\boldsymbol{d}) \, \mathrm{d}\Omega - \int_{\Gamma_0^{(e)}} \boldsymbol{N} \cdot \hat{\boldsymbol{t}}_0 \, \mathrm{d}\Gamma \Big\} \right]^{(e)} \tag{6.61}$$

$$= \sum_{e=1}^{\mathrm{n_{ele}}} \left[\delta \boldsymbol{d} \big\{ \boldsymbol{f}_{\mathrm{int}}^{(e)}(\boldsymbol{d}) - \boldsymbol{f}_{\mathrm{ext}}^{(e)} \big\} \right] = 0 \tag{6.62}$$

where $\boldsymbol{f}_{\mathrm{int}}^{(e)}(\boldsymbol{d})$ is the displacement-dependent internal element force vector and $\boldsymbol{f}_{\mathrm{ext}}^{(e)}$ is the displacement-dependent element load vector. Considering the assembly of the element-wise quantities $\boldsymbol{f}_{\mathrm{int}}^{(e)}(\boldsymbol{d})$ and $\boldsymbol{f}_{\mathrm{ext}}^{(e)}$ to the corresponding global quantities $\boldsymbol{F}_{\mathrm{int}}(\boldsymbol{D})$ and $\boldsymbol{F}_{\mathrm{ext}}$, yields the following system of equations,

$$\boldsymbol{R}(\boldsymbol{D}) = \boldsymbol{F}_{\mathrm{int}}(\boldsymbol{D}) - \boldsymbol{F}_{\mathrm{ext}} = \boldsymbol{0} \tag{6.63}$$

where the global displacements $\boldsymbol{D}$ is a vector the size of the global number of degrees of freedom $\mathrm{n_{dof}}$. Due to the nonlinear relationship between the $\boldsymbol{S}$ and $\boldsymbol{E}$ in Eq. (6.61), Eq. (6.63) describes a multidimensional nonlinear system of equations requiring an iterative solution scheme, such as the typically employed Newton-Rhapson method. The method consists of a linearized consideration of $\boldsymbol{R}$ at $\boldsymbol{D}^i$, obtained from the Taylor series expansion (ignoring higher order terms),

$$\mathrm{Lin}\, \boldsymbol{R}(\boldsymbol{D}^i) = \boldsymbol{R}(\boldsymbol{D}^i) + \frac{\partial \boldsymbol{R}(\boldsymbol{D})}{\partial \boldsymbol{D}} \bigg|_{\boldsymbol{D}^i} \boldsymbol{\Delta} \boldsymbol{D}^{i+1} \tag{6.64}$$

where i represents the current nonlinear Newton iteration step and $\boldsymbol{\Delta} \boldsymbol{D}^{i+1} = \boldsymbol{D}^{i+1} - \boldsymbol{D}^i$. For each iteration step, $\mathrm{Lin}\, \boldsymbol{R}(\boldsymbol{D}^i)$ is required to vanish, thus requiring the solution of the linearized form and the

updated state variable, respectively,

$$\mathbf{\Delta D}^{i+1} + \mathbf{K}_T^{-1} \mathbf{R}(\mathbf{D}^i) = \mathbf{0} \tag{6.65}$$

$$\mathbf{D}^{i+1} = \mathbf{D}^i + \mathbf{\Delta D}^{i+1} \tag{6.66}$$

with the *tangential stiffness matrix* $\mathbf{K}_T = \partial \mathbf{R}(\mathbf{D})/\partial \mathbf{D}$. The iterative scheme is applied until $||\mathbf{R}(\mathbf{D}^i)||$ reaches a user defined tolerance. The advantage of this method lies in the fact that this relation can be manipulated so that the solution of $\mathbf{D}^i$ can be obtained without requiring the explicit inversion of $\mathbf{K}_T$.

6.1.4.2. Prestressing

The aortic wall is subjected to a substantial amount of blood pressure, pulsating typically at 1 Hz between diastolic and systolic pressures, i.e. between 80 and 120 mmHg (10.67 and 16.00 kPa). Typical CT angiography employed and considered here utilizes a gated (to the electrocardiogram (ECG)) image acquisition technique that ensures that the repeated image acquisition occurs under the least amount of aortic motion, namely during late diastole. Therefore, the CT angiographic data represents the aorta under diastolic blood pressure. It also implies that the aortic wall geometry extracted from CT data is not stress/strain free. To recover the so-called "prestressed" state of the CT-acquired aortic geometry under diastolic pressure, a modified updated Lagrangian formulation (MULF) strategy was performed. This strategy has previously been shown to be effective in approximating prestressed-state of patient-specific aortic geometries in the case of AAAs [223, 224]. For a detailed explanation of MULF prestressing, the reader is referred to [127, 128, 222]. The following gives a brief overview of the key components.

It is clear that the only non-trivial solution of the balance equation in Eq. (6.59) where $\mathbf{S} \neq \mathbf{0}$, is when either the deformation gradient is not unity, i.e. $\mathbf{F} \neq \mathbf{I}$ when non-zero displacements yield a non-unity deformation gradient, i.e. $\mathbf{u} \neq \mathbf{0}$.

In the Total Lagrange Formulated FE that starts with the known, unloaded, reference configuration Ω_0, considered thus far, cf. Eq. (6.59), the deformation gradient resulting from the current load increment t is calculated as follows: The current displacement increment $\Delta \mathbf{x}_{t+1}$ is obtained by iteratively solving the nonlinear system of balance equations, Eq. (6.63). Thereby, the displacement in the current configuration of the previous load increment can be updated additively, $\mathbf{x}_{t+1} = \mathbf{x}_t + \Delta \mathbf{x}_{t+1}$, and the deformation gradient $\mathbf{F}$ calculated accordingly, cf. Eq. (6.3). $\mathbf{F}$ can then be used to calculate the corresponding stresses and strains.

Contrarily, in the MULF FE that starts with the known, loaded, current configuration Ω, the deformation gradient is now determined from the current load increment t by a multiplicative update of a specially defined independent imprinted deformation gradient, instead of an incremental summation of displacements as follows: The current displacement increment $\Delta \mathbf{x}_{t+1}$ is used to determine the deformation increment $\mathbf{F}_{t+1}$, following Eq. (6.3),

$$\mathbf{F}_{t+1} = \frac{\partial \mathbf{x}_{t+1}}{\partial \mathbf{x}_t} = \mathbf{1} + \frac{\partial \Delta \mathbf{x}_{t+1}}{\partial \mathbf{x}} . \tag{6.67}$$

$\mathbf{F}_{t+1}$ is then used to update the above-mentioned specially defined independently imprinted deformation gradient $\tilde{\mathbf{F}}$ to obtain the (total) deformation gradient,

$$\mathbf{F} = \mathbf{F}_{t+1} \tilde{\mathbf{F}} \tag{6.68}$$

where $\tilde{\mathbf{F}}$ acts as a history variable, storing all prior multiplicative updates to the deformation gradient. Since the conventional way of determining $\mathbf{F}$ is not performed, it is noteworthy to mention that $\mathbf{X}$ is not needed to calculate $\mathbf{F}_{t+1}$, $\tilde{\mathbf{F}}$ and therefore also $\mathbf{F}$. This is because in this method, $\mathbf{x} := \mathbf{X}$. Thereby, without deforming the current configuration Ω, the stresses and the strains can be determined from the

multiplicatively updated $\boldsymbol{F}$, offering a suitable approximation of the stresses and strains in the imaged arterial geometry.

MULF yields a clear advantage over a strategy of considering inverse design (ID) analysis of determining such a stress/strain state, since ID can only yield a non-unique solution when considering finite deformation, as is the case for loaded arterial geometries.

6.1.4.3. Element technology

Despite the wide applicability of FE methods, the discretized formulation yields certain limitations in terms of the widely-described element locking effects. In short, although a general definition of locking is seldomly attempted, it can basically be described as a deviation of the discretized solution relative to the analytical solution due to an artificial over-stiffening of the system matrix by so-called parasitic stresses. The severity of such locking effects can stem from certain geometrical factors, e.g. element aspect ratios, element type, but also from material aspects, e.g. incompressibility requirement. Many remedies have been proposed to either partially or completely circumvent such locking effects, as reviewed by Koschnick [203]. An often proposed partial circumvention of this problem is to increase the polynomial order of the chosen shape functions to decrease geometrical approximation, cf. Eq. (6.61), but quickly becomes inordinately expensive in relation to the benefit obtained. Therefore, the following two remedial steps were taken.

Volumetric locking effects become especially critical when considering a near-incompressible constitutive formulation using piece-wise linear element shape functions, as is considered in the remainder of this work. It is because the element is incapable of point-wise fulfilling the near-incompressibility requirement set by the constitutive formulation. This effect can be completely circumvented by employing the F-bar method as first proposed by de Souza Neto et al. [80]. It basically entails the isochoric-volumetric split of the deformation gradient, already introduced in Eq. (6.42) given as,

$$\boldsymbol{F} = \boldsymbol{F}_{\text{vol}}\,\bar{\boldsymbol{F}} = \left(\det \boldsymbol{F}^{\frac{1}{3}}\boldsymbol{1}\right)\left(\det \boldsymbol{F}^{-\frac{1}{3}}\boldsymbol{F}\right) = J^{\frac{1}{3}}\,\bar{\boldsymbol{F}}\,. \tag{6.69}$$

Furthermore, the accordingly split deformation gradient is evaluated only at the centroid of the element, given as,

$$\boldsymbol{F_0} = \boldsymbol{F}_{\text{vol},0}\,\bar{\boldsymbol{F}}_0 \tag{6.70}$$

Using these relations, the so-called F-bar deformation gradient $\overline{\boldsymbol{F}}$ is calculated from a multiplicative mixture of the isochoric part of the deformation gradient $\bar{\boldsymbol{F}}$ and the volumetric part of the deformation gradient evaluated only at the centroid $\boldsymbol{F}_{\text{vol},0}$ as follows,

$$\overline{\boldsymbol{F}} = \boldsymbol{F}_{\text{vol},0}\,\bar{\boldsymbol{F}} = \left(\frac{\det \boldsymbol{F}_0}{\det \boldsymbol{F}}\right)^{\frac{1}{3}}\boldsymbol{F} \tag{6.71}$$

where the subscript "0" refers to it only being evaluated at the centroid of the element. Thereby, by modifying $\boldsymbol{F}$ into $\overline{\boldsymbol{F}}$ in the standard FE formulation, an approximate averaged enforcement of the near-incompressibility constraint replaces the point-wise fulfillment of this requirement, circumventing the effects of volumetric locking. The significant improvement in results owing from the use of the F-bar elements in the context of aortic occlusion was demonstrated in the diploma thesis of Hirschvogel [163]. In the loading context considered, it delivered results comparable to quadratically interpolated elements, but at computational costs comparable to linearly interpolated elements.

Shear locking effects associated especially with piecewise-linear shape functions were partially circumvented by using a mesh consisting only of hexahedral elements with a suitable element aspect ratio, due to the increased shear locking effects associated with tetrahedral elements and large aspect ratios [203].

6.1.4.4. Specialized boundary conditions

Apart from the standard Dirichlet and Neumann boundary conditions of the BVP defined in Eq. (6.27) and (6.28), certain specialized consideration of these boundary conditions, especially in FE solution defined in Cartesian coordinates are worth noting.

The hydrostatic pressure exerted by blood to the luminal surface of the artery or by saline liquid to the inner surface of the EAB was numerically applied considering an *orthopressure* application of tractions. Here, orthopressure refers to the prescribed traction applied in the direction normal to its surface in the current configuration. Therefore, the external element force vector term $\boldsymbol{f}_{\text{ext}}$ occurring in Eq. (6.62) is technically not independent of displacements. Such an orthopressure load forms part of a class of Neumann boundary conditions referred to as *follower* loads. The reader is referred to Wriggers [361] for its consideration in the FE formulation as was employed here.

Since the clamp model used for aortic occlusion only considered prescribing displacements of the clamping surfaces, cf. Section 6.1.4.4, clamp movement/displacement mimicking real, clinically used cross-clamps had to be realized. This was achieved by formulating the prescribed rotational movement of the clamp surfaces around an arbitrary axis in terms of a quaternion formulation. In this way the prescribed displacement of the nodes in the clamp surface of the new load step $\hat{\boldsymbol{u}}_{t+1}^{clamp}$ can be given as,

$$\hat{\boldsymbol{u}}_{t+1}^{clamp} = f(\boldsymbol{q}(\hat{\dot{\boldsymbol{\omega}}}_{t+1}, \hat{\boldsymbol{\omega}}_t, \hat{\boldsymbol{X}}_0^{\text{rot}})) \tag{6.72}$$

where $\boldsymbol{q}$ represents the current attitude quaternion that enables the rotation of each node in the clamp surface around an axis and angular acceleration described by $\hat{\dot{\boldsymbol{\omega}}}$ with its origin at $\hat{\boldsymbol{X}}_0^{\text{rot}}$. Such a quaternion formulation has been implemented into the *BACI* framework.

6.1.4.5. Frictional contact mechanics

In-depth computational consideration and development of frictional contact mechanics methodology have been performed by members of our institute [133, 283], but also elsewhere [156, 361]. The following briefly considers aspects of frictional contact employed in the consideration of aortic occlusion are considered.

The BVP presented in Section 6.1.2 can be adapted to include the consideration of frictional contact mechanics. Such changes basically consist of considering the equilibrium described in Eq. (6.26) and (6.28), but now for two bodies, $\Omega^{(1)}$ and $\Omega^{(2)}$ making contact on the two contact surfaces $\Gamma_c^{(1)}$ and $\Gamma_c^{(2)}$, often referred to as the slave and master contact surfaces, respectively. Self-contact can be defined analogously, but only considering a single body. In this work, self-contact was only allowed to occur when the master-slave pair of contact surfaces was explicitly defined on the same body.

Traditionally, the contact constraints required to describe both components of the contact traction $\boldsymbol{t}_c^{(1)}$, namely the normal (or contact pressure) p_n and tangential components (or tangential traction) $\boldsymbol{t}_\tau$ of contact have been defined in terms of inequalities. The normal contact constraint is formulated as the classical Karush-Kuhn-Tucker conditions, which enforces impenetrability, does not allow adhesive stresses and comprises a complementarity condition that constrains the gap $g(\boldsymbol{X}^{(1)})$ to zero when non-zero tractions occur, while also forcing the contact pressure to zero when the gap exists, formulated as,

$$g(\boldsymbol{X}^{(1)}) \geq 0\,, \qquad p_n \leq 0\,, \qquad p_n\, g(\boldsymbol{X}^{(1)}) = 0\,. \tag{6.73}$$

The tangential contact traction is formulated according to the phenomenological Coulomb's law for friction, that can be formulated using the following inequalities,

$$\psi_c := ||\boldsymbol{t}_\tau|| - \mu_t|p_n| \leq 0\,, \qquad \boldsymbol{v}_{\tau,\text{rel}}(\boldsymbol{X}^{(1)}) + \beta\boldsymbol{t}_\tau = \mathbf{0}\,, \qquad \beta \geq 0\,, \qquad \psi_c\beta = 0\,. \tag{6.74}$$

Here, the Coulomb limit ψ_c is defined to constrain the magnitude of the tangential traction vector to not exceed the product of the normal contact pressure and the friction coefficient μ_τ which, also defined as the *slip condition*. Whenever this inequality holds, one of two distinct physical conditions occur, namely the stick and slip states. The former, defined by the scalar parameter $\beta = 0$, forces the tangential velocity to be zero. The latter, defined by $\beta > 0$, yields relative tangential sliding of the two bodies according to the slip rule given by second equation in Eq. (6.74). The complementarity function for tangential friction is given by the last equation in Eq. (6.74), which separates the two distinct physical states, namely stick and slip.

An array of different methods exist to enforce such contact constraints, including the penalty, augmented Lagrange method and Lagrangian multipliers. The latter is used throughout this investigation, since it has the significant advantage of allowing the exact enforcement of the set contact constraints, i.e. no modifications, whereas the others only approximately fulfill these constraints. This advantage comes at the cost of introducing additional unknowns, i.e. the so-called *Lagrange multipliers*, $\boldsymbol{\lambda}$. They can be interpreted as the negative contact tractions $-\boldsymbol{t}_c^{(1)}$ maintaining the contact constraints that lead to a mixed variational formulation yielding a saddle point-type system matrix or system of equations to be solved. The superscript (1) is used to indicate that it only needs to be calculated on one contact surface and not on both – here always the slave-side.

Formulating the contact constraints as variational inequalities in the continuous settings and also considering the current configuration for ease of comparison, the weak form of the PVW to be solved as given in Eq. (6.57) can be extended as,

$$\delta W_{\text{int,ext}} + \int_{\Gamma_c^{(1)}} \boldsymbol{\lambda} \cdot (\delta \boldsymbol{u}^{(1)} - (\boldsymbol{u}^{(2)} \circ P))\, \mathrm{d}\Gamma = 0 \tag{6.75}$$

$$\int_{\Gamma_c^{(1)}} g(\delta \lambda_n - \lambda_n)\, \mathrm{d}\Gamma \geq 0 \tag{6.76}$$

$$\int_{\Gamma_c^{(1)}} \boldsymbol{v}_{\tau,\text{rel}} \cdot (\delta \boldsymbol{\lambda}_\tau - \boldsymbol{\lambda}_\tau)\, \mathrm{d}\Gamma \leq 0 \tag{6.77}$$

where the latter two equations arise from the contact constraints. The function P is analogous to χ in Eq. (6.1), but here it smoothly maps the slave surface onto the master surface such that $P : \Gamma_c^{(1)} \to \Gamma_c^{(2)}$. It must be noted that the PVW relations hold for an arbitrary choice of test and shape functions, but must adhere to certain constrained space restrictions, not expanded upon here.

A number of specialized steps are performed to numerically solve for these equations. Firstly, a segment-to-segment mortar method is used to discretize the contact surfaces, characterized by the weak fulfillment of contact constraints. Secondly, upon discretization into FE, a dual Lagrangian multiplier approach that considers dual test and shape functions for the contact nodes. These shape functions fulfill a biorthogonality condition which allows the additional Lagrangian multipliers, that enforce the contact constraints, to be condensed into the global system of equations. Thereby, a system of equations is yielded with the same size as if no contact degrees of freedom were present. Not only does it reduce the global problem, but the global matrix structure is changed from a saddle-point to a non-symmetric one. Thirdly, in order to increase the robustness, but retain the above-mentioned advantages of these dual Lagrange multiplier method, is to consider a Petrov-Galerkin approach. In this approach, the test and shape functions are intentionally chosen differently, i.e. dual and standard shape functions, respectively [284] – in contrast to the standard Bubnov-Galerkin approach used for structure FE, cf. Section 6.1.4.1. Finally, the contact conditions are reformulated into so-called complementarity conditions, which express the inequalities of Eq. (6.73) and (6.74), in equalities. This reformulation enables the application of semi-smooth Newton methods required to solve such contact problems, because they become sufficiently smooth for the con-

struction of frictional contact operators. For detailed consideration of these numerical aspects, the reader is referred to the above-mentioned references.

Specific to the simulations performed, the following values for frictional coefficients were considered: Friction between the aorta and the cross-clamps was chosen high, i.e. $\mu_\tau = 0.6$, in order to avoid the vessel being pushed laterally by the clamps – which mimics that what happens clinically. The cross-clamping contact simulations also proved to be more stable compared to using a lower μ_τ. Contact between the aorta and the EAB was assumed to behave similar to a standard (untreated) low-density polyethylene (LDPE) catheter making contact with the intima of a vessel, and taken as $\mu_\tau = 0.04$ as experimentally measured by Caldwell et al. [53]. Contact between the constrainer and the aorta was assumed to be high, i.e. $\mu_\tau = 0.6$, because it is a wanted property of the constrainer and can be accordingly included in the design. Finally, self-contact of the intimal surfaces of the aorta upon cross-clamping was considered to be frictionless, i.e. $\mu_\tau = 0.0$, since the displacement-based movement induced by clamps is assumed to produce little or no tangential movement between the self-contacting surfaces.

6.1.4.6. Effective numerical solver strategy

All the methods employed in every simulation presented in this dissertation are implemented in the in-house finite element software *BACI* [**?**] and used accordingly. It is a C++ code developed at our institute and integrates the open-source libraries of the Trilinos Project of the Sandia National Laboratories [161].

For large finite element models such as those considered here, solving the linear system of equations, cf. Eq. (6.65) often accounts for the most computational cost within each time/load step. In order to consider further aspects of effective solution strategies, the linear system of equations can also be written generally as,

$$\mathbf{A}\mathbf{x} = \mathbf{b} \tag{6.78}$$

where $\mathbf{A}$ represents the square system matrix, $\mathbf{x}$ the discrete unknowns to be solved for and $\mathbf{b}$ the so-called right-hand side. The local shape functions used in the FE method implies an $\mathbf{A}$ that will typically be a sparse matrix with a noticeable band structure. Due to the popularity of the FE method, a large amount of research have been done on solving matrices of such structures – e.g. Quarteroni et al. [289], from which a brief general overview of the main solution strategies are given below.

The solution strategies can be divided into two categories, namely direct and preconditioned iterative solution strategies. Direct solution strategies typically utilize an LU-decomposition of $\mathbf{A}$. However, for larger problems, it becomes exceedingly inefficient and memory consuming, due to Gaussian elimination, the unavoidable "fill-in" effect caused by factorization and sub-optimal, non-straightforward parallelization of such direct solution strategies. Preconditioned iterative solution strategies, particularly the Krylov subspace methods, such as the conjugate gradient (CG) and the generalized minimal residual (GMRES) solvers make up the second category. Additional to the use of these solvers, the main reason behind the use of preconditioners are that the efficiency of the iterative linear solvers is mainly controlled by the condition number of $\mathbf{A}$, i.e. the ratio of the largest to the smallest eigenvalue of $\mathbf{A}$. Thereby, the purpose of the preconditioner is to transform the linear system given by Eq. (6.78) into an equivalent system with a reduced condition number by scaling it with an appropriate linear operator. Examples of preconditioners include Jacobi, Gauss-Seidel, incomplete factorization (ILU), geometric multigrid (GMG) and algebraic multigrid (AMG) methods. After preconditioning, the chosen Krylov solver acts as a solution accelerator, of which the output is again preconditioned. This iterative process is continued until a user-specified tolerance is reached.

Even though such preconditioned iterative solutions methods represent the current state-of-the-art techniques for solving large linear systems of equations, these methods typically yield non-optimal performance when applied off-hand. This is because its performance is usually related to the underlying properties of $\mathbf{A}$. As such, parameter tailoring and the choice of a problem-specific preconditioner becomes

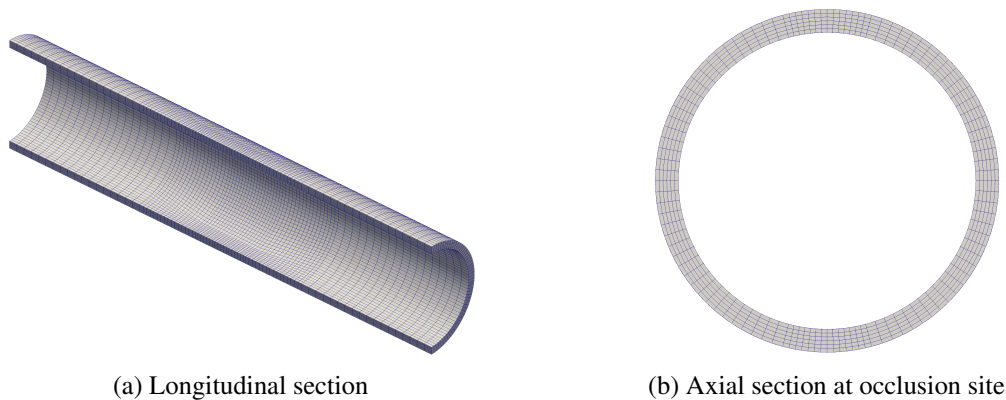(a) Longitudinal section (b) Axial section at occlusion site

Figure 6.1.: The computational discretization of the idealized aorta considered here, with refinements at the occlusion site as shown in (a), and specifically at the pinching sites, in the top and bottom regions of (b).

crucial. The linearized system of equations originating from the consideration of aortic occlusion will be especially poorly conditioned and have a non-diagonally dominant structure, stemming especially from the condensed form of the dual Lagrange multipliers used in mortar contact, cf. Section 6.1.4.5, and the near-incompressibility requirement of the aortic wall modeled, cf. Section 6.1.3 and 6.2.2.1. In order to solve these problem-specific linear systems of equations, a paralallizable direct solver (SuperLU) was used [84], which was integrated in the *BACI* solving environment.

6.2. Modeling of selected manipulation maneuvers causing large deformation

6.2.1. Geometry, FE discretization and boundary conditions

The following section gives an overview of the how the geometries were obtained, the computational FE meshes constructed for the different structural models considered, followed by a brief consideration of the mesh requirements. Detailed information pertaining to all structural simulations considered is given in Appendix A.1.

6.2.1.1. Idealized aortic wall

The idealized aorta was modeled as a straight tube with an inner (luminal) diameter of 29.7 mm, according to a recent morphological study on luminal dimensions of the ascending aorta [216]. A length of 250 mm was chosen to eliminate all potential boundary effects of the fixed cut surfaces. A uniform spatial wall thickness of 2.3 mm was assumed according to the average measured thickness of an atherosclerotic artery [44, 298]. The geometry was constructed and meshed in Cubit v13.1 (Sandia National Labs., Albuquerque, NM, USA), yielding a pure hexahedral mesh with a refined region at the occlusion site, becoming coarser as one moves further away from the occlusion site. Once the mesh was obtained, nodesets were specified and exported as an exodus-type file. Along with appropriate boundary conditions and material models and corresponding parameters, the input file for the FE solver, *BACI* was constructed. Mesh details and refinements are shown in Figure 6.1 and listed in Table A.1.

The vessel was fixed at the truncated surfaces, i.e. Dirichlet boundary condition prescribing the displacement to zero. In order to approximate the physiological stress/strain state in a vessel under blood

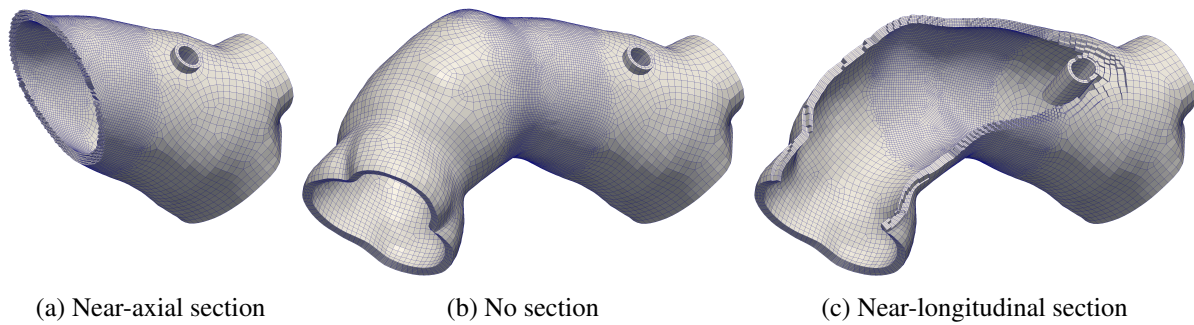| (a) Near-axial section | (b) No section | (c) Near-longitudinal section |

Figure 6.2.: The computational discretization of the patient-specific aorta considered here, showing arbitrary plane sections passing through the discretization that were not allowed to cut the elements, in (a) and (c).

pressure, a prestressing step was first performed (Section 6.1.4.2). In this stage of loading, an orthopressure was ramped up linearly to 60 mmHg. After this was reached, the occluder movement/loading was commenced.

6.2.1.2. Patient-specific aortic wall and cannula tip

The lumen of the ascending aorta and aortic arch of a 66 year-old male patient with mild calcified atherosclerotic lesions was segmented from CT-data, followed by appropriate smoothing and trimming steps using Mimics 16.0 (Materialise, Leuven, Belgium), similar to the process described in Maier [222], of which the details will not be repeated here. Computational meshing was achieved by importing the luminal geometry into Cubit 13.1 (Sandia National Laboratories, Albuquerque, NM, USA), to which a straight end-hole arterial cannula tip geometry of internal diameter 6.6 mm was included, cf. Table A.3. Nodes on the cannula-vessel interface were shared. The luminal surface was meshed with quadrilateral elements. From this surface mesh, six layers of hexahedral elements were extruded normal to the luminal surface and merged with the mesh of the cannula, resulting in a pure hexahedral mesh of the arterial wall and arterial cannula tip with a uniform spatial aortic wall thickness of 2.3 mm, as used for the idealized aorta above. Therefore, all elements had a radial edge length of 0.38 mm. The surface mesh, from which the wall mesh was extruded, was refined locally relative to the importance of certain features to be captured by the model. Since the location of the pinching sites were variable, the entire occlusion site of the aorta was given the mesh size used to resolve the pinching sites in the idealized aorta, cf. Figure 6.1. Mesh details and refinements are shown and listed in Figure 6.2 and Table A.1, respectively. As can be seen from this figure, the occlusion site received the finest mesh, with the mesh size gradually increasing the further is moved away from the occlusion site. Furthermore, the characteristic aortic root bulbs can be seen at the proximal end of this vessel, while it distally, the geometry was truncated immediately distal to the brachiocephalic artery branch.

The same boundary conditions used for the idealized vessel were used for the patient-specific cases, as explained in the preceding section.

6.2.1.3. Occluders

The computational meshes used for each occluder considered, for both idealized and patient-specific cases of aortic occlusion, are shown in Figure 6.3, while geometric and mesh information are listed in Table A.1 and expanded upon in the following.

(a) Clamp surface   (b) EAB   (c) Narrow constrainer   (d) Wide constrainer   (e) Profiled constrainer
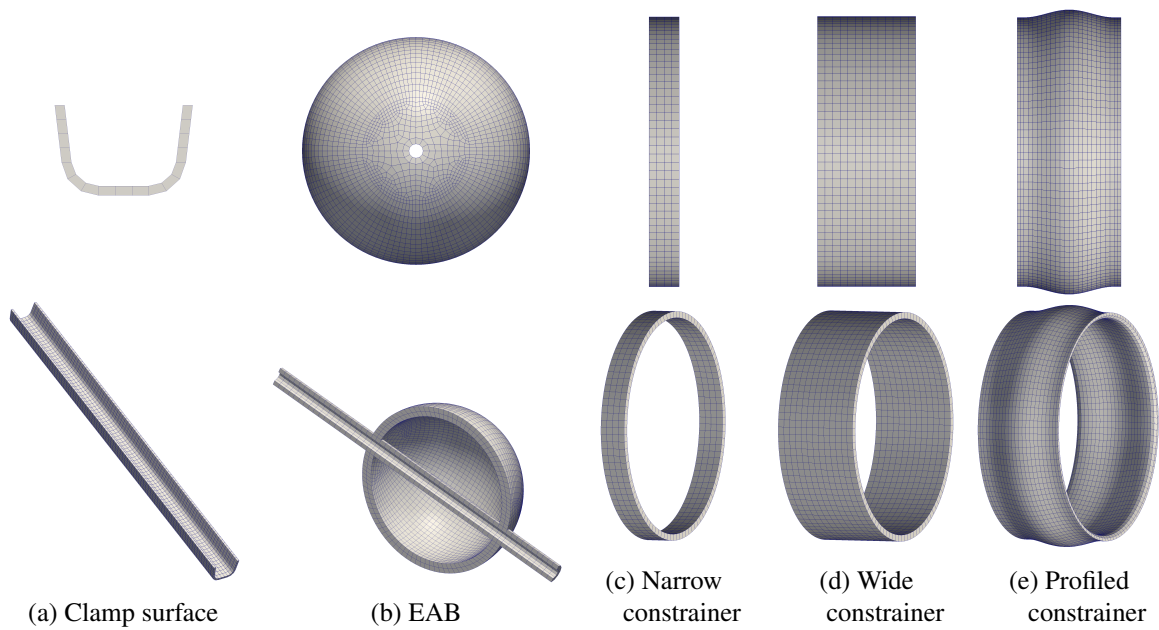
Figure 6.3.: The meshes used for each occluder considered, showing either a side or axial view of each component (top) and an isometric view (bottom). Note that these meshes are not shown in the same relative scale.

The cross-clamp surface dimensions were extracted from standard, clinically available DeBakey cross-clamps, while only a thin layer of the clamping surface was kept to not only reduce the computational complexity, but also since the impact due to the specific clamp movement was of specific interest – not the mechanical response of the cross-clamps. Three different hinge configurations of the cross-clamps were considered: parallel, above-mentioned DeBakey and also Cosgrove/Chitwood-type clamps with a crab-pincher-like hinge, as shown in Figure 6.4. Parallel clamps were included because of its relative simplicity and comparability to some experimental studies. The crab-pincher type clamp was included, due to its extreme hinge configuration and frequent use in the minimally invasive clinical setting. Dimensions of the clamps and the respective hinge locations are listed in Table A.2.

The displacement of these extracted clamps surfaces were prescribed according to their respective hinge configurations by utilizing the quaternion formulation described in Eq. (6.72). This ensured movement of these clamps surfaces as were they still connected to the actual clamp geometries.

Apart from the specific hinge configurations that distinguished the different clamps considered, it is worth noting that each of the hinged clamps, i.e. not the parallel clamps, had a *parallel-gap-width* $t_{\mathrm{pg}} = 3 \; mm$. This means that upon clamp closure, when the two opposing clamp surfaces are parallel relative to each other, this gap between these surfaces exist.

For the EAB, the geometric details, the inflated pressure simulated, its mounted-upon catheter and its soft catheter boundary material are given in the context of its material parameter fitting in Section 6.2.4.2.

Three different constrainers as part of the novel proposed constrained endo-aortic balloon occlusion (CEABO) were investigated: a narrow, wide and profiled constrainer, with widths (in axial direction) L_{a} of 4, 12.85 and 12.85, respectively. The configuration is described in full in Section 7.3. While the first two were simply modeled as straight rings barely in contact with the vessel (constrainer-vessel gap of

(a) Parallel   (b) Standard DeBakey   (c) Crab-like pinching Cosgrove/Chitwood
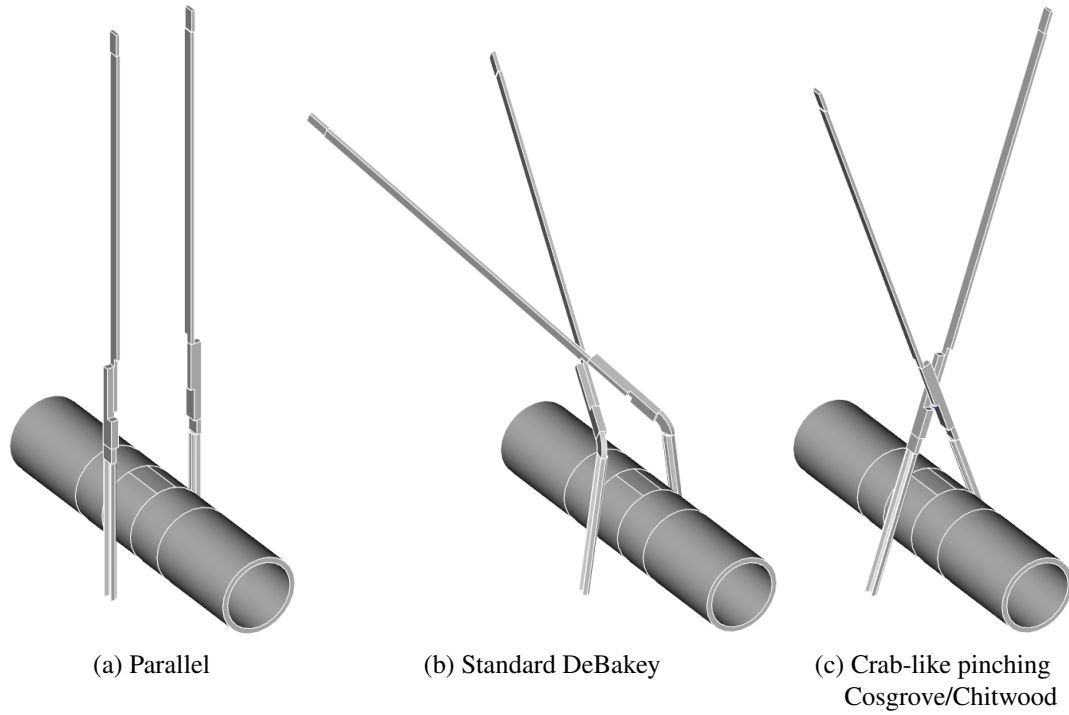
Figure 6.4.: Representations of the three different hinge configurations used for the cross-clamps. Although only the clamps surfaces were modeled, the movement thereof were based on these configurations.

0.05 mm), the latter had a smooth profiled cross section described by,

$$C(z) = \frac{D_{\mathrm{i}}}{2}\left[1 - c_0\left(1 - \cos\left(\frac{2\pi(z - z_0)}{t_{\mathrm{w}}}\right)\right)\right] \tag{6.79}$$

$$x = C(z)\cos(\theta) \tag{6.80}$$

$$y = C(z)\sin(\theta) \tag{6.81}$$

where z is the axial direction, D_{i} is the same diameter as the narrow and wide constrainers, with an expansion factor $c_0 = 0.0275$ yielding a maximum constrainer-vessel gap of 1.05 mm. The resulting geometry is shown in Figure 6.3e.

The cross-clamps, cannula, EAB, EAB-catheter and all three constrainers were also discretized with purely hexahedral elements in Cubit v13.1 (Sandia National Laboratories, Albuquerque, NM, USA).

All the simulations performed and corresponding geometry and discretization details are indicated in Table A.2 under their "Simulation abbr.", which include occluding the idealized and the patient-specific aortas. The idealized aorta was occluded with the following cross-clamps: parallel cross-clamps $CC_{||}$, crab-pincher type cross-clamps CC_{crab} and standard clinically used cross-clamps CC_{std}. Furthermore, the idealized aorta was occluded with standard endo-aortic balloon occlusion $EABO_{\mathrm{pure}}$, as well as three different variations of constrained endo-aortic balloon occlusion investigated, namely with a narrow constrainer $CEABO_{\mathrm{n,0}}$, a wide constrainer $CEABO_{\mathrm{w}}$ and a profiled constrainer $CEABO_{\mathrm{p,0}}$. These simulations were also repeated for the narrow and profiled constrainers with an offset between the EAB and the constrainer of 2 and 4 mm, respectively. These simulations are referred to as $CEABO_{\mathrm{n,2}}$ and $CEABO_{\mathrm{n,4}}$, respectively for the narrow constrainer and analogously as $CEABO_{\mathrm{p,2}}$ and $CEABO_{\mathrm{p,4}}$,

respectively for the profiled constrainer. Although ample visualizations have been given to show the different simulations performed, an exemplary synopsis of all the occluders investigated in the context of the idealized aorta is shown in Figure 7.5. The patient-specific aorta was occluded at two different axial positions. These positions were the distance measured along the luminal centerline, relative to the cannula: $L_a^{\text{occl/cann}} = 15$ and 30 mm, respectively. At each position, the aorta was cross-clamped with standard clamps at three different axial rotations of the clamps, namely $CC_{0°}^{\text{Calc},i}$, $CC_{30°}^{\text{Calc},i}$ and $CC_{60°}^{\text{Calc},i}$ at the positions $i = 1, 2$. The cross-clamps were positioned orthogonal to the vessel axis at the respective axial positions, as from visual inspection. The patient-specific aorta was also occluded with EABO, namely $EABO^{\text{Calc},i}$ with the positions $i = 1, 2$. These patient-specific occlusion configurations are exemplary shown in Figure 9.3. For a comparative evaluation to ascertain the influence of the included calcifications, three simulations were redone omitting the calcification contribution, namely $CC_{0°}^{\text{noCalc},i}$, $CC_{30°}^{\text{noCalc},i}$ and $EABO^{\text{noCalc},i}$ at the position $i = 1$.

6.2.1.4. Mesh requirements

The computational mesh properties indicated in Table A.1 represent outcomes of the term paper by Schlenk [306] and the Masters' thesis of Hirschvogel [163], as well as reflecting the mesh sizes used by Gasser et al. [124] and Famaey et al. [103], cf. Section 7.1. Therefore, the mesh refinements used in the presented structural simulations are considered as sufficient to resolve all quantities of interest.

6.2.2. Materials: Aortic wall

The section begins with a detailed consideration of the histological morphology of large arteries, followed by a review of appropriate modeling approaches and the final choice of material model and the associated parameters.

6.2.2.1. Large artery morphology and mechanically relevant constituents

From a morphological and histological point of view, the arterial system has been extensively described. The following aims to give a brief overview of the mechanically relevant aspects thereof, as mainly drawn from the comprehensive overviews by Humphrey [169] and Thubrikar [335] unless otherwise stated.

The arterial system facilitates the transport of oxygenated blood from the heart throughout the entire body and also acts as reservoirs for blood pressure due to its distensibility. The main constituents of a healthy artery are cellular, e.g. endothelial cells, smooth muscle cells (SMCs), fibroblasts etc., and an extra-cellular matrix (ECM) consisting mainly of elastin, collagen, connective tissue etc. Properties of arteries undergo gradual, but significant changes as one descends down the arterial tree, i.e. moving from the heart into distal bifurcations. Not only does the individual artery diameter decrease, but the combined diameter increases, and the wall thickness and microstructure also varies. Due to the application considered in this dissertation, further consideration is mainly given to the aorta.

The aorta, along with its immediate branches, can be classified as elastic arteries and make up the largest arteries in the arterial tree. The aorta is characterized by a mostly passive elastic response, as opposed to more muscular arteries further down the arterial tree where local blood flow can be regulated to a certain extent by vaso-dilation and constriction, due to the presence of an abundance of SMCs. Such a passive elastic response plays an important role in augmenting and maintaining forward flow of blood throughout the cardiac cycle.

All types of arteries principally consist of three concentric layers, namely the intima (inner layer), media (middle layer) and the adventitia (outer layer), as shown in Figure 6.5. The intima consists of a single layer of endothelial cells fixed to a very thin collagenous basal lamina. The aorta also typically

has a subendothelial layer consisting of connective tissue and SMC, but from a mechanical point of view of the whole artery, still plays a negligible role. Intimal thickening may increase with age or disease progression, although it will in turn also increase the mechanical contribution to the entire aortic wall mechanical response. An internal elastic lamina generally forms a noticeable boundary to the media, while an external elastic lamina forms a much less noticeable boundary between the media and adventitia. These elastic laminae structurally allow the transmural exchange of nutrients, electrolytes, water, as well as cellular communication. The media itself consist of concentric arrangement of SMC and elastic fibers into so-called musculo-elastic fascicles or elastic fibers. Such fascicles can basically be seen as layers of SMC separated by very thin, fenestrated sheets of elastic fibers. Throughout these elastin sheets, bundles of tiny collagen fibrils are interwoven. The adventitia predominantly consists of dense bundles of collagen fibers, with fibroblasts, elastic fibers, nerves and potentially tiny vessels (vaso vasorum) supplying the vessel itself with blood. These collagen fibers are generally longitudinally oriented.
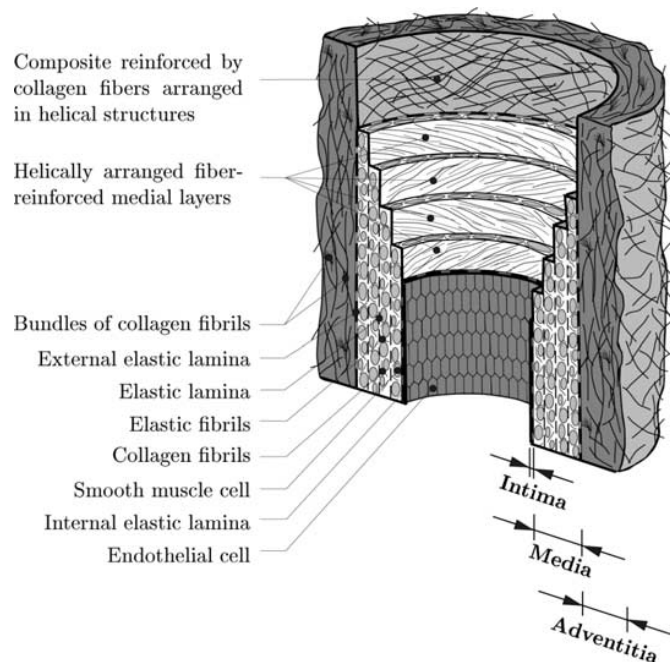
Figure 6.5.: Representative aortic histological morphology, from [167] with permission.

The ECM provides the majority of mechanical relevance in the aorta, apart from the presence of SMCs. Collagen fibers in the media and adventitia provide the fundamental mechanical strength of an artery to prevent over-dilation during physiological loading. Under these loading conditions, collagen fibers are generally undulated. The straightening of collagen during supra-physiological loads yields very stiff response and beyond strain of approximately 10%, collagen fibers will break. Collagen fibers have a half-life of typically 0.5 to 3.0 months, depending on certain homeostatic parameters. On the other-hand, the elastic fibers are stretched under physiological loading, providing its characteristic elastic response and can normally be stretched to a strain of 150% without breaking. Thereby, elastic fibers also enable the storage and return of mechanical energy under pulsatile blood pressure conditions. Furthermore, due to certain biochemical properties which make it resistant to degradation, elastic fibers can remain stable for years. The presence of proteoglycans, and all the subsequent molecules that bind to it, play a very important role in the mechanical response of the arterial wall, since it efficiently binds water in the ECM. Such interstitial water not only provides a medium in which diffusive processes can occur, but also provides the

non-fibrous portion of resistance to any compressive loading and along with other molecules, yield the viscosity ascribed to the non-fibrous portion of the ECM, or the so-called matrix or ground substance.

Aging has a profound effect on the overall material properties of an artery. Apart from pathologies occurring such as atherosclerosis, cf. Section 6.2.3, probably the most profound change in normal arteries is caused by the progressive degrading of elastic fibers as a function of age, thereby explaining the stiffer, less distensible behavior of arteries at advanced age [108].

In an elastic artery like the aorta, the relative thickness distribution of these layers are typically 11%-57%-32% for the intima, media and adventitia, respectively [309]. The smaller quantity of SMC in the aorta, compared to more muscular arteries, is made up by an increased concentration of elastic layers and collagen fibers.

6.2.2.2. Modeling approaches

The arguably most fundamental development in modeling the hyperelastic behavior of arteries came from a study by Fung [115]. Studying the simple uniaxial elongation of an arterial sample, the authors noted the linear relationship that was observed between the stiffness, defined as $\frac{\mathrm{d}\boldsymbol{P}_{11}}{\mathrm{d}\lambda_1}$, and the stress $\boldsymbol{P}_{11}$. Here $\boldsymbol{P}_{11}$ refers to the diagonal term of the second-order 1st Piola-Kirchhoff in the direction of elongation, and λ_1 the stretch ratio in this direction. Solving for $\boldsymbol{P}$ yielded an exponential description, albeit one-dimensional stress-stretch relation. From this information, the authors postulated the existence of a scalar potential function for the elastic 3D stress-strain behavior of soft tissue, namely the SEF as,

$$\Psi = c\left(e^Q - 1\right). \tag{6.82}$$

Here, Q was taken as a polynomial function of the components of $\boldsymbol{E}$, and was later shown that it was sufficient to only consider the quadratic terms, i.e. $Q = a_1 E_{11}^2 + a_2 E_{22}^2 + a_3 E_{12}^2 + a_3 E_{21}^2 + 2a_4 E_{11}^2 E_{22}^2$ for a 2D description. This relation formed the basis for the current considerations of modeling arteries. Noteworthy, is that apart from the phenomenological nonlinearities, this study also described other very important aspects of biological soft tissue response, namely material anisotropy, strain-rate dependency, relaxation and failure properties.

Although Eq. 6.82 is extremely applicable due to the versatility of the exponential function to fit experimentally derived parameters, a major limitation is the lack of physical interpretation of the experimentally fitted parameters and no *a priori* restriction placed upon these to ensure convexity of the SEF. The latter fact implies that a set of parameters could be fitted that result in a non-convex SEF [167].

A more recent, improved and widely used group of models for describing the stress-strain behavior of arteries have been based on the composite n-fiber family model, as first introduced by the Holzapfel group [167]. In this model , the modeling approach is to consider the respective isotropic contribution of the amorphous, elastin matrix/ground substance and anisotropic contribution of the collagen fibers. By additionally considering an isochoric-volumetric split of Eq. (6.43), the SEF can be written in the form given above in Eq. (6.52). Here, the isochoric isotropic and anisotropic parts are respectively given by,

$$\bar{\Psi}_{\mathrm{matr}} = \frac{c}{2}(\bar{I}_1 - 3) \tag{6.83}$$

$$\bar{\Psi}_{\mathrm{fib}}^i = \frac{k_1^i}{2k_2^{\bar{i}}} \sum_i^n \{\exp[k_2^i(\bar{E}^i)^2] - 1\}, \ \text{ for } i = 1, 2, ..., n \tag{6.84}$$

with n equal to the total number of families of fibers. The parameter $c > 0$ is a stress-like material parameter related to the shear modulus of the isotropic part, while in the anisotropic part representing each fiber family, $k_1^i > 0$ is a stress-like material parameter, while $k_2^i > 0$ is a dimensionless parameter. Holzapfel et al. [167] initially proposed $\bar{E}^i = \bar{I}_4^i - 1$ and $n = 2$ and that the media and adventitia be

modeled separately, since experimentally, distinct directions of two families of fibers were observed for each layer. Here, such a fourth invariant can be defined separately for each family of fibers. Furthermore, each family of fibers were assumed to be mechanically equivalent, i.e. $k_1^1 = k_1^2 = k_1$ and $k_2^1 = k_2^2 = k_2$. Thereby, experimental results could be used to determine the four constants, namely c, k_1, k_2 and α_{fib}, cf. Eq. (6.54), for each layer respectively.

In an attempt to account for the occurrence of fiber dispersion, i.e. the natural occurrence of fibers deviating from each predominant fiber family direction, the Green-Lagrange strain-like term in Eq. (6.84) was extended to,

$$\bar{E}^i = \kappa_{\text{d}}\bar{I}_1 + (1 - 3\kappa_{\text{d}})\bar{I}_4^i - 1 \tag{6.85}$$

where $0 \leq \kappa_{\text{d}} \leq \frac{1}{3}$ represents a parameter for fiber dispersion [125, 168], which also needs to be fitted to experimental results. At the limit of $\kappa_{\text{d}} = 0$, $\bar{E}^i$ reduces to the one in Eq. 6.84, while at $\kappa_{\text{d}} = \frac{1}{3}$, the anisotropic SEF reduces to an exponential purely isotropic SEF. Thereby, κ_d models fiber dispersion as a linear mixture of an exponential isotropic and anisotropic strain energy function.

Ultimately, however, fiber dispersion modeled as in Eq. (6.85) represents an axisymmetric occurrence of fiber dispersion, while experimental results show significantly greater in-plane than out-of-plane fiber dispersion [309]. Furthermore, even considering residual stresses present in an unloaded artery, modeling an artery using two distinct layers fitted to experimental results do not give a continuous transmural distribution of stresses [124] as is expected and can therefore not be considered physiological. Finally, the contribution of the mostly circumferentially SMC are not considered separately, and as such will be implicitly contained in the constituents considered.

These factors, among st others, motivated the formulation of a slightly different approach by the Humphrey group, smearing all the anisotropic constituents together, i.e. the collagen fibers and SMCs in all the layers of the artery, as probably first proposed by Baek et al. [20], which is the same as Eq. (6.84) with $n = 4$, but neglects a term they included to describe the degree of muscle activation. Here, $n = 4$ was chosen based on the distinct families of fibers in the media and adventitia, respectively, obtained from the above-mentioned experimental evidence by Holzapfel. Developments of the model have included assumptions about the direction of the four families of fibers, namely that two was fixed in the circumferential and axial directions respectively, i.e. $\alpha_{\text{fib}}^1 = 0°$, $\alpha_{\text{fib}}^2 = 90°$, while the other two diagonal families of fibers were assumed to be symmetrically orientated around the circumferential direction, i.e. $\alpha_{\text{fib}}^3 = \alpha_{\text{fib}}^4$, cf. Eq. (6.54). Therefore, only one angle has to be experimentally determined. Furthermore, assuming the mechanical equivalence of the two diagonally oriented fibers, reduces the number of unknowns to be fitted experimentally to eight, namely, $c, k_1^1, k_2^1, k_1^2, k_2^2, k_1^{3,4}, k_2^{3,4}, \alpha_{\text{fib}}^{3,4}$. Additional aspects incorporated include mass fractions of each constituent, an extra fiber of families to model the passive response of SMC, and also strain energy contribution of collagen fibers in compression to mimic that of SMC in compression [55, 358]. The most recent study, however, reveals that only $n = 4$, with no mass fractions or active response, and only one varying angle for all four fiber families (as explained above) were considered to collectively capture all collagen fiber families, passive SMC and any other potential mechanisms not yet quantified, such as lateral cross-links, physical entanglements, etc. [297].

6.2.2.3. Choice of material model and associated parameters

This last-mentioned study by Roccabianca et al. [297] is used in this dissertation as the working constitutive relationship to model the aorta, due to its improvement upon the mature model provided by the Holzapfel group, as well as refinements made since its introduction by the Humphrey group. Furthermore, this study reveals not only an important literature review of the inter-study variability of experimentally measured parameters and the current need for a standardization of bi-axial testing of the human aorta, but also performs a type of reasonability test of experimentally derived parameters. The reasonability test is

performed by calculating an estimation of the distensibility of an idealized tube under a generally assumed in vivo prestretch, using 19 experimental data sets from different studies fitted to the currently considered material model. In summary, the different components of the chosen Humphrey material model that make up the general form of a SEF used for arterial modeling are,

$$\Psi_{\text{vol}} = \frac{\kappa}{4}(J - \ln J - 1) \tag{6.86}$$

$$\bar{\Psi}_{\text{matr}} = \frac{c}{2}(\bar{I}_1 - 3) \tag{6.87}$$

$$\bar{\Psi}_{\text{fib}}^i = \frac{k_1^i}{2k_2^i}\sum_i^4\{\exp[k_2^i\bar{E}_i^2] - 1\}, \quad \text{for } i = 1, 2, 3, 4 \tag{6.88}$$

where volumetric model is the one of Ogden from Eq. (6.48) and the contained variables are defined as,

$$\bar{E}_i = \bar{I}_4^i - 1 \tag{6.89}$$

$$\bar{I}_4^i = \begin{cases} (\bar{\lambda}_{\text{fib}}^i)^2 = (\bar{\lambda}_{\text{fib}}^{\theta\theta,i})^2\cos^2\alpha_{\text{fib}}^i + (\bar{\lambda}_{\text{fib}}^{zz,i})^2\sin^2\alpha_{\text{fib}}^i, & \bar{\lambda}_{\text{fib}}^i \geq 0 \\ 1, & \bar{\lambda}_{\text{fib}}^i < 0 \end{cases} \tag{6.90}$$

$$\alpha_{\text{fib}}^1 = 0°, \quad \alpha_{\text{fib}}^2 = 90°, \quad \alpha_{\text{fib}}^3 = \alpha_{\text{fib}}^4 = \alpha_{\text{fib}}^{3,4} \tag{6.91}$$

$$k_1^3 = k_1^4 = k_1^{3,4}, \quad k_2^3 = k_2^4 = k_2^{3,4}. \tag{6.92}$$

As seen in Eq. (6.90), all of the fiber families are considered to carry no load in compression, as motivated by the undulated configuration of collagen and idealized micromechanical model analysis [13, 167]. Even if some slight compressive loads are borne by the families of fibers or SMC, these are expected to be captured in part by the ground matrix and the (near) orthogonally orientated families of fibers. This assumption was further supported by findings from a preliminary study at our institute [163], showing that above-mentioned assumptions of collagen fibers bearing compressive load [55] caused clear unphysiological buckling during large deformations induced by aortic clamping.

The parameters chosen for modeling the ascending aorta and aortic arch are those measured by Haskett et al. [158] for 9 samples of the ascending aorta, as refitted to the chosen four-fiber family model in Roccabianca et al. [297] and also shown to fulfill its stated reasonableness requirements, listed in Table 6.1. The other two reasonable data sets for the ascending aorta both had $c < 1 \cdot 10^{-6}$ kPa, which was considered insufficient for simulating large deformations during aortic occlusion due to the lack of isotropic stiffness. Furthermore, a micromechanical analysis revealed that the isotropic contribution to the strain energy is important to ensure numerical stability of phenomenological fiber reinforced materials such as considered here [13], cf. Eq. (6.86) to (6.92). Finally, although the k_2 dimensionless parameter of the chosen set was reported as $7.65 \cdot 10^{-6}$, a numerical parameter study considering an idealized bi-axial setup using the chosen bulk modulus κ, revealed an insensitivity in the stress/strain response up to $k_2^1 = 1.0$, and was accordingly chosen as $k_2^1 = 0.1$, in line with other similar fiber-family reported as $k_2^2 = 0.1$. Setting $k_2^1 = 0.1$ still yielded a solution that was <1% from the solution using the reported parameters, whereas $k_2^1 = 1.0$ started to have a more substantial influence. This parameter choice resulted in more stable numerical behavior, as is evident when considering the effect that such a small k_2^1 would have on the strain energy defined by Eq. (6.88).

In order to model the near-incompressibility of the aortic wall, a bulk modulus was chosen as $\kappa = 0.3$ MPa, cf. Eq. 6.86. Its evaluation and choice is further considered in Section 7.6.3.3.

Despite the fact that the chosen Humphrey model is still phenomenological, i.e. contributions of the individual constituents to the strain energy are lumped into the parameters of the *a priori* defined structure of the SEF, it represents the current state-of-the-art in aortic wall modeling.

Table 6.1.: Choice of aortic wall parameters from Haskett et al. [158], refitted by Roccabianca et al. [297].

c [kPa]	k_1^1 [kPa]	k_2^1 [-]	k_1^2 [kPa]	k_2^2 [-]	$k_1^{3,4}$ [kPa]	$k_2^{3,4}$ [-]	$\alpha_{\text{fib}}^{3,4}$ [°]
47.43	35.23	0.1	40.84	0.1	15.21	2.58	48.98

Finally, it is also worth noting the near-transversely isotropic behavior of the Humphrey model with the given set of parameters. This small degree of anisoptropy have been frequently reported for aortic material at different levels of the arterial tree (e.g. [158]) and have lead many researchers to use isotropic models in ranges of physiological loading, e.g. [223, 290]. However, in the context of the supra-physiological loading brought on by aortic occlusion, it was considered advantageous to consider the more advanced model presented here. The comparatively stiffer behavior of an isotropic material under a more complex loading than simple uniaxial loading was demonstrated in the Master's thesis of Hirschvogel [163]. Here, it was shown that fitting experimental results to an isotropic and anisotropic model respectively, yielded the same results for the range of strains input into the parameter fitting algorithm, cf. Eq. (6.98). However, once exceeding this range, the isotropic model yielded an excessively, unphysiological, stiffening behavior compared to the anisotropic model.

6.2.3. Materials: Calcification in atherosclerotic lesions

In this section, the origins of atherosclerosis are considered, with special focus on the occurrence of calcifications in these lesions. Thereafter, appropriate modeling approaches are considered, followed by the choice of modeling approach and its associated parameters.

6.2.3.1. Origins of calcific atherosclerotic lesions

Atherosclerosis is a very widely studied vascular pathophysiology due to its association with cardiovascular diseases in general, yet not fully elucidated due to the multifactorial influences relating to its genesis and proliferation. Atherosclerosis is a focal disease that most probably originates due to some mechanical injury or dysfunctional changes to the endothelium, while it has also been proposed to be caused by the increased aortic wall stresses brought on by elevated blood pressure. Atherosclerosis starts as fatty streaks deposited in the sub-intimal layer in infants and young children. Based on various risk factors, it can progress into atherosclerotic lesions over many years. Such risk factors include hypertension, smoking, hypercholesterolemia, hyperlipidemia and diabetes mellitus. Its progression is driven by an imbalanced lipid metabolism causing lipid accumulation, as well as a mal-adapted immune response which results in a chronic inflammatory state of the arterial wall. Despite the potential growth, many atherosclerotic lesions remain stable for years, while others may either continue to progress and may lead to vessel stenosis or obstruction, or even lesion rupture. Stenosis and obstruction is of course dangerous in terms of downstream tissue ischemia, while rupture risks the release of embolic material, which carries its own downstream occlusive risks including myocardial and/or neurological infarction, cf. Part I. Atherosclerotic lesions can occur at any level of the arterial tree, but especially at complex arterial morphologies such as bifurcations and curvatures. This summary given above was extracted from the excellent reviews by Thubrikar [335] and Weber and Noels [352]. For a full biological description of the origin and progression of atherosclerosis, the reader is referred to these reviews.

In the context of this dissertation, clarification with regards to the specific terminology used is warranted: The *atheromatic* lesion refers to the non-cellular components that makes up a part of the *atherosclerotic* lesion. The latter consists of a fibrous cap forming the luminal barrier, behind which lies a lipid core

surrounded by a capsule of proliferated SMCs. Deposits of calcium can occur anywhere in this capsule as well as the fibrous cap.

An important sub-category of atherosclerosis research is the occurrence of arterial calcification associated with atherosclerosis, especially in terms of its mechanical significance. A comprehensive overview of the biological aspects has been done by Sage et al. [301] and Alexopoulos and Raggi [3], among st others. What follows is a brief summary thereof: Vascular calcification was initially considered to be a passive, unregulated, inevitable, degenerative process where discarded calcium deposits accumulate in the vessel wall, and is simply a consequence of aging. Currently, however, it is generally accepted to be an active process resembling osteogenesis (bone formation). As such, arterial calcium deposits resemble bone from a nano- to a macro-scale level. The reason why this happens is not entirely clear, but one proposed explanation may be a last resort immune response against progressing atherosclerosis. While some investigations have led some researchers to conclude that a stabilizing, repairing effect of calcification in plaques, others report an increased fragility, while overall, the calcific morphology might be determinant of risk. Although calcifications were considered to only occur in late stages of atherosclerosis, small calcific crystals (5–10 μm) are already found in early lesions in a patients' third decade of life. The calcification occurring in atherosclerotic lesions is most probably a cause, but also a consequence of cardiovascular disease. It is a cause, because it induces cellular osteogenic differentiation – responsible for the arterial calcifications that resemble bone. It is a consequence, because it impacts plaque stability by causing a compliance mismatch between adjacent regions of steeply varying stiffnesses. Plaque rupture is suspected to be the greatest contributor to myocardial and cerebral infarction due to arterial calcification. Furthermore, as a consequence, it also increases the rigidity of the aorta due to medial calcification, which can lead to hypertension, left ventricular hypertrophy, ischemia etc. It should also be noted that arterial calcifications can also occur independent of atherosclerosis in patients with chronic kidney disease or diabetes.

6.2.3.2. Modeling approaches

The explicit modeling strategy to incorporate calcifications into the presented aorta model briefly presented here was developed at our institute by a predecessor of the author. For a comprehensive overview of the origins and importance of this strategy, its superiority over other published methods and the concomitant insights resulting from this strategy in the context of AAAs, the reader is referred to the dissertation of Maier [222], as well as in Maier et al. [224]. Below follows a brief description thereof.

Basically, the explicit modeling strategy employed, exploits the increased attenuation of calcific deposits (resembling bone, cf. previous Section) in the aortic wall as obtained from computer tomographical (CT) x-ray images measured in Houndsfield (HU) units, combined with the common coordinate system shared by the CT images and the FE mesh of the aortic wall, cf. Section 6.2.1.2. Thereby, a 3D linear interpolation scheme is employed to relate an HU-value associated to each voxel from the CT data to each specific finite element that make up the FE mesh of the aortic wall, made possible by the shared coordinate system. In this way, additional stiffness brought on by the calcification in the aortic wall is related to the HU-value associated with the finite element, and is incorporated into the SEF of the entire aortic wall Ψ_{ao} by extending Eq. (6.52) as follows,

$$\Psi_{\mathrm{ao}} = \bar{\Psi}_{\mathrm{matr}}(\boldsymbol{C}) + \bar{\Psi}_{\mathrm{fib}}(\boldsymbol{C}) + \Psi_{\mathrm{vol}}(J) + \bar{\Psi}_{\mathrm{calc}}(\boldsymbol{C}) + \Psi_{\mathrm{vol,calc}}(J) \qquad (6.93)$$

where the last two terms, not yet considered, were added and defined as,

$$\bar{\Psi}_{\mathrm{calc}}(\boldsymbol{C}) = \alpha_{\mathrm{HU}}(\bar{I}_1 - 3) \qquad (6.94)$$

$$\Psi_{\mathrm{vol,calc}}(J) = \frac{\kappa_{\mathrm{calc}}}{4}(J - \ln J - 1). \qquad (6.95)$$

in which the isochoric term is of a NeoHookean isotropic form with a HU-dependent shear modulus α_{HU}, cf. Eq. (6.45), while the volumetric term is similar to the one used in Eq. 6.48, but now with a HU-dependent bulk modulus $\kappa_{\mathrm{calc}} = 2\frac{\alpha_{\mathrm{HU}}}{1-2\nu}$.

The isochoric stiffness added to the arterial wall was made conditional by defining thresholds of HU-values below which no calcification is assumed to exist $\mathrm{HU}_{\mathrm{min}}$ and above which is assumed to correspond to pure calcification in the corresponding aortic wall $\mathrm{HU}_{\mathrm{max}}$. Thereby, an element-wise stiffening related to the x-ray attenuation can be assigned to the patient-specific FE mesh. The range of values between these two thresholds can accordingly be modeled as a transitional stiffness region, defined as,

$$\alpha_{\mathrm{HU}} = \begin{cases} 0, & \mathrm{HU} \leq \mathrm{HU}_{\mathrm{min}} \\ \frac{1}{2}\big(\sin(\frac{\pi(\mathrm{HU}-\mathrm{HU}_{\mathrm{min}})}{\mathrm{HU}_{\mathrm{max}}-\mathrm{HU}_{\mathrm{min}}} - \frac{\pi}{2}) + 1\big)\alpha_{\mathrm{HU,max}}, & \mathrm{HU}_{\mathrm{min}} < \mathrm{HU} < \mathrm{HU}_{\mathrm{max}} \\ \alpha_{\mathrm{HU}} = \alpha_{\mathrm{HU,max}}, & \mathrm{HU} \geq \mathrm{HU}_{\mathrm{max}} \end{cases} \qquad (6.96)$$

and is plotted in Figure 6.6. The importance of the existence of such a smooth transition was also highlighted in Maier et al. [224], ascribed to the fact that including no transition causes unrealistic stress peaks in the wall stresses.
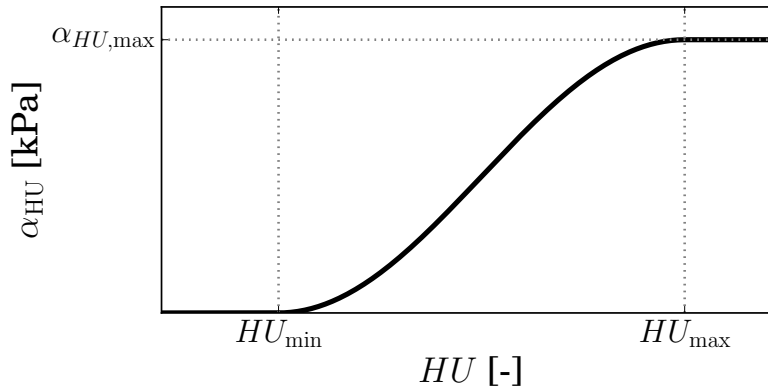

Figure 6.6.: The conditional isotropic shear modulus as a function of the x-ray attenuation from CT scans, demonstrating the smooth transition between no calcification and pure calcification, describing Eq. (6.96).

6.2.3.3. Choice of modeling approach and associated parameter choices

Although the above-mentioned explicit methodology trumps all other presented in computational studies on mechanical stresses in patient-specific arterial calcifications, cf. [222], certain discretion needs to be considered when choosing adequate parameters.

Firstly, the exact relation between the calcified wall stiffness, quantified by α_{HU}, and the x-ray attenuation HU need to be determined. Following Maier et al. [224], this parameter was set to 8.929 MPa. Secondly, some uncertainty exists with regards to adequate thresholds to be set. Although it has been reported that the threshold for arterial calcification was $\mathrm{HU} + \min > 200$ [79], the contrast agent in the blood stream caused $\mathrm{HU} > 200$. Therefore, following the convention of Maier [222], $\mathrm{HU}_{\mathrm{min}}$ was set to 335 HU in order to be avoid maximum blood HU values from spilling over onto the wall, while $\mathrm{HU}_{\mathrm{max}}$ was assumed to be 630 HU, based purely on observational estimation. Finally, although arterial calcification occurs mainly on the intimal and medial levels, making up approximately two thirds of the

vessel wall, cf. Section 6.2.2.1, mapping revealed calcifications in the outer third of the wall. Calcification contribution in these outer layers were, however, not excluded, due to the inability of distinguishing between different layers that prompted the use of a smeared model for the aortic wall, cf. Section 6.2.2.3. Furthermore, the inner (intimal) wall boundary can be much accurately segmented in relation to the outer (adventitial) wall boundary due to the contrast enhancement of the lumen, meaning that any local intimal and/or medial thickening that occur at atherosclerotic lesions cannot be captured by the constant wall thickness assumption. Therefore, since the calcifications can clearly be identified in the CT images as being part of the aortic wall and due to the homogeneous aortic wall properties assumed through the wall thickness, the calcifications were included even when they occurred in the outer layers of the aortic wall of the FE mesh that geometrically represents the adventitia.

The non-calcific constituents of an atherosclerotic lesion were not considered, since apart from the slight softer behavior of the lipid pool, the all other constituents simply consist of the normal arterial constituents, just in different proportions. The significant mechanical effect of arterial calcifications justly assumed to override its influence, as reviewed in the dissertation of Brinkhues [49], especially in the context of the large deformations associated with aortic occlusion.

6.2.4. Materials: Occluder and cannula structure modeling

The following section briefly covers the material models and associated parameters used for the non-biological objects in the selected manipulation maneuvers.

6.2.4.1. Cross-clamps, constrainer and cannula

Each different type of cross-clamping considered was modeled as a thin, clamp insert-type surface driven on the inner, non-contacting surface by a prescribed displacement delineated from real clamp movement, cf. Section 6.2.1.3. In other words, the clamp was effectively infinitely stiff, while the insert surface was modeled as a simple St.-Venant-Kirchhoff material, cf. Eq. (6.49) using the parameters for polyurethane with $E = 48$ MPa and $\nu = 0.475$ [74]. The same material was also used to model both the constrainer and the cannula.

6.2.4.2. Endo-aortic balloon (EAB)

To determine adequate material parameters representing a typical large diameter EAB, pressure-volume data for a clinically used "Endoclamp" EAB was taken from a product brochure [97]. Furthermore, the pressure-volume relationship of a thin-walled sphere, made of an incompressible Yeoh isotropic material, Eq. (6.46), subjected to an internal pressure is considered,

$$P_{\mathrm{EAB}}(r) = 4\frac{H}{R}\left[\frac{R}{r} - \left(\frac{R}{r}\right)^7\right]\left\{c_1 + 2c_2\left[2\left(\frac{r}{R}\right)^2 + \left(\frac{R}{r}\right)^4 - 3\right] + 3c_3\left[2\left(\frac{r}{R}\right)^2 + \left(\frac{R}{r}\right)^4 - 3\right]^2\right\} \quad (6.97)$$

where the balloon pressure P_{EAB} is related to the volume via the sphere radius in the reference R and current configuration r, as well as the reference balloon wall-thickness H. See the diploma thesis of Hirschvogel [163] following Holzapfel [166] for derivation details. For computational reasons, the following assumptions were incorporated: the wall-thickness was chosen as 1.5 mm, even though reported catheter balloons are typically two orders of magnitude thinner [126]. However, this thickened wall will then be reflected in the stiffness parameters c_1, c_2 and c_3 when performing a fit to the available pressure-volume data. Evidently, the Yeoh material model was chosen to fit these parameters, cf. Eq. (6.46). Furthermore, since only two such data points are given in the above-mentioned brochure, i.e. a minimum and maximum value of the inflated EAB, a third point below the range of the preceding two points was used
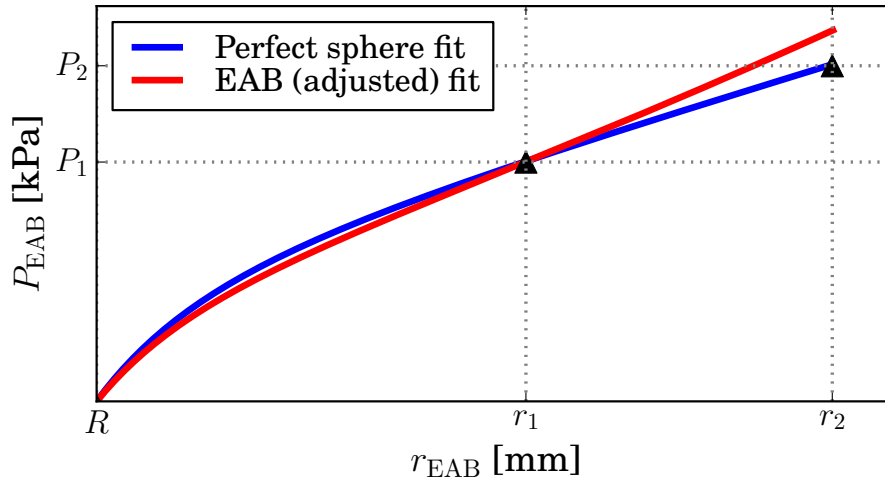
Figure 6.7.: The EAB pressure-volume relationship. Data available from manufacturer information (r_1, P_1 and r_2, P_2, black diamonds) were used for parameter fitting. The parameters were fitted to an inflating an idealized thin thin-walled hollow sphere compared. Compared to the actual FE model used, the parameters were adjusted (as indicated) in order to reach the same volume, i.e. r_2.

to facilitate computational simplification by having a zero-pressure in the reference configuration when $r = R$. Using a standard Levenberg-Marquart algorithm from Matlab (R2012a, Mathworks Inc., Natick, MA, USA), a nonlinear optimization of the following objective function was performed,

$$e = \sum_{j=1}^{k} \left[(P_{\text{EAB}}^{\text{exp}} - P_{\text{EAB}}^{\text{theory}})_j^2 + (r_{\text{EAB}}^{\text{exp}} - r_{\text{EAB}}^{\text{theory}})_j^2 \right] \tag{6.98}$$

for each experimental-theoretical pair j of the total number data pairs k considered.

Since the actual FE model of the EAB was not a perfect thin-walled hollow sphere but rather a discretization of a thin-walled hollow sphere fixed to a stiff catheter through its center, cf. Section 6.2.1.3, the fitted model parameters were slightly adjusted for the actual FE simulations used. The goodness of fit of both the obtained and adjusted parameters are depicted and listed in Figure 6.7. The final chosen parameters are given in Table 6.2, along with the parameters for the catheter and the soft catheter boundary used to mimic the response of the elongated femorally inserted catheter. As will be seen in Section 9.1, this allowed for the EAB to move relatively freely during inflation, as is also seen clinically.

Table 6.2.: The parameters used to model the response of the endo-aortic ballon and the associated EAB-catheter.

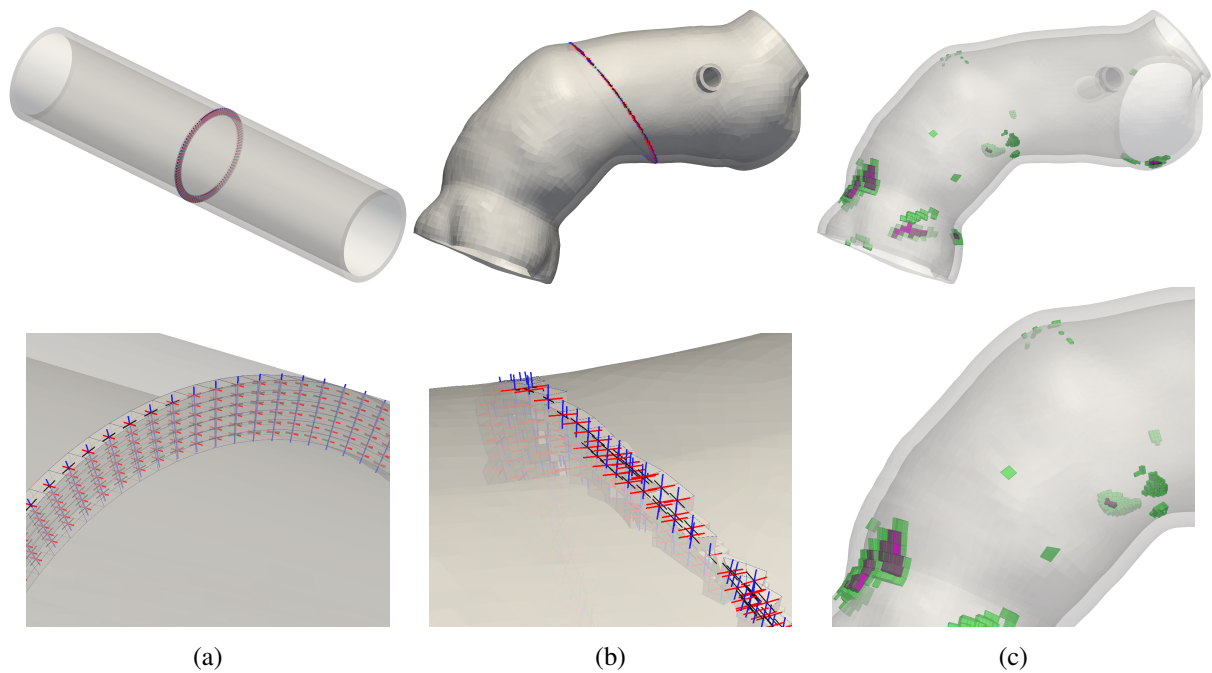|	c_1 [kPa]	c_2 [kPa]	c_3 [kPa]	κ [kPa]	Source
EAB	60.9	18.2	0.74	$2.39 \cdot 10^3$	Eqs. (6.97) and (6.98)
Soft catheter boundary material	c_1 [kPa]	c_2 [kPa]	c_3 [kPa]	κ [kPa]	Source
	$1.25 \cdot 10^3$	$-0.3 \cdot 10^3$	$0.08 \cdot 10^3$	$49.2 \cdot 10^3$	[182]
Catheter	E [kPa]	ν [-]			Source
	$48.0 \cdot 10^3$	0.475			[74]

Figure 6.8.: Mapping patient-specific quantities to the computational mesh, showing the whole model (top) and a zoomed in region of interest (bottom). In terms of mapping of the fibers, (a) and (b) show the axial (red), circumferential (black) and the radial (blue) directions of a strip of elements through the occlusion site, seen to obey the defined vessel geometry and not the element orientation. Calcification mapping yielded calcified lesions in the transitional zone (green) and those representing pure calcifications (purple), cf. Eq. (6.96).

6.2.5. Mapping of patient-specific quantities

Two patient specific quantities had to be mapped to the FE discretization of the patient-specific aortic wall, namely the fiber directions and calcific parts of atherosclerotic lesions, simply referred to as calcifications.

To add the patient-specific calcifications to the wall elements, the CT data were used to determine the average voxel HU value corresponding to a FE at the same point in space, mapped to the element centroid, cf. Section 6.2.3.2. Having the element-specific HU value enabled its relation to increased stiffness brought about by the presence of calcifications in the aortic wall, as defined by Eq. (6.94) and (6.96). The results of the calcification mapping are shown in Figure 6.8a.

In order to model the two main families of collagen fibers occurring in the aortic wall, it was necessary to determine the local circumferential, axial and radial directions throughout the aortic wall [124]. By fitting a centerline through the patient-specific lumen geometry using Mimics 16.0 (Materialise, Leuven, Belgium), the shortest distance between the element center and the centerline, as well as the tangent to the centerline was used to calculate and map the circumferential, radial and axial directions accordingly to each finite element representing the aortic wall. According to these directions, the fiber-direction for each element in the patient-specific mesh can be determined, as shown in Figure 6.8a, as is needed for the fiber directions of the Humphrey model, cf. Eq. (6.92). The results of the fiber mapping, or rather determining the local circumferential, radial and axial directions for each element are shown in Figure 6.8b. It must be noted that no direct measurements of the patient-specific fiber directions were made, but were rather based

on experimental data indicating clear trends of collagen fiber distribution in the region of the ascending aorta relative to its circumferential, radial and axial directions, cf. Section 6.2.2.2.

6.3. Fluid mechanics

6.3.1. Kinematics and constitutive relations

In the Eularian/spatial approach used to formulate the kinematics of the flow problem, fluid flow is considered from the perspective of an observer situated at a fixed spatial point. Flow is therefore described in terms of the velocity vector of a particle passing through the fixed point $\boldsymbol{v}$ in the spatial configuration. The acceleration of this particle can be described through the spatial/material time derivative as,

$$\dot{\boldsymbol{v}}(\boldsymbol{x}, t) = \frac{\mathrm{D}\boldsymbol{v}}{\mathrm{D}t}(\boldsymbol{x}, t) = \frac{\partial \boldsymbol{v}}{\partial t} + \frac{\partial \boldsymbol{v}}{\partial \boldsymbol{x}} \frac{\partial \boldsymbol{x}}{\partial t} = \frac{\partial \boldsymbol{v}}{\partial t} + \boldsymbol{v} \cdot \boldsymbol{\nabla} \boldsymbol{v} \qquad (6.99)$$

Here, the first term describes the local time derivative that vanishes in the steady state, while the last term describes the convective rate of change.

An additional essential kinematic quantity to be considered is the strain rate tensor defined as,

$$\boldsymbol{\varepsilon}(\boldsymbol{v}) = \frac{1}{2} \big[\boldsymbol{\nabla} \boldsymbol{v} + (\boldsymbol{\nabla} \boldsymbol{v})^{\mathrm{T}} \big] . \qquad (6.100)$$

The constitutive relation for a Newtonian fluid can be defined with the help of this strain rate tensor of as,

$$\boldsymbol{\sigma} = 2\mu_{\mathrm{f}} \, \boldsymbol{\varepsilon}(\boldsymbol{v}) - \bar{p} \boldsymbol{I} \qquad (6.101)$$

with μ_{f} being the dynamic viscosity and $\bar{p}$ the hydrostatic pressure of the fluid.

6.3.2. Governing equations

The incompressible Navier-Stokes equations utilized for modeling blood flow are based on the local conservation of mass and linear momentum. Although time varying effects are now accounted for, these balance equations are constructed similarly to their structural counterparts, of which the details are omitted. With the help of defining the kinematic viscosity $\nu_{\mathrm{f}} = \mu_{\mathrm{f}}/\rho$ and the kinematic pressure $p = \bar{p}/\rho$, and using Eq. (6.100), a density-scaled strong form of the incompressible Navier-Stokes equations in the absence of body forces are given in the convective form by,

$$\frac{\partial \boldsymbol{v}}{\partial t} + \boldsymbol{v} \cdot \boldsymbol{\nabla} \boldsymbol{v} - 2\nu_{\mathrm{f}} \boldsymbol{\nabla} \cdot \boldsymbol{\varepsilon}(\boldsymbol{v}) + \boldsymbol{\nabla} p = 0 \qquad (6.102)$$

$$\boldsymbol{\nabla} \cdot \boldsymbol{v} = 0 \qquad (6.103)$$

with the former describing the conservation of linear momentum, while the latter describes the continuity condition. Combining these with the initial and Dirichlet and Neumann boundary conditions,

$$\boldsymbol{v}_0 = \boldsymbol{v}(t=0) = \hat{\boldsymbol{v}}_0 = 0 \qquad \text{in } \Omega \qquad (6.104)$$

$$\boldsymbol{v} = \hat{\boldsymbol{v}} \qquad \text{on } \Gamma_u \qquad (6.105)$$

$$(1/\rho) \boldsymbol{\sigma} \cdot \boldsymbol{n} = \hat{\boldsymbol{t}} \qquad \text{on } \Gamma_\sigma \qquad (6.106)$$

yield the initial boundary value problem (IBVP) to be solved for.

6.3.3. Numerical solution

In the following section, certain key aspects required to numerically solve the above-stated IBVP is considered, including the Finite Element (FE) formulation and the specialized boundary conditions employed.

6.3.3.1. Finite Element method for fluids

As with the structural problem considered, the strong form of the IBVP given by Eq. (6.102) to (6.106) is reformulated in terms of the weak form by considering the integral form, weighted with appropriate test functions identifiable as variations of the velocity and the pressure fields, i.e. δv and δp. Since no special additional method peculiarities were considered and the derivation having been done extensively elsewhere, e.g. Donea and Huerta [93] or the dissertation by Gamnitzer [119], the derivation and formulation of the residual-based variational multiscale (or stabilized) finite element method used is omitted here.

It is worth mentioning that this stabilized fluid FE approach used, considered standard inf-sup stable *Q1P1*-elements and featured stabilization terms such as streamline upwind Petrov-Galerkin, pressure-stabilizing Petrov-Galerkin and grad-div terms, because turbulence effects were not considered.

6.3.3.2. Specialized boundary conditions

The Dirichlet boundary conditions for each simulation, defined by Eq. (6.105), consisted of a parabolic velocity profile prescribed on the inflow boundary and no-slip conditions prescribed for all non-moving wall boundaries where flow was not allowed to cross, i.e. $v = 0$. WSS was evaluated on all arterial wall boundary nodes and calculated as the tangential component of the traction vector at these no-slip nodes. The Neumann boundary conditions for each simulation, defined by Eq. (6.106), consisted of applying zero traction on the outflow boundary, since each simulations only has a single inflow and single outflow boundary surface. Instabilities in the flow velocity occurring at the outflow boundaries due to recirculating flow patterns were penalized according to a novel method based on utilizing the normal component of velocity at the boundary, described in Gravemeier et al. [138], which effectively stabilizes flow entering the domain at outflow boundaries without the without requiring additional constraints.

6.4. Modeling of selected manipulation maneuvers disrupting physiological hemodynamics

6.4.1. Geometry, FE discretization and boundary conditions

As in the concomitant structural section above, the following section gives an overview of how the geometries were obtained, the computational FE meshes constructed for the different models considered, followed by a brief consideration of the mesh requirements. Detailed information pertaining to all fluid simulations considered is given in Appendix A.2.

6.4.1.1. Aortic lumens

The same inner (luminal) diameter was chosen for the fluid simulations considering an ideal aortic geometry as for the structural wall, i.e. 29.7 mm, cf. Section 6.2.1.1. A vessel luminal length of 60 mm was used with each cannula considered, with the following exceptions: the incompletely clamped artery and the shielded, backward-facing simulations, see Table A.4, required longer lumen domains. The meshing of the luminal geometry is described in the following subsection.

For the patient-specific considerations of cannular flow through a straight, end-hole cannula, the deformed luminal geometry extracted from the cross-clamping simulations $CC_{0°}^{\text{Calc},1}$, $CC_{30°}^{\text{Calc},1}$ and $CC_{60°}^{\text{Calc},1}$

were used, cf. Section 6.2.1. All of these simulations started with a straight end-hole cannula at the same position, sharing nodes at the cannula-vessel interface, which was free to move during cross-clamping. The resulting ascending aorta luminal geometries investigated are shown repeatedly in Section 9.2, exemplary in Figure 9.9.

The boundary conditions applied to the patient-specific models were analogous to those used for the idealized aorta, i.e. parabolic inflow profile entering the cannula, no-slip boundary at the cannula walls, vessel wall and truncated occlusion region and the stabilized outflow Neumann boundary condition at zero pressure, cf. Section 6.3.3.2.

6.4.1.2. Cannulas

A series of simulations were performed to comprehensively evaluate the impact of cannular flow in terms of cannula orientation, insertion depth, clinically available cannula tips design and the influence of cannular flow on an incompletely clamped aorta. Simulations performed and corresponding geometry and discretization details are listed in Tables A.3 and A.4, respectively. For a visual representation of the cannula tips considered, see Figure 8.2. The simulations performed are indicated under "Simulation abbr.", as will subsequently be referred to.

All geometries were created in Cubit 13.1 (Sandia National Labs., Albuquerque, NM, USA) and 3-Matics 8.0 (Materialise, Leuven, Belgium) and exported as an STL-geometry. This geometry was then meshed in Harpoon 5.0 (Sharc Ltd., Manchester, UK) with a hexahedral-dominated hybrid mesh, i.e. consisting of hexahedral, wedge, pyramid and tetrahedral shaped elements. A fine boundary layer mesh was included on the aortic wall and cannula inner surfaces, respectively, as specified in Table A.3. Specific mesh refinement zones were applied to specifically resolve the flow in the cannula itself, as well as the jet exiting the cannula until it hit the aortic wall for the first time. Furthermore, apart from a base mesh level size assumed for the rest of the fluid domain, the bottom aortic wall, cannular inflow, cannular inner surface and vessel outflow surface received a higher refinement of its lateral edge length. Similar to the process described in Maier [222], this mesh was then imported into IcemCFD (Ansys, Canonsburg, PA, USA), where nodesets were specified and exported as an exodus-type file fully describing the mesh and various nodesets. Similar as with the structural models, these exodus-type files along with appropriate boundary conditions and material models and corresponding parameters were used to construct the input file for the FE solver, *BACI*.

To evaluate cannula orientation, a straight, end-hole cannula $Endh_{\mathrm{str}}$ was orientated in 6 different directions (or incidence angles), namely $Endh_{\theta_{\mathrm{trans}},\theta_{\mathrm{long}}}$, for $(\theta_{\mathrm{trans}}, \theta_{\mathrm{long}}) = (0°, 0°), (0°, -30°), (30°, -30°), (30°, 0°), (30°, 30°), (0°, 30°)$, with $Endh_{0°,0°} \equiv Endh_{\mathrm{str}}$ These angles respectively indicate the transverse and the longitudinal cannulation incidence angles with respect to the cannula axis orientated perpendicular to the vessel axis.

The cannula depth was evaluated considering the same cannula, pointing straight downwards, but at four different insertion depths, namely $Endh_{\mathrm{d},i}$ for the insertion depths $i = -5, 0, +5, +10$ mm, where $Endh_{\mathrm{d},0} \equiv Endh_{\mathrm{str}}$.

For simple comparative reasons, physiological flow through this idealized aorta was also simulated $Phys_{hb}$ using the same mesh used in $Endh_{\mathrm{str}}$. Here, a parabolic-profiled patient-specific inflow entering through the vessel was considered as extracted from [196], yielding an average flow rate of 3.37 l/min.

The influence of different cannula tip designs was evaluated by considering the following different cannula tips (given here with the corresponding short simulation names): a straight end-hole cannula $Endh_{0°,0°}$ (considered above), a forward-facing (downstream-pointing) curved end-hole cannula $Endh_{\mathrm{curv}}$, a straight side-hole cannula $Side_{\mathrm{str}}$, a curved side-hole cannula $Side_{\mathrm{curv}}$, a straight hybrid cannula $Hybr_{\mathrm{str}}$ and a curved hybrid cannula $Hybrid_{\mathrm{curv}}$. Furthermore, a novel shielded cannula design was derived from a patent by Murphy and Lilly [264] in an attempt to show the possibility of improved flow

from a new design not yet clinically available. It consisted of the same curved end-hole cannula used above, but now backwards-facing (upstream-pointing) with the jet pointing into a shield suspended in front of it, meant to disperse flow prior to hitting the aortic wall, namely $Endh_{\text{curv}}^{\text{sh}}$. The shield geometry was obtained by considering a circular disk with diameter of 15 mm and deforming it by fixing the center and pulling four points along its outer circumference away from its center in the direction of its axis, as shown in Figure 6.9. Based on a preliminary study of this configuration, the shield was also tilted downward at an angle of $7°$ in an attempt to reduce jet flow from hitting the upper vessel wall. All relevant dimensions and respective sources are indicated in Table A.4, while the different cannula tip designs are indicated in Figure 6.9.

To evaluate the influence of the large aortic deformation owing from aortic cross-clamping on the impact of the cannular flow, the following incompletely occluded, prestressed and pressurized aortic models were considered incorporating a straight end-hole cannula: the idealized aortic geometry for parallel cross-clamps $Endh_{\text{ic}}$, as well as the patient-specific geometry cross-clamped with standard clinically used (De-Bakey) cross-clamps at three different axial orientations of the clamps, namely $Endh_{\text{CC},0°}^{\text{patspec}}$, $Endh_{\text{CC},30°}^{\text{patspec}}$ and $Endh_{\text{CC},60°}^{\text{patspec}}$. The latter three simulations were performed with the cross-clamps at axial position 1, cf. Section 6.2.1.3. Further details pertaining to the simulations are given in respective sections presenting their results.

Throughout all these simulation, all models were built considering specific geometrical consistencies, including using the same idealized ascending aorta as was used for the structural simulations, a consistent distance between the cannulation site and the vessel outflow and the same cannula conduit length for every simulation considered.

6.4.1.3. Mesh requirements

Due to the complex flow conditions involved when considering a high-velocity jet hitting a non-flat surface, a mesh-convergence study was performed considering a straight end-hole cannula pointing perpendicular to the vessel axis. A representative mesh used for this investigation is shown in Figure 6.10.

The two most critical mesh parameters of interest were the base-level (or average lateral edge length) size h_{b} and the first (wall) element size h_{f}, i.e. the element thickness in the radial direction of the vessel. The boundary layer mesh covering the wall of the aorta had a lateral edge length equal to the base-level size, while the first element size, an expansion factor and number of layers was specified.

In order to investigate whether the jet reaching the opposite aortic wall was sufficiently resolved, base-level sizes of $h_{\text{b}} = 0.5, 0.75, 1.0, 1.25$ mm were considered. In order to investigate whether the WSS captured at the "jet-landing" site, first (wall) element sizes of $h_{\text{f}} = 0.05, 0.1, 0.2, 0.4$ were considered, while the expansion factor and number of layers were kept constant at 1.7 and 7, respectively.

The converged mesh size was accordingly applied for all cases of arterial cannular flow, i.e. for those considering the idealized and the patient-specific aorta.

6.4.2. Materials: Blood

As comprehensively reviewed by Nichols and O'Rourke [269], blood can be essentially considered as a suspension of red blood cells (RBCs or erythrocytes), white blood cells (WBS or leukocytes) and platelets (or thrombocytes) suspended in a blood plasma. The latter presents a viscous Newtonian character, i.e. the viscosity remains constant for all fluid shear rates – related to the strain rate of Eq. (6.100) by a given constitutive model. Most significant constituent that lends blood its non-Newtonian character are RBCs, which make up approximately 99% of the particulate matter in blood and account for 40–45% of blood by volume. The non-Newtonian, shear-thinning behavior of blood implies that at low shear rates, viscosity is high and *vice versa*. High apparent viscosity at low shear rates are attributed to cell aggregation

(a) $Endh_{\mathrm{curv}}$

(b) $Side_{\mathrm{curv}}$

(c) $Hybrid_{\mathrm{curv}}$

(d) $Endh_{\mathrm{curv}}^{\mathrm{sh}}$

(e) $Endh_{\mathrm{ic}}$

(f) $Endh_{\mathrm{CC},0°}^{\mathrm{patspec}}$
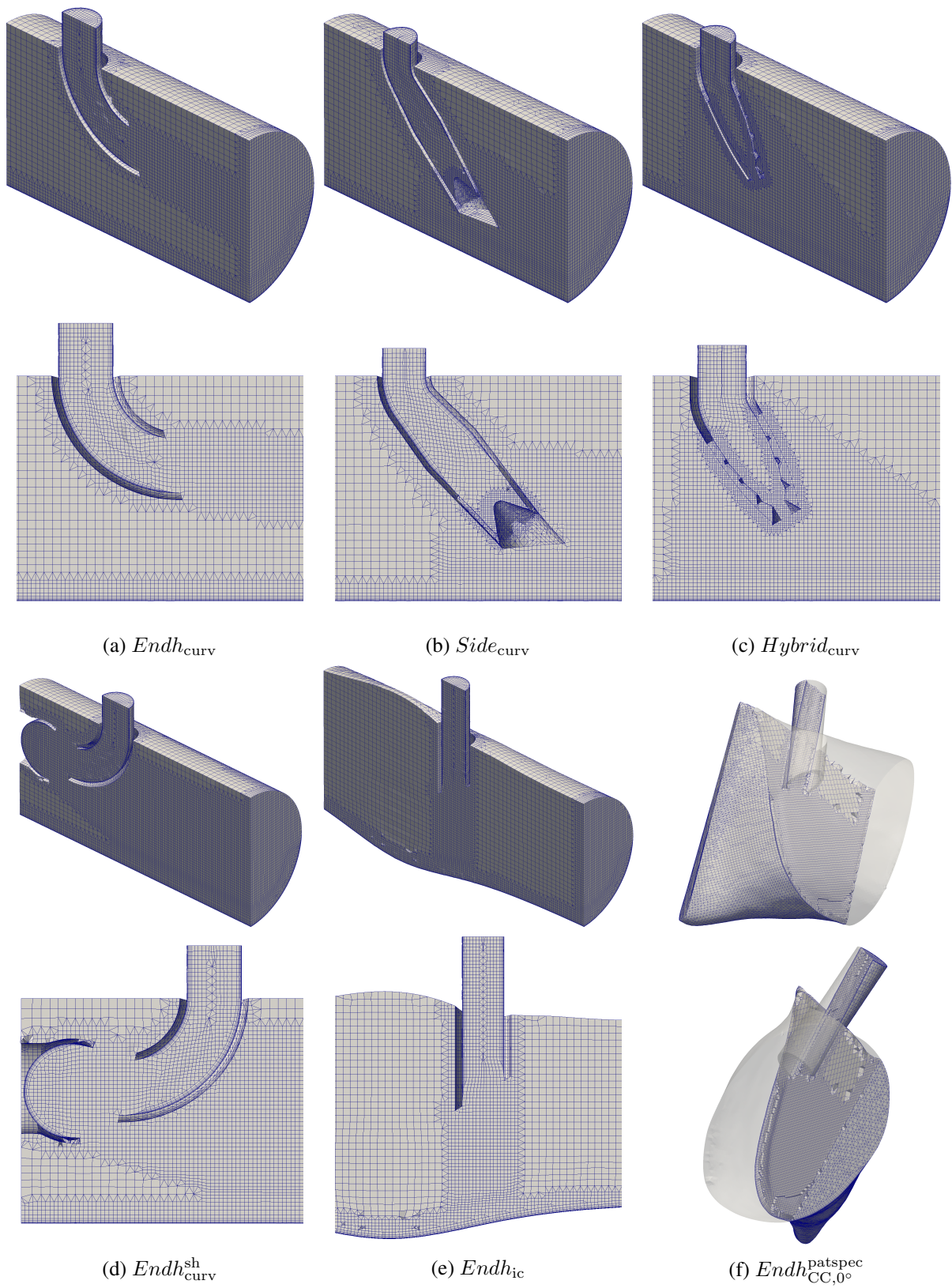
Figure 6.9.: The meshes used for representative examples of the different cannulas considered.

(a) Isometric view of axial cross-section

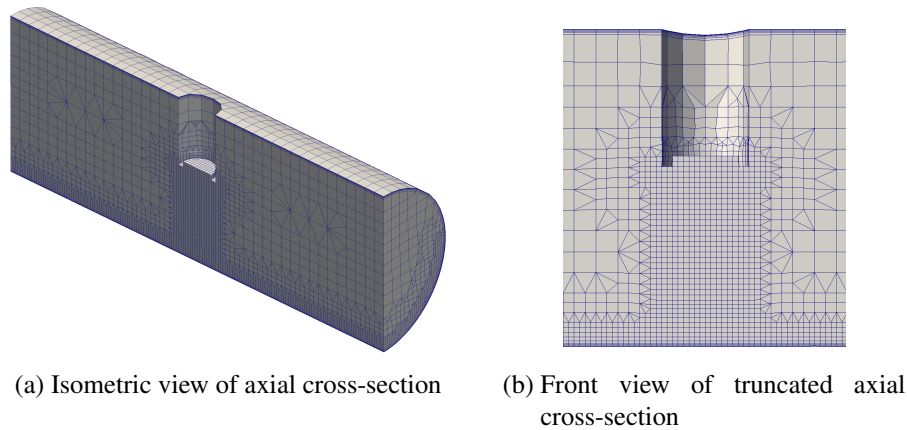(b) Front view of truncated axial cross-section

Figure 6.10.: A representative mesh used to investigate sufficient mesh resolution for resolving the jet prior to hitting the aortic wall and the WSS induced at the wall, indicating the first element size h_f and the base-level size h_b.

into Rouleaux-type structures, which are broken up under higher shear rates causing a effective drop in viscosity. At high shear rates, i.e. larger than $100\ \mathrm{s}^{-1}$, blood achieves its minimum viscosity value, μ_∞. Especially considering smaller vessels, i.e. smaller than 1 mm lumen diameter, noticeably larger non-linear effects of viscosity changes due to higher shear rates are observed in smaller vessels. The whole blood viscosity also increases according to an increase in hematocrit, i.e. percentage of RBC in blood per volume. Blood as a whole also exhibits an effective viscoelasticity, which is mainly attributed to the viscoelastic response of the RBCs itself. Due to these characteristics, blood is generally accepted to be a shear-thinning viscoelastic fluid.

From a modeling perspective, given the context of the flow considered and the phenomena of interest, certain simplifying assumptions have been shown to be justifiable in literature. Despite being a widely researched topic, only certain studies are mentioned as needed.

Investigating the non-Newtonian effects of pulsatile blood flow in large arteries, Gijsen et al. [131] considered experimental and computational setups of a blood analog fluid through a $90°$ bend. Upon experimental verification of computational non-Newtonian fluid models, a comparison of non-Newtonian to Newtonian models showed that for peak systole, i.e. peak forward flow, that the velocity gradients on the inner and outer curvature were practically identical, whereas considering the velocity profile of the Newtonian fluid presented a comparatively "dipped" shape. The authors suggested that it is due to a comparatively smaller characteristic viscosity of the Newtonian fluid used for the experiment. When rescaling the Newtonian to that of the non-Newtonian fluid, good agreement in velocity distribution was found. Furthermore, specific dimensionless measures were evaluated that are indicative of the influence of viscoelastic effects on the velocity distribution. Since these measures were found to be well below a critical value, the effect of viscoelastic effects were considered negligible.

In contrast to the clearly apparent differences mentioned above, much less apparent differences between Newtonian and non-Newtonian models have been reported [178, 278], and are expected to only occur for a fraction of the cardiac cycle when recirculation causes low shear rates. This behavior holds for the above-mentioned threshold of blood being characterizable by Newtonian flow for shear rates larger than $100\ \mathrm{s}^{-1}$. A comparative numerical study between these different models undertaken in the context of complex patient-specific geometries also revealed the negligible influence that the consideration of a non-Newtonian fluid has in this context, except in areas of recirculation where low shear rates occur [19]. In such areas, WSS is usually underestimated.

The arterial cannular flow hemodynamics of interest in this investigation features continuous, high velocity flow in large bore conduits where shear rates are expected to be very high. Furthermore, arterial cannula technical data released and most experiments considered use either water or a water/glycerin mixture as working fluid, cf. Section 3.1.2. Therefore, considering all the reviewed information and wanting to evaluate macro effects of flow, it was deemed reasonable to model blood as a Newtonian fluid, cf. Eq. (6.101) in the context of considering the local influence of arterial cannular flow on WSS and velocity distribution entering the aortic arch. In the latter equation, the dynamic fluid viscosity μ_f can be considered equivalent to the dynamic viscosity of a non-Newtonian fluid where maximum shear thinning has already occurred, taken as a constant $\mu_\infty = 0.004$ g/mm s and a constant density $\rho_f = 0.00106$ g/mm^3, according to values for blood previously reported in a similar study [196].

7. Aortic occlusion: comparison of existing and new techniques

Je le pansai, Dieu le guérit.

— Ambroise Paré

From all the experimental studies reviewed in Sections 2.1.1, 2.2.1 and 2.3.1, it can be deduced that current experimental knowledge of iatrogenic injury during aortic occlusion, regards its main consequence as the injury induced at the pinching regions. General disturbance of certain structural components of the aortic wall has also been reported *a posteri*, e.g. endothelial erosion, spongy or inflammatory lesions of the media and adventitia etc. However, the location of these disturbances relative to the occluder configuration (location and orientation) is mostly omitted. Consequently, clinicians are faced with the often unavoidable need to perform aortic occlusion, while lacking in-depth knowledge pertaining to the injury mechanisms and its progression. This has even lead some to propose theories on how to safely occlude a vessel, probably based purely on intuition 2.1.2. In this regard, computational evaluations have played and will play a significant role in gaining insight into the detailed mechanisms by which injury to the aortic wall might be induced and progress by the occluder.

In this chapter, a solid structural computational study is performed to consider different occluders in the context of occluding an idealized aorta. The specific aim is to evaluate the performance of different occluders – existing and newly proposed – in the absence of patient-specific variability. The models evaluated here have been introduced in Section 6.2. The structure of this chapter consists of a review of previous studies in this regard, the formulation of functional requirements for optimal aortic occlusion, the introduction of a novel occlusion technique and the consideration of requirements that have often been neglected in past studies. Thereafter, the computational results are presented and comparatively evaluated, followed by an in-depth discussion of the overall performance of the different occluders, other general findings, limitations and ended with concluding remarks and future perspectives.

7.1. Existing computational perspectives

Recently, computational models have shed a much more detailed light on additional potential mechanisms of the injury difficult to identify and quantify experimentally. However, the number of such investigations is limited, with only a few cross-clamping investigations performed, while no previous computational investigation has explicitly considered *endo-aortic balloon occlusion* (EABO).

7.1.1. Previous cross-clamping investigations

Probably the most simplified computational evaluations of cross-clamping were performed by Chen et. al [62, 63], considering a 2D fluid-structure-interaction (FSI) setup of a vessel being clamped. However, some fundamental scientific concerns arise when considering these investigations, including the use of a 3D material model in this 2D setup, no vessel pressurization or prestressing, as well as the unaddressed issues pertaining to the highly deformed, coarse mesh of the fluid domain. Therefore, the usefulness of these outcomes is limited and not further considered.

Evaluation of cross-clamping an idealized aorta, similar to the one considered in this chapter, has previously been investigated to a limited extent, as expanded in the following.

Gasser et al. [124] considered a two-layered tube, representing the media and adventitia, from which the material parameters were obtained experimentally from a human coronary artery (left anterior descending). A two-fiber Holzapfel-type model was used, cf. Eq. (6.84). The residual stress present in the unloaded configuration was modeled and pressurized up to systolic blood pressure. A linear, mixed FE element formulation (three-field variational principle) was used, discretized with eight elements in the radial direction. The main finding was made by considering the stress at a point on the intimal surface at a non-pinched site along the circumference: whereas the normalized circumferential stress was slightly reduced upon clamping, the normalized axial stress increased four-fold relative to that of the physiologically modeled value. This is especially significant considering that the dominant collagen fiber distribution in the media is mainly orientated in the circumferential (not axial) direction, implying that the matrix substrate (elastin) will bear most of the load and very likely experience critical loading. Furthermore, the largest component of the axial loading will be carried by the adventitia. This finding is significant, especially considering the body's low turnover-rate of elastin and that this phenomenon was not known prior to this publication. However, the extent to which this finding is influenced by the discontinuity in stress through the thickness of the vessel due to the two-layered approach is unknown. Furthermore, the vessel was not completely occluded, leaving severity of compressive stresses due to intimal self-contact and the according pinching site impact unexplored.

Calvo et al. [54] repeated the simulations of Gasser et al. [124], but now incorporated an uncoupled damage model into the material model of the aortic wall. Uncoupled in this context refers to the fact that the damage in the fibers and matrix substrates were independent of each other. Although it is unclear whether residual stresses were accounted for, their results yielded the expected softening effect. Consequently, the resulting normalized axial stress considered above, was now only increased by 3.6 times its unoccluded value (as opposed to the above-mentioned four-fold increase). This uncoupled damage model confirmed the dangers of matrix substrate injury by Gasser et al. [124], since the main component of damage was obtained for the matrix substrate, while practically absent in the fibers.

More recently, Famaey et al. [103] also presented results of a computational study investigating cross-clamping, principally evaluating a 0.2 mm long tube-segment, but also considering a longer tube of 4 mm. The authors considered a Holzapfel-type model which included fiber dispersion, cf. Eq. (6.85). Material parameters were fitted to a series of experiments of rat abdominal aortas. Residual stresses were accounted for, similar to the strategy followed by Gasser et al. [124]. Reduced integration elements in the software package Abaqus Explicit (Dassault Systemes, Waltham, MA, USA) were used, i.e. the so-called *C3D8R* elements, which in contrast to the F-bar elements considered in this dissertation, cf. Section 6.1.4.3, evaluate *both* the volumetric and isochoric components only at a single integration point in the element center. The main findings from this study was basically the evolution of circumferential stress at different sites in the tube-segment, as well as the effect of varying material parameters and clamp surface profile. Furthermore, for the longer tube, a peak in radial stress at the pinching site and a small increase of the axial stresses were also observed, although the increase relative to the physiological load was not reported. While the vessel appears to be completely occluded, no mention was made of the intimal self-contact considerations, the level of occlusion, compressive stresses upon occlusion or whether occlusion would have occurred. In a later study by the same group [104], constituent-specific damage was incorporated in the material model. However, in re-performing these clamping simulations, only the damage of the SMC component was considered and the results were not quantitatively compared to the previous study. As such, the value of those results in this context is limited. Although they claim that their computational model was validated by their experimental results, the presented curves comparing their experiment to their model, i.e. the applied clamp force (cf. Fig. 12 [103]), shows a clearly unconvincing trend. This large deviation of the experimental from the computational outcome can be attributed to a number of factors.

These factors include the fact that a different rat abdominal aorta was clamped compared to the ones from which the material parameters were obtained, FE element technology which exhibits an overly soft behavior in bending [85] that is clearly evident in cross-clamping, the accuracy of the contact formulation used, the choice of bulk modulus, etc. Therefore, their statement claiming that the computational model was fully validated based on a single, potentially variable measure that poorly coincides with experimental results, needs to be considered with the needed reservation.

Finally, it is worth noting that all of these studies considered only frictionless contact of parallel clamps, using node-to-segment approaches for evaluating contact and a penalty strategy to enforce the contact constraints (or at least as could be deduced from the supplied information), in contrast to the mortar methods with the use of Lagrangian multipliers used in this dissertation, cf. Section 6.1.4.5. Mortar methods have the advantage over node-to-segment methods of being variationally consistent by enforcing the contact constraints over the entire surface and not just at the contact nodes. Furthermore, problems can be encountered on coarsely segmented kinked surfaces, as well as in nodes dropping over edges during the simulation, cf. [133].

7.1.2. Previous EABO investigations

As far as the author could determine, no previous computational studies have been performed to explicitly consider EABO. Procedures with a similar configuration compared to EABO includes angioplasty, coronary stenting and carotid stenting procedures, which have often been considered in a computational setting, e.g. [54, 123].

However, it should be noted that some fundamental comparative differences between these procedures and EABO exist. These differences include the fact that such balloons are much longer than its inflated diameter and feature an inflation dominated by (cylindrical) radial expansion only, compared to EABO consisting of a spherical balloon with an expanded diameter in the same range as the balloon length. This ratio between expanded balloon diameter and length is determinant of balloon stability, which seems to not be worth considering in the angioplasty/stenting applications owing to the fact that balloon contact is frequently considered as frictionless. In contrast, the influence of frictional contact of a spherically expanding balloon during EABO becomes more important, as taken into account in this dissertation.

Therefore, due to these fundamental differences, no studies were found that yielded useful comparisons with regards to the proposed endo-aortic balloon (EAB) model used in the current investigation, cf. the proposed , Section 6.2.1.3.

7.2. Functional requirements for optimal aortic occlusion

The detailed review of large deformation aortic manipulation in Chapter 2 allows for the formulation of functional requirements that need to be fulfilled by an optimal aortic occlusion technique. Therefore, a safe, efficient and reliable aortic occlusion technique should:

1. Minimize vessel damage by ensuring

    a) the minimization of strains exerted in the aortic wall,

    b) the maximizing the potential of occlusion occurring,

    c) a low and uniform distribution of the occlusive load exerted in the aortic wall;

2. Provide stable and therefore reliable occlusion;

3. Enable the clinician to accurately position the occluder in the *in vivo* configuration of the vessel;

4. Minimize the total intimal surface disruption;

5. Enable the clinician to determine whether the vessel is occluded and when its occluded for the first time during occlusion, using only clinically determinable parameters;

6. Minimize deformation of the vessel;

7. Be simple, meaning that it should

   a) maintain or decrease standard occlusion and CPB times,

   b) Prevent cluttering (take up as little space of the surgical field as possible);

8. Be cost-efficient.

Therefore, a vascular occlusion technique is required that minimizes damage, that disrupts as little of the intima as possible and allows for a known occlusion at the desired location at the minimum required occlusive load. Furthermore, it should be stable, simple and cheap. Throughout of the rest of this chapter, these functional requirements will be repeatedly referenced in line with evaluating the performance of existing and new occlusion techniques.

7.3. Novel occluder design: Constrained endo-aortic balloon occlusion (CEABO)

A novel solution for safer, more efficient and more reliable aortic occlusion proposed here, is the use of the "DEVAAL-constrainer" that will henceforth only be referred to as the "constrainer". It is a device to be used in conjunction with EABO. Furthermore, the occlusion technique of using the constrainer with EABO will be referred to as *constrained endo-aortic balloon occlusion* (CEABO). The ultimate function of the constrainer is to make EABO safer and more reliable, without over-complicating it, while providing efficient occlusion of the vessel.

The constrainer is basically a thin, bendable but inextensible strap (or band) that can be wound around the vessel to be occluded and fixed at a desired diameter. The configuration of the constrainer around the vessel during EAB inflation, as well as the demonstration of its main functionality, is shown in Figure 7.1, while the three design variations tested in this dissertation have already been shown in Figure 6.3. The dimensions of these variations are indicated in Table A.2.

By winding and fixing the constrainer around the vessel at the site where the EAB will be inflated, the constrainer acts as an external constraint against the expanding vessel due to EAB inflation. This is evident from Figure 7.1, when considering how much less the vessel is deformed during CEABO compared to EABO. Thereby, as will be demonstrated quantitatively in more detail below, the constrainer also significantly limits the damaging strain induced in the vessel, while simultaneously enabling the occluder to more efficiently apply the force to the vessel that is needed to occlude it – the occlusive load.

7.4. Requirements complicated to evaluate and those neglected in prior investigations

Alone from the literature reviewed, it is clear that only considering the damage or potential of damage is not sufficient to evaluate the complete safety, efficiency and reliability of any occluder – whether existing or new. For the sake of argument, consider a hypothetical cross-clamp design that induces less damage
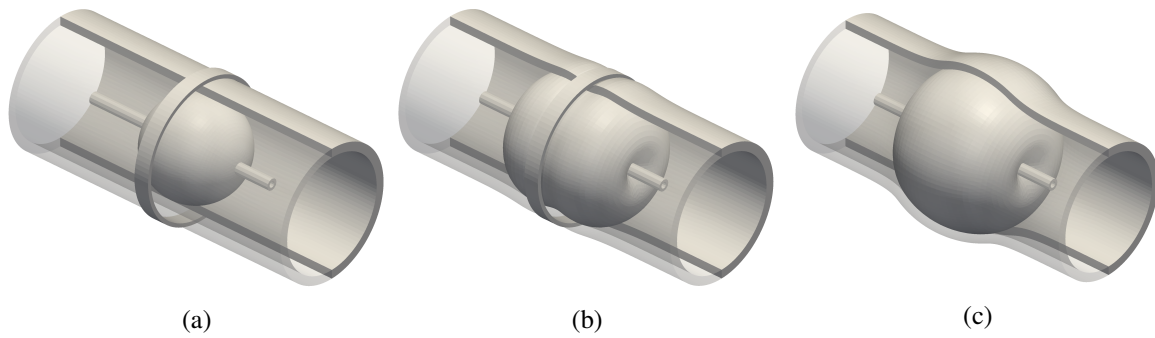
(a) (b) (c)

Figure 7.1.: The proposed new device concept for safer, more efficient and more reliable aortic occlusion: the DeVaal-*constrainer* (abbreviated as *constrainer*), showing (a) its basic configuration prior to EAB inflation, i.e. CEABO, (b) CEABO after inflation and (c) without the constrainer, i.e. EABO.

during clamping than current designs, but which possesses clamp-arms that are unable to stretch transversely across the entire aortic wall. Consequently, this "safer" cross-clamp would be utterly useless, since it would not be able to occlude the vessel.

Exactly for this reason, the comprehensive functional requirements of a safe, efficient and reliable occluder have been formulated in the preceding section so that every occluder can be evaluated based on *all* its required functionalities. While the final resulting damage or the potential of damage has held the predominant, if not exclusive, focus of the reviewed investigations, some aspects have remained largely neglected or proven complicated to evaluate.

These aspects will be considered in the following subsections and be evaluated throughout the rest of this dissertation with a previously unreported level of detail.

7.4.1. Occlusion

In the following, a computational post-processing strategy is presented to evaluate the potential of occlusion occurring during the application of an occluder. The main reason for evaluating such a measure is to evaluate the ability of an occluder (the medical instrument) to occlude a vessel in relation to the impact that the occluder has on the vessel upon its application, i.e. a measure of the occlusion performance. By knowing this ability, its occlusive efficiency can be evaluated based on how well it was able to occlude relative to the amount of strain that was induced in the vessel wall.

As far as the author could determine, whether or not a vessel is actually occluded, or to what extent or level it has been over-occluded is hardly even mentioned in the reviewed experimental and computational investigations. Here, over-occlusion, or the level thereof, can be defined as the occlusive load applied above and beyond that which is necessary to achieve occlusion. In an experimental setting, occlusion itself may be trivial, assumed or left unevaluated, while over-occlusion is seldomly considered, with the exception of two older studies investigating the existence of a *minimum vascular occlusive force* (MVOF) [94, 337]. Even the most sophisticated experimental studies to date investigating occlusion-related aortic damage neither elaborated on occlusion nor over-occlusion – only possibly providing some information on the occlusive load, i.e. the notch level/ clamping force [18, 102, 225, 226] or an EAB pressure range [8, 106]. Similarly, previous computational studies have also neglected occlusion or the level thereof. Understandably, the evaluating of occlusion in a computational setting is not trivial, but will be considered in detail below.
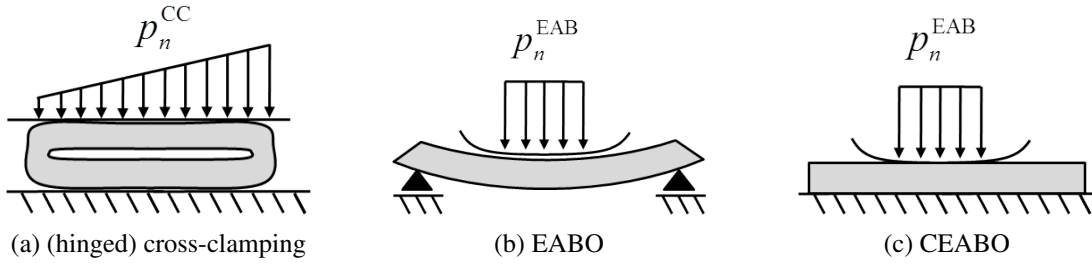
Figure 7.2.: A depiction of the fundamental differences of occluder loading configurations, showing the expected normal contact pressure p_n applied by each occluder, as well as simplified boundary conditions.

The occlusive load, in this context, purely refers to the load that the occluder applies on the vessel in order to occlude it – it does *not* indicate whether or not a state of occlusion was reached. The level of occlusion can be defined as the first instance that the occlusive load will result in occlusion, and any occlusive load beyond that. In other words, the level of occlusion would be a parameter that describes the additional load that the occluder applies to the vessel after occlusion has occurred for the first time. However, such a global measure is difficult to define, because the occlusive load applied by the occluder on the vessel is not necessarily directly related to whether the level of occlusion is increased. This is clear from the hypothetical example given at the start of this section and also when considering the different configurations by which various occluders apply a load on the vessel, i.e. cross-clamps apply an external displacement-driven load via two flat rigid surfaces moving on a hinged rotation, while EABO applies an internal, distributed, pressure-driven load from the EAB spherically expanding from within the vessel. Furthermore, CEABO applies the same load as EABO, but also provides additional external (to the vessel) constriction of the spherically expanding EAB, as depicted in Figure 7.2 for the different configurations. A comparative measure is required that is independent of the occluder configuration or vessel properties. Another hindrance to defining and evaluating a parameter considering the level of occlusion is that it is dependent on the unknown instance that occlusion first occurs, i.e. the occlusion threshold.

The difficulty of evaluating the level of occlusion or whether occlusion has occurred is circumvented by proposing a measure of *occlusion potential*, p_n^{occl}. This measure is defined as the maximum contact pressure (normal contact traction) represented by a continuous contour line of contact pressure exerted on the intima, circumnavigating the lumen of the vessel, forming a closed line. In other words, the potential of occlusion only exists when there exists a non-zero contact pressure that stretches across the entire lumen circumference, which forms a closed line. The referred to contour lines connect regions of the same contact pressure, as depicted in Figure 7.3a,b, and defined as follows,

$$\mathcal{S}_c = \left\{ \mathcal{C}(p_n) \mid 0 < p_n < \max(p_n) \right\} \tag{7.1}$$

$$\mathcal{S}_c^{\text{closed}} = \left\{ \mathcal{C}(p_n) \in \mathcal{S}_c \mid \text{CIRCUMNAVIGATED, CLOSED} \right\} \tag{7.2}$$

$$\mathcal{S}_c^{\text{open}} = \mathcal{S}_c \setminus \mathcal{S}_c^{\text{closed}} \tag{7.3}$$

$$\mathcal{P}^{\text{closed}} = \left\{ p_n \mid \mathcal{C}(p_n) \in \mathcal{S}_c^{\text{closed}} \right\} \tag{7.4}$$

$$p_n^{\text{occl}} = \max(\mathcal{P}^{\text{closed}}) \tag{7.5}$$

where $\mathcal{S}_c$ is the set of all possible contour lines (or curves) $\mathcal{C}$ formed by the contact pressure p_n on the luminal (intimal) surface, $\mathcal{S}_c^{\text{closed}}$ is a subset of $\mathcal{S}_c$ that form a closed lines that have circumnavigated the luminal surface, i.e. *valid lines along which occlusion can occur*. Contour lines that do not fulfill the criteria of Eq. (7.2), are indicated as invalid or $\mathcal{S}_c^{\text{open}}$. Furthermore, $\mathcal{P}^{\text{closed}}$ is the set of contact

pressure values corresponding to each contour line in $\mathcal{S}_c^{\text{closed}}$, where the occlusion potential p_n^{occl} is then the maximum value of contact pressure from this set.

Practically, to enable the automatic extraction of the occlusion potential required a precise definition of Eq. (7.2). Given ideal alignment of the idealized aortas relative to the global Cartesian axes (x and y are orthogonal to the vessel axis in z-direction), allowed a relatively simple, though coarse, strategy to obtain the valid lines along which occlusion can occur, i.e. $\mathcal{S}_c^{\text{closed}}$, by using a simple bounding box BB as follows,

$$\mathcal{Q}_c = \left\{ q \mid q \in \mathcal{S}_c \right\} \tag{7.6}$$

$$\mathcal{Q}_{c,1} = \left\{ q \in \mathcal{Q}_c \mid q_x > BB_{x,\max} \right\}; \quad \mathcal{Q}_{c,2} = \left\{ q \in \mathcal{Q}_c \mid q_x < -BB_{x,\min} \right\};$$
$$\mathcal{Q}_{c,3} = \left\{ q \in \mathcal{Q}_c \mid q_y > BB_{y,\max} \right\}; \quad \mathcal{Q}_{c,4} = \left\{ q \in \mathcal{Q}_c \mid q_y < -BB_{y,\min} \right\} \tag{7.7}$$

$$\mathcal{S}_c^{\text{closed}} = \left\{ \mathcal{C}(p_n) \in \mathcal{S}_c \mid \exists q_1 \in \mathcal{C}(p_n) : q_1 \in \mathcal{Q}_{c,1} \wedge \exists q_2 \in \mathcal{C}(p_n) : q_2 \in \mathcal{Q}_{c,2} \right. \tag{7.8}$$
$$\left. \wedge \exists q_3 \in \mathcal{C}(p_n) : q_3 \in \mathcal{Q}_{c,3} \wedge \exists q_4 \in \mathcal{C}(p_n) : q_4 \in \mathcal{Q}_{c,4} \right\}$$

These equations basically state that if one considers the set of points $\mathcal{Q}_c$, made up of every point q on every contour line in $\mathcal{S}_c$, cf. Eq. (7.6), then there potentially exists a subsets of points $\mathcal{Q}_{c,i}$ for $i = 1, 2, 3, 4$ with x-coordinates and y-coordinates of these subsets, q_x and q_y, respectively, that fall outside of a certain bounding box BB described by the near-extremes of the occluder coordinates, as illustrated in Figure 7.3d. If there exists points in a specific contour line contained within all four of these subsets, then it is included in $\mathcal{S}_c^{\text{closed}}$. To maintain simplicity of this method, all of evaluations of obtaining $\mathcal{S}_c^{\text{closed}}$ were performed with the given models in the reference configuration.

Based on the employed contact formulation, cf. Section 6.1.4.5, the contact tractions were only evaluated (and therefore only available) on the slave side. For the EAB-related occluders, the EAB-contact surface was chosen as the slave surface. Accordingly, considering an undeformed EAB outside radius $R_{\text{EAB,o}} = 12$ mm, the bounding box BB required in Eq. (7.7) was defined as $[-(R_{\text{EAB,o}} - h_{\text{x}}^{\text{closed}}), (R_{\text{EAB,o}} - h_{\text{x}}^{\text{closed}}); -(R_{\text{EAB,o}} - h_{\text{y}}^{\text{closed}}), (R_{\text{EAB,o}} - h_{\text{y}}^{\text{closed}})]$, which described a general bounding box according to $[\min(x), \max(x); \min(y), \max(y)]$, as illustrated in Figure 7.3d,f. Here, $h_{\text{x}}^{\text{closed}}$ and $h_{\text{y}}^{\text{closed}}$ describes the relaxation distance used to for the bounding box to sufficiently capture $\mathcal{S}_c^{\text{closed}}$. Naturally, due to the idealized problem setup, the length of the BB in the z-direction could simply be allowed to stretch along the entire vessel length.

Since the different cross-clamp simulations only had explicitly defined inner self-contact surfaces on the vessel lumen (intimal surface), it meant that contour lines were only evaluated on one half of the vessel. Accordingly, a contour line only had to have points in the first three subsets of points conditions to identify $\mathcal{S}_c^{\text{closed}}$. In other words, for cross-clamps, Eq. (7.7) became,

$$\mathcal{S}_c^{\text{closed}} = \left\{ \mathcal{C}(p_n) \in \mathcal{S}_c \mid \exists q_1 \in \mathcal{C}(p_n) : q_1 \in \mathcal{Q}_{c,1} \wedge \exists q_2 \in \mathcal{C}(p_n) : q_2 \in \mathcal{Q}_{c,2} \right. \tag{7.9}$$
$$\left. \wedge \exists q_3 \in \mathcal{C}(p_n) : q_3 \in \mathcal{Q}_{c,3} \right\}$$

Accordingly, considering an undeformed vessel with an inside radius of $R_i^{\text{v}} = 14.85$ mm, the bounding box was defined as $[-(R_i^{\text{v}} - h_{\text{x}}^{\text{closed}}), (R_i^{\text{v}} - h_{\text{x}}^{\text{closed}}); -(R_i^{\text{v}} - h_{\text{y}}^{\text{closed}}), 0]$, with the same general bounding box formulation as used above. Since these two explicitly defined surfaces were separated by a line of nodes, the maximum theoretical range that a $\mathcal{S}_c^{\text{closed}}$ could stretch in the x-direction, for the given discretization size of idealized aorta used, implied a minimum $h_{\text{x}}^{\text{closed}} = 0.0208$ mm. However, this requirement was relaxed to $h_{\text{x}}^{\text{closed}} = 4.85$ mm, in order to sufficiently distinguish between the differences in $\mathcal{S}_c^{\text{closed}}$, and therefore in p_n^{occl}, that occurred due to variation in the hinge configuration of the cross-clamps. The relaxation in the y-direction could be made stricter, chosen as $h_{\text{y}}^{\text{closed}} = 0.85$ mm, as illustrated in Figure 7.3c,e.

$p_n \, [\mathrm{kPa}]$

$p_n \, [\mathrm{kPa}]$

(a) Cross-clamps

(b) EAB-related occluders
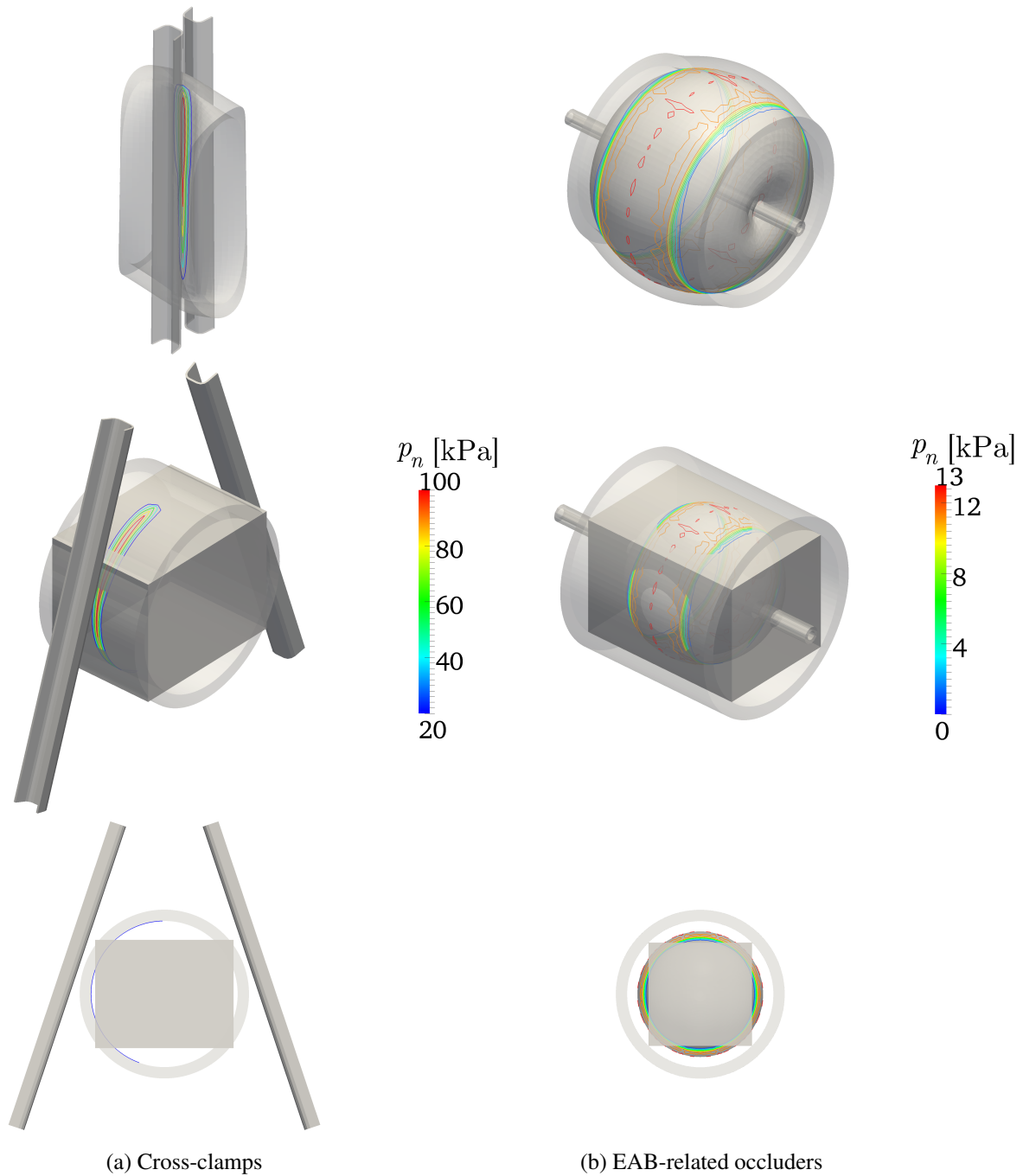
Figure 7.3.: The extraction of the occlusion potential for the two types of occluders considered, showing the contact pressure contour lines in the current configuration (top), an isometric view of the bounding box BB used to aid in determining the valid contour lines along which occlusion can occur $\mathcal{S}_c^{\mathrm{closed}}$ in the reference configuration (middle), and an axial view of the same BB (bottom). Only a shortened section of the aorta is shown.

The actual postprocessing was achieved by considering a computationally reasonable number of contact pressure contour lines on the undeformed EAB or luminal surface, depending on the type of occluder considered. Using both the occlusion potential and contour interval extracted at each load step, the entire process of identifying the occlusion potential, i.e. Eq. (7.1) to (7.5), was repeated for a smaller contact pressure range surrounding the previously extracted occlusion potential, due to computer memory limits reached when specifying a too large number of contours. This process was repeated until the contour interval was approximately 0.1 kPa. An example of such a set of contour lines evaluated with regards to the stated criteria for extracting lines along which occlusion can occur is shown for EABO in Figure 7.3b.

As can be seen in Figure 7.3, the contour lines are not smooth, but rather display a kinked character. This can be ascribed to the fact that the postprocessing software employed to perform this extraction, i.e. Paraview, cf. Section 6.2.1, performs the contour operation by performing linear interpolation between the nodal values. Nevertheless, despite the kinked character thereof, sufficient and comparable occlusion potential information could be extracted.

Two final remarks of this strategy to extract the occlusion potential needs to be made. Firstly, the level-set character of the contour lines $\mathcal{C}$ implies that the unlikely case exists where a contour line may be found that is valid, i.e. satisfying all four conditions, yet not forming a closed line. However, in the current model setup, occlusion potential could be confirmed visually and did not indicate the occurrence of such a case. Secondly, it will not suffice in a more complicated geometrical consideration of aortic occlusion, e.g. for a patient-specific geometry. Accordingly, in Section 9.1, the occlusion potential was extracted per hand and left for future investigations to consider a more robust strategy.

Using this newly defined measure of occlusion potential, it is therefore possible to evaluate the occlusive ability and efficiency of any occluder with any type of configuration, independent of the occlusion threshold, because it is independent of the occluder. Occlusion potential is therefore only dependent on the physics that will ultimately be responsible for occlusion itself: the sufficient contact pressure distributed continuously around the entire intimal surface.

No previous measure has been used or defined to consider the actual physics of occlusion for the application at hand or related, as far as the author could determine. Although the occlusion potential does not relay any information about the state of occlusion, it provides the comparative basis needed to evaluate the occlusion efficiency of completely dissimilar occluders. Should a threshold become available of when occlusion occurs from experimental or computational findings, it will simply be a value above which the vessel will be occluded, and anything beyond this threshold can be considered as over-occlusion.

7.4.2. Occluder stability

The lack of satisfactory occluder stability in the context of EABO has frequently been cited as a major disadvantage, despite all of the advantages of using the EABO-system, cf. Section 2.2. Nevertheless, this lack of satisfactory occluder stability has received very limited attention in literature, when considering its evaluation [346] or its remedy [308].

In the computational results presented, occluder stability is evaluated in terms of the resultant force exerted by the occluder in the direction of the vessel axis at the occlusion site. The occlusion site refers to the axial coordinate of where the occluder is applied. Due to the equilibrium required for each load step of each simulation, this resultant contact force exerted by the occluder would of course be zero. Therefore, the occluder resistance force was obtained by only considering the positive force components in the vessel direction. This quantity will be referred to as the *migration resistance force* of the occluder, F^{migr}, and is basically one of the two components of force needed to keep the occluder in equilibrium relative to the
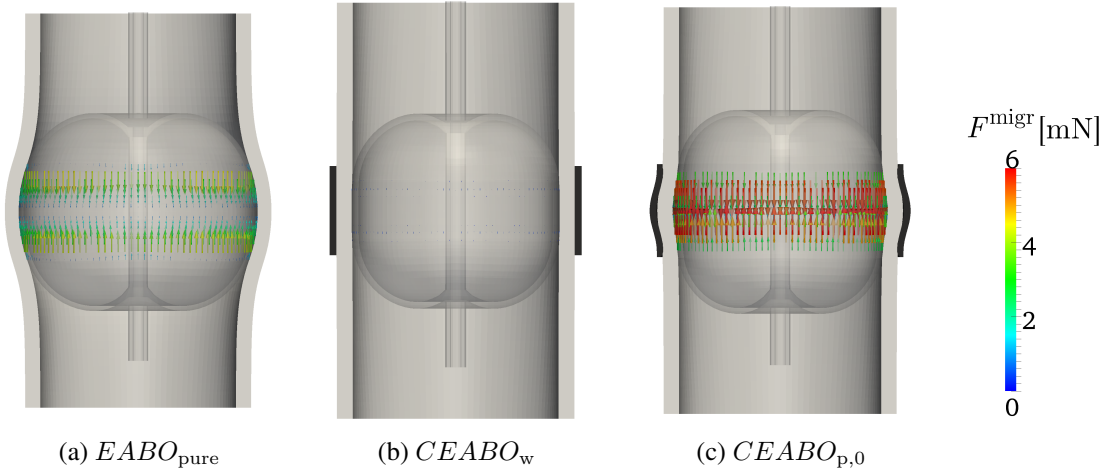
(a) $EABO_{\text{pure}}$ (b) $CEABO_{\text{w}}$ (c) $CEABO_{\text{p,0}}$

Figure 7.4.: The occluder migration resistance force visualized for different EAB-related occluders at $|P_{\text{EAB}}| = 0.8$.

vessel axial direction. It is depicted in Figure 7.4 and defined as,

$$F^{\text{migr}} = F_n^{\text{migr}} + F_\tau^{\text{migr}} = \frac{1}{2} \sum_{i=1}^{n_{\text{nd}}^{\text{occl}}} |\boldsymbol{F}_{n,i} \cdot \boldsymbol{n}^{\text{vess}}| + \frac{1}{2} \sum_{i=1}^{n_{\text{nd}}^{\text{occl}}} |\boldsymbol{F}_{\tau,i} \cdot \boldsymbol{n}^{\text{vess}}| \qquad (7.10)$$

with the normal and tangential contact force vectors, $\boldsymbol{F}_n$ and $\boldsymbol{F}_\tau$ respectively projected in the direction of the vessel axis $\boldsymbol{n}^{\text{vess}}$, summed over all the nodes on the vessel making contact with the occluder $n_{\text{nd}}^{\text{occl}}$. For the CEABO simulations, this refers specifically exclusively to the contact between the EAB and the vessel.

7.4.3. Applied clamp force

Although the applied clamp force is frequently reported in experimental studies, it has seldomly been reported for computational investigations. The force required to clamp the aorta extracted in a similar way as the occluder migration resistance force. An advantage of this measure of force is that it is one of the few parameters that is comparable to published experimental results for validation purposes.

A strategy similar to the one presented above was used to obtain the *total applied clamp force*, F^{cl}. It consisted of the resultant force exerted normal to the vessel axis and in-line with the plane in which the clamps remain during the hinged clamp movement, defined as,

$$F^{\text{cl}} = F_n^{\text{cl}} + F_\tau^{\text{cl}} = \sum_{i=1}^{n_{\text{nd}}^{\text{occl}}} |\boldsymbol{F}_{n,i} \cdot \boldsymbol{n}^{\text{cl}}| + \sum_{i=1}^{n_{\text{nd}}^{\text{occl}}} |\boldsymbol{F}_{\tau,i} \cdot \boldsymbol{n}^{\text{cl}}| \qquad (7.11)$$

with the the normal and tangential contact force vectors, $\boldsymbol{F}_n$ and $\boldsymbol{F}_\tau$ respectively projected in the direction of the clamp surface normal $\boldsymbol{n}^{\text{cl}}$, summed over all the nodes on the vessel making contact with the occluder $n_{\text{nd}}^{\text{occl}}$.

7.5. Comparative functional performance

In the following section, results comparing the functional performance of the existing and newly proposed occluders are given, as obtained by the computational simulations presented. Brief discussions on related

findings accompany these results, and continual referral to the fulfillment of the stated requirements will be made. The occluders simulated comprised of three different sets of cross-clamps (parallel, standard and crab-pincher), EABO and CEABO with three different constrainer designs (narrow, wide and profiled), as reflected in the simulations performed: $CC_{||}$, CC_{crab}, CC_{std}, $EABO_{pure}$, $CEABO_{n,i}$, $CEABO_w$, $CEABO_{p,i}$ for $i = 0, 2, 4$ indicating the occluder-EAB offset, as outlined in Section 6.2 and Table A.2.

Two independent variables are used throughout the results to allow for direct comparability of certain dependent variables obtained from specific types of occluders. Firstly, for direct comparability between the cross-clamping simulations, *the normalized clamped luminal area* $|A_{cl}^{lumen}|$ was used. It was obtained by extracting the luminal area along a an axial slice positioned at the occlusion site, passing through the clamped aorta and the clamp surfaces in the current configuration, and normalized to the corresponding luminal area in the reference configuration. Therefore, a $|A_{cl}^{lumen}| = 1.0$ meant that the luminal area in the current configuration was the same as that of the reference configuration, while $|A_{cl}^{lumen}| = 0.0$ implied full occlusion. Secondly, for direct comparability between the EAB-related occluders, *the normalized EAB pressure* $|P_{EAB}|$ was used. It was obtained by normalizing the current EAB pressure to the maximum EAB pressure simulated, i.e. 46.67 kPa. Therefore, $|P_{EAB}| = 1.0$ represents the maximum EAB pressure considered. Furthermore, the *normalized EAB volume*, $|V_{EAB}|$, is also referred to. It was obtained by normalizing the EAB-volume in the current configuration to the EAB-volume obtained when it was inflated by itself, i.e. not considering a vessel, up to the maximum P_{EAB} defined in Section 6.2.4.2.

The strain measure considered throughout was the Euler-Almansi strain, as defined for the 3D case considered here in Eq. (6.15). It was useful to consider its relation in 1D for explanatory purposes, defined as,

$$\varepsilon_{EA} = \frac{1}{2}\Big(1 - \frac{L^2}{l^2}\Big) \tag{7.12}$$

where L and l are the undeformed and deformed lengths, respectively. This measure is particularly suited to evaluate high compressive strains in the finite strain setting.

Furthermore, the *maximum shear strain* and *von Mises strain* were also considered, respectively calculated from the principal strain components ε_1, ε_2 and ε_3 as,

$$\varepsilon_{\tau,max} = \varepsilon_1 - \varepsilon_3 \tag{7.13}$$

$$\varepsilon_{VM} = \sqrt{\frac{1}{2}\big[(\varepsilon_1 - \varepsilon_2)^2 + (\varepsilon_2 - \varepsilon_3)^2 + (\varepsilon_1 - \varepsilon_3)^2\big]} \tag{7.14}$$

Although, the $CEABO_w$ simulation could only be completed to $|P_{EAB}| = 0.61$ (see below), its poor performance in terms of stability seen in the acquired results, cf. Section 7.5.3, justified the inclusion of this incomplete set of results.

7.5.1. Local progression of strain during occlusion

Figure 7.5 gives an overall impression for the impact that each occlusion technique had in yielding a complex loading and deformed configuration of the vessel.

The next and probably most significant comparable feature of the impact that an occluder had on the vessel, was the progression of different maximal strain measures during occlusion, at different local regions of interest (ROIs) on the vessel. The ROIs considered were located at the proximal and distal pinching sites, as well as the inferior and superior clamping regions as indicated. Due to the planar symmetry of the problem, only the inferior clamping region was considered, while for the EAB-related occlusion techniques, no pinching sites were considered, due to its radial symmetry. Each ROI consisted of extracting results from the vessel wall falling within a sphere ($R = 2$ mm) centered mid-wall at the desired location as shown in Figure 7.6a. For comparative purposes, the strains in the occlusion ROI were also extracted,
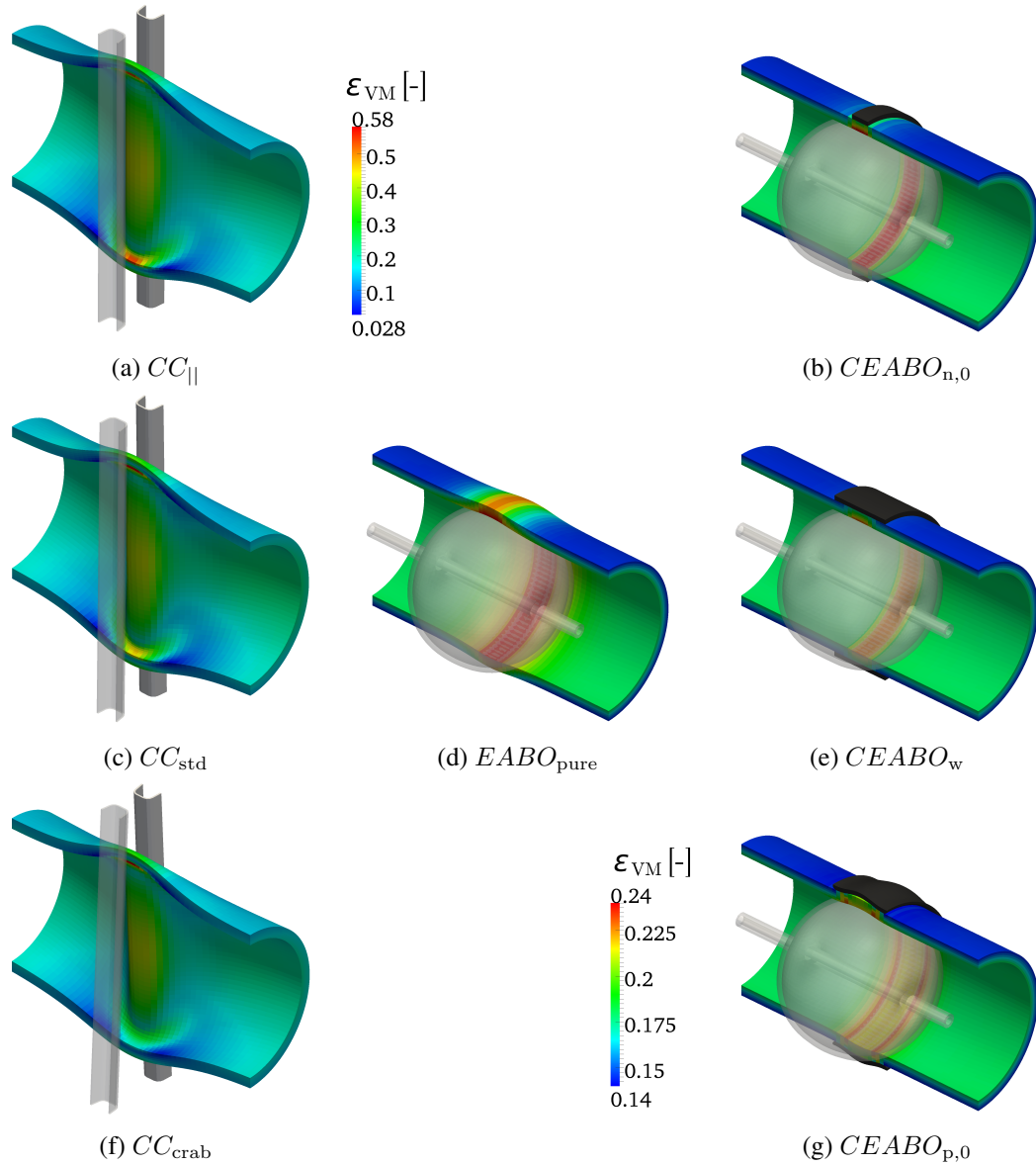
Figure 7.5.: The von Mises strains for all the occluding techniques considered in the deformed configuration at a comparable intermediate stage of occluder progression. For the different cross-clamps, these results were extracted at $|A_{cl}^{lumen}| \approx 0.2$ and the results refer to the top color bar. For the EAB-related occluders, these results were extracted at $|P_{EAB}| \approx 0.6$ and the results refer to the bottom color bar.

(a) Local ROIs

(b) Occlusion ROI

(c) CC_{crab}

(d) $EABO_{\mathrm{pure}}$
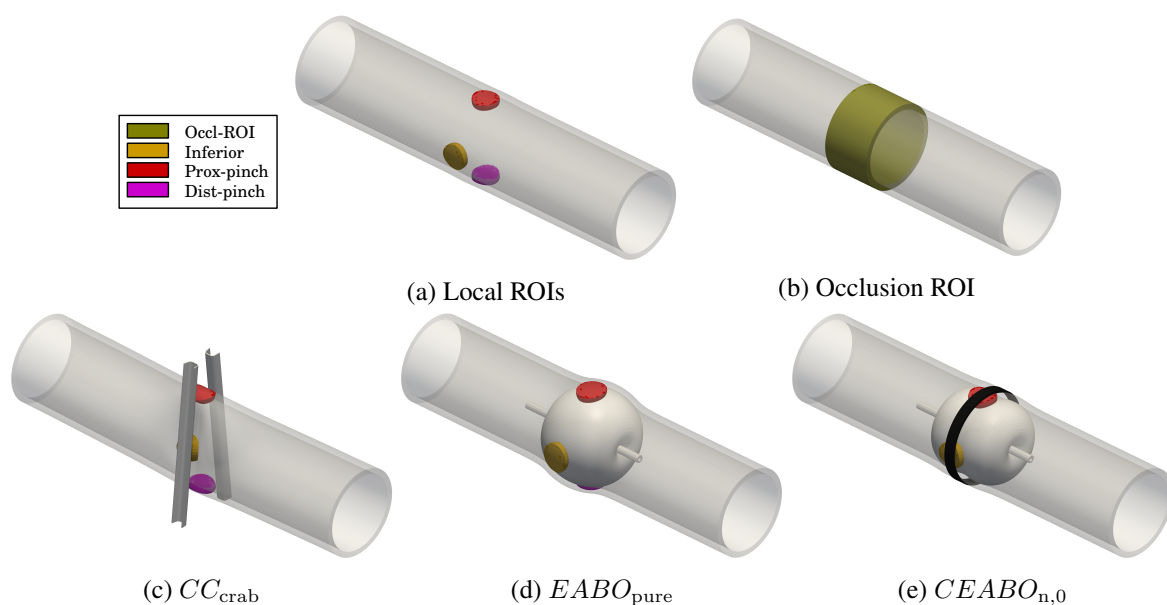
(e) $CEABO_{\mathrm{n,0}}$

Figure 7.6.: The progression of strains plotted in Figure 7.7 were extracted from (a) the inferior, proximal pinching site and distal pinching site, as well as from (b) the entire occlusion region.

consisting of a 20 mm tubular section of the idealized vessel, centered at the occlusion site, as shown in Figure 7.6b. Including the occlusion ROI made it possible to evaluate whether peak strains captured inside a ROI were the highest in the occlusion region or not. The resulting strains from these ROIs are shown in Figure 7.7

For cross-clamping, as shown in Figure 7.7a, it should be noted that for the hinged clamps (CC_{std} and CC_{crab}), the inferior ROI results did not match the landing site of the clamp, as reflected by the response mismatch between this ROI and the entire occlusion region. Secondly, the non-monotonous increase in the first principal strain (positive values indicate tensile strain) can be ascribed to the fact that a prestressed cylindrical vessel under a hydrostatic load was occluded, meaning that as the cross-clamps closed, the principal directions in the different ROIs changed. Furthermore, as the occluder progressed, the strain of a certain measure that dominated the overall strain response, changed. This was also clearly evident in the resulting third principal strains (negative values indicate compressive strain), showing that up to a range of $|A_{\mathrm{cl}}^{\mathrm{lumen}}| \approx (0.28 : 0.18)$, a maximum dominated that was only captured by the occlusion region, while after this point, it was clearly situated in the proximal pinching region. Thirdly, it can be seen that the first principal strains were dominant in the inferior region – or more precisely, the clamp surface landing site – for the majority of the clamp closure progression. However, prior to intimal self-contact, the strain in the proximal pinching region started to dominate. It is noteworthy that the strain in the inferior ROI was in a very similar range compared to the pinching site, although the pinching site showed a much greater increase upon intimal self-contact. Fourthly, it should be noted that large tensile and compressive strains occurred at the pinching sites. Finally, in terms of third principal strains, as already mentioned, an uncaptured region initially dominated the maximum compressive strains, although ultimately, and at a point prior to when tensile strains started to dominate, the strain in the proximal pinching site dominated. Here, the compressive strain in the inferior ROI only sharply increases once intimal self contact occurs.

For the strain response of the EAB-related occluders, shown in Figure 7.7b, it is evident from the first principal (maximum tensile) strains that these occluders yielded an overall smaller tensile stretch in the vessel wall, while at the same time maximizing the compression to the vessel wall. *Very significant*, is the

(a)

(b)
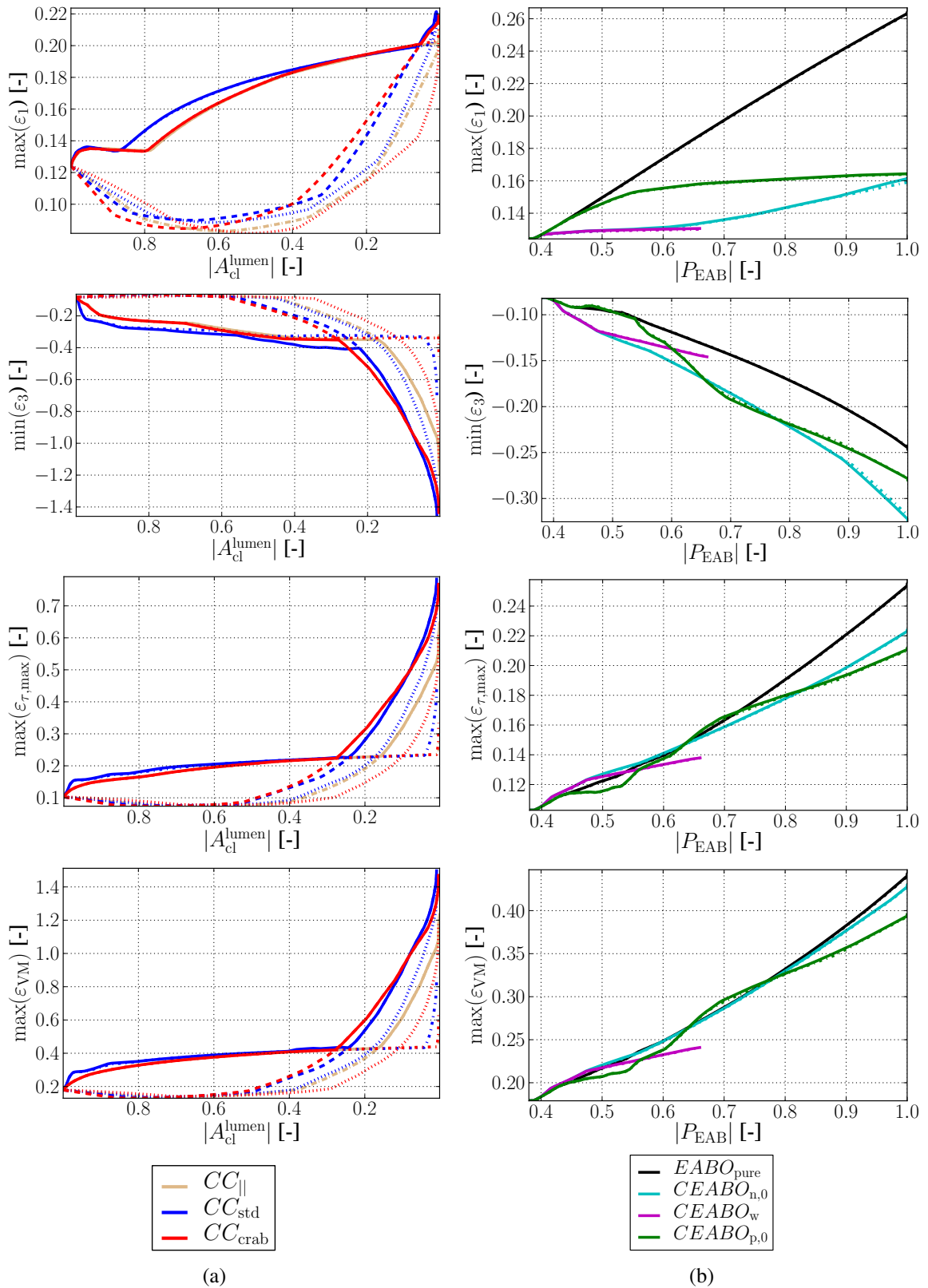
Figure 7.7.: The progression of maximum values of first principal ε_1, third principal ε_3, maximum shear $\varepsilon_{\tau,\max}$ and von Mises $\varepsilon_{\mathrm{VM}}$ strain, respectively, during occlusion for the different (a) cross-clamps and (b) EAB-related occluders at the following extracted regions: entire occlusion region (solid lines), the inferior region (dash-dot lines), distal pinching site (dotted lines) and proximal pinching sites (dashed lines). These locations are graphically shown in Figure 7.6.

way in which the constrainers were able to substantially limit the maximum stretch in the vessel – no constrainer yielded an increase of the first principal stress of more than ~15%, while it showed an increase in the third principal strains that was substantially higher than $EABO_{\mathrm{pure}}$. Both are desired features, but the latter needs to be qualified: an increase in compressive strain is an unavoidable consequence for enabling occlusion of a vessel lumen – regardless of the type of occluder. However, the distribution and magnitude of these compressive strains along the entire occlusion site were important – all of which are not entirely evident from the results presented in the figure above, but further considered in the next subsection. Nevertheless, comparing only the maximum tensile strains between the constrainers, $CEABO_{\mathrm{n,0}}$ initially outperformed $CEABO_{\mathrm{p,0}}$, since the inflating balloon still needed to push the entire aortic wall into the depression of the profiled constrainer. Once the aortic wall was completely pushed into the profile, the contribution of an increase of EAB-pressure was dramatically decreased. It can also be seen that the maximum strains were not captured by the inferior region, but rather in the occlusion region. This can be ascribed to the main contact occurring further away from the center of the EAB, where it makes contact with the slanted surfaces of the profile, cf. Figure 7.5. For $CEABO_{\mathrm{n,0}}$, although the constrainer restricted the tensile strain induced in the vessel wall nearly immediately after EAB contact, a further increase in EAB-pressure caused stress-concentrations on the outer edge of the constrainer and can be related to the thinness of the constrainer itself, ultimately performing worse than $CEABO_{\mathrm{p,0}}$ in limiting the tensile stretch. Although $CEABO_{\mathrm{w}}$ was not completed, with the results shown and the known configuration, it is expected to outperform the former two constrainers, since it allowed no further stretch of the vessel.

In generally comparing the cross-clamping and the EAB-related occlusion techniques, a large difference between the resulting first and third principal strains can be observed – both for regimes of occlusive loading that is required to achieve occlusion. The maximum shear and the von Mises strain do not grant much additional insight into the mechanical phenomena at stake, but rather provide a summary of effects. However, it is clear that a significant maximum shear strain is induced, especially in the cross-clamping simulations, in which case it can be mainly ascribed to the pinching of the vessel wall.

The extent of impact by the exerted compressive strain was difficult to evaluate. Although it might appear that the compressive strains dominated, cf. Figure 7.7, it should be noted that the formulation of the Euler-Almansi strain does not allow for the direct comparison of strains in compression and in tension, cf. Eq. (7.12). In the function described by this equation, the negative limit of stretch yields a strain of $-\infty$, while the positive limit of stretch asymptotically increases to 0.5. Damage of the vessel will depend depending on whether some tensile, compressive or shearing strains exceed some local material-specific (mostly unknown) threshold. Tensile damage has been most widely described, as reviewed in Section 6.2.2, due to the relative ease of its evaluation. Compression and shear damage evaluation for arteries are scarcely reported in literature, which can be ascribed to the complexity of measuring such damage in soft biological tissues. This lack of information comes from a general lack of understanding of the exact mechanisms responsible for compressive and shear damage in soft tissue, as reflected in the widely researched area of deep tissue injuries, i.e. injuries caused to skeletal muscle due prolonged compressive and shear loading, e.g. patients lying on a particular side of their bodies for a prolonged time without adjustment [303, 322]. One plausible mechanism that has been hypothesized and is very likely applicable to the compression of arteries, is that the damage to muscle fibers occurs due to excessive mechanical deformation and the subsequent disruption of the fibers [322]. The mechanisms for fiber damage in arteries are likely similar for tensile, compressive and shear damage, but have different (yet unknown) paths of loading along which it occurs. Additionally, compressive damage has been shown to also depend not only on the magnitude, but also the duration of the applied load [18, 322]. All of these factors should also be taken into consideration when interpreting the maximum shear and von Mises strains, because both of these are influenced by the given formulation yielding high values for the compressive strains.

7.5.2. Requirement: Minimize vessel damage

In order to further evaluate *how* effective an occluder was at minimizing strain induced by the occluder, while maximizing the occlusive potential and evenly distributing the intimal contact load, i.e. requirements 1, these related parameters are plotted in Figure 7.8.

As can be expected, the trend of the response for the maximum intimal contact pressure and the occlusion potential did not differ much for the different occluders. However, clearly apparent was the much larger strain that had to be induced by the cross-clamps to achieve intimal self-contact at all, when compared to the EAB-related occluders. Considering only the different cross-clamps, it can be seen that a significant amount of strain had to be induced before a state could be reached where occlusion could even be possible, i.e. $p_n^{\mathrm{occl}} > 0$. Furthermore, the maximum contact traction induced, the stage when occlusion potential was first reached and the corresponding amount of strain induced, clearly depended on the hinged configuration. In other words, the more the configuration of a cross-clamp deviated from perfectly parallel, the worse the impact was due to the excessive strains experienced by the proximal pinching site, cf. previous subsection, and the worse the intimal contact would contribute to the occlusion potential. Therefore, the worst cross-clamp performance in terms of the stated requirements were delivered by CC_{crab}, followed by CC_{std} and then $CC_{||}$.

In terms of the EAB-related occluders, it can be seen that each constrainer considered was superiorly efficient in facilitating an increase in the occlusion potential, while significantly limiting the maximum (tensile) first principal strain induced in the vessel. Comparatively, the efficiency of $EABO_{\mathrm{pure}}$ to increase the occlusive potential, but also intimal contact traction, declined beyond a very early stage at $\varepsilon_{\mathrm{VM}} \approx 0.19$. At some point it even caused more tensile strain that the cross-clamps, although the compressive strains remained relatively low. Unfortunately, so too did the occlusion potential. Comparing between the different constrainers, the configuration by which the vessel made contact with the EAB and the differently shaped constrainers yielded a similar trend as described in the previous subsection: the nearly immediate restriction of the constrainer of $CEABO_{\mathrm{n},0}$ yielded initial good performance, but was eventually surpassed by the profiled constrainer of $CEABO_{\mathrm{p},0}$, while $CEABO_{\mathrm{w}}$ is expected to outperform both of the former in the stated requirements.

Importantly, it can be seen that $CEABO_{\mathrm{p},0}$ yielded a comparable gradient of occlusion potential over first principal strain as the cross-clamps, but at a global increase of first principal strain that is approximately *half* the increase yielded by cross-clamps. Furthermore, it also showed a lower gradient of increasing the third principal strains was achieved than cross-clamps, but once again at nearly *half* the increase yielded by the cross-clamps. Comparatively, $EABO_{\mathrm{pure}}$ clearly performed extremely poor, having a clearly limited ability of increasing the occlusion potential, while causing significant tensile strains.

Finally, all the different CEABO variations evaluated revealed highly desirable performance features in terms of the minimizing potential vessel damage, not achievable by the other occlusion techniques considered. This included the constrainer's ability to maximize the third principal (compressive) strains in the vessel while limiting the first principal (tensile) strains. Furthermore, combined with the results presented in this section about how the slight increase in a relatively low first principal strain caused a steep increase in occlusion potential with a concomitant increase in the third principal strains.

7.5.3. Requirement: Provide stable, thus reliable occlusion

As defined in Section 7.4.2, the occluder stability is one of the two components of force in the axial direction of the vessel keeping the occluder in its applied position, i.e. in equilibrium. Even though an issue of cross-clamps migrating has not been previously reported, the migration resistance force for the cross-clamps and the EAB-related occluders are shown in Figure 7.9.

(a)

(b)

(c) CC_{crab}

(d) $EABO_{\text{pure}}$

(e) $CEABO_{\text{p,0}}$
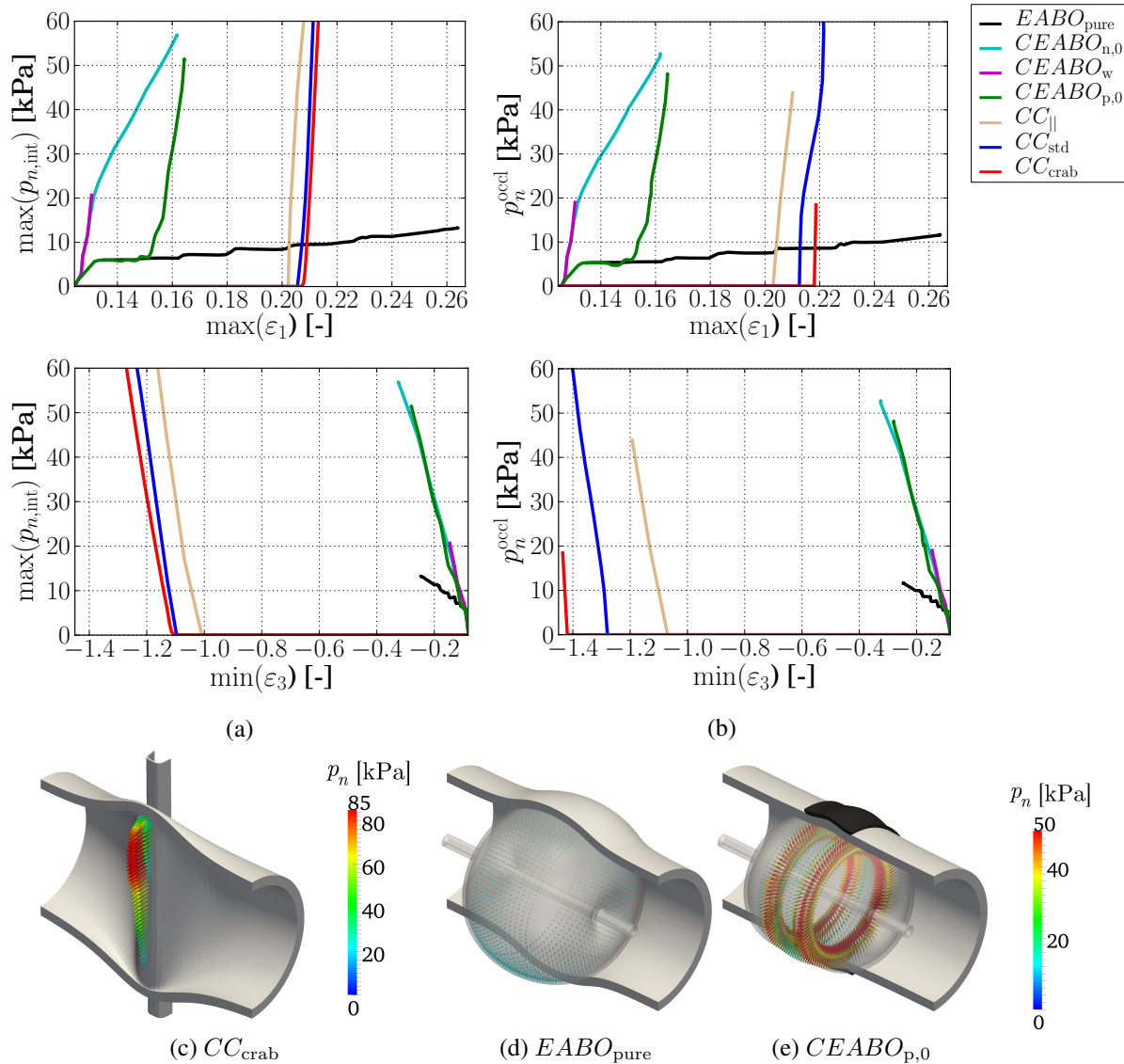
Figure 7.8.: The occlusion efficiency of each occluder, in terms of minimizing the impact on the vessel, showing (a) the maximum intimal contact pressure p_n^{int} and (b) the occlusion potential p_n^{occl} plotted against the maximum first (top) and third (bottom) principal strains, respectively. These strains were evaluated in the occlusion region, depicted in Figure 7.6b. Axial sections of representative models are shown to indicate the characteristic contact pressure exerted on the intima. The two color bars represent the values displayed for cross-clamps and EAB-related occluders, respectively.
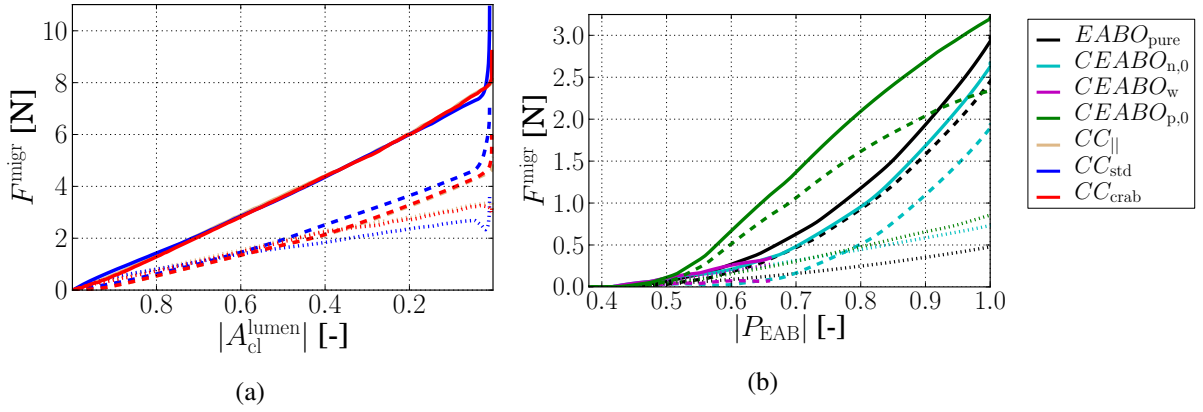
Figure 7.9.: The total migration resistance force F^{migr} (solid lines) made up of the components of the induced normal (dashed lines) and tangential (dotted lines) contact force, respectively, shown for a) the different cross-clamps and b) the EAB-related occluders. Note the definition of the normal and tangential components in Eq. (7.10).

Although the migration resistance force increased sharply for $EABO_{\mathrm{pure}}$, as well as for the other CEABO-simulations, it was still much lower than any of the cross-clamps. As soon as cross-clamping resulted in intimal self-contact, the migration resistance force rose sharply. The high resistance yielded by $EABO_{\mathrm{pure}}$ can be ascribed to the slanted surfaces of the vessel wall yielded by the expanding EAB. Both the $CEABO_{\mathrm{n,0}}$ and $CEABO_{\mathrm{p,0}}$ also yielded good resistance, but because of different configurations: the former because the EAB bulged around the sides of the constrainer, and the latter because of the constriction of lateral EAB expansion by the slanted surfaces of the profiled constrainer. Here, $CEABO_{\mathrm{w}}$ was expected to perform the poorest due to its migration resistance being mainly dependent on the frictional component. All these effects are shown as visual representations in Figure 7.8.

It is interesting to note how the total cross-clamp migration resistance force was made up of a near-similar contribution of force from the normal and the tangential components. A lower frictional coefficient than was chosen here will subsequently imply a greater potential increase in instability prior to occlusion. This implies that the surgeon not only needs to over-clamp the aorta to ensure occlusion, but in the case of a lower contact friction, potentially also needs to ensure occluder stability. For the EAB-related occluders, the normal contact force yielded the largest contribution to the migration resistance force. This can be ascribed to the slanted surfaces created by the EAB in different configurations as described above.

The quantity of migration resistance force needs to be evaluated with caution. A higher value does not necessarily mean more stability, but also depends on the configuration of the occluder. To aid in its evaluation, one has to consider the application of an axial load to the occluder to disturb the equilibrium of forces between F^{migr} and $-F^{\mathrm{migr}}$. For the cross-clamps, such a load will cause it to move, while the new F^{migr} during this applied axial load will remain close to the pre-disturbed value, because the clamp arm displacement is locked into place by the ratchet system, cf. Figure 2.1. Similarly for $EABO_{\mathrm{pure}}$ and $CEABO_{\mathrm{w}}$, such a load will cause the EAB to move, while the F^{migr} will remain close to the pre-disturbed value, because after having been displaced axially, the EAB is still surrounded by a stretched vessel ($EABO_{\mathrm{pure}}$) or a wide-region of constrained vessel expansion ($CEABO_{\mathrm{w}}$). For $CEABO_{\mathrm{n,0}}$, such a load will push a larger portion of the EAB to bulge out around the constrainer in the direction of the load. This will result in the EAB becoming very unstable, and it will slip out of the constrained region and effectively recover EABO, i.e. poor stability. However, for $CEABO_{\mathrm{p,0}}$, the EAB will be forced in
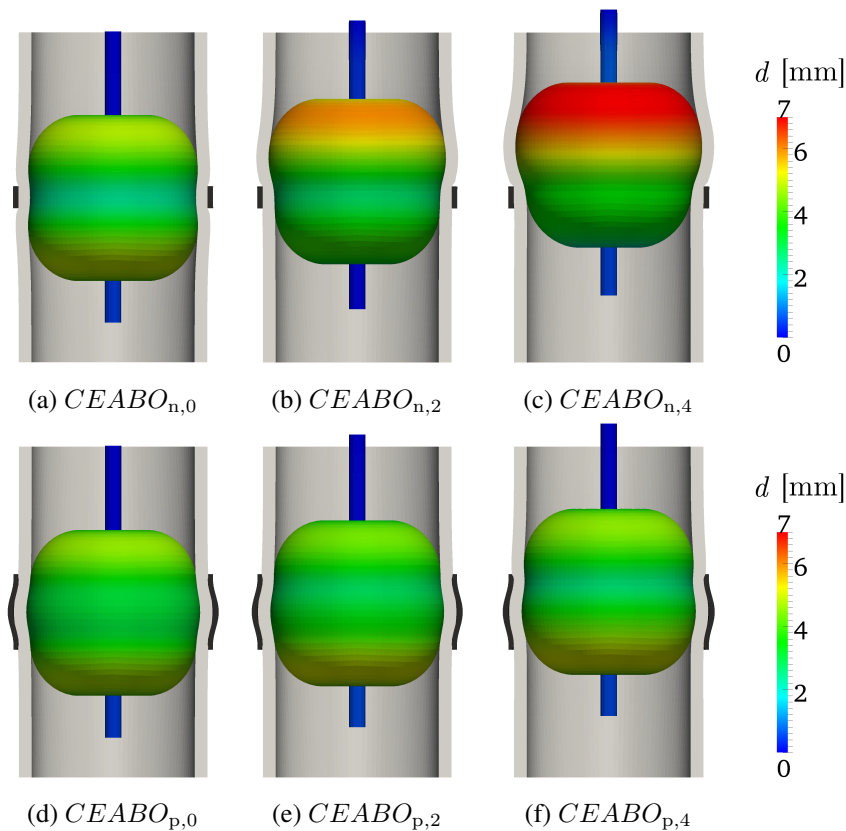
Figure 7.10.: The ineffective ability of the narrow constrainer, but the superior ability of the profiled constrainer to enable accurate positioning of the occluder, but also ensure the stability of the EAB, even when the alignment between the EAB and the constrainer is mismatched, showing EAB displacements at $|P_{\mathrm{EAB}}| = 1.0$.

the direction of the smallest diameter of the constrainer, thereby effectively preventing the EAB from moving, i.e. the F^{migr} will increase (up to a certain point) – good stability.

7.5.4. Requirement: Enable accurate occluder positioning

While the positioning of cross-clamps at the desired site of occlusion is trivial, EABO is much more difficult. If the EAB-catheter is inserted femorally, it has to be located either manually by palpation (i.e. more manipulation) or approximated by intra-operative fluoroscopy. The difficulties with determining its position are clear.

Tying in with the previous requirement, a simple demonstration is considered here to indicate the efficiency of the narrow and the profiled constrainer to aid in determining the position of the EAB and ensuring that the vessel is occluded where specified. Figure 7.10 shows the results of $CEABO_{\mathrm{n,i}}$ with $i = 0, 2, 4$ compared with $CEABO_{\mathrm{p,i}}$ with $i = 0, 2, 4$.

As shown in this figure, it is clear that the profiled constrainer facilitates the positioning of the EAB, even when the EAB and the constrainer are not perfectly aligned. Contrarily, the misalignment between the narrow constrainer and the EAB will cause the EAB to slip away from of the constrainer region.

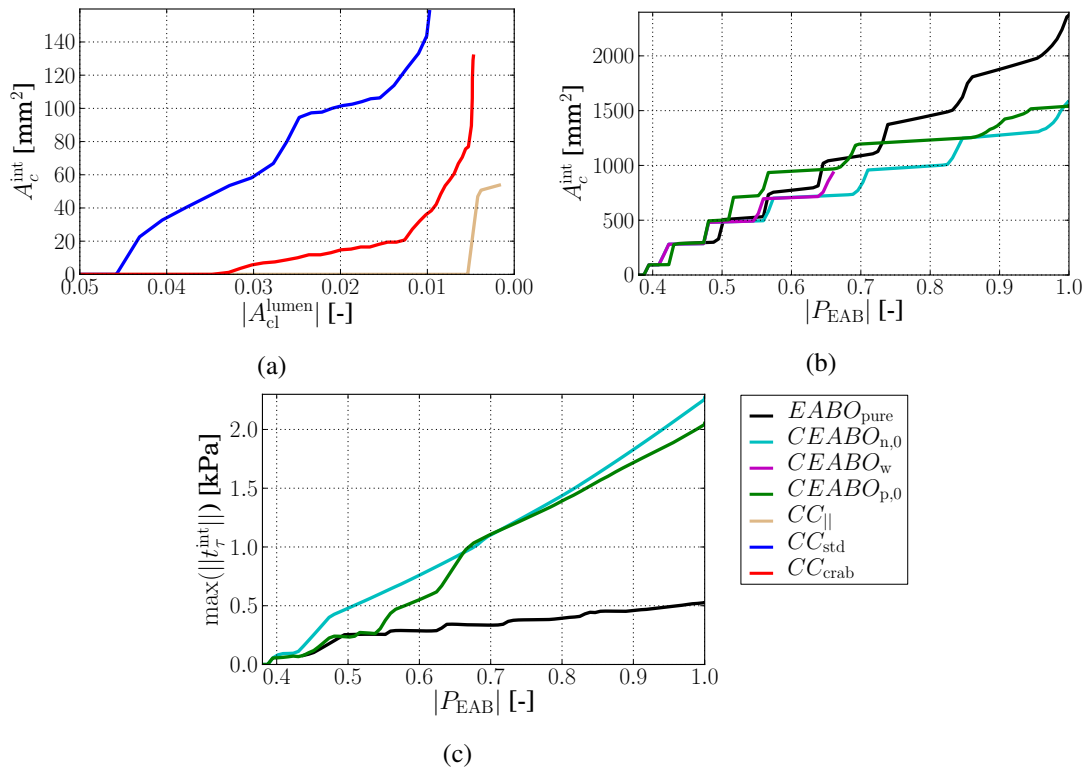Figure 7.11.: The intimal surface area in contact A_c^{int} due to the (a) different cross-clamps and (b) EAB-related occluders. Furthermore, the progression of the maximum tangential contact traction magnitude for the EAB-related occluders is shown in (c).

7.5.5. Requirement: Minimize intimal surface disruption

As explained above, a degree of normal contact traction is required to achieve and increase the occlusion potential and is an unavoidable part of occluding the vessel. However, the tangential contact traction and the total area of the intima that will come into contact with the occluder (EAB-related occluders) or itself (cross-clamping) can additionally disrupt the intima. These two variables are plotted in Figure 7.11. As stated in Section 6.1.4.5, the tangential contact traction for the displacement-controlled movement of the clamps was assumed to have a negligible frictional coefficient and therefore are not considered further.

These results clearly show that the thin clamp arms will result in a significantly smaller area of the intima coming into contact, while the constrainers are only partially effective at reducing this area, since it is clearly dependent on the EAB-size. The cross-clamps once again demonstrate the effect of the hinge configuration, while it should be noted that no cross-clamping simulation was able to reach $|A_{\mathrm{EAB}}| = 0$. An unintended, yet telling consequence of the model setup was that the out-of-plane hinge of CC_{std} and a high chosen friction coefficient, which led to the cross-clamps to pull more vessel material towards the occlusion site, causing a slightly larger final contact area, as can be seen in Figure 7.11a. The discrete step sizes in the resulting area plotted can be ascribed to the postprocessing of the area, where contact area was simply calculated proportionally to the nodes in contact.

The maximum tangential contact traction induced clearly shows that the desired properties of the constrainer, i.e. efficiently and uniformly transferring the normal contact traction while inducing limited strain in the wall, came at the cost of an increased maximum tangential contact traction.

Finally, it must be noted that occlusion will always result in some degree of intimal disruption, whether during EABO or CEABO, or even when intimal self-contact occurs during cross-clamping. This has repeatedly been shown experimentally, cf. Section 2.1.1 and 2.3.1. One study made an exemplary conclusion by stating that neither the pressure nor the duration of cross-clamping can be adequately controlled to prevent intimal disruption [18] – in a study where the tangential contact traction can safely be assumed to have been negligible. Therefore, simply the compression along the luminal circumference of the vessel at the occlusion site is already sufficient to cause intimal disruption. Furthermore, despite the intimal disruption, it is mainly only a surface phenomenon, whereas higher strains in the vessel wall will be responsible for deeper and more comprehensive damage of the vessel, cf. Section 7.5.1. Interestingly, Margovsky et al. [226] reported an increase in the area of endothelial damage under a higher applied load for the same cross-clamp affecting the same area, suggesting the area in contact is not the sole determinant of intimal disruption, but also the level of stress/contact traction it is exposed to.

7.5.6. Requirement: Enable clinically determinable occlusion

For an occluder to enable clinically determinable occlusion, clinically known parameters need to be easily relatable to the occlusive state and the level of occlusion. As thoroughly explained in Section 7.4.1, the occlusion potential is a (scalar) parameter that combines this information into a single parameter. For this reason, the occlusion potential is plotted against the applied clamp force and the normalized EAB pressure, respectively, in Figure 7.12. The non-smooth character of the occlusion potential curves can be ascribed to the postprocessing of the occlusion potential, as referred to in Section 7.4.1.

As expected, $CC_{||}$ yielded a straight curve, because perfectly parallel cross-clamps clamping an idealized vessel should result in a linear relation between the occlusion potential and the applied clamp force, as seen in Figure 7.12a. This characteristic increase was also assumed by the two earlier studies investigating minimum vascular occlusion force (MVOF), cf. Section 7.4.1 and also experimentally measured when clamping a sheep's carotid or femoral artery [225]. However, as soon as the cross-clamp hinge configuration deviated from a parallel configuration, these results indicate that the relation lost its linear character. As can be seen in the results of CC_{std}, the occlusion potential was applied increasingly less effectively as the applied clamp force was increased, evident from the convex curving progression. Note that the results for CC_{crab} only represented two non-zero values for the occlusion potential and thus did not allow for a more detailed interpretation. Furthermore, as can be seen in the figure, a very steep gradient was yielded, i.e. a small change in clamp force caused a large change in occlusion potential.

For the EAB-related occluders, it can be seen in Figure 7.12b that very soon after EAB-vessel contact has occurred (from $|P_{\mathrm{EAB}}| \approx 0.4$), the ability of the EAB to increase the occlusion potential during $EABO_{\mathrm{pure}}$ was drastically reduced (from $|P_{\mathrm{EAB}}| \approx 0.43$), while the constrainers managed to maintain a steady, near-linear increase. It can once again be observed that the occlusion potential for the profiled constrainer initially rose slowly due to the vessel being pushed into the profile of the constrainer, but eventually reached a linear character since any further increase in EAB-pressure increases the intimal contact traction and therefore also the occlusion potential. Furthermore, this near-linear response for all the constrainers had a steady gradient to allow finer control of the occlusion potential upon varying the EAB-pressure. This was also seen in Figure 7.8.

The near-linear relation between the occlusion potential and the EAB-pressure, a feature displayed by all the constrainers considered, was the most promising response of all the occluders towards the enabling of a clinically determinable occlusion threshold. This is because despite the nonlinear response of the vessel, the loading configuration implied that the constrainer limited the radial expansion of the vessel, causing the contact pressure to increase due to the EAB pushing practically pressing against an incompressible strip of material (the vessel wall), as depicted in Figure 7.2c. The variability in the EAB-pressure vs. occlusion potential response will therefore fundamentally depend only on the compression
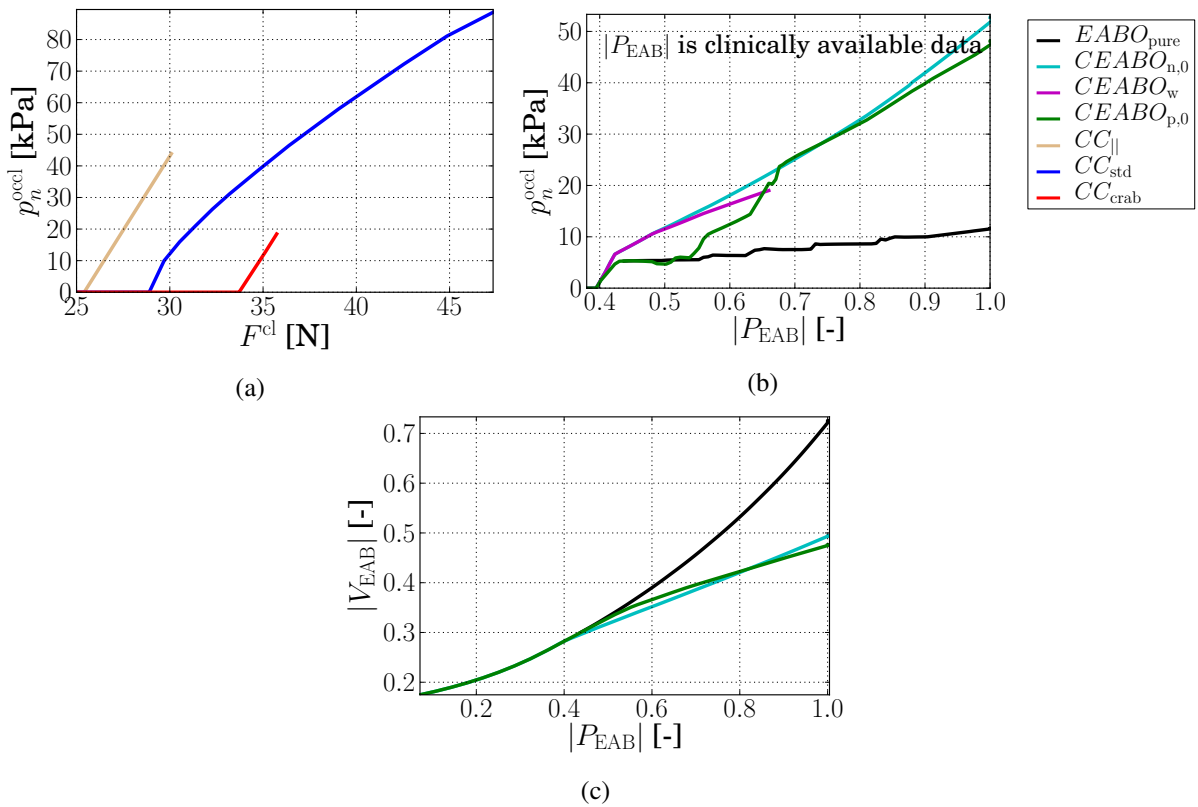
(a)

(b)

(c)

Figure 7.12.: Evaluation of the potential for a clinically determinable state and level of occlusion, by considering a clinically determinable parameter of occlusion with the occlusion potential for (a) the cross-clamps and (b) EAB-related occluders – showing also the pressure-volume relationship for the latter occluders in (c).

of the vessel wall. In contrast to this, during EABO, the EAB presses against this incompressible strip of material that is only limited by the amount by which it can stretch laterally with an expanding EAB, as shown in in Figure 7.2b. Here, the variability will not only depend on the vessel wall compression, but also the stiffness of the surrounding wall in the circumferential and axial directions. Finally, the loading configuration of cross-clamps must also be considered, as shown in Figure 7.2c. It is clear that although the cross-clamp configuration also similarly limits the expansion of the strip of material (the vessel wall) as during CEABO, it is dependent on the compression of twice the wall thickness and the pinching of the vessel wall will introduce additional variability to the load required, due to the unknown stiffness resulting from the clamped pinching sites. Material inhomogeneities are expected to aggravate these variabilities for cross-clamping and for EABO. For CEABO, the influence of such inhomogeneities are expected to be minimal, because the hydrostatic pressure-driven, load controlled configuration of the EAB pressing the vessel wall against a non-expanding surface will naturally cause an even distribution of the contact traction.

Consequently, determining a safe level of occlusion during CEABO becomes predominantly dependent on the geometry, with very little influence of the material parameters. Thereby, these results effectively demonstrated the superior ability of CEABO to enable the (simple) prediction of the lowest required EAB pressure required to safely occlude a vessel, by using only clinically determinable parameters.

Table 7.1.: The relative functional performance of the different occlusion techniques in providing safe, efficient and reliable occlusion, with the scores indicating how well an occlusion technique fulfilled the stated requirements – "5'" being the best and "1" the worst.

Functional requirement		$CC_{\parallel}$	CC_{std}	CC_{crab}	$EABO_{\mathrm{pure}}$	$CEABO_{\mathrm{n},0}$	$CEABO_{\mathrm{w}}$	$CEABO_{\mathrm{p},0}$
1a	*Minimize vessel damage*: minimize strain	1	1	1	2	3	5	4
1b	*Minimize vessel damage*: maximize occlusion potential	1	1	1	2	5	5	4
1c	*Minimize vessel damage*: ensure low and uniform distribution of occlusive load	1	1	1	3	4	5	5
2	Provide stable (i.e. reliable) occlusion	5	5	5	2	1	1	4
3	Enable accurate positioning of occluder	5	5	5	1	2	2	3
4	Minimize total intimal surface disruption	5	5	5	1	2	2	2
5	Enable clinically determinable occlusion threshold	2	1	1	2	5	5	5
6	Minimize vessel deformation	1	1	1	2	3	5	4
7a	*Simple*: maintain/decrease standard occlusion and CPB time	3	3	3	2	2	2	2
7b	*Simple*: do not clutter surgical field	1	1	1	3	2	2	2
8	Be cost efficient	3	3	3	1	1	1	1
Total		**28**	**27**	**27**	**21**	**30**	**35**	**36**

7.5.7. Requirement: Minimization of vessel deformation

As exemplary demonstrated in Figure 7.5, CEABO performed the best at minimizing the vessel deformation, followed by EABO, while any type of cross-clamping severely deformed the vessel.

7.6. Discussion

The presented computational study made use of state-of-the-art material models with experimentally derived parameters, advanced contact formulations, specified FE element technology suited for the application, occluder models accurately representing that which is used clinically and the consideration of measures previously not considered or sparsely evaluated. Thereby, it was possible to not only obtain previously unevaluated, quantitative, clinically relevant, mechanical insights into each of the occlusion techniques considered, but also provided the means to allow for the evaluation and comparison of key requirements needed for safe, efficient and reliable occlusion, as considered in the following.

7.6.1. Summary of functional performance/requirement fulfillment

In order to evaluate the overall comparative outcome of how well each occlusion technique fulfilled the stated requirements, a relative scoring system was employed following the convention defined in Appendix B. The resulting scoring of all the occlusion techniques is shown in Table 7.1. These scores were based on the computational results presented in the preceding section and the fundamental and clinical aspects of aortic occlusion reviewed in Chapter 2.

The requirements not assessable through the computational study of this chapter need some further clarification: The simplicity of the occlusion technique as to maintain/decrease the standard occlusion and CPB times were derived from the comparative findings presented in Table 2.1 showing that it is not entirely clear which method will incur the most time. This is because the "all-in-one" features of the EABO-system negates the insertion of an additional cardioplegic catheter. The cluttering of the surgical field by CEABO was assumed to be minimal, while the cost is of course slightly higher than EABO, because an additional component would be required.

Another interesting observation is that in terms of relative performance of all the occluders, the standard and crab-like cross-clamps did not differ in their performance. Note that parallel clamps are not available clinically. Of course, compared with each other, the standard cross-clamps produced comparative occlusion potential at lower induced strains, but other than that, very little differences were found. Combined with the clinical uncertainty of occlusion naturally resulting in over-occlusion, it is questionable whether standard cross-clamps would ultimately be safer than crab-like cross-clamps, especially in a high-risk situation, i.e. in the presence of calcified lesions. This is because both cross-clamps will severely damage the vessel, especially at the pinching sites, even if the standard cross-clamps will do so to a slightly lesser extent.

It must be noted, that these scores do not include any weighting of importance nor exclusion criteria. For instance, the importance of occluder stability might be considered to be more important than its cost, underlining the value of weighting each score by an importance ratio/percentage. Furthermore, $CEABO_{n,0}$ and $CEABO_w$ displayed such poor fulfillment of ensuring occluder stability, that its performance should actually exclude it from being further considered. Matters of weighting and exclusion increases the subjectivity of such an evaluation, and is best done by the end-users of the occluder – the clinicians.

Nevertheless, the presented score card reflects the current trend of clinicians to no longer use EABO, but rather cross-clamps, cf. Section 2.3.2. Taking a closer look at the scores, the cross-clamps are considered more favorable based on their simplicity, cost and ability to provide stability and accurate positioning. This finding arose despite its poor performance in preventing damage and minimizing deformation.

Furthermore, the score card also indicates the clear potential of CEABO with a profiled constrainer to be a feasible alternative to cross-clamping and EABO. This can be attributed to the main functionality of the constrainer: maximizing the occlusive load uniformly over the intimal surface, while constraining the tensile strain (and therefore damage) induced. Furthermore, no previous occluder has practically shown any potential of offering a clinically determinable occlusion threshold. Finally, requirements not tested by the computational models presented are easily evaluated since the only complexity that CEABO will add to the already clinically accepted EABO, is the placement and securing of the constrainer around the vessel at the desired site of occlusion.

But once again, the weighting of importance will play an important role: if occluder choice is clinically guided by the consideration of minimizing vessel damage (and therefore also patient-outcome), then it is definitely the best option. Furthermore, as opposed to all other occlusion techniques, $CEABO_{p,0}$ was occlusion technique exhibited the least comparatively poor performance, i.e. a very good performance overall. However, this poorly fulfilled requirement is the cost of the occluder. As discussed in Section 2.3.2, the material costs for EABO clearly exceeds those of cross-clamping, although no proper evaluation of the total treatment cost has been made. Regardless, the cost of a medical device is definitely also a strong proxy for clinical procurement decision-making.
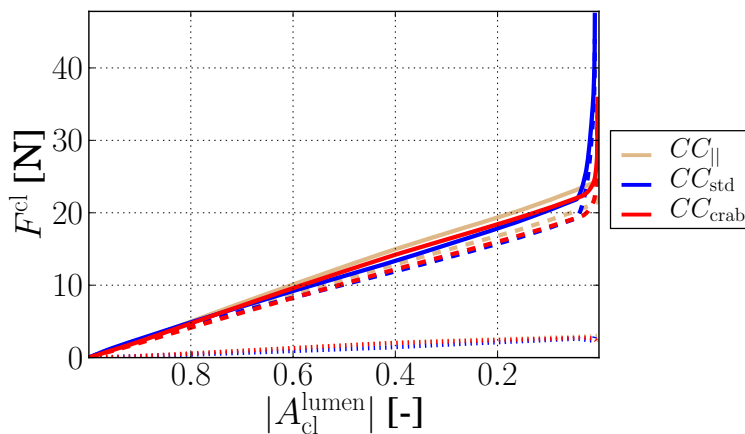
Figure 7.13.: The progression of the applied clamp force F^{cl}, also showing the components of normal (striped lines) and tangential (dotted lines) contact force which make up the total value (solid lines).

7.6.2. General findings

7.6.2.1. First steps towards validation of the presented models

Although the applied clamp force did not reflect a specific requirement, its outcome yields certain important perspectives, especially in terms of validating the model, as stated in Section 7.4.3. The progression of the applied clamp force during cross-clamp closure for the different clamps considered is shown in Figure 7.13. It is worth noting that the majority of the total applied clamp force consists of the corresponding normal components of the contact force, i.e. the choice of frictional coefficient had a minimal influence. Furthermore, the applied clamp force expectedly rose steeply as soon as intimal self-contact occurred for the first time. Another feature visible in these results, is that CC_{std} had an out-of-plane hinge and a large friction coefficient, causing the cross-clamp progression to pull more vessel material towards the occlusion site. This resulted in an earlier state of inner self-contact and a larger clamp force, as also seen in Figure 7.10.

These results provide valuable insights into the actual validity of these models in terms of its comparison to occluding an actual artery under *in vivo* loading conditions. In considering either carotid or femoral arteries of sheep, [226] used an experimentally derived formula to determine the applied clamping force based on the external diameter, the clamped thickness of the vessel and the contact area of the clamps – all for different notch levels of the clamp. For carotid and femoral arteries with mean external diameters of 7.2 and 5.3 mm, clamping forces of 3.76-6.61 N and 5.68-9.57 N for notch levels 3–6 were reported, respectively. Unfortunately, the clamped thickness was not reported although used in their formulation. However, the idealized artery modeled is expected to be in the range of twice the thickness and diameter of the carotid and the femoral artery in humans. If it can be assumed that the inter-species scaling between sheep and humans are minimal and that these ranges of dimensions hold, or perhaps slightly smaller for sheep weighing 40-50 kg, then the range of applied clamping forces resulting from the presented computational models are at least in a reasonable range and definitely in the right order of magnitude.

Regretfully, all of the other studies considered where an actual artery was clamped did not provide sufficient information to determine or derive the applied clamp force [8, 18, 90, 106, 157]. Furthermore, the scale of the difference between the human aorta considered here and studies cross-clamping the aorta

of a small rodent(s) [94, 103, 337] was considered too large for comparative purposes. These studies reported applied clamp forces in the range of 1 N.

Since full validation of the presented models was not possible and beyond the scope of this investigation, the stresses induced in the vessel wall were also not reported. Although this information was available from the chosen constitutive models, it was intentionally excluded. This was done because the strain yields a good and interpretable analog to the stress in the vessel, while also avoiding placing too much emphasis on stress quantities that are not yet validated. In this regard, the force quantities reported above also need to be evaluated with the proper consideration.

Finally, it should be noted that currently, the applied clamp force seems to be the only computational parameter directly comparable with an experimental parameter. As considered further in Section 7.6.3.3, it is clear that computationally, the clamping force will be dependent on a number of different factors that are not trivial to isolate. This is also evident from the curve that Famaey et al. [103] put forth as validation for their cross-clamping simulations, which actually showed a rather poor correlation.

7.6.2.2. The perils of load-controlled clamping

Probably the most fundamental difference between the application of the load between cross-clamping and an EAB-related occlusion, is that the former is displacement-controlled and the latter is load-controlled. It has frequently been suggested that load-controlled cross-clamps would be desirable, since quite simply, the load would be controllable. Examples of concepts based on this premise include a study by Darcin [76], in which the clamp surfaces were covered with balloon inserts of which the internal pressure can be controlled, effectively controlling the applied load. Another example is the concept presented by Luo et al. [218] proposing the incorporation of a shape memory alloy into the cross-clamp arm in order to limit the maximum load that can be applied to the aorta. Of course, the already mentioned studies on MVOF (Section 7.4.1) were also performed presupposing the feasibility of load-controlled cross-clamping.

However, from the results shown in Figure 7.13, it can be seen that for an idealized artery, the clamp force very steeply rises when intimal contact first occurs. This marked increase does not necessarily imply a proportional increase in the occlusion potential, cf. Figure 7.8. Therefore, since parallel cross-clamps are not clinically available, the clamp force at which occlusion will be first reached, will depend on the hinge configuration and exactly where the vessel is located relative to the hinge. This point of when occlusion first occurs will also lie somewhere on the steep gradient of the force response (only after intimal self-contact has occurred). Additionally, reaching such a point will not only require very sensitive load-control, but the desired level of applied clamping force where occlusion is first reached will be very sensitive to any variations of the clamping force measurement. Furthermore, should it be possible to find the clamping force where occlusion first occurs, then occluder stability might become an issue if the friction between the vessel and the clamp surfaces are insufficient, cf. the values obtained for $EABO_{\text{pure}}$ in Figure 7.9. This is because currently in the clinical setting, the stability of cross-clamps are increased by increasing the applied clamping force. Finally, as already depicted in Figure 7.2, the variability of the load required to sufficiently compress the vessel wall at the pinching sites will also play an important, non-trivial role in determining the load required to achieve occlusion. Factors such as variable local vessel wall thickness, material inhomogeneities and clamp orientation relative to the vessel axis all contribute to this variability, cf. Figure 7.13.

Therefore, the complexity of a load-controlled cross-clamping setup and the variability that are faced, seems to not justify further research on the topic. In the light of the presented results, it seems more reasonable to rather pursue alternative new solutions, such as CEABO, that is introduced here.

These above-mentioned aspects also further emphasize the reason why clinically determinable occlusion has not been practically realizable, despite being a desired feature of an occluder.

7.6.2.3. General model response characteristics

The results of the presented models of different aortic occlusion techniques qualitatively correspond to what has previously been reported, as reviewed in Section 7.1. These phenomena include an elevated axial stress in the region making contact with the cross-clamp, cf. inferior region of Figure 7.7, and also elevated tensile and compressive strains in the pinching sites.

The presented models further provide previously unevaluated detail using different cross-clamp configurations, considering EABO and also three design variations of the newly proposed occlusion technique, CEABO, as well as a detailed insights into the resulting strains and contact phenomena induced.

Although the idealized vessel was modeled to be 150 mm long, a limited influence on the strain response of the vessel was observed due to the complete fixation of the boundaries, i.e. the Dirichlet boundary condition preventing the displacement of the vessel ends, cf. Section 6.2.1. The influence of that the boundaries had are best explained by considering Figure 7.14, followed by the numerical results shown in Figure 7.15 of representative examples. In the former figure, the directions of the first principal strains experienced in each element are shown as lines, for a single "slice" of elements in the vessel wall.

Figure 7.14a shows such a slice taken at the boundary and the occlusion site of CC_{crab}, respectively. It can be seen that while the first principal strains were initially directed in the circumferential direction, the increase in clamp-progression changed its direction. However, its magnitude was practically not influenced as the occluder progressed, cf. Figure 7.15a. This change in the first principal direction, but not its magnitude, then explains the concomitant increase and decrease of the second and third principal strains, respectively, due to the large deformation of the vessel. Therefore, the influence of the strains induced at the fixed boundaries were considered to have a sufficiently small impact on the strains at the occlusion site to be considered negligible.

The results for $EABO_{\mathrm{pure}}$ yielded no change in principal strain directions or magnitudes in the slices extracted at the boundaries, as shown in Figure 7.15b. Furthermore, it can clearly be seen that for the EAB-related occluders, as shown in Figure 7.14b that the first principal strain remained in the circumferential direction at the occlusion site at the full EAB-pressure. Therefore, the influence of the strains induced at the fixed boundaries on the strains at the occlusion site could also be neglected.

7.6.3. Limitations

Considering all of the excellent research on modeling of the arterial stress-strain response as reviewed and used here, cf. Section 6.2.2, these models still require further improvement. In the following, brief comments are made concerning the limitations of the presented models, which nevertheless represent the current state-of-the-art.

7.6.3.1. Occluder models

Cross-clamping with clinically available clamps technically do not deliver a purely displacement-driven/dependent load, due to the slenderness in the clamp arms and the presence of the parallel-gap-width, cf. Section 6.2.1.3. This parallel-gap-width has a good average dimension of 3 mm, implying that the pinched thickness of the average large-bore artery with a pinched thickness of 3 mm or less will experience clamp surfaces that are nearly parallel upon first intimal self-contact. A vessel with a clamped thickness less than the parallel-gap-width will benefit from the relatively slender clamp-arms hinging on the distal pinching-site, thereby increasing the pressure on the proximal pinching-site. However, a thicker clamped thickness or an excessive cross-clamp load will result in the clamp-arms hinging on the proximal pinching site and cause a decrease in the occlusive load towards the distal pinching-site. This effect could not be evaluated in the presented models due to the prescribed displacement of the clamp surfaces itself. Such effects will

$|A_{\mathrm{cl}}^{\mathrm{lumen}}| = 1.0$

$\varepsilon_1 \; [\text{-}]$
0.065
0.064
0.06
0.056
0.052
0.05

$\varepsilon_1 \; [\text{-}]$
0.18
0.16
0.12
0.08
0.04
0.03

$|A_{\mathrm{cl}}^{\mathrm{lumen}}| = 0.4$

$|A_{\mathrm{cl}}^{\mathrm{lumen}}| = 0.02$

(a) CC_{crab}

$\varepsilon_1 \; [\text{-}]$
0.26
0.24
0.2
0.16
0.12
0.1

$\varepsilon_1 \; [\text{-}]$
0.135
0.13
0.12
0.11

(b) $EABO_{\mathrm{pure}}$ (c) $CEABO_{\mathrm{n,0}}$

$|P_{\mathrm{EAB}}| = 1.0$
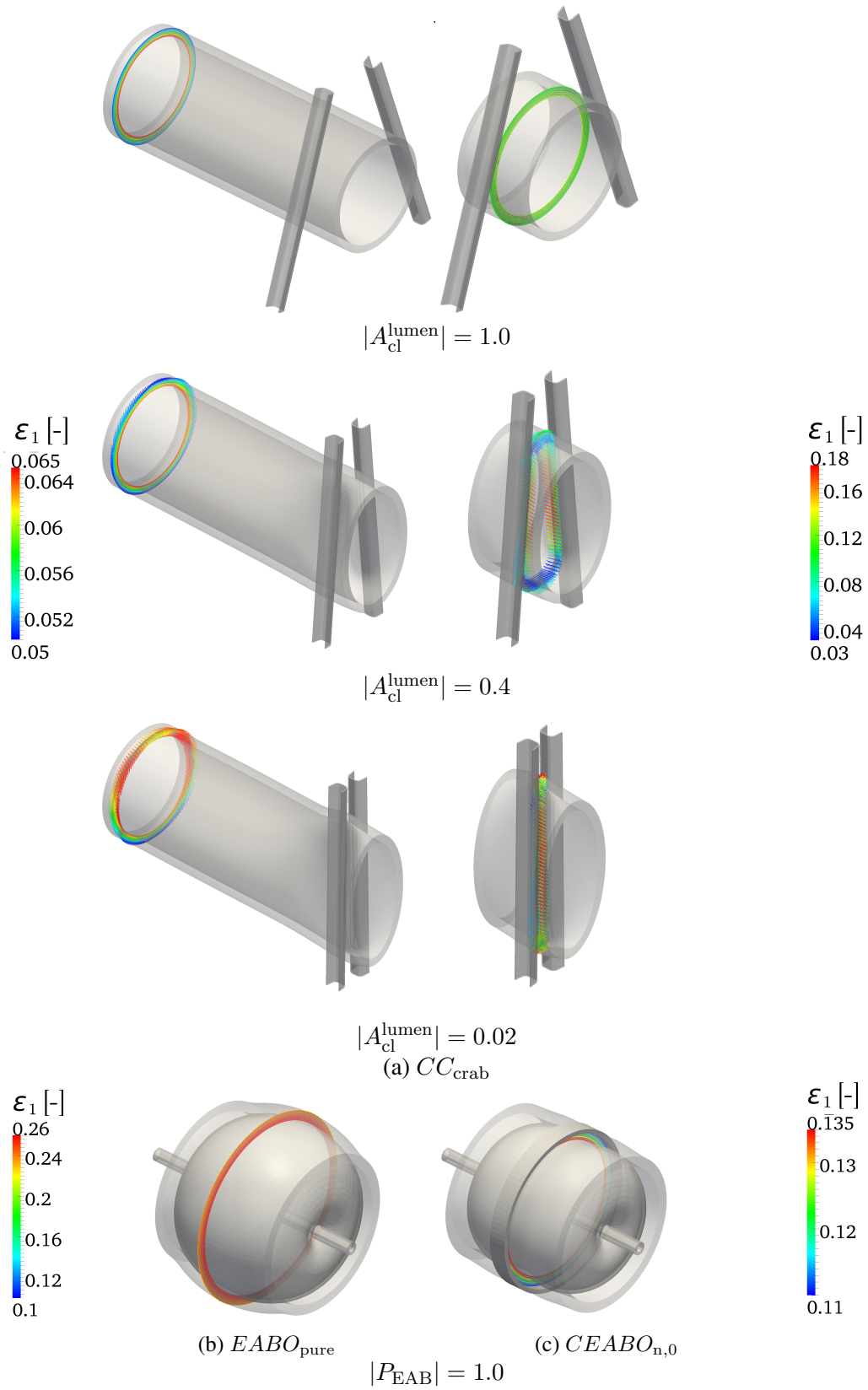
Figure 7.14.: The first principal strain directions of a "slice" of elements taken from the vessel wall, show-ing the directions of (a) a boundary and occlusion site slice for different stages of progression of CC_{crab}, and the occlusion site slice at a maximum EAB progression for (b) $EABO_{\mathrm{pure}}$ and (c) $CEABO_{\mathrm{n,0}}$. Note that the boundary slice indicated in (a), corresponds to the slice that is the closest to the boundary, shown in Figure 7.15c and d.
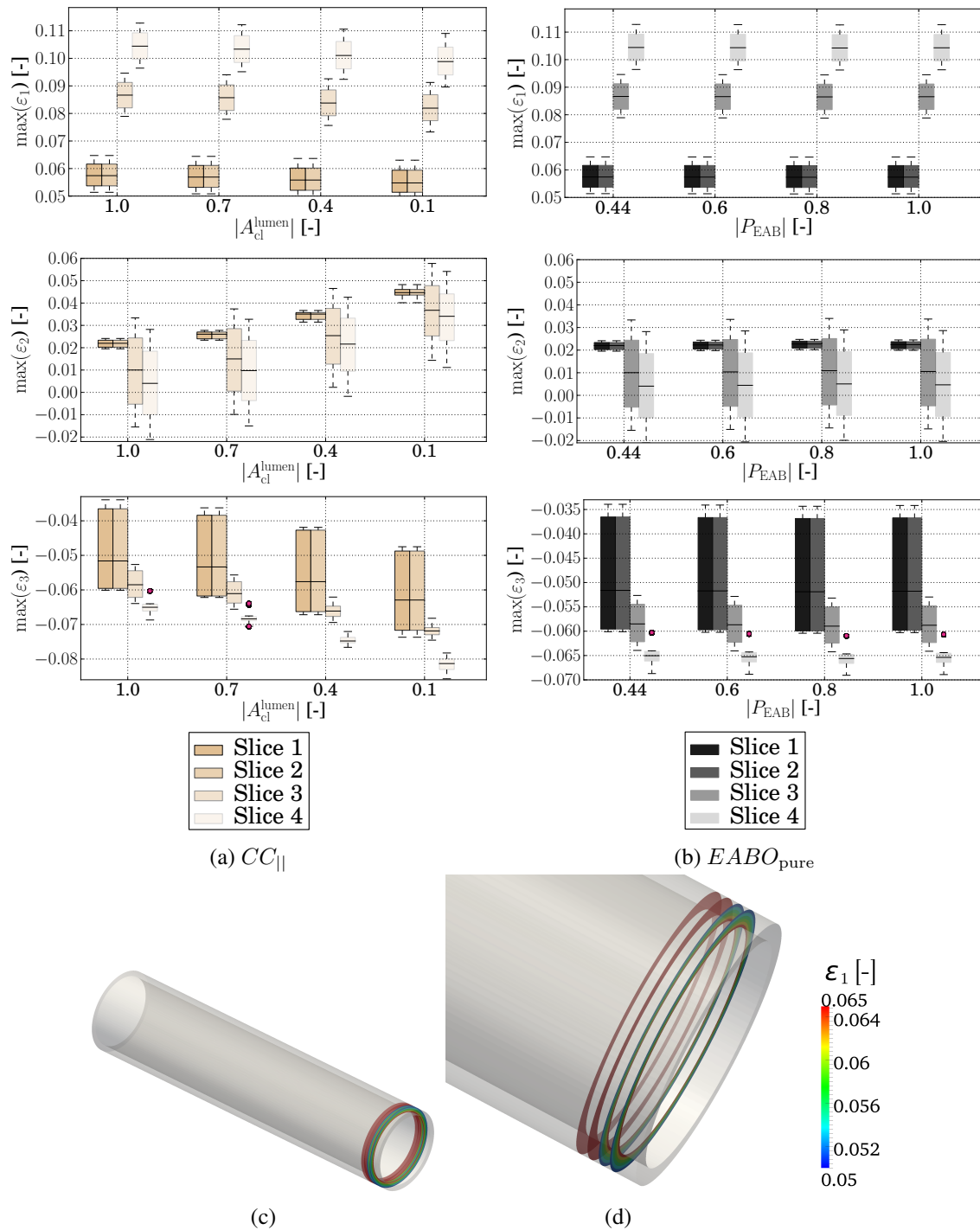
Figure 7.15.: The distribution of strain data at different equi-spaced axial slices, showing the results for two representative occluders in (a) and (b). The location of the slices relative to the boundary occlusion site are shown in (c) and (d). The axial slice intervals were 1.5 mm, starting 3.5 mm from the boundary progressing towards the occlusion site, considering the total vessel length of $L_{\mathrm{v},a} = 150$ mm.

become critical when clamping arteries with increased wall-thickness, especially with crab-pincher cross-clamps and should be considered in future investigations. However, given the already poor performance of any type of cross-clamps in terms of minimizing damage, the main question of interest will be whether a thicker vessel wall or an excessive clamping load could actually be responsible for a decrease in occlusion potential in increased applied clamp force.

Furthermore, the prescribed rotational movement of the clamp-surface around a fixed axis implied that the real configuration of the cross-clamps were not perfectly captured, especially considering the crab-pincher clamps. In reality, this type of clamp consists of one fixed arm, while only the opposite arm is moved. The effect of this exact configuration is not known and should be considered in the future.

Due to the boundary conditions chosen to fix the EAB in place, it was not possible to accurately determine how much resistance the EAB-catheter would provide in stabilizing the EAB. However, considering that the catheter is femorally inserted, its contribution is expected to be limited, due to the translational freedom of movement of the catheter in the much larger aorta.

7.6.3.2. Boundary conditions

As shown in Section 7.6.2.3, the fixation of the vessel at its furthest boundaries had a very limited influence on the strains yielded at the occlusion site.

The other main limitation of the presented model was that a constant follower-load on the entire intimal surface was used to model the hydrostatic pressure that would be exerted by the blood. However, no variation in this pressure due occluder-intima or intima-intima contact was considered. It meant that upon intimal contact, the hydrostatic load was still exerted upon the region in contact, which is obviously unphysical. However, equilibrium was of course always maintained after completion of each simulated time step. Thereby, some variation in the occluder-intima loading magnitude might exist, compared to reality. Nevertheless, this influence is expected to be more or less constant throughout and expected to yield only a slight difference in the presented results. However, the full effects of this phenomenon need to be considered in future studies.

Furthermore, once a valid line along which occlusion can occur was formed, i.e. $\mathcal{S}_c^{\mathrm{closed}}$ exists, the hydrostatic load remained unchanged. Clinically, however, occlusion of the ascending aorta during CPB will mean that the higher pressure from the systemic circulation is cut off from the proximal side, where the pressure will drop because of a (partially) emptied heart. Its effect was not investigated, but is expected to be less than the fully pressurized side.

Finally, no consideration was given to dynamics, which will especially be critical when doing a more in-depth evaluation of occluder stability faced with dynamic loads, such as an instantaneous and substantial change in blood pressure on either side of the occlusion site.

7.6.3.3. Modeling the pinched aortic wall

Modeling of the pinched aortic wall can safely be considered as the most challenging feature of the presented simulations, because it involves a number of aspects that lay bare the limitations of the chosen model assumptions, as considered in the following.

Hyperelastic material modeling Firstly, despite the maturity and development behind the used material model, itself and others commonly used in literature, remain phenomenological in nature. No specific components are considered, but rather lumped together in a model describing a general, near transversely isotropic response, assuming that the fibers in compression can bare no load. As demonstrated from a micromechanical perspective by Ateshian [13], no such phenomenological models can fully mimic the strain induced anisotropy generated. This is because in the deformed configuration under a load causing

a mix of fibers in tension and compression, the material symmetry is only dictated by those fibers in tension. Material symmetry depends on the single fiber angular distribution and strain field in the deformed configuration, which cannot be represented by these lumped models.

Secondly, when considering the parameter fitting from experiments to material models like the Humphrey model used here, Eq. (6.86) to (6.88), it is important to note the non-uniqueness of the final fit, as well as the fact that the parameter values were not bounded during the fitting procedure – as was the case in the study of Roccabianca et al. [297] where the chosen parameters for the aortic wall were obtained from, cf. Section 6.2.2.3. This publication featured five sets of data for each direction measured from five different loading protocols of bi-axial tests extracted from literature. Thereby, 10 sets of data were available to fit the 8 unknown parameters. However, as shown in some preliminary studies conducted at our institute (unpublished data), when the angle of the diagonal fiber direction, $\alpha_{\text{fib}}^{3,4}$, was allowed to vary, a unique set of parameters could be obtained for every angle. Furthermore, when no parameter bounds are set, it is possible for that parameter to reach very small values (close to zero), as can be seen in the resulting fits done by Roccabianca et al. [297], e.g. consider the values from data sets shown to be "reasonable" for the Labrosse and Martin sets of data for the ascending aorta, with the isotropic (matrix) component $c < 10^{-6}$. Although this result may be mathematically valid, it will otherwise yield numerical instabilities and is physically questionable. Conversely, very large values of c will cause an increased bending stiffness of the material [81, 163]. Nevertheless, the chosen parameters reflect a valid response of the arterial wall, with diagonal fiber angles in the range of what is typically measured for the adventitia and media [309]. Additionally, these limitations were considered during the choice of the material parameters, as reflected in Section 6.2.2.3.

Thirdly, not only the large inter-study variability in experimental protocol, but also the according variability between estimated parameters has also been exemplarily demonstrated in the publication of Roccabianca et al. [297]. Despite the concerns expressed above, this large variation of biological data, also in the context of vascular tissue, has been well documented. The sensitivity of the presented models to a variation in material parameters were not tested.

Fourthly, the matter of tissue incompressibility and the modeling thereof remains a highly debated issue. The incompressibility of any cardiovascular tissue is often postulated for loading under a physiological regime, based on the fact that its main constituent is water, e.g. [169, 349]. However, experiments already performed in the 1980's by Fung's research group revealed that a very small percentage of water is extruded from a vessel wall under compressive stress, deeming it slightly incompressible. Furthermore, in using their exponential type model, cf. Eq. (6.82), a completely different set of material parameters was obtained from the fitting procedure when assuming near-incompressibility as opposed to perfect incompressibility [68]. Since incompressibility in computational models is frequently modeled by penalizing the volumetric change of volume, as done in the presented work, cf. Eq. (6.86), perfect incompressibility will never be reached, since it would require a bulk modulus κ (or penalty parameter) of infinity. This does not prove problematic, because it is not observed experimentally [256], further justifying the assumption of near-incompressibility.

Fifthly, tying in with the previous point: difficulty arose when choosing a value for the bulk modulus representing the correct amount of compressibility, since its choice will influence the stresses quantities, as well as the conditioning of the system matrix to be solved. For isotropic materials, the bulk modulus is easily derived from the given shear modulus and the desired Poisson's ratio. For the fiber-reinforced hyperelastic model employed here, this choice is not so obvious, infrequently elucidated upon, and will have a significant effect on the stress values [268]. In the computational studies of cross-clamping reviewed, Gasser et al. [124] simply chose a high bulk modulus 10 MPa, given the shear modulus of 27 kPa and 7 kPa for the media and adventitia, respectively. Famaey et al. [103] did not indicate the unit used for the reported bulk modulus, but if consistent with the other parameters presented in another publication [105], they chose 5 MPa, given a shear modulus of 23.63 kPa. No further consideration was given to this matter

in this publication. The parameters used in this investigation were in the same range and ratio as these two studies, cf. Table 6.1. The bulk modulus was simply chosen based on a similar ratio between the bulk and the shear moduli and one that ensured acceptable and feasible numerical solution times. No further consideration was given to the matter of incompressibility, although in the light of the reviewed data, a sensitivity analysis of this parameter is warranted, which should precede the full model validation in a future study.

Finally, it must be noted that the isochoric-volumetric split of the SEF employed here, cf. Eq. (6.42), has recently been shown to produce unphysical results because of the hydrostatic component of the load [268, 348]. This occurs because the strain energy of the fibers only contributes to the total strain energy when the isochoric stretch component is larger than one (no contribution for fibers under compression) and not the actual (original, coupled isochoric-volumetric) fiber stretch. Therefore, the tensile stretch from the volumetric loading of an element will not contribute to the strain energy and consequently to all its derived quantities. The implications, as well as the remedy to this material limitation is unknown, but the cause can be attributed to its inherent formulation. However, it should be noted that the internal hydrostatic pressure (modeling the influence of the blood pressure) and the load from the EAB always acted orthogonal to the wall and therefore out-of-plane with the fibers of families. This partially minimizes the stated unwanted effect, since the resulting strain energy will predominantly come from the contributions of Ψ_{vol} and $\bar{\Psi}_{\mathrm{matr}}$, cf. Eq. (6.86) and (6.87), respectively. Furthermore, despite the compressive load from the cross-clamps, the pinching site appears to have been dominated by isochoric loading, as evident from looking at the deformed computational mesh (Figure 7.8), as well as from the quantitative results showing how the strains in at the pinching sites dominated. However, this was not analyzed further and definitely requires further consideration in future investigations.

Modeling of damage The experimental biaxial tension data to which the chosen parameters were fit were up to a $\varepsilon \approx 0.15$, while the actual fit was only done up to $\varepsilon \approx 0.12$. From the presented results, it is clear that the applied occlusive load induced strains beyond this range and therefore relied on the validity of this data being extrapolated. Due to the limited strength of both the fibered, matrix and cellular components responsible for the mechanical strength, inclusion of a suitable damage model would reveal more accurate information with regards to the resulting damage [54, 228, 354]. Such a damage model would especially be important to not only reveal primary regions of damage, but also secondary effects due to primary material failure. Additionally, inclusion of damage modeling will be key when considering the stress-strain state of the aorta after occlusion or due to repeated occlusion, but was beyond the scope of this investigation. Nevertheless, the regions of increased strain can be interpreted as regions with a higher potential for primary damage occurring.

Additionally, as already discussed in Section 7.5.1, the effect of damage under tensile loading is not the only concern, but also loading in compression and in shear. Although experimental studies on occlusion have not been able to distinguish between the different types of loading responsible for damage, it is clear that the compressive loading at the pinching sites played a significant role in damage, as seen in the resulting lacerations on the intimal surface due to cross-clamping, cf. Figure 2.2. This has not been considered in previous computational studies on aortic occlusion that incorporated damage models, cf. [54, 103]. Furthermore, since the duration of aortic occlusion during CPB is typically more than 30 minutes [18], the influence of compressive soft tissue damage mechanisms will be all the more critical [303, 322].

Finite element technology As discussed in Section 6.1.4.3, a number of aspects were incorporated into the presented models to minimize the effects of numerical locking. These included the so-called F-bar elements, purely hexahedral meshes and high mesh refinement in areas of extreme loading (stretch, compression, bending). In this way, volumetric locking effects could be eliminated, while shear locking effects could be partly circumvented. However, the extremeness of the loading at the pinching sites (severe bending, shear and compression) requires further evaluation to justify the extent of the shear locking effects.

Patient-specific aspects There are a number of patient-specific factors that will be responsible for variability in the results presented, including the lack of patient-specific geometry and heterogeneous material distribution due to natural biological variation of the wall thickness, as well as local stiffening of wall due to aging processes and calcifications. Due to the importance of these aspects to provide more clinically relevant results, it is considered further in Chapter 9.

7.7. Conclusions and future perspectives

7.7.1. Computational models

Apart from supplying certain restrictions associated with the presented models, the limitations presented above emphasize the challenging consideration of the computational modeling of aortic occlusion. This is because it entails modeling the aortic material under a complex state of loading, with the aorta consisting of a composite, nearly-incompressible, anisotropic material in a range of loading where damage to its components are likely to occur. Furthermore, these components not only have different damage thresholds, but the thresholds themselves are dependent on the type and duration of loading. Additionally, the mechanical interaction between these components and inter-component interactions are not fully understood. All of these aspects clearly show the pressing need for future investigations to improve material models of such complex composite materials.

Nevertheless, despite these limitations, a single parameter, i.e. the applied clamp force, cf. Section 7.6.2.1, indicated that the presented results were at least in a suitable range, although there were many factors that could have influenced this quantity. Therefore, although not fully validated, at the very least, the extracted results represented qualitative results within a reasonable quantitative range. This observation was also seen in the curve that [103] claimed to have validated their results. As stated in Section 7.1.1, such information cannot be used to fully validate the model. These authors did not consider reasons for their presented deviation, as was done in the preceding paragraphs.

The performance of the different constrainers designs during CEABO were of special interest. This occluder loading configuration, cf. Figure 7.2, resulted in the least extreme loading of the vessel wall, i.e. predominantly compressive loading, compared to the complex and extreme loading of the other occluders. This was also intended in its design, and also had the added benefit of presenting less effects that would bring its computational results into question.

The models of this dissertation improved upon and extended the work of all previous computational studies on the subject, i.e. modeling real clinically used and new occluders, using a more suited material model and better FE technology. However, much future work is required to be able to model this complex state of loading in the given material. Models with these capabilities will not only provide valuable information in improving the safety, efficiency and reliability of occluders and new occluder designs, but will also prove valuable in applications of robotic surgery, where soft tissue response due to manipulation by robotic components will become increasingly important.

7.7.2. Occlusion potential and thresholds

The newly formulated measure of an occlusion potential presents a whole new array of research questions: can an experimental setup be designed to effectively evaluate the occlusion potential and occlusion threshold? Since the occlusion threshold is a pressure value, one possibility might be to keep the occluder loading constant and vary the fluid pressure to extract such levels experimentally. Furthermore, can this measure be successfully related to the occlusion potential derived from computational results?

Since the occlusion potential is only dependent on the normal contact traction (or contact pressure) and whether a closed contour line formed along the to-be-occluded surface, it will also be especially useful

when considering so-called "wet" contact conditions. Here, only "dry" contact conditions were considered. The progression of the occlusion potential might be different than reported here, since the fluid pressure could influence the contact pressure, but its validity is not expected to be compromised. Furthermore, although it was defined here for occluding a vessel, without a loss of generality, this definition can be used to evaluate occlusion potential for any type of geometry, although its automated extraction, as given in Eqs. (7.6 to 7.4.1) will most likely have to be altered.

Finally, it should be noted that occlusion potential is not limited to vascular occlusion, but will be useful in the occlusion of any type of conduit where the over-loading or damage in one or both of the materials in contact become critical, e.g. occluding only a part of the aorta (partial clamping, cf. Section 2.4), occluding other biological conduits such as the intestines, the esophagus, etc. Furthermore, industrial application using polymer seals to separate fluid pressure between two compartments can also benefit from such a measure, e.g. an O-ring used to separate the combustion chamber from the piston-shaft and rotor housing – if such a similar measure does not already exist.

7.7.3. Improvement of existing occlusion techniques: cross-clamping

As already discussed in this chapter, cross-clamping is a dangerous procedure in terms of inflicting vessel damage. Having a hinge-configuration that deviates the least from a parallel orientation will make the impact slightly less, but will be dependent on the applied load – which arbitrarily depends on how strongly the clinician chooses to apply the clamps. Furthermore, clamps provide a predominantly displacement-driven load, whereas the value of load-controlled clamping is questionable, simply due to the sensitivity required, the high magnitude of unavoidable damage that will be caused, especially due to pinching but large deformation in general, and the unknown state of occlusion.

Aspects that require further research attention are understanding the influence of clamping inserts, and how it can be improved upon. Furthermore, not considered in this chapter, was the influence of applying the cross-clamps to the aorta, whilst deviating from an orthogonal angle with the vessel axis. What will the influence be of a potentially larger contact area between the clamps and the vessel? And will such an adjusted clamp position also implicate more arterial wall material in the pinching site, cause more damage? This aspect inherently occurs in patient-specific cases and has been further considered in Section 9.1.2.3. Finally, as already mentioned in Section 7.6.3.1, the parallel-gap-width needs to be fully investigated when considering occlusion of vessels with clamped wall thicknesses larger than the parallel-gap-width – and potentially how such a parameter can be optimized along with the slenderness of the clamp arms to improve the cross-clamp load delivery.

7.7.4. Improvement of existing occlusion techniques: EABO

As extensively reviewed here, the main problem with EABO is its stability, but ultimately its entire cost-to-benefit ratio. The most apparent improvement to this occlusion technique, as comprehensively analyzed in the preceding chapter, is the addition of a constrainer to achieve CEABO. No other improvement to the EABO system itself without the use of a constrainer is foreseeable, because the problems associated with EABO do not depend on the EABO-system itself, but rather on the unconstrained stretching of the vessel to be occluded.

From the preceding analysis, it was also clear that the profiled constrainer would be the best, but much room for improvement remains. This includes optimizing the profile shape to the inflated EAB – or even optimizing both. It is noteworthy that the exemplary results were obtained using CEABO with a profiled constrainer with a maximum profile amplitude of 1 mm, with a shape not directly considering the inflated shape of the EABO. Furthermore, it is apparent that the frictional response between the EAB and the vessel are unwanted and unnecessary, because occluder stability is largely determined by the normal

component of contact force, cf. Figure 7.9, whereas EABO relies strongly on both the normal and frictional components. Therefore, as opposed to EABO, CEABO can be made even safer by considering an EAB with a treated surface to lower the frictional coefficient, e.g. [53], because its stability is largely provided by the normal contact pressure exerted on the slanted edge of the profiled constrainer. Of course, the final delivery of such a new and improved device will require additional detailed design, material selection, application considerations and regulatory approvals, not considered here due to being beyond the scope of this investigation.

Finally, although cross-clamping might still have the advantage of simplicity and stability, CEABO offers improved patient protection and a high cost-to-benefit ratio – which is (or at least should be) the deciding factor for the clinical acceptance of a vascular occlusion technique. Furthermore, a safer procedure responsible for better clinical outcomes does not only hold the potential to reduce patient morbidity and mortality, but will also subsequent patient-care costs. In the light of such expected benefit, initial high material costs might be justifiable. However, before all of this can be considered, the experimental and then clinical efficiency and usability of CEABO still needs to be demonstrated in future studies.

8. Proximal flow characteristics resulting from high-velocity arterial cannular flow jet(s)

Problems are only opportunities in work clothes.

— Henry J. Keiser

From the comprehensive review of the different aortic manipulation maneuvers that will disrupt physiological hemodynamics during arterial return in Chapter 3.1, it is evident that the complete influence is multi-factorial in nature. However, as with the aortic occlusion considered in the previous chapter, current experimental and clinical data supply a non-specific, incomplete understanding in terms of the type of disturbance, its extent and the consequences of arterial return. Thereby, clinicians are left to make case-specific decisions about key aspects of a treatment, based either on an existing solution shown to have yielded acceptable (or at least predictable) outcome with its associated variation, or a supposedly improved solutions with outcome variability that is simply not known. Of course, these two extremes form the boundaries of a spectrum of different cases that require clinical decision-making. Nevertheless, especially considering the complexity and the variability, but also the range of disturbances that can be traced back to the region of the aorta where the oxygenated blood is fed back into the systemic circulation (arterial return), computational evaluations of the influences of proximal flow disturbances produced by arterial cannular flow become essential. However, such evaluations, as presented here, often lack findings that can be translated into clinical practice. Consequently, such evaluations are urgently needed to increase the knowledge base in order to aid in better (case- or) patient-specific clinical decision-making.

This chapter considers the fluid computational study of proximal flow disturbances caused by arterial cannular flow jets for various cannula variations. In this context, these proximal disturbances refer to any non-physiological effect of the fluid on the region of the ascending aorta between the occlusion site and first major branching of the aorta into the brachiocephalic artery. The specific aim is to evaluate of the proximal disturbances caused by the cannula configuration, i.e. the tip orientation and its insertion depth, as well as the tip design – clinically used and a newly untested cannula – in the absence of patient-specific variability. The models used to evaluate these effects have been introduced in Section 6.4. The structure of this chapter entails a review of previous computational studies performed in this context, the formulation of functional requirements for optimal proximal flow characteristics during arterial return, the consideration of computational mesh requirements and the introduction of a newly proposed cannula tip design not yet clinically available. Thereafter, comparative evaluations of the computational results are performed, followed by a detailed discussion of the overall comparative outcomes due to cannula variations considered, other general findings, limitations of the current study and closed off with concluding remarks and future directions.

8.1. Existing computational perspectives

A number of investigations in recent years have focused on the disruption of physiological hemodynamics due to arterial return. These are considered in detail in the following, specifically from the perspective of

assessing the proximal influence of the impinging jet, as well as considering its comparative value with the results of this investigation.

8.1.1. Arterial return during VAD

The development of ventricular assist devices (VAD) in recent years have lead to a number of investigations considering the effects of arterial return during VAD, i.e. getting the blood from the VAD back into the systemic circulation (native aorta). Although such a configuration is not exactly equivalent to an arterial cannula pointing into the aorta, many similarities exist: most devices provide continuous flow and possess an aortic outflow conduit, sutured to the aorta (end-to-side anastomosis). Such a configuration is very similar to the cannulas considered in this investigation. Information about additional flow coming from the heart during VAD support or related aspects are not considered in the following.

Probably the first series to consider these flow effects of VAD arterial return on the physiological hemodynamics is by May-Newman et. al [232, 233]. Both studies considered different angles of attachment of the conduit having a diameter of 12 mm. The first study only considered an idealized ascending aorta, i.e. a short tube, while the second study considered an idealized aortic arch with no branches, i.e. a curved tube. The lack of mesh information (global mesh refinement is reported, but no element sizes) and the over-simplified geometry makes it difficult to conclude on the quantities reported. However, qualitatively it can be stated that the angle of conduit attachment and its position along the aortic arch significantly influenced the WSS and flow fields.

A more comprehensive series of studies by Yang et. al was performed investigating the effect the VAD yielding continuous flow [364], pulsatile flow [366], and a comparison of these two flow regimes [365]. Since the first two studies built up to the third, specifics given below refer specifically to the third study. A VAD outflow conduit with an inner diameter of 6 mm in the shape of a bent tube was modeled to be anastomosed to the ascending aorta of the aortic arch obtained from pediatric patient (8 yrs) with an aortic inlet diameter of 11.6 mm. Full flow through the conduit was 1 l/min, yielding a maximum inflow Reynolds number of 1011 and 4269 for continuous and pulsatile flow, respectively. Turbulence was considered using an implicit Large Eddy Simulation strategy and quantities averaged of an appropriate number of flow cycles. A hexahedral-dominated hybrid mesh with a boundary mesh layer to resolve the viscous sub-layer caused during turbulent flow, as well as the WSS. Suitable mesh refinement yielded acceptable results with a first element size of $h_{\mathrm{f}} = 0.05$ mm and a base level size of $h_{\mathrm{b}} = 0.7$ mm, cf. Section 8.5 below. In terms of the conduit jet hitting the opposite wall, a stagnation point is described in this region where the WSS is at its lowest and pressure at its highest. Although not explicitly reported, estimated from the graphical representations, peak WSS was ∼150 Pa and ∼350 Pa (time-averaged), and peak pressure was ∼9 kPa and ∼15 kPa at the opposite wall for continuous and pulsatile flow, respectively. It should be pointed out that peak WSS values over the entire aortic arch were reported occurring at the kinks on the fluid boundaries, i.e. suture line of the conduit into the aorta, the inflow boundary and a bifurcation region. However, simply from a physical point of view, these quantities raise some concerns. One possible explanation might be that errors occurred in computing the surface normals at these kinks, which will significantly influence the computation of the WSS, cf. Eq. (8.4) below. Apart from a hemolysis index reported, the division of the flow into the respective branches of the aortic arch was given much attention and finally considered a purely resistive outflow boundary condition, i.e. pressure at the outflow was increased proportional to the flow. It was once again emphasized that the physiological hemodynamics are largely disrupted – for both continuous and pulsatile VAD inflow. Furthermore, the position of the conduit along the aorta also played a significant role in this regard. However, a restriction on the findings of the pulsatile flow simulations are that only resistive boundary conditions were considered at the outlets, which cannot capture certain important time-dependent impedance characteristics of the downstream vasculature [173].

8.1.2. Arterial return during CPB

The previous studies considering the hemodynamic disturbances caused by arterial cannular flow are specifically reviewed for extracting information relevant to this investigation.

One of the first studies on this topic was reported by Tokuda et al. [336], simulating a single case of a curved end-hole cannula located at the ascending aorta, pointing towards the upper branches of the aortic arch. However, due to the preliminary state of this study, reflected in paucity of information regarding the cannula shape, inner diameter, mesh adequacy, concerns about high flow rates considered without consideration for turbulence and the simplified boundary conditions used (zero pressure at all outlets), it is not further considered.

A more thorough attempt in the same year was reported by Pekkan et al. [277], comparing physiological and pulsatile CPB neonatal aortic hemodynamics considering all branches from the aortic arch. A cannula with an inner diameter of 2.46 mm was used to supply 0.61 l/min at 94 bpm yielding a peak Reynolds number of 1936 and a peak jet velocity of $\sim$3000 mm/s. No turbulence modeling was considered. Global mesh refinement was performed, but no details were given on mesh sizes or any local mesh refinement. Resistance boundary conditions were applied at the outlets, with the flow patterns significantly altered when the split ratios were changed by 10%, i.e. split between the amount of blood entering the first three branches of the aortic arch and the descending aorta. The split ratio is dependent on the values of resistance at each outlet in relation to the others. Apart from a hemolysis index considered and different indexes for quantifying the efficiency by which the pulsatility was transferred, the local effects observed for the cannular flow were high WSS at the landing site (WSS = 147 Pa), but also a decrease in perfusion pressure of the branches past which the jet flowed – a Venturi-type effect. Despite meticulous attention to ensure realistic boundary conditions, the outflow boundary conditions appeared to lack crucial time-dependent impedance considerations, as mentioned above. Furthermore, the mesh resolution at the walls was not reported, the cannula was unfortunately/conveniently pointed along the longest traverse section of the aortic arch and the study consisted only of a single case. Therefore, the influence of the cannular flow on the landing site is difficult to verify due to the uncertain mesh resolution used and represents a best-case scenario for the impact that the cannula can have on the aortic wall. Furthermore, it should be mentioned that although a clamped neonatal geometry was employed, no particular effects of this clamped geometry was reported, presumably also because the cannula was pointed in the opposite direction of the clamp-site.

In an attempt to thoroughly investigate the influence of cannula position, orientation, but also the cannular jet-induced Venturi effect described above, Kaufmann et. al simulated arterial cannular flow through a curved end-hole cannula for patient-specific geometries [187, 188]. However, no indication was given of the computational methods employed, the mesh size, mesh convergence, cannula size/type, specifics about all the cannula positions and orientations tested. Furthermore, a constant static pressure boundary conditions was applied to all the outlets. Since the pressure at these outlets should represent the response of distal vasculature, a resistive boundary condition at the very least is critical, especially considering the flow characteristics that were investigated. Due to these shortcomings, this series was not further considered.

In a more recent study series by Kaufmann et. al [189, 190], a similar setup as the preceding was investigated, but now reporting that a global mesh sensitivity study was performed. These investigations differed from the former due to the inclusion of a simplified auto-regulatory boundary condition at the outflow of the cerebral vessels based on a desired, non-patient-specific cerebral perfusion pressure vs. cerebral blood flow rate. Unfortunately, once again very little information was given about the cannula geometry and the computational methods used, especially considering the high cannular flow rates considered (4.5 to 6 l/min). Furthermore, the auto-regulation boundary conditions were only applied to the cerebral vessel outlets, not other outlets where auto-regulation can be active. However, interesting to note

is that results indicated that the inclusion of such boundary conditions lessened the disruption of flow to the cerebral vessels during CPB – i.e. a reduced influence of the above-mentioned jet-induced Venturi effect that potentially caused back-flow through one or more of the aortic arch branches. Nevertheless, such conclusions need further elucidation, since it does not include time varying or system-specific feedback to enable closed-loop auto-regulation, e.g. [195].

A recent series of studies by Menon et. al extended the neonatal simulation performed by Pekkan et al. [277], considering two different straight end-hole cannula orientations ($D_i = 2.0$ mm, $Q_{in} = 1$ l/min, $Re = 2150$, resistive outflow boundary conditions) [239]. The follow-up study considered model setup, but now with 17 different orientations of the same end-hole cannula and an additionally proposed end-hole cannula with a with diffusive tip, of which the diffusive cone angle was also varied [238]. The first study considered considered an unstructured Cartesian grid with mesh sizes adequate to consider it as a direct numerical simulation (DNS) of the considered flow. Despite the high mesh resolution, aspects like WSS could not adequately be assessed due to the type of mesh used and was therefore not reported. The main finding was that the orientation can influence the pressure-drop vs. flow rate characteristics of the cannular flow and in turn, also the amount of hemolysis induced. In the second study, an unstructured tetrahedral mesh was used with refinement only done to adequately resolve vessel outflows, bringing into question values of WSS reported. However, it was shown that with the employed resistive boundary conditions, (unwanted) flow reversal in the brachiocephalic artery caused by cannular flow at all tested orientations from the straight end-hole cannula can be prevented when adding a diffusive tip to the considered cannula. In other words, more diffused flow will benefit cerebral circulation during CPB.

In a recent study series by Avrahami et. al [14, 15], arterial cannular flow through three different aortic cannula tips for four patient-specific aortic arches at six different orientations at effective flow rates of between 4.5 and 5.5 l/min was considered – 44 models were considered in the second study (the bigger of the two studies). The cannulas used were end-hole cannulas with a straight, curved, and curved with backward suction tip, respectively – evaluation of this novel tip design characteristics itself has been reviewed in Section 3.1.2.2. Findings once again indicated the significant and varying influence that the cannula tip design/geometry, cannula orientation and the patient geometry had in the resulting aortic flow character. Furthermore, two different clamping orientations applied to the aortic geometries were considered, although only pictorial details are given as to the relative location thereof or how the geometry was accordingly deformed. No further mention to the influence of the clamped geometry was reported. Since flow rates at the cerebral vessel outflows were prescribed and only one layer of boundary mesh elements of an unspecified size were given yielding values of WSS compared with studies that clearly were not capable of resolving the WSS [254, 336], the ultimate value of these results are qualitative at best.

8.1.3. Summary of findings from literature

Whether from VAD or from cannular flow, it is clear that the cannulation site, patient-specific geometry, cannula orientation, tip design, flow character (continuous or pulsatile) and flow rate all had a significantly disrupting effect on the the physiological arterial flow.

But probably the most important aspect to note, from a modeling perspective, is that these variations are not trivial to model. In order to accurately model such effects, an accurate geometry of the cannula tip, inserted at the actual cannulation site, orientated in the given direction is required. Furthermore, an appropriate computational mesh size in the fluid field in general and also specifically along the aortic wall is necessary. It was also clear that the outflow boundary conditions play a very important role in the resulting flow structures and directions when considering such flow through a domain with multiple outlets. In this context, it also becomes paramount to include time varying effects such as impedance of the distal vasculature and auto-regulation mechanisms when considering time-varying flow.

Further modeling aspects that do require further consideration in this context is the influence of considering turbulence modeling in high flow regimes typical of CPB, including its proximal effects where the jet lands and its distal effects in influencing the resulting flow structures. Moreover, no comparative effect of the influence of using a non-Newtonian fluid was considered, but it was expected to be minimal due to the high expected shear rates caused by cannular flow, cf. Section 6.4.2, especially proximally. Only the studies by Kaufmann et. al considered a non-Newtonian fluid model but neglected to show any results justifying the necessity of its use. Finally, the influence of vessel distensibility was not considered and would also require further consideration in future studies.

8.2. Functional requirements for optimal proximal flow characteristics during arterial return

The formulation of the functional requirements listed below did not only require the detailed knowledge gained from the reviewed literature, cf. Sections 3.1 and 8.1, but was updated iteratively as new insights were obtained from the computational study presented below. As such, a cannula that delivers optimal arterial cannular flow has to,

1. Minimize the impact on the blood by

   a) Ensuring adequately low shear rates/pressure drop induced by cannula tubing (preceding the tip) and the tip design,

   b) Offering a suitable, bio-compatible surface coating;

2. Maximize jet dispersion by

   a) Minimizing jet exit strength – defined in Section 8.6.3,

   b) Minimizing peak WSS exerted at the (primary) jet landing site,

   c) Minimizing the danger zone area – defined in Equation 8.3,

   d) Facilitating (physiologically) distributed flow entering the aortic arch;

3. Prevent jet from landing near the occlusion site;

4. Be simple, meaning that it should

   a) Constrain the tip insertion depth,

   b) Possess a small inserted tip size,

   c) Provide straight-forward insertion and extraction;

5. Robustly yield similar performance despite clinical variations, including cannulation site, orientation, insertion depth, flow rate etc.;

6. Minimize cannulation site leakage;

7. Be reliable in the sense that the tip will not break, crack, bend or come off – and thereby hampering its performance;

8. Be cost-efficient.

Requirements 1 and 2 were specifically separated, because these aspects are not simply inversely related, as discussed in Section 3.1.2.2. Evidently, the functional requirements of cannular flow for optimal *distal* flow conditions will naturally overlap these. However, no further consideration was given to distal flow requirements, due to the stated scope of this computational evaluation.

As with aortic occlusion, it is once again not sufficient to say that one cannula is better than another based on any one single parameter, cf. Section 7.4, but has to take all of the functional requirements into consideration. This is evident from the multitude of requirements formulated above. Many of the parameters that are not easy to define or evaluate are further considered in Section 8.4.

8.3. New cannula tip design: Shielded cannular flow

As already introduced in Section 6.4.1.2, the shielded, backward-facing, curved end-hole cannula (henceforth: shielded end-hole cannula) was derived from an idea published in a recent patent [264] and considered as a potentially safer alternative for cannular flow. It is conceived to better disperse the jet prior to hitting the aortic wall, thereby reducing the "sandblasting" effects. Its efficiency of achieving this goal, was of course not evaluated in the patent. Based on the reviewed literature, formulated requirements and practicality considerations, the backward-facing configuration with our own proposed shield geometry (as opposed to the others presented in this patent) was considered better to evaluate. No filter-like membrane that was proposed in this patent was considered, due to its potential abrasive consequences to the intima when deploying an intra-aortic filter, cf. Section 4.2.2.1.

8.4. Measures to evaluate specific requirements

The computational results obtained required a number of or specific postprocessing steps to extract and evaluate the requirements of interest, as expanded upon below.

In order to ensure comparability in the amount of dissipation owing to the conduit of the cannula tip (not the cannula tubing), the same *tip conduit length* of $L_a^c = 25$ mm was assumed, cf. Table A.3. For the end-hole cannulas, this distance stretched from the center of the cannula outflow orifice upstream along its centerline. For the side-hole cannula, this length stretched from the diverting cone upstream along its centerline. While for the hybrid cannula, it stretched from the start of the final orifice upstream along its centerline.

The jet strength and the flow exiting the vessel was evaluated by considering four equi-spaced slices consistently positioned to capture not only the velocity distribution through that slice, but to also be able to observe the dissipation of the flow strength through the decreasing velocity of each consecutive slice. Only forward/outward flow velocity magnitude, or here defined *exit velocity*, formulated as,

$$v_{\text{exit}} = \begin{cases} ||\boldsymbol{v}||, & ||\boldsymbol{n}^{\text{slice}} + \boldsymbol{n}^{\text{vel}}|| \geq 1 \\ 0, & ||\boldsymbol{n}^{\text{slice}} + \boldsymbol{n}^{\text{vel}}|| < 1 \end{cases} \tag{8.1}$$

considering each node in a slice, with $\boldsymbol{n}^{\text{slice}}$ being the outward normal of the slice, i.e. in the main direction of cannula outflow, and $\boldsymbol{n}^{\text{vel}}$ the normalized nodal velocity – essentially allowing for the removal of the component of flow moving backwards/inwards through the slices. Only considering the exit velocity allowed for the comparable distribution of flow originating from arbitrarily shaped cannulas – whether evaluating it close to the jet outflow region or only at the vessel outflow region. To evaluate jet strength, equi-spaced, consecutive, spherical slices were used for evaluating the exit velocity, as shown in Figure 8.6.3 below. The center point of these spherical slices was positioned at the cannula conduit length starting point – see above – and the following slice-radii was used for each tip, with radii equal to

$7.0, 8.0, 9.0$ and 10.0 mm, respectively The only exception was for the shielded end-hole cannula, where planar slices were positioned along the flow direction of the fluid leaving the shield, as also shown in the above-mentioned figure. These planar slices were taken at the same intervals as the spherical slices above, relative to the shield outflow, namely distances of $5.0, 6.5, 7.0$ and 8.5 mm away from the shield outflow, respectively. To evaluate vessel outflow distribution, equi-spaced, consecutive, planar slices were used positioned axially along the vessel centerline close its outflow, as shown in Figure 8.7. The slices were separated by a constant interval of 3.75 mm, starting from 0.5 mm into the flow domain relative to the outflow and progressing inwards. A larger interval was used than used for the jet exit velocity distribution described above, in order to capture a broader impression of vessel outflow exit velocity attenuation.

The pressure drop ΔP was evaluated by considering a planar slice through the cannula (resulting in a surface), 4 mm from its inflow surface at each timestep. Since each considered simulation only had a single inflow and outflow, with a zero traction Neumann boundary condition at the outflow surface, the pressure drop was calculated obtaining a single value for the pressure in the slice by performing the following,

$$\Delta P = \frac{1}{A_{\text{slice}}} \int P_{\text{slice}} \mathrm{d}A - \frac{1}{A_{\text{slice}}} \int P_{\text{out}} \mathrm{d}A \tag{8.2}$$

where P_{slice} represents the all the discrete nodal values of pressure in the slice integrated over each discretized surface element area $\mathrm{d}A$ of the area of the slice $A_{\text{slice}} = \sum \mathrm{d}A$. P_{out} simply refers to the resulting pressure at the outflow surface.

Since it was found that the WSS was exceedingly high and varied for different cannula tip configurations and designs, it was desirable to have a measure quantifying not only the peak WSS, but the entire area that exceeds some threshold of injury occurring. Basic science experiments by Fry [111] found that endothelial erosion already occurs at a WSS exceeding 40 Pa. Accordingly, a *danger-zone area*, A_{danger}, is defined as the sum of each discretized vessel surface area element A_j^{v}, calculated proportional to the nodes in the ratio of the nodes of that particular surface element yielding a WSS above the damage threshold $\mathsf{n}_{\text{nd}}^{\text{danger}}$ to the total number of nodes in the same surface element n_{nd}, formulated as,

$$A_{\text{danger}} = \sum_{j}^{\mathsf{n}_{\text{ele}}} A_j^{\text{v}} \left[\frac{\mathsf{n}_{\text{nd}}^{\text{danger}}}{\mathsf{n}_{\text{nd}}} \right]_{A_j^{\text{v}}} \qquad \text{with} \qquad \mathsf{n}_{\text{nd}}^{\text{danger}} = \mathsf{n}_{\text{nd}}(\text{WSS} > 40 \text{ Pa}). \tag{8.3}$$

8.5. Mesh resolution required for capturing proximal arterial cannular jet effects

In order to obtain an adequate computational mesh to capture all relevant physical effects of the problem under consideration, the mesh resolution was evaluated for sufficiently resolving the jet based on the values of the nodal pressure p and WSS on the vessel wall at the jet landing site, as described in Section 6.4.1.3.. As seen in the literature reviewed in Section 8.1, the WSS in similar fluid dynamical considerations has often been very poorly evaluated due to insufficient mesh resolution. This comes despite its notable sensitivity to the mesh height orthogonal to the wall being well described in literature, e.g. [119, 285]. This high sensitivity originates from the WSS that can effectively be calculated as,

$$\text{WSS} = \mu_{\text{f}} \frac{\mathrm{d}\boldsymbol{v}}{\mathrm{d}y_n} \tag{8.4}$$

with y_n being the direction orthogonal to the wall. The typical steep nature of this velocity gradient near to the wall naturally considering a no-slip wall boundary condition, implies that the discretization size is crucial for the accurate evaluation of the WSS. Otherwise, the WSS will be significantly underestimated if it remains under-resolved.
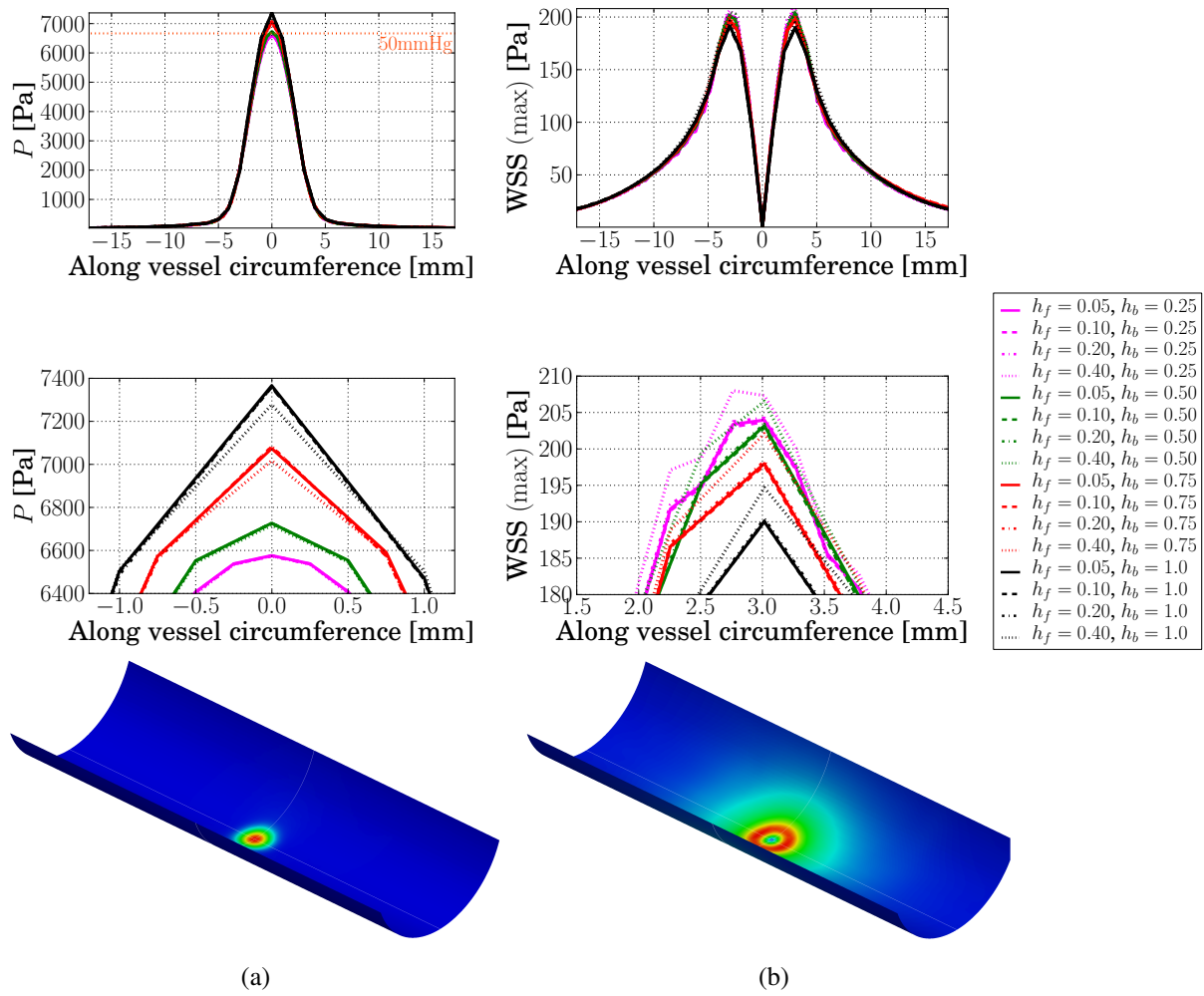
Figure 8.1.: The steady state results for the mesh convergence study showing for (a) pressure and (b) WSS magnitude, showing a complete (top) and close-up (middle) of the results extracted along a line on the circumference of the vessel wall (bottom).

All of the results for the mesh convergence study were extracted after a steady state flow of 3 l/min was reached. The pressure and WSS measured along a line on the wall surface where the jet landed is shown for each base-level size h_b and first element size h_f used in Figure 8.1. As shown, the symmetry of the problem allowed to easily position the line along the circumference, and the vessel surface in its axial direction, in order to capture the respective peak values obtained. The results extracted along the axial direction of the bottom vessel wall yielded similar results as shown in Figure 8.1, but was omitted for brevity.

As can be seen in the figure, the pressure exerted on the wall is mainly dependent on h_b, while the WSS is mainly dependent on h_f. As referred to above, it can be seen that the coarser h_f cause an exponentially worsening result in the WSS.

Based on these results, a mesh size was chosen to provide adequate accuracy while also affording reasonable computational costs. The chosen mesh resolution for all the simulations considered below was with $h_f = 0.2$ mm and $h_b = 0.5$ mm. These values corresponded to those reported by Yang et. al, cf. Section 8.1.1, also being the only of the computational studies found to evaluate the mesh sensitivity

pertaining to adequately capturing the WSS. In order to facilitate adequate meshing for all of the different cannula geometries, the h_b had to be slightly adapted, but never more than 10% of the specified value. The complex geometries of the hybrid cannulas were resolved by halving the h_b at these regions. Apart from the vessel surface, the cannula surface also received the same boundary layer mesh, but with one less layer, cf. Table A.3.

8.6. Comparative functional performance

The following subsection considers the comparative evaluation of the fulfillment of each stated requirement that was quantifiable from the presented models. Continual reference to these requirements are made throughout. Each related finding is briefly discussed along with the presented results. Measures considered that were not defined in Section 8.4 are briefly defined when necessary.

All of the different simulations performed, accompanying parameters and geometrical info are given in Section 6.4 and Table A.4.

Seven different cannula tip designs were considered, including straight and curved end-hole, straight and curve side-hole, straight and curved hybrid and the shielded end-hole cannula, with the simulations respectively referred to as, $Endh_{\mathrm{str}}$, $Endh_{\mathrm{curv}}$, $Side_{\mathrm{str}}$, $Side_{\mathrm{curv}}$, $Hybr_{\mathrm{str}}$, $Hybr_{\mathrm{curv}}$, $Endh_{\mathrm{curv}}^{\mathrm{sh}}$.

Four different insertion depths of the straight end-hole cannula were considered with the base insertion depth (given the subscript $\mathrm{d}, 0$) determined by the actual insertion depth-constraining flange. The simulations performed were $Endh_{\mathrm{d},-5}$, $Endh_{\mathrm{d},0}$ ($\equiv Endh_{\mathrm{str}}$), $Endh_{\mathrm{d},+5}$, $Endh_{\mathrm{d},+10}$. In the presented results, a change of cannula insertion depth *always* referred to these simulations performed only with the straight end-hole cannula at the same base orientation.

Six different orientations of the straight end-hole cannula were considered relative to a base orientation of the cannula pointing perpendicular to the vessel axis (given the subscript $0°, 0°$), with the simulations respectively referred to as, $Endh_{0°,0°}$ ($\equiv Endh_{\mathrm{str}}$), $Endh_{0°,-30°}$, $Endh_{30°,-30°}$, $Endh_{30°,0°}$, $Endh_{30°,30°}$, $Endh_{0°,30°}$. In the presented results, a change of cannula orientation *always* referred to these simulations performed only with the straight end-hole cannula at the same base insertion depth.

As introduced in Section 6.4.1.2, one additional simulation was performed with the same end-hole cannula at base orientation and insertion depth, but now with a longer vessel to include the consideration of the clamped geometry, clamped with parallel clamps to $|A_{\mathrm{cl}}^{\mathrm{lumen}}| = 0.4$, cf. Section 7.5. This simulation was referred to as $Endh_{\mathrm{ic}}$. The cannula was intentionally constrained to not move and therefore possessed exactly the same cannula configurations as $Endh_{\mathrm{str}}$.

It must be noted that the straight end-hole cannula used for the mesh convergence study shown in the previous section differed from the one considered here, in that the former practically had no cannula conduit length, as seen when comparing Figures 6.9 and 6.10.

All cannular flow simulations were evaluated at a cannular flow rate of 3 l/min, unless otherwise indicated. The flow rate was ramped up linearly from 0 to 3 l/min in 3 s and kept constant until 4.5 s was reached. Single values reported represent data extracted at a time step between 4 and 4.5 s, whereas means and standard deviations reported refer to all corresponding quantities extracted from a time of 3 to 4.5 s.

8.6.1. General flow characteristics

Analogous to the aortic occlusion evaluation, it is helpful to first obtain a general comparative impression for the jet shape yielded by each considered cannula tip design and configuration, i.e. the orientation and insertion depth, as well as the subsequent downstream effects. Figure 8.2 depicts the respective velocity

magnitudes thresholded above 800 mm/s for representative examples of the different cannula tips and configurations considered.

These figures effectively demonstrate the often cited Coanda effect of the flow adhering to the vessel wall [180, 238, 239]. Even though it seemed to not occur for those cannula tips capable of dividing and deflecting the jets, i.e. the non-end-hole cannulas, it was only less pronounced. The flow adhering to the wall that is not visible in these figures can be ascribed to the more efficient jet dissipation responsible for lower velocities that will be thresholded out of these visual representations.

8.6.2. Requirement: Minimize impact on blood

To assess the cannula tip design's impact on blood damage, the pressure drop defined in Section 8.4, is plotted for the different cannula tip designs, insertion depths and orientations considered in Figure 8.3. As reviewed in Section 3.1.2.2, the pressure drop has often been used as a measure for the amount of hemolysis occurring.

Regarding the different tip designs, it can be seen that despite its comparatively smaller inner diameter, side-hole and hybrid cannulas performed better than the straight and curved end-hole cannulas. The straight hybrid cannula performed even better than the straight end-hole cannula. Furthermore, considering the influence of the cannula curvature on the respective designs, it appeared that the sharp curvature of the hybrid cannula caused a much higher dissipation compared to the smoother curved side-hole cannula. However, despite the smooth curvature of the curved end-hole, as well as its larger inner diameter, it yielded a comparatively much higher pressure drop compared with the straight end-hole cannula than the two previously mentioned designs. Finally, the shielded end-hole cannula performed the worst. Despite larger variations of the pressure drop over time, the pressure drop remained significantly high.

The variation in insertion depth of the straight end-hole cannula indicated an increase in pressure drop for an increase in depth, except at the deepest level, where the pressure drop decreased markedly and the fluctuation of pressure drop over extracted time period also decreased. The different orientations of the straight end-hole cannula displayed a distinct value for each orientation. As with the insertion depth, the pressure drop at different orientations also did not correlate with the cannula outflow-to-wall distance, which was 17.8, 17.6, 17.6, 13.6, 17.6 and 22.5 for each orientation in the order given in the figure.

8.6.3. Requirement: Minimize jet strength

Jet strength was evaluated by considering the exit velocity distribution attenuation through consecutive, equi-spaced slices through the flow field at the cannula outflow. Spherical slices were used for all cannula considered, except the shielded end-hole cannula, where planar slices were considered, cf. Section 8.4. The resulting distributions are shown in Figure 8.4.

The curved end-hole cannula displayed the strongest and most weakly dissipated jet, followed by the curved side-hole and curved hybrid cannulas. Considering Figure 8.2, it can be seen that the curve in the cannula geometry is responsible for concentrating/skewing the velocity profile towards its outer curvature, cf. basic fluid mechanical studies of flow through a curved pipe. The ability of side-hole and hybrid cannulas to split the main jet into smaller jets visibly appears to have aided the quicker attenuation of maximum jet exit velocities. The shielded end-hole cannula drastically reduced the jet exit velocity, also compared to using no shield, but still delivered a slowly attenuating exit velocity. Slight variations observable in the maximum exit velocity can be attributed to the fact that these distributions are extracted in a steady flow state at a single timestep and subjected to an instance in the naturally expected jet flow variation, cf. Section 8.7.3.3.

(a) $Side_{\mathrm{str}}$ (b) $Side_{\mathrm{curv}}$ (c) $Endh_{\mathrm{curv}}$

(d) $Hybr_{\mathrm{str}}$ (e) $Hybr_{\mathrm{curv}}$ (f) $Endh_{\mathrm{curv}}^{\mathrm{sh}}$

(g) $Endh_{\mathrm{d},0}$ (h) $Endh_{\mathrm{d},+5}$ (i) $Endh_{\mathrm{d},+10}$

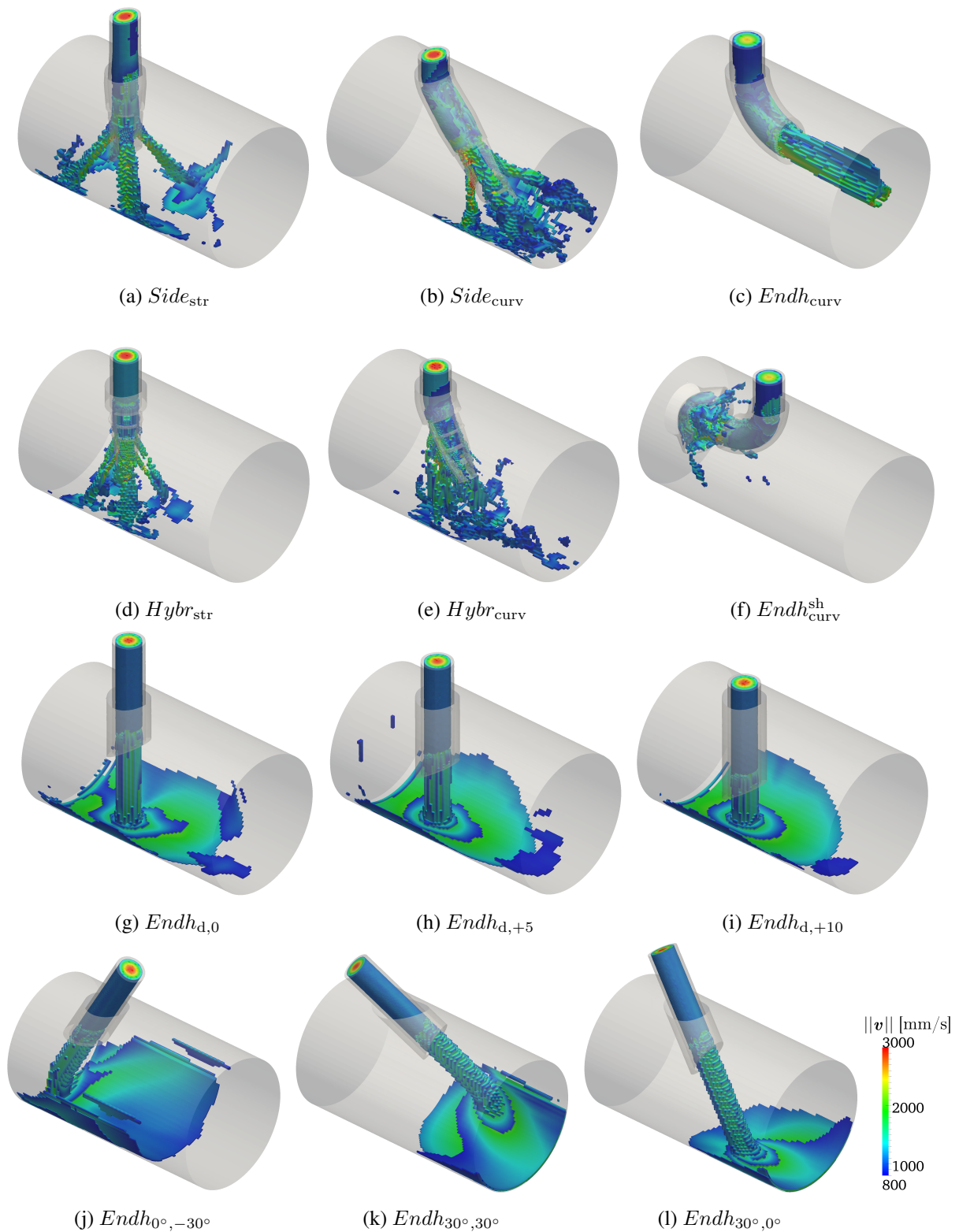(j) $Endh_{0°,-30°}$ (k) $Endh_{30°,30°}$ (l) $Endh_{30°,0°}$

Figure 8.2.: Velocity magnitude thresholded above 800 mm/s of its maximum, showing the different cannula tip designs (a)-(f), different representative insertion depths (g)-(i) and different representative orientations (j)-(l). Flow was prescribed at the cannula inflow and was free to exit the vessel distally (bottom, left of each figure).
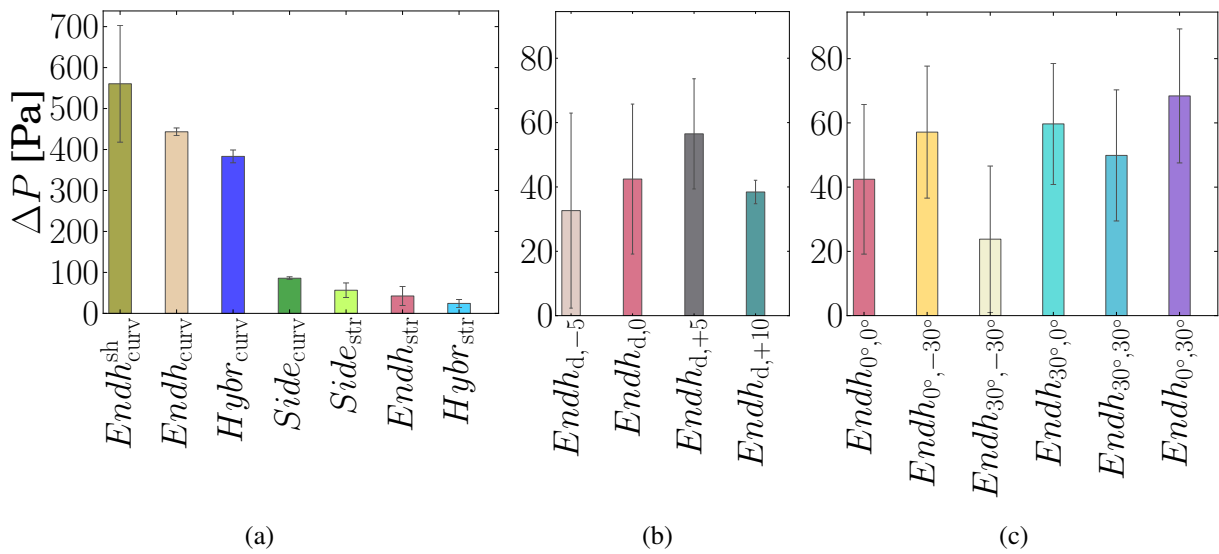
Figure 8.3.: The pressure drop for (a) the different cannula tip designs considered, in a descending order, (b) straight end-hole for a change of insertion depth and (c) straight end-hole for a change in orientation.

8.6.4. Requirement: Minimize peak WSS

The peak WSS yielded by each cannula configuration is shown in Figure 8.5.

Comparing the jet exit velocity attenuation in Figure 8.4 and the results presented here, an apparent correlation is seen between the strongest jets (deduced from the attenuation of the exit velocity distribution) resulting in the highest inflicted WSS. Multiple discrepancies responsible for not seeing a one-to-one correlation of these results can be ascribed to the following: The side-hole and hybrid cannulas divided and deflected the main jet, effectively resulting in faster dissipation of the resulting jet over a distance, cf. Figure 8.2. Furthermore, the orientation by which the jet hit the vessel wall played a significant role, whereas the insertion depth did not, cf. Figure 8.5b,c. Consequently, the size and the poorly dissipated character of the curved end-hole jet is expected to inflict a significant amount of WSS, despite potentially resulting in an increased jet angle of incidence.

8.6.5. Requirement: Minimize danger zone area

The danger-zone area that was inflicted by each considered cannula configuration is shown in Figure 8.6. Although the damage threshold obtained from literature was 40 Pa, three additional, higher thresholds were evaluated to provide an impression for the severity of the WSS inflicted.

The results of the second and third orientations of the end-hole cannula are marked with a (*) because the danger-zone area extracted for these orientations only represent the level of WSS experienced on the vessel wall, not on the truncated surface representing the occluded aorta. Therefore, it must not be interpreted that these orientations inherently yield a smaller danger-zone area, as is evident from Figure 8.6e. As a matter of fact, the results seem to indicate the the orientation and the insertion depth of the jet has little effect on the size of the danger-zone area, at least for the straight end-hole cannula. In the presented results, its clear that the danger-zone area is much greater influenced by the cannula tip design.

The tip design clearly had the biggest impact on the on the size of the danger-zone area. The different damage thresholds for the danger-zone area indicated how the WSS distribution followed the peak WSS

(a) $Endh_{curv}$

(b) $Side_{curv}$

(c) $Hybr_{curv}$

(d) $Endh_{curv}^{sh}$
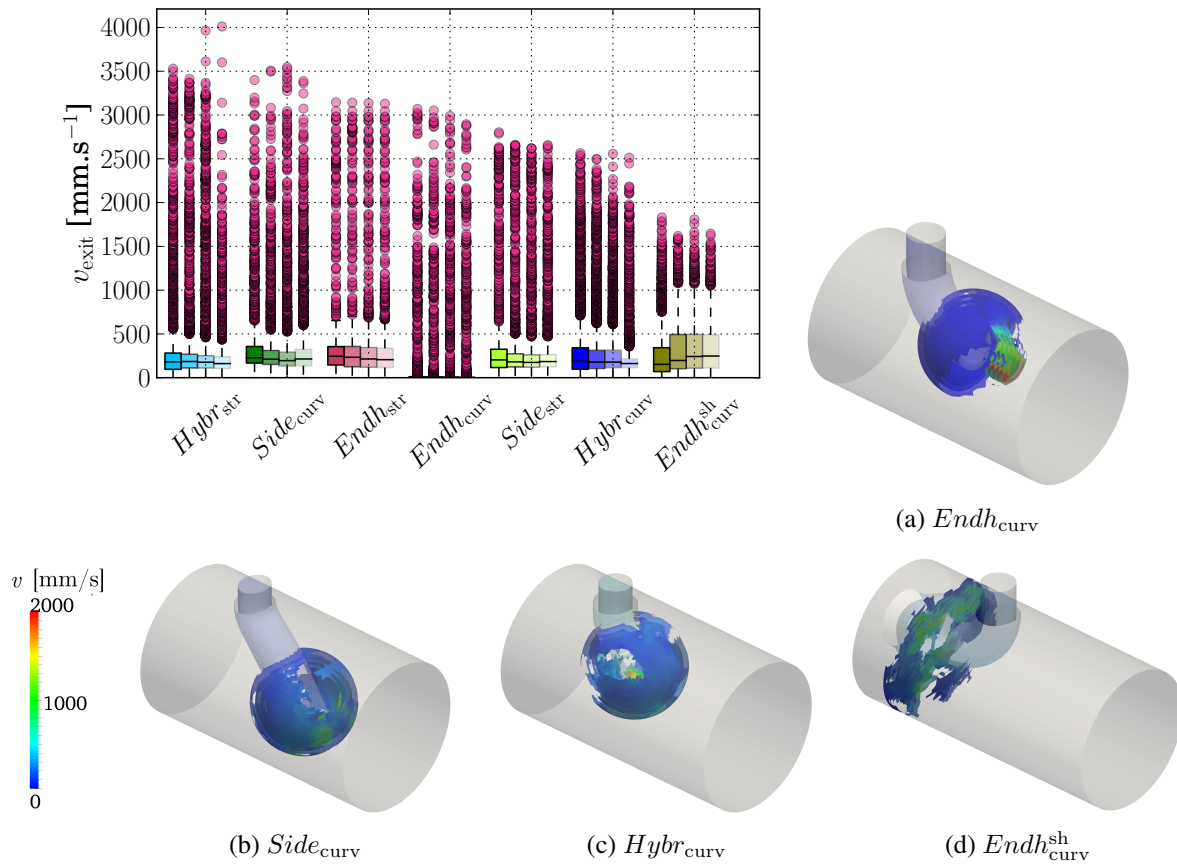
Figure 8.4.: The attenuation of jet velocity over consecutive, spherical/planar, equi-spaced slices positioned relative to the cannula outflow, showing (a) the exit velocity distribution (flow in the opposite direction is excluded) per slice, with increasing transparency indicating further away from the cannula outflow. The cannulas are sorted according to the maximum velocity measured at the final slice. Standard box plot parameters with outliers indicated as purple dots. (b)-(e) show representative examples visualizing the exit velocity.

(a)

(b)

(c)

(d) $Endh_{0°,0°}$

(e) $Endh_{0°,-30°}$

(f) $Endh_{30°,30°}$

(g) $Side_{\mathrm{curv}}$

(h) $Hybr_{\mathrm{curv}}$

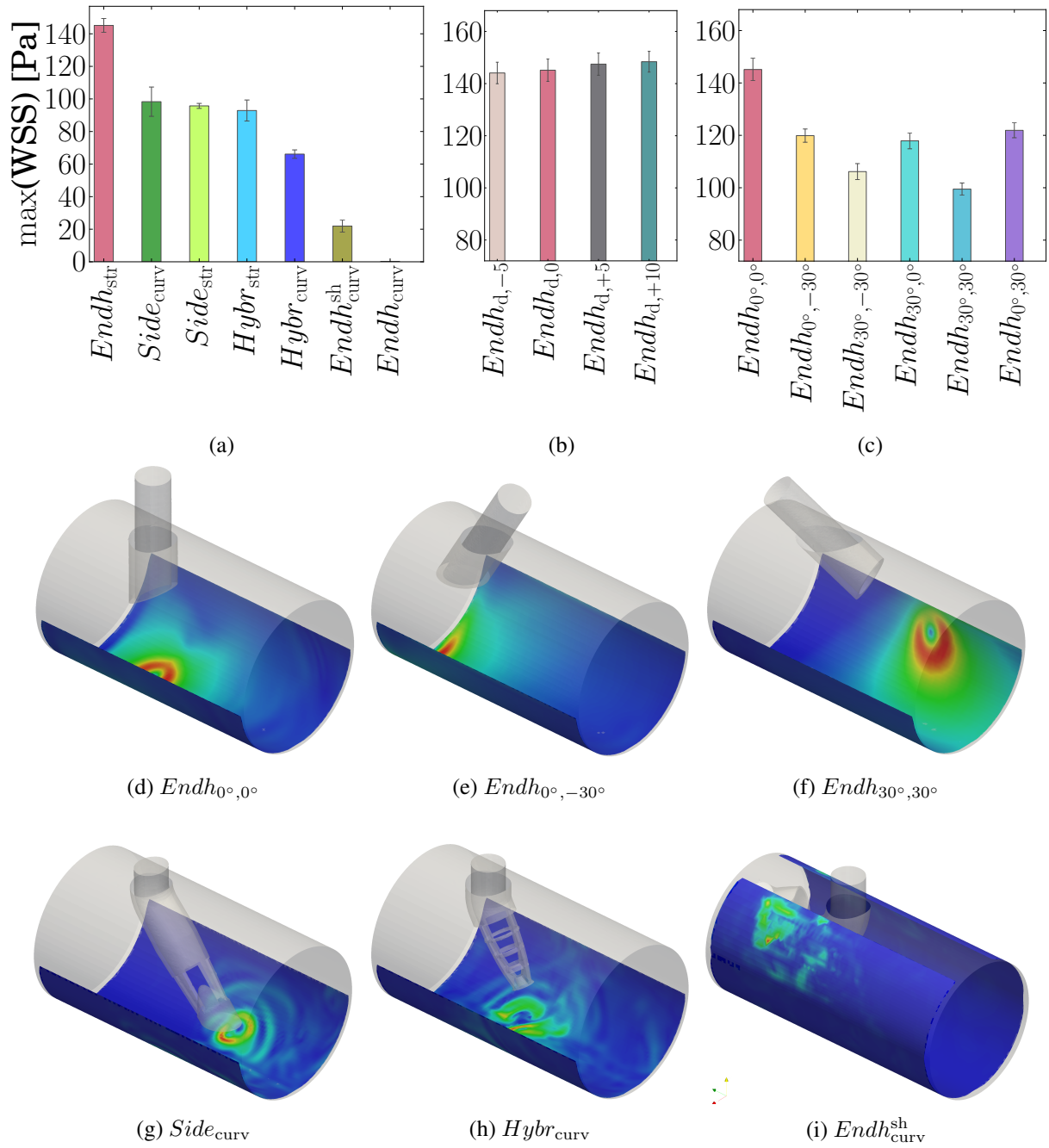(i) $Endh^{\mathrm{sh}}_{\mathrm{curv}}$

Figure 8.5.: The maximum WSS magnitude for (a) the different cannula tip designs, in a descending order, (b) straight end-hole for a change of insertion depth and (c) straight end-hole for a change in orientation and visualization thereof for selected cases (d)-(i).

(a)

(b)

(c)

(d) $Endh_{0°,-30°}$

(e) $Side_{str}$

(f) $Hybr_{str}$

Figure 8.6.: The danger zone area, i.e. the area with a WSS larger than the damage threshold. Each increasing degree of transparency indicates a different damage threshold, i.e. $40, 50, 60, 70$ Pa, shown for (a) the different cannula tip designs, in a descending order, (b) straight end-hole for a change of insertion depth and (c) straight end-hole for a change in orientation and vi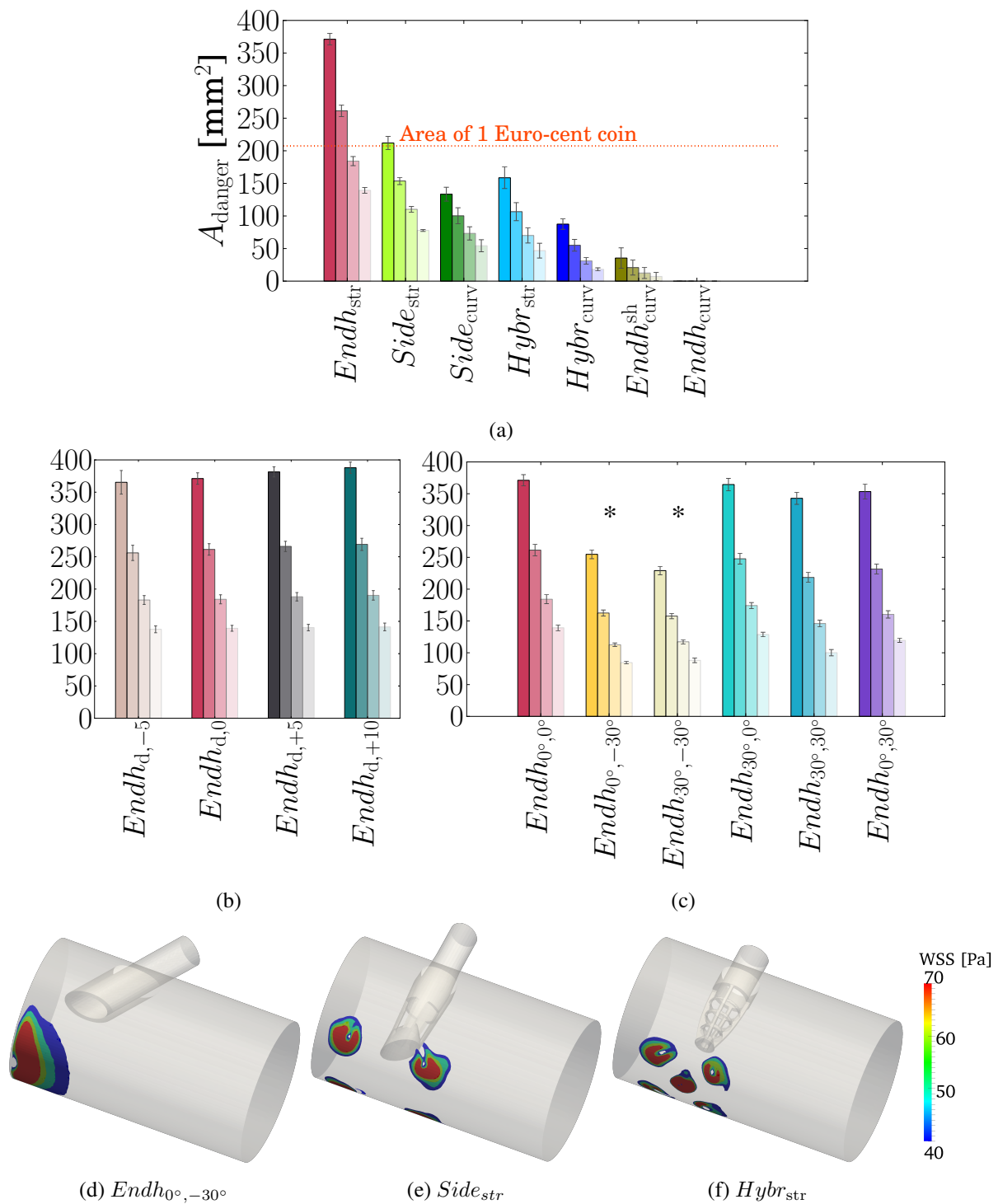sualization thereof for selected cases (d)-(f). The (*) indicates truncated results due to problem setup – see text for details.

and naturally, although not linearly, declined away from the peak. While the insertion depth only showed a small increase in danger-zone area for the straight end-hole cannula, the orientation had a slightly greater influence.

Finally, its worth pointing out that although the hybrid and side-hole cannulas have already been shown to be relatively proficient in dispersing the jet, thereby resulting in a lower WSS and smaller total danger-zone area, the danger-zone area was dispersed over a larger region of the intima. This is evident from Figure 8.6f, showing how the diverting jets are spread out over a large region of intima. Therefore, in the event that an intimal lesion was identified pre-operatively, it will be particularly challenging to ensure that a specified region is not affected by the resulting jets – it is expected that a jet that is only sufficiently strong to cause damage at a lesion is more dangerous than an even stronger jet pointed at a non-lesion region.

8.6.6. Requirement: Facilitate distributed proximal vessel outflow

Comparable to the evaluation of jet strength in Section 8.6.3, the exit flow velocity distribution of consecutive, equi-spaced, planar slices distributed along the vessel outflow are evaluated here, as defined in Section 8.4. Thereby, the aim was to evaluate what the distribution of flow entering the aortic arch will look like, how the distribution and the attenuation will be affected by the cannula tip design and configuration, and finally which setup yielded the distribution with the closest character to the physiological. The results are indicated in Figure 8.7.

Comparing the results to the jet exit velocity attenuation, cf. Figure 8.4, it can be seen that the dissipation of the velocity reaching the aortic arch was significantly influenced by the cannula configuration in the vessel. Whereas the straight hybrid cannula yielded the highest jet exit velocities, it yielded the lowest vessel outflow exit velocities. Furthermore, since the jet of the curved end-hole cannula never hit the aortic wall, it expectedly resulted in the worst distributed flow. Therefore, the peak cannula velocity measured can never be used as an indication for how efficiently or inefficiently a cannula will provide adequate flow entering the aortic arch.

As expected, pointing the jet in the direction of the outflow caused a worse distribution of outflow exit velocity, reflected in the poor distributions by the different curved cannula tips, cf. compare with straight tips, Figure 8.7a, and the straight end-hole cannula orientations pointed towards the outflow, Figure 8.7c. Pointing the straight cannula $30°$ towards the outflow, i.e. $Endh_{0°,30°}$ and $Endh_{30°,30°}$, yielded results comparable to the curved end-hole cannula where the jet never landed on the vessel wall surface. These results also show the effectivity of dissipating the jet velocity by pointing it straight to the vessel wall. At least for the straight end-hole cannula, its effects in terms of outflow exit velocity distribution is comparable to pointing it proximally/upstream, cf. $Endh_{0°,-30°}$. However, pointing the cannula proximally can be beneficial in this regard when the surface configuration that the jet lands on promotes better mixing/dispersion of the jet, cf. $Endh_{-30°,-30°}$ and $Endh_{curv}^{sh}$.

Interestingly, the insertion depth of the straight end-hole cannula also indicated the efficiency by which the wall dissipated the jet. Figure 8.7b shows that for the shallowest insertion depth $Endh_{d,-5}$ the dissipation was the worst and progressively became better, with an especially large jump between the shallowest and the subsequent insertion depth.

8.6.7. Requirement: Keep jet away from occlusion site

As referred to at the beginning of this section, a first attempt was made to consider the consequences resulting from the interaction between the cannular flow and the largely deformation aorta caused by cross-clamping. The comparative influence between the non-clamped and incompletely clamps aortic geometry is shown in Figure 8.8, showing the resulting maximum WSS and danger-zone areas.

(a)

(b)

(c)

(d) $Endh_{\mathrm{curv}}$

(e) $Side_{\mathrm{curv}}$

(f) $Hybr_{\mathrm{curv}}$
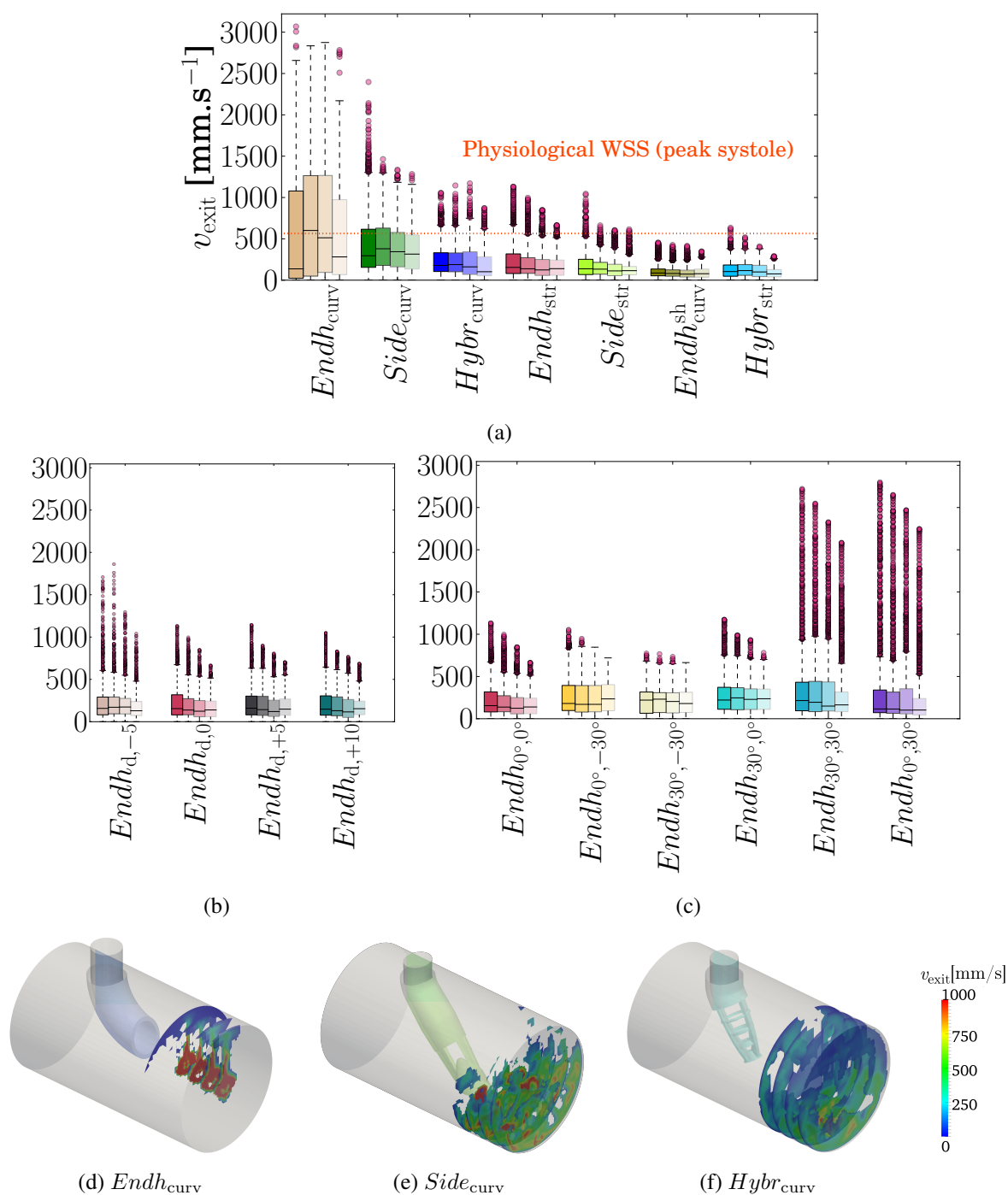
Figure 8.7.: The vessel outflow exit velocity distribution that will enter the aortic arch, evaluated over consecutive, planar, equi-spaced slices positioned along the vessel axis at its outflow, showing (a) the exit velocity distribution per slice, with increasing transparency indicating slices positioned closer to the cannula outflow. The cannulas are sorted according to the maximum velocity measured at the final slice. Standard box plot parameters with outliers indicated as purple dots. (b)-(e) show representative examples visualizing the exit velocity.

(a)

(b)

(c) $Endh_{str}$

(d) $Endh_{ic}$

WSS [Pa]

Figure 8.8.: Comparing the idealized influence of an incompletely clamped vessel to an unclamped vessel, considering (a) the peak WSS and (b) the danger-zone area, with each increasing degree of transparency indicates a different damage threshold, i.e. $40, 50, 60, 70$ Pa. The visualization of how the danger-zone morphology changed is shown in (c) and (d).
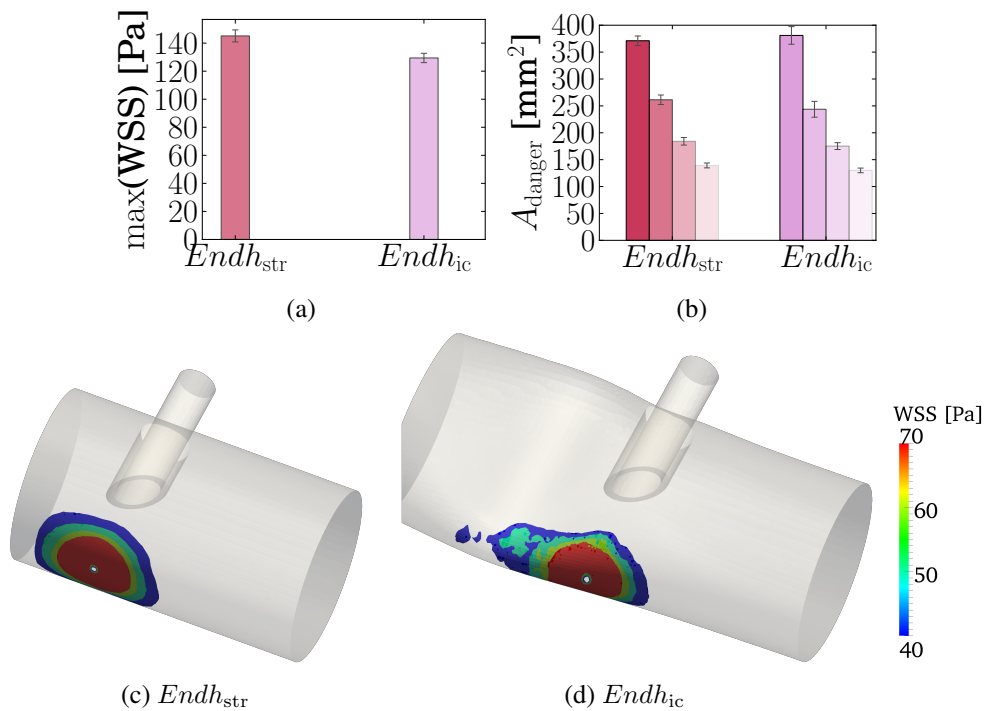
The resulting peak WSS and danger-zone area are only slightly affected. However, as can be seen in Figure 8.8, the deformed geometry was responsible for a change in the morphology of the danger-zone towards the pinching site.

8.6.8. Requirement: Robustness despite clinical variations

A robust cannula design can be defined as a cannula that yields a consistent performance despite clinical variation. When considering only the variations incorporated here, i.e. different tip designs, as well as insertion depth and orientation of the straight end-hole cannula, it is evident that conclusive trends about the robustness of cannula performance can only be drawn for the straight end-hole cannula. This is simply because the variation in the results when changing the straight end-hole cannula configuration was significant and complex in nature and extrapolation of results cannot be done with confidence. At least for the straight end-hole cannula, it can be seen that it does not reveal robust performance under the variations considered.

The only other remark about robustness can be made is that it is expected to depend on how well the jet is dispersed *prior* to hitting the wall, meaning that the jet attenuation presented is the closest estimate of a cannulas robustness.

Table 8.1.: The relative functional performance of the different cannula tip designs in providing optimal *proximal* arterial cannular flow, with the scores indicating how well a tip design fulfilled the stated requirements – "5'" being the best and "1" the worst.

Functional requirement		$Endh_{str}$	$Endh_{curv}$	$Side_{str}$	$Side_{curv}$	$Hybr_{str}$	$Hybr_{curv}$	$Endh_{curv}^{sh}$
1a	Minimize blood impact: Ensure low pressure drop	4	2	4	4	5	2	1
1b	Minimize blood impact: Suitable surface coating	-	-	-	-	-	-	-
2a	Disperse jet: Minimize jet exit strength	2	2	3	1	1	3	5
2b	Disperse jet: Minimize peak WSS	1	2	3	3	3	4	5
2c	Disperse jet: Minimize dangerzone area	1	2	2	3	2	3	5
2d	Disperse jet: Distribute flow physiologically	4	1	4	2	5	4	5
3	Keep jet away from occlusion site	2	3	1	3	1	2	3
4a	Be simple: constrain cannula tip depth	-	-	-	-	-	-	-
4b	Be simple: small size of inserted tip	3	3	2	1	1	1	2
4c	Be simple: easy insertion/extraction	-	-	-	-	-	-	-
5	Be robust, despite clinical variation	-	-	-	-	-	-	-
6	Minimize cannulation site leakage	-	-	-	-	-	-	-
7	Have reliably performing tip	-	-	-	-	-	-	-
8	Be cost efficient	-	-	-	-	-	-	-
Total		**17**	**15**	**19**	**17**	**18**	**19**	**26**

8.7. Discussion

In order to achieve the most comprehensive insights to date of the trade-offs and complexities regarding proximal effects of arterial cannular flow, computational models were used because of their superior ability to allow easy parameter variations and flexibility in design. The models also allowed the realistic prediction of such characteristics without the need for complex experimental studies. Sophisticated, advanced, state-of-the-art fluid formulations and modeling strategies were used to correctly and accurately simulate the flow through an arterial cannula inserted into an idealized aorta, as considered in the following.

8.7.1. Summary of functional performance/requirement fulfillment

As done for the occlusion techniques in Section 7.6.1, a comparative evaluation was made to assess the performance of the different cannula tip designs. The same scoring system of the relative requirement fulfillment was used, of which the convention is described in Section B. The resulting relative performance is shown Table 8.1. The indicated scores were based on the computational results presented in this chapter, as well as experimental and clinical information reviewed in Chapter 3.

8.7.1.1. General remarks

This relative comparison did not take any weighting of importance or exclusion criteria into consideration. Therefore, the importance of one criteria over another was neglected and no exclusion criteria was set to exclude a cannula tip from the comparison based on insufficient fulfillment of a requirement. Despite

being important aspects to consider, it introduces more subjectivity which is better left to the clinical users of these cannulas, i.e. the clinicians.

Two requirements not directly evaluated computationally was to keep the jet away from the occlusion site and to ensure a small tip size. Accordingly, these parameters were rated with a maximum score of "3". The former was rated purely on visual inspection from the thresholded velocities and danger-zone areas depicted in Figure 8.2 and 8.6, respectively. The latter was rated based on a simple physical measurement of tip length in the main cannula axis direction, i.e. from the flange to limit insertion depth to the furthest vertical point that the cannula reached upon insertion. The inserted depth was 16, 17, 22, 18, 22 and 24 mm for the cannulas considered in the order given in the table.

The robustness of the cannula performance under the clinical variation considered was not evaluated, due to a lack of information. The varying results from the straight end-hole cannula upon clinical variation simply does not allow the reliable extrapolation of its performance to the different cannula tips considered, as mentioned above. Other requirements not evaluated here were either fulfilled equally good by all tips, e.g. constraining insertion depth, or simply not considered here.

Furthermore, as mentioned above, all parameters used to evaluate the functional fulfillment were influenced by the idealized aortic geometry. The only exclusively cannula dependent property evaluated was the jet exit strength.

Finally, despite the limitations associated with such a comparative evaluation and that the focus of this evaluation only the proximal effects of arterial cannular flow, the scores listed reflects a very important consideration: Each cannula tip evaluated presented its specific drawbacks and advantages. No proposed cannula tip, no matter how advanced, yielded outstanding performance. The only two outliers was the curved end-hole and the shielded end-hole. The worse performance of the former was marginal, while the better performance of the latter needs to be seen in the context of the high pressure drop that it induced to attain this improved performance.

8.7.1.2. Complex influence of insertion depth and cannula orientation

One of the main observations from the presented results were that few outcomes with regards to insertion depth and orientation were trivial, as expanded upon in the following.

The variation of insertion depth of the straight end-hole cannula yielded the following: The pressure drop did not correlate with the progression of insertion depth, cf. Figure 8.3b, while although the orientation inherently changed the insertion depth (or rather: tip-to-wall distance), the insertion depth was not the only determinant of this outcome. It was also influenced by the jet incidence angle and the geometry at the jet landing site. The same observation was seen for the maximum magnitude of WSS, which increased only slightly with an increase in insertion depth, but changed unintuitively for a change in insertion depth due to the cannula orientation. Interestingly, the danger-zone area was hardly influenced by either the jet the insertion depth or the orientation.

However, a deeper insertion depth was responsible for better distribution of flow entering the aortic arch, cf. Figure 8.7. The similar maximum WSS and danger-zone areas seemed to suggest that it was not due to an increased dissipation of the jet at its landing site, but rather because an increased insertion depth pushes more fluid along the circumferential direction of the vessel, thereby improving the flow mixing, cf. thresholded velocities of $Endh_{d,0}$ and $Endh_{d,+10}$ in Figure 8.2. Further support for this observation was found in the deepest insertion depth yielding a sudden decrease in pressure drop after gradually increasing with insertion depth, cf. Figure 8.3b. This phenomenon is ascribed to the fact that the fluid immediately next to the jet along the circumference is pushed away sufficiently far to effectively reduce its effect on the resulting pressure drop. Clearly, the non-flat surface that the jet hit had a significant influence on the flow properties.

The change in orientation angle of the straight end-hole cannula yielded results of a dissimilar trend than changes to the insertion depth. The orientation *did* have a large influence on the distribution of flow entering the aortic arch, with cannulas pointing more towards the vessel outflow yielding the poorest distributions. Interestingly, the best distributed flow entering the aortic arch, and therefore also the best dispersed jet was obtained for the jet pointed perpendicular to the aortic wall, i.e. $Endh_{0°,0°}$. Even pointing the jet upstream (in the direction of the aortic valve) did not dissipate the jet as proficiently. However, this increased jet dissipation clearly came at the cost of relying on the aortic wall as the means of jet dissipation, as is evident in the higher WSS induced, cf. Figure 8.5. The orientation also had a large influence on the WSS because of the resulting geometry that the jet lands upon, e.g. skew on a vertically blocked off cylindrical surface (Figure 8.5d), skew on a slanted cylindrical surface (Figure 8.5f), etc., as referred to above.

8.7.1.3. Complex influence of the cannula tip design

The cannula tip geometry was responsible for further complexities present in the outcomes, since it resulted in a jet/multiple jets entering the aorta with different sizes, angles of incidence and insertion depths, as considered in the next subsection.

The side-hole and hybrid cannulas increased the dispersion of the flow leaving the cannula tip by subdividing the jet into smaller jets, which would have effectively also dissipated the total jet energy. However, when comparing the jet and vessel outflow exit velocity distributions (Figure 8.4 and 8.7), it was clear that these sophisticated cannulas still relied excessively on the aortic wall as the means to dissipate the jets leaving the cannula tip. This is evident from the significant WSS and danger-zone areas that these cannulas yielded, cf. Figure 8.5 and 8.6. Only the shielded end-hole cannula relied significantly less on the aortic wall as its means for dissipating its jets, although at a price of an increased pressure drop.

As indicated in the results of the jet attenuation, the curvature of the tip itself concentrated the velocities towards the outer curvature of the tip, i.e. yielding a skewed flow profile with velocities. In this regard, all curved tip designs performed poorer compared to both their straight counterparts, but also overall. Therefore, it can be deduced that such a bend in the cannula geometry plays a negative, significant role in the jet exit velocities and its attenuation. Evidently, it seems that the designers of the curved side-hole and hybrid cannulas did not take this skewed velocity profile due to tip curvature into consideration, or otherwise deemed it sufficiently unimportant, based on the axisymmetric tip geometry. Notable, is that compared to the curved to straight tip designs of these cannulas, the jet exit velocity is definitely influenced by the curvature of the cannula tip, cf. Section 8.4. Moreover, seemingly poor consideration of resulting flow fields by manufacturers is exemplified when considering different views of the thresholded velocities yielded by the curved and straight hybrid cannulas in Figure 8.9. For the curved hybrid cannula, it can be seen that the effect of the curvature and the positioning of its side-holes rendered its resulting jet to almost assimilate that of a straight end-hole cannula, i.e. most of the highest velocity flow simply flows straight through the cannula and is hardly orientated in the direction of the cannula tip curvature.

Perhaps serendipitously, this seemingly unintended flow characteristics caused good dissipation of the jet prior to hitting the aortic wall, but was achieved at a cost of pressure drop similar to other curved cannulas, cf. Figure 8.3, and was less effective in yielding a well-distributed vessel outflow than its straight counterpart. This can be ascribed to the fact that the tip design of the straight hybrid cannula was more effectively employed in subdividing the jet than the curved cannula and also directing some of the cannula outflow upstream, thereby causing the best overall dissipation of the jet, as can be seen in the stated figure and Figure 8.7. The flow patterns in Figure 8.9 seems to indicate the over-design of the curved hybrid tip.

Interestingly, as can also be observed in Figure 8.9, even though the first two layers of side-holes do not appear to aid in the subdivision of the cannular jet or the flow field at all, it presumably played a

Side view   Isometric view

(a) $Hybr_{\mathrm{str}}$ (b) $Hybr_{\mathrm{curv}}$
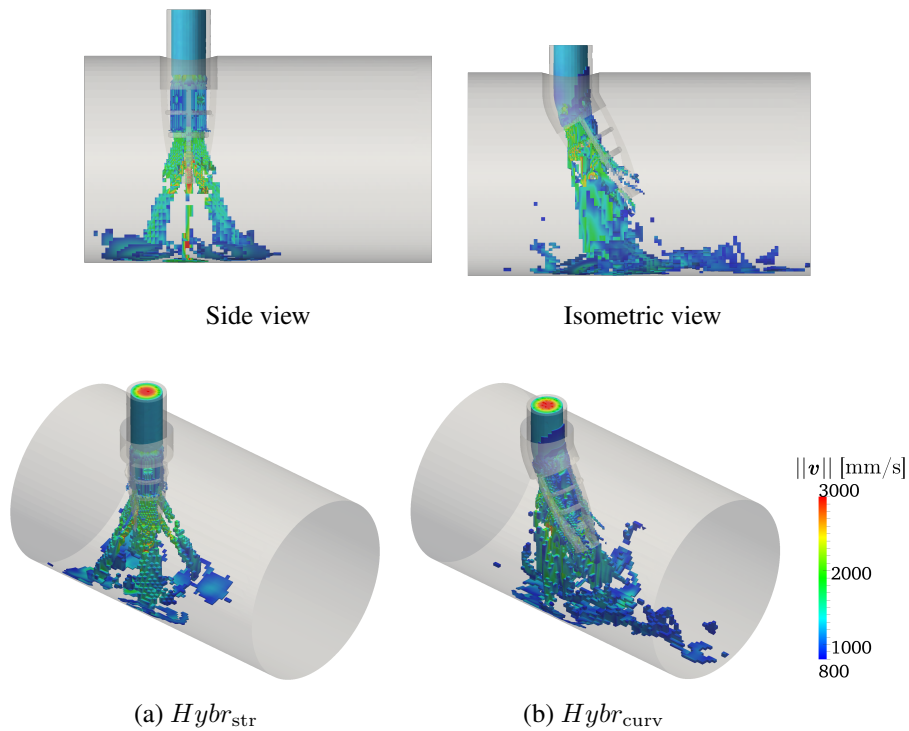
Figure 8.9.: Multiple views of the thresholded velocity demonstrating the similarity of flow structures yielded between the straight and curved hybrid cannulas, cf. Figure 8.2d and e.

role in the exemplary low pressure drop obtained over this cannula tip – lower than the straight end-hole cannula, even though it also had a smaller effective inner diameter. The effective subdivision of the jet by the curved side-hole cannula demonstrated how the location of the side-holes relative to the curvature can effectively aid in lowering the pressure drop, cf. Figure 8.3.

Although the jet of the curved end-hole cannula never hit aortic wall in this model setup, different measures evaluated yielded keen insights into this much debated, sometimes trivialized topic of: which is better – the straight or curved end-hole cannula?, cf. Section 3.1.2.3. As mentioned in the previous paragraphs, the side-hole and hybrid cannulas partially succeeded in dissipating the jet by subdividing it, while the tip curvature caused an increase in flow velocity towards the outer curvature of the cannula. Therefore, the curved end-hole cannula yielded a strong and poorly dissipated jet entering the aortic arch, as is evident when once again comparing the cannula and vessel outflow exit velocity distributions (Figure 8.4 and 8.7). Comparing the range of the maximum exit velocity of the jet at the cannula outflow with that of vessel outflow, the curved end-hole cannula only showed an attenuation of roughly 30%, while the second worst performing cannula, i.e. the curved side-hole cannula, already yielded roughly 60% velocity attenuation. Therefore, efficiency by which the curved end-hole jet is dissipated clinically to cause a lessened impact in terms of WSS is unclear, but expected to not be negligible compared to the other cannulas considered. It is clear however, that the distribution of flow entering the aortic arch will be significantly worse than all the other cannulas considered. The only foreseeable benefit of using this cannula tip instead of the straight end-hole cannula, as deduced from the presented results and literature reviewed, is that it will hopefully cause the jet to land beyond the final cerebral branch of the aortic arch (left subclavian) and that particles dislodged by the jet to be directed into the descending aorta, although local patient-specific geometry and flow characteristics dictate that this cannot be guaranteed. Therefore,

only based on its proximal performance evaluated here and the literature reviewed in Section 8.1.2, cerebral perfusion characteristics are expected to be poor and preferential guidance of embolic material into any one cerebral vessel remains a definite possibility.

8.7.1.4. Complex interaction between cannular flow and clamped aortic geometry

The change of the morphology of the inflicted danger-zone area shown in Figure 8.8 is a particularly interesting/worrying finding, because of the experimental, clinical and computational findings reviewed in Sections 2.1 and 7.1.1 , namely that the pinching site is the most vulnerable site to get damaged during clamping. Therefore, it is expected that the problem of intimal injury at the pinching site will be aggravated by an increased WSS induced in this area. Furthermore, the distance between the cross-clamps and the cannulas, the jet incidence angle, as well as the relative angle between the clamp surfaces and the cannula axis can all be responsible for directing high velocity flow over the damaged pinching sites.

8.7.1.5. Multiple implicated risks

From the reviewed literature, presented results and discussion, it is clear that direct comparison of the danger of one cannula configuration compared to another is not straight-forward, because there are different aspects of danger to be considered. Such dangers include the influence of a high pressure drop/shear rate on blood damage, the influence of the jet inducing high WSS that can dislodge particulate matter and the jet responsible for an overall poorly distributed flow entering the aortic arch, thereby risking hypoperfusion or even directing emboli into a specific cerebral vessel. However, of all the literature reviewed, only a subset of these requirements formulated here are considered and consequently do not provide the full scope of consequences of a certain cannula configuration as presented here. However, despite all of the clinical variations incorporated in the present study, additional variations still exist, as discussed below in Section 8.7.3.2. These factors clearly indicate the enormous scope of the problem.

Furthermore, since the arterial cannula provides flow through a conduit roughly five times smaller than the native aortic diameter, a high speed jet will naturally be responsible for unphysiological consequences to the flow entering the aortic arch. Although considering some of the most advanced cannula tip designs available clinically, the WSS damage threshold of 40 Pa was always surpassed and the maximum fluid velocity entering the aortic arch was considerably more than the maximum value achieved during pulsatile physiological flow at a comparable time-averaged flow rate, cf. Figure 8.7. These values were reached despite considering a cannular flow rate that clinically translates to ∼50% CPB flow. The trade-offs achievable between certain aspects were evident, but not necessarily linear, due to this multi-factorial nature of this problem. Even the newly considered cannula tip design, the shielded end-hole cannula, was also subjected to trade-offs in its overall performance: it delivered a comparatively very high pressure drop, despite good attenuation of jet and vessel outflow exit velocity and consequently low WSS induced.

8.7.2. General findings

8.7.2.1. First steps towards validation of presented models

Experimental validation from data in literature is problematic, because as mentioned previously, only one experimental study by Verdonck et al. [347] was performed evaluating the performance of the tip itself, and not only the combination of the tip and the cannula tubing, i.e. the entire cannula. The investigation by Verdonck et al. [347] showed that, when considering the tip alone, the side-hole cannulas performed better than the straight and curved end-hole cannulas in terms of pressure drop. The straight side-hole performed significantly better than the curved side-hole cannula. However, upon a closer look at these results, it is evident that the curved side-hole only performed marginally better (∼5%) better than the

straight end-hole cannula. Accordingly, based on the difference in inside diameters, using water flowing at 1.3 l/min, these results indicated qualitatively similar trends as was presented in Figure 8.3.

The only other comparable measure often reported in literature is the peak velocity of the cannular flow. Andersen et al. [7] reported the peak flow velocities measured with MRI for water at 3 l/min, measured near the outflow of the cannula tip. They observed the same asymmetric character of the flow through the curved cannulas as presented here. Furthermore, although they used 24 Fr cannulas with differing inner diameters than those considered here, e.g. their curved side-hole cannula had a diameter 11% larger than used here, while their straight end-hole cannula was 15% smaller than used here. Taking these considerations into account, peak velocities for their 24 Fr cannulas ranged between 1750 and 2750 mm/s, which compared reasonably well with the peak jet exit velocity of the first slice of Figure 8.4, ranging between 2800 and 3400 mm/s. This range excludes the results of the shielded end-hole and hybrid cannulas, since they were not considered by Andersen et al. [7].

Therefore, although not validated quantitatively due to difficulties in comparability, as is clear from the previous two sections, the results presented here indicated qualitative correspondence to the stated experimental results, as well as indications of falling within a suitable range.

The limiting factors which determine the inter-study comparability and consequently also its value to aid in model validation, is further considered below in Section 8.7.3.1.

8.7.2.2. WSS and danger-zone area

The wall shear stress (WSS) is generally a difficult value to evaluate, both experimentally and computationally.

As excellently reviewed by Reneman et al. [295], it is clear that the experimental measurement resolution will also significantly influence the calculation of WSS, for the same reasons as for the computational simulations, cf. Section 8.5, i.e. flow-induced WSS in this context is derived from velocity measurements and not directly measured. The highest current resolution that a typical clinically used ultrasound device yields maximum measurement resolutions between 0.25 and 0.3 mm, while an MRI protocols that enable velocity measurement can only yield resolutions of 1.0 to 1.25 mm. Therefore, based on the mesh sensitivity study performed here, systems that can deliver this resolution will underestimate the actual WSS. Nevertheless, as far as the author could determine, no previous experimental study even attempted to quantify WSS under arterial cannular flow conditions.

From the prior computational studies reviewed in Section 8.1.1, only the studies by Yang et. al reported consideration of the sensitivity of the boundary layer mesh size to capture WSS, i.e. the size of the layers of elements immediately covering the aortic wall. Thereby, they also emphasized the importance of considering the mesh sensitivity when needing to evaluate the WSS, as was done here in Section 8.5. Although Yang et. al only considered a flow rate of 1 l/min through a conduit with an inner diameter 9% smaller than the straight end-hole cannula considered here, they reported WSS at the jet landing site roughly between 150 and 180 Pa, cf. Section 8.1.1, which correlate well with the straight end-hole cannula yielding 145 Pa. All other studies either considered a sufficiently fine mesh but of purely Cartesian elements [238], or simply only mentioned that global mesh refinement was done to prove the adequacy of the mesh resolution. However, the combination of such a statement and distinctly lower values of WSS reported, seemed to reveal that no explicit attention was given to obtain a mesh that will sufficiently capture the induced WSS, if any at all.

The results for the WSS measured, as well as the accompanying danger-zone area reveals a previously presumed, but not quantified influence of the jet on WSS – the dangerous, inaccurately named "sandblasting" effect. Furthermore, as considered in detail in Section 8.7.1, these results reveal non-obvious trends with changes in orientation and cannula tip design. Finally, based on the resulting danger-zone area, the influence of WSS is significant and earnestly needs to be incorporated in future investigations. This

is especially critical, due to its large potential impact and the comparatively little detailed consideration it has received in previous investigations.

8.7.3. Limitations

8.7.3.1. Direct comparability of tip designs

A number of different factors limit the direct comparability of the cannula tip designs as presented here, but also between different studies. All of these factors need to be taken into account when comparing these tip designs – some of which were considered here, some beyond the scope of this investigation – as expanded upon in the following.

Cannula configuration relative to vessel geometry The presented results show how the tip design and cannula configuration, i.e. insertion depth and orientation, had a varying and complex influence on each of the evaluated parameters. Inherently, every cannula performance parameter evaluated depended on the vessel geometry and its configuration therein – and therefore hampered direct comparison even between cannulas. This was because positioning of each specific cannula tip design and configuration was done relative to the cannulation site, as is clinically relevant, and not to obtain some sort of comparative position/orientation within the vessel lumen. However, the only performance parameter independent of the vessel, as mentioned above, was the exit velocity measured over consecutive slices at the cannula outflow, expected to only be dependent on the tip design. Furthermore, although helpful, neither the peak jet flow velocity nor its distribution ever appear in product brochures, and is not always reported in experimental studies. All other measures, including the pressure drop over the cannula, were clearly dependent on each aspect of the cannula configuration within the given vessel geometry.

Rated cannula size does not reflect its inner diameter The difference of the cannula inner diameters considered here, cf. Table A.4 will obviously influence the direct comparability of these results for the different tip designs, cf. Table 3.3. However, as mentioned previously, these tip inner diameters were intentionally kept to reflect the performance of cannulas that are clinically available and rated as having the same size – all 24 Fr in (outside) diameter, cf. Section 3.1.2.2. Furthermore, inter-study comparability of arterial cannula performance is generally difficult to evaluate, due to the variation of inner diameters, which is seldom reported.

Entire cannula vs. cannula tip only As eluded to in Section 3.1.2.2, one of the major drawbacks that further hamper comparability, is that experimental studies always reported the pressure drop over the *entire* cannula and did not distinguished between the pressure drop over the tip and the tube, respectively. The only exception was a study performed by Verdonck et al. [347], which intentionally considered the pressure drop over the tip and the entire cannula, respectively, due to the rightly noted variation in cannula length and tapering geometry of different cannulas. Although these authors used water at a flow rate of 1.3 l/min and did not consider the hybrid cannulas nor exactly the same cannulas evaluated here (although they consistently chose a single series of cannulas from the same manufacturer, all rated as 24 Fr), their comparison yielded two important findings.

Firstly, different cannula tips from the same clinically used series assessed in their experiments, with an unreported although presumably tapered geometry, yielded cannula tubing pressure drops that varied between 1.5 and 3 mmHg, which represented roughly 15 and 20% of the pressure drop over the entire cannula. However, the cannula tubing preceding an additional custom tip also evaluated in this study, consisted of a straight pipe and consequently yielded a pressure drop of ∼30 mmHg, which is more than ten times that of the other cannulas considered and represented more than 90% of the total drop over the cannula. Secondly, the pressure drop over the tip and the cannula tubing show an inter-dependent relationship and also depended on the flow rate. Considering only results of a straight end-hole cannula with a presumably, yet not reported tapered cannula tubing geometry, these authors effectively demonstrated

the how an increased flow rate caused a near linear increase in pressure drop over the considered cannula tubing, while yielding an exponential increase over the cannula tip. This implies that the pressure drop for two cannulas with exactly the same tip design and inner diameter, but with different cannula tubing will cause a different pressure drop over each tip and cannula tubing, respectively. This complex relationship has not been previously considered, apart from this investigation by Verdonck et al. [347].

Consequently, these results clearly emphasized the importance of taking the significant pressure drop induced by the cannula tubing preceding the cannula tip into account and differentiating between the pressure drop of these two components of the cannula in order to obtain more comparable results of cannula performance. Furthermore, this phenomenon helps to explain inter-study disparities in cannula performance measured, as reviewed in Section 3.1.2.2. It also justifies the comparably low pressure drops extracted from the presented results (compared to those reported in literature), which only considered the pressure drop over the tip, *in absence of preceding cannula tubing* and at a relatively low flow rate for its size, cf. Figure 8.3.

Modeling definition of tip conduit length   In order to improve comparability in the presented models, the cannula tubing was omitted from the considered computational studies. Nevertheless, apart from the different inner diameters physically measured, another factor hampered the comparability: the modeling definition of a common conduit length of the tip. As explained in Section 8.4, the tip conduit length was chosen to be constant for each cannula. The difficulty therein lies in choosing a comparable starting point for this line at the cannula outflow. For example, consider the end-hole and side-hole cannulas. For the former, the tip conduit length stretched from the cannula outflow to its inflow and was therefore fully enclosed by the tubular cannula wall over its entire length. For the latter, it stretched from the diverting cone center to the inflow, and was only fully enclosed by tubular cannula wall from the point where the side-holes started down to its inflow. Prior to this point, the fluid was free to flow into the vessel conduit, effectively resulting in a closed tube length of 12% of shorter than the end-hole cannula. Accordingly, the hybrid cannulas were even less comparable, resulting in 48% shorter closed tube length than the end-hole cannulas.

Such an observation indicates that the reduced closed tube length contributed to the comparatively lower pressure drop obtained from the side-hole and hybrid cannulas shown in Figure 8.3, apart from its ability to disperse the jet. However, its influence is expected to be limited, since it only entails an extra small portion of straight tubing that will increase the pressure drop accordingly. Its effect on other parameters investigated here are not further considered, although would foreseeably also be limited.

Clinically available cannula comparability and its improvement   Understandably, manufactures predominantly test and publish only pressure drop vs. flow rate data for cannular flow into an open tank using water at room temperature for a set of their cannulas. Such information brochures also only considers those cannulas tested from the manufacturer. And even though its only pressure drop vs. flow rate data, it is not compared to cannula performance of other manufacturers, nor are such brochures geared towards making such comparisons easy. As is evident from the preceding discussion, the value of such data only gives a *limited comparable impression* of cannula performance, because of the multitude of different factors that hamper cannula comparison, but also due to myriad of factors responsible for clinically variable conditions, considered in the next subsection.

Nevertheless, this relative cannula performance published by manufacturers communicates some indication of cannula performance to clinicians, yet supplies inadequate information for the engineers evaluating the clinical performance of the specific tip design. In an attempt assess comparability in a more rigorous manner, the models evaluated in the presented computational investigation provided a more comparable evaluation of tip designs than has previously been reported – neither from manufacturers or past experimental or computational studies – as well as insights into the influence of cannula configuration.

Limited comparability is indicative of the status quo   Ultimately, this direct incomparability can be considered a limitation, because it hinders the objective evaluation of the optimal cannula tip, but also

configuration as a whole, in terms of the stated requirements. On the other hand, this direct incomparability demonstrates the variation of flow conditions that will occur in current clinical practice due when choosing a cannula of the same French-size – as was intended when choosing the cannulas to evaluate. Furthermore, it also indicates the lack of information that a clinician is faced with when choosing the optimal cannula when performing CPB on a specific patient.

8.7.3.2. Clinical variations not considered

Various other important clinical variations exist that were outside of the scope of this investigation. These factors are briefly mentioned below.

Of the considered cannula geometries, only the insertion depth and orientation of straight end-hole cannula was evaluated. But as is evident from the presented findings, changes in the configuration influenced the performance of this simple cannula tip geometry in a non-trivial manner. As such, it will be important to consider these aspects for each cannula tip individually. Such an evaluation will also be helpful to understand the robustness of cannula performance despite clinical variation – a currently scarcely evaluated performance parameter.

Other variations of tip-designs, as those shown in Figure 3.1, were not further considered, due to minimal variations in cannula characteristics from the considered models. Furthermore, the two other principally different tip-designs shown in Figure 3.1, which were not simulated, included the Medos X-flow and the Dispersion cannula. The former was not considered due to its reportedly infrequent use and the latter due to its poor performance. The Dispersion cannula has been found to cause pressure gradients of larger than 100 mmHg for the required flow rates [180], which has previously been shown to cause hemolysis [50].

A very important factor not considered was the influence of a change in flow rate. Although not evaluated for the straight end-hole cannula model considered in the comparative functional performance of Section 8.6, the simplified version of this model was considered at different flow rates for the mesh convergence study, cf. Section 8.5. To demonstrate the effect of an increasing flow rate, the danger-zone area is plotted for four different cannular flow rates in Figure 8.10. Discrepancies between these result and those shown in Figure 8.6 can be attributed to an almost non-existent cannula conduit length, i.e. practically no dissipation caused by flow through the cannula tip. Whereas 1 l/min did not yield WSS larger than the damage threshold, the increase in danger-zone area dramatically increased with an increasing flow rate – increasing by more than 50% from 2 to 3 l/min, and by slightly less than 50% from 3 to 4 l/min. Furthermore, for cannulas of the size considered, the flow rate is typically between 5 and 6 l/min. Of course, an increase in flow rate will also have a significant and nonlinear impact on the other parameters evaluated.

Although currently rarely used in CPB, pulsatile arterial cannula flow was not considered here. Although largely abandoned due to dangerously high peak velocities reached and no conclusive benefit over continuous flow CPB seen in patient outcome, it still maintains a valid position in the VAD community. Based on the literature reviewed and the detailed evaluations performed here, further consideration of pulsatile arterial return would urgently require an in-depth consideration of its flow characteristics.

A number of patient-specific factors will also play an important role on proximal flow characteristics of arterial cannular flow, as reviewed in Section 8.1. The patient-specific ascending aorta geometry largely deformed as a consequence of aortic clamping is considered in the next chapter.

8.7.3.3. Computational aspects

Some limiting aspects with regards to the computational models presented are further elucidated in the following.
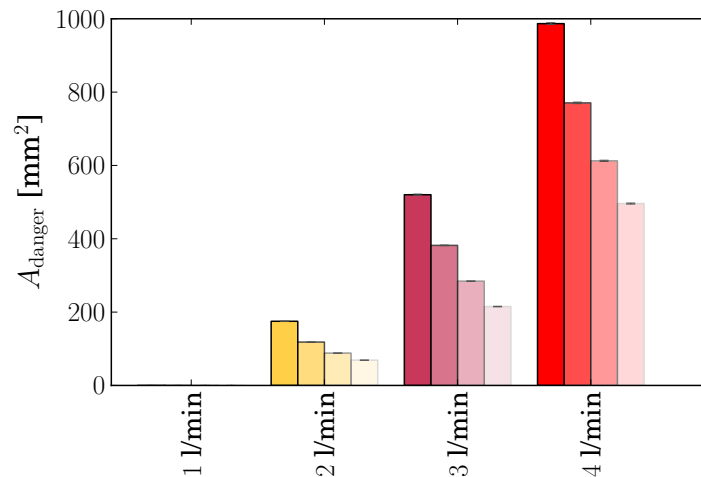
Figure 8.10.: The influence of different flow rates on the inflicted danger-zone area, considering the straight end-hole cannula model used for mesh convergence. Each increasing degree of transparency indicates a different damage threshold, i.e. $40, 50, 60, 70$ Pa.

Apart from the cannular jet causing a stagnation point(s) when hitting the aortic wall, such points were also present in the side-hole and hybrid cannula tips itself. In order to sufficiently resolve such stagnation points, a mesh size twice as small as the required base level size (h_b) was used, as shown in Figure 6.9. However, no further mesh sensitivity was tested to determine whether or not these stagnation points were sufficiently resolved and needs to be expanded upon in future studies.

The presented results only considered a base-line set of parameters. A potentially helpful parameter would have been to evaluate the shear rates for determining a hemolysis index, cf. Section 8.1. A further interesting effect to evaluate would be the magnitude of the Coanda effect (if it can be quantified) and its implications for flow distal to the cannulation site.

No modeling of turbulence effects was incorporated in the simulated models. Although the flow rate was limited to 3 l/min, the resulting Reynolds numbers Re for pipe flow actually meant that the flow was expected to be in the transitional region between laminar and turbulent. Additionally, following the results and discussion of Menon et al. [239] considering a detailed fluid dynamical evaluation of cannular flow jets blown into a large reservoir, the following should be noted: Firstly, such a submerged jet will already yield flow instabilities at $\mathrm{Re} = 225$ [75], justifying the fluctuations present in the time-averaged results presented here, since the Re considered was at least ten times greater for all the cannulas considered. However, despite the meticulous mesh sensitivity presented here, as seen in Figure 8.1, the axial and circumferential discretization size is expected to have also contributed to the variation observed in the results. Secondly, submerged jets have been shown experimentally to only display full turbulence when $\mathrm{Re} > 1.10^5$ and therefore the cannula flow considered here can safely be assumed as transitional [87]. Thirdly, Menon et al. [239] demonstrated that the core length of the jet from a straight end-hole cannula, demarcated using an isocontour definition of a coherent irrotational structure, increased with higher Re. The end of this core length is characterized by significant oscillations that increased exponentially over time. Already at $\mathrm{Re} = 650$ the core length was 20 times the inflow diameter, suggesting that in the considered simulations, such an irrotational core always reached the vascular wall. Furthermore, the core length also represented the main region of jet flow energy dissipation and correlated to the resistance of the cannula outflow, i.e. would influence the pressure drop over the cannula. Fourthly, at higher $\mathrm{Re} = 2150$, Menon et al. [239] found that the core could not be clearly demarcated and yielded complex vortical

structures and turbulent characteristics. However, apart from the such characteristics displayed during cannular flow and prior to the jet landing site, it is not entirely clear how the flow characteristics will change upon hitting a non-flat surface of the aorta at a particular angle – and how fast relaminarization of the flow will occur due to the amount of energy dissipated. Evidently, the consideration of turbulent effects will refine the results with regards to the energy dissipated through the different cannula tips and by the aortic wall. However, in the context of the considered simulations, turbulent effects were assumed to be suitably small. A combination of the numerical damping caused by the stabilized fluid element formulation with an unperturbed inflow profile entering the flow domain and the relatively short distances between the cannula outflow and the jet landing site causing significant energy dissipation (evident from the difference between cannula and vessel outflow exit velocity distributions) was considered key elements allowing the numerical solution to always converge, despite no consideration of turbulence. It is foreseen that these turbulent effects will become more pronounced at higher flow rates and distal effects of cannular flow, neither having been considered here.

8.8. Conclusions and future perspectives

8.8.1. Improved cannula design

The presented results and discussion clearly demonstrates that much room for improvement still remains to improve arterial cannular flow characteristics. Such improvements are definitely not limited to tip design, but includes all aspects that will influence the flow performance characteristics, e.g. the cannula tubing that precedes the tip, the cannula material that is determinant of its inner diameter, its relative position in the aorta, the aorta size, etc.

These findings, obtained from the reviewed literature and presented computational study, provide previously unreported detail, insights and much needed input for improved cannula design. Furthermore, these findings are also expected to emphasize the importance of systematic incorporation of patient- and procedural-specific aspects into clinical design-making, pertaining specifically to cannulation site choice and cannula tip choice, e.g. if occluding near the occlusion site, it would be preferable to use a curved tip, if mild to heavy atherosclerotic lesions exists at the cerebral artery orifices, it would be preferable to use a straight tip, etc. These aspects should serve as input to future work further quantifying such aspects.

As is evident from the different sources of clinical variations considered, a major benefit in future cannula design will be a cannula that provides robust flow characteristics despite clinical variation. Certainly, some aspects of clinical variability will remain unavoidable, e.g. when a higher flow rate is required due to a decrease in cerebral saturated oxygen pressure. However, a major component of the variability influencing the flow characteristics show great potential of being surmounted, namely the influence of the vessel geometry and resulting cannula configuration. Therefore, a highly desirable cannula design is one that can yield robust flow performance that is (largely) independent of its insertion depth, orientation or specific location along the chosen cannulation site. Of course, its performance must not only be robust, i.e. nearly constant despite changes in cannula configuration, but also good, i.e. high jet exit velocity attenuation, low pressure drop etc.

One cannula tip design that presents evidence of being able to fulfill such requirements of yielding robust flow characteristics, is the shielded end-hole cannula considered here. This is because the shield was able to relatively sufficiently disperse the high velocity jet *prior to* hitting the aortic wall, yielding the comparatively lowest peak jet exit velocity – the only functional measure expected to be independent of the vessel. The influence of a change in cannula configuration on measures that were dependent on the vessel are expected to be small, specifically due to the proficient dissipation of the jet. However, the shield position and geometry, as considered here, has the overriding limitation that it induces an exceedingly high pressure drop. This is a very important feature that will need to be improved upon prior to its adoption

in the clinical setting. For exactly this reason, use of the Dispersion cannula was discontinued, despite its proficient ability to disperse the jet, cf. Section 8.7.3.2. Nonetheless, the use of a shield as presented here provides the potential of a larger non-native surface upon which the jet can be dispersed. The original blasting plate-type shield suggested in the patent describing this idea, from which this shielded geometry was improved upon, cf. Section 6.4.1.2, is expected to provide little benefit over the Dispersion cannula's performance, due to its geometric similarity. Success of a shielded cannula design will depend upon whether the shield-cannula-configuration can be optimized to still yield such sufficient jet dissipation, but at a significantly lower pressure drop comparable to existing cannulas. A proficiently performing shield then also presents the potential of including passive flow altering elements for inducing helically rotating flow, thereby more closely imitating the physiological flow, cf. Section 3.1.2.3 .

8.8.2. Clinical relevance and the need for a new clinical reference

As mentioned in Section 8.7.3.1, clinicians are supplied with flow rate vs. pressure curves of water at room temperature flowing into a reservoir from cannula manufacturers. Combining this data to a desired patient flow rate, calculated according to the cardiac index [239] (usually related to body surface area), a cannula is chosen. Such data from manufacturers thereby provide clinicians with a consistent reference, despite the potentially (significantly) influence to the desired cannular flow characteristics that will be caused by the myriad of potential clinical variation factors and the difficulty of comparing performance between different cannulas.

Even though many experimental, clinical and computational studies have been performed to elucidate on the influence of such clinical variations, none succeed in incorporating all possible variations, including the computational study presented here, cf. Section 8.7.3.2. Therefore, although most studies improve upon the detail investigated or expand on the number of aspects considered, it ultimately provides the clinician with general qualitative performance trends that cannot be guaranteed to occur in each patient-specific case.

In this regard, computational investigations offer the potential of relaying arterial cannula flow performance for a patient-specific case. Obtaining a patient-specific geometry is relatively straight forward. Creating a sufficient mesh for capturing the needed effects with modern meshing software is also achievable with existing commercially available software. Despite the latter aspects being possible, current methods are semi-automated at best and are consequently very time-consuming. Such models are also computationally expensive to solve – the reviewed studies in Section 8.1 typically considered models with $\sim 6.10^6$ degrees of freedom. Furthermore, modeling of the outflow boundary conditions at the truncated ends of multiple arteries has only recently become more reliable and is crucial in simulating accurate flow patterns in the aortic arch [173, 190, 195] – a feature that is definitely not standard in commercial software and will need some further research input to mature. Moreover, the influence of the distensibility of the aortic wall will also be required for improved information regarding arterial cannular flow characteristics [248]. Finally, despite the long lead time to produce such a model, the complexities that need to be incorporated to reflect physically reliable flow conditions and the subsequent computational costs required to solve such a problem, current computing speeds are only able to yield a solution time in the order weeks or several days at best. As such, notions of computational steering in this context, i.e. real-time changes to a running computation, are currently a non-realizable option and at least in the near future.

Therefore, the simplifying assumptions inherent in data from manufacturers, the insufficient incorporation of all clinical variations in experimental studies, and the complexity, time and cost limitations of computational studies underlines the need for an improved clinical reference. Such a reference is considered in the next subsection.

8.8.3. A new paradigm for arterial cannular flow evaluation

As emphasized in the previous subsection, the clinical relevance obtained from all previous investigations of arterial cannular flow, including this one, is only of qualitative value, due to the potential (significant) influence of clinical variation. Consequently, *prior to attempting yet another experimental or computational study*, it is worth considering whether clinically relevant and translatable results will actually be obtainable. If not, then it is worth considering a new paradigm of investigating arterial cannular flow, derived from the presented computational study. This newly proposed paradigm is only discussed conceptually for central cannulation, while further refinements and considerations are left for future studies.

As is evident from all of the functional requirements formulated in Section 8.2, yet never explicitly mentioned in previous studies, is that the aim of the arterial cannula should be to yield flow that assimilates the physiological flow of that patient – of course at an acceptable pressure drop and induced WSS. Therefore, a reasonable comparative measure would be the characteristics of the flow that enters the aortic arch, i.e. a region close to the cannulation site, as considered here. One cannula is then considered better than another when it produces flow exiting the proximal region that closer resembles the typical distributed physiological flow character.

Consequently, a foreseeable experimental setup will need to test different cannulas flowing into an anatomical relevant range of different sized tubes, exiting into an open reservoir. Pressure drop measurements will then reflect the combined influence of the cannula tubing, cannula tip and the cannulated vessel. A measure of jet dissipation – and indirectly the WSS induced – can then be derived by comparing this combined pressure drop with the currently published data, i.e. pressure drop over the cannula flowing into an open reservoir. A further key aspect would be to measure the flow velocities, realizable with standard ultrasound measurements. Thereby, the flow profile exiting the tube segment can be obtained, in order to evaluate the extent of flow distribution that will enter the aortic arch. Cannula position and orientation can foreseeably also be varied to establish cannula performance extremes. Such experimental information can then be combined into a Moody-diagram type chart to enable clinicians to derive the arterial cannular flow performance based on clinically determinable parameters, such as the required flow rate, vessel diameter at the cannulation site and distance between cannulation site and the brachiocephalic artery orifice, i.e. the first branch after the ascending aorta.

Once such information is available, non-dimensionalization could foreseeably be performed, resulting in a measure that supplies an estimate of distribution of flow that will enter the aortic arch within a certain confidence limit affected. This confidence limit will be based on the variations in measurements obtained through the cannula configuration extremes experimentally investigated. Of course, such an experimental setup will not guarantee the specified arterial flow characteristics in the patient-specific case. But it will provide an improved clinical reference, because it also incorporates the effect of the vessel and the resulting velocity profile distribution entering the aortic arch. Thereby, it is expected to significantly improve upon previous attempts at non-dimensional characterizing of arterial cannular flow, which did not take the cannulated vessel into account [258, 347].

Furthermore, this experimental setup can then be extended to a patient-specific computational model only considering the ascending aorta. Such a model should be able to provide flow information that can be matched to patient-specific, time-resolved perfusion data obtainable from MRI. As such, even though flow in the entire aortic arch is not simulated, the cannula configuration and tip can be altered to achieve an outflow as close as possible to the patient-specific flow distribution entering the aortic arch. Such a computational setup will require a computational mesh that is a fraction of the size of needed to simulate whole aortic arch hemodynamics. The time to extract the geometry will also be significantly shorter and simpler boundary conditions will suffice due to only considering a single inflow and a single outflow. It also offers a much more realizable platform upon which cannula tip design and configuration robustness can be evaluated, but also to develop tip designs particularly designed to achieve a wanted physiologically

distributed flow entering the aortic arch – the ultimate goal that a cannula design should aim for. And lastly, it offers of a computational strategy that makes its translation into actual daily surgical planning much more feasible, compared to whole arch simulations.

9. Patient-specific aortic manipulation: occlusion and arterial cannular flow

> *Indeed, the day any two surgeons are found to apply exactly the same surgical techniques will be a notable one!*
>
> — Peter Alson [5]

Whereas the computational investigations of the previous two chapters focused on investigating aortic occlusion and proximal arterial cannular flow effects *in the absence of* patient-specific variation, cf. Chapters 7 and 8, the current chapter is specifically concerned with incorporating a number of these clinically relevant variations, never previously considered or only in part. The scope, importance and the need for an improved understanding of the mechanisms by which these critical aortic manipulation maneuvers will cause injury, and thereby influence patient outcome, have been thoroughly expounded upon in the previous chapters. Furthermore, the preceding work also laid the computational foundation that allows the incorporation of such patient-specific aspects, thereby allowing a computational investigation to achieve previously unattainable insights, as presented here.

In this chapter, aortic occlusion is considered in the context of patient-specific variations pertaining to aortic geometry, local material inhomogeneities, as well as occluder configuration relative to these inhomogeneities. Furthermore, proximal arterial cannular flow effects are considered in the context of patient-specific geometrical variations caused by the occluder configuration relative to a straight end-hole cannula. In both cases, the aim is to assess the sensitivity by which the outcome will vary with regards to subtle changes to the manipulation configuration, i.e. determined by the surgical technique. Due to the in-depth discussion and similarities of the investigations presented in the previous chapters, many aspects equally applicable in this chapter will omitted. The current chapter is structured in such a way to consider each of these two aortic manipulation maneuvers separately, with the outcome of the structural study of aortic occlusion was used as input for the fluid study of proximal cannular flow effects. For each maneuver, brief simulation-specific aspects are considered, the comparative impact of the different configurations are considered, followed by a discussion and concluding remarks.

9.1. Aortic occlusion

9.1.1. Simulation specifics

The simulations performed to consider the stated patient-specific influences during aortic occlusion were introduced in Section 6.2.1.3 and listed in Table A.2. The simulations included the consideration of standard (DeBakey) cross-clamps and endo-aortic balloon occlusion (EABO), referred to as $CC_{0°}^{\mathrm{Calc},i}$, $CC_{30°}^{\mathrm{Calc},i}$ and $EABO^{\mathrm{Calc},i}$ $CC_{60°}^{\mathrm{Calc},i}$ at two different positions along the ascending aorta $i = 1, 2$. As indicated by the subscript of the cross-clamping simulations, three different orientations of the cross-clamps at each position were considered, i.e. the relative angle by which the cross-clamps were rotated around the vessel axis. Furthermore, to investigate the influence of the calcifications, the following simulations were performed without the consideration of the calcification stiffness, i.e. $\Psi_{\mathrm{calc}} = 0$, cf. Eq. (6.93):

$CC_{0°}^{\mathrm{noCalc},i}$, $CC_{30°}^{\mathrm{noCalc},i}$ and $EABO^{\mathrm{noCalc},i}$ at the position $i = 1$. Furthermore, a straight end-hole cannula was also included in the aortic geometry, as indicated in Figure 6.2.

Whereas the displacement of the clamp surfaces were prescribed, cf. Section 6.1.4.4, the endo-aortic balloon (EAB) was inflated while only fixed on its proximally truncated surface, i.e. on the border of the soft boundary material used to simulate the yield of an EAB-catheter inserted femorally, cf. Section 6.2.4.2. This effectively allowed the EAB to change its position as it came into contact with the vessel wall, until further EAB expansion would yield a uniform increase in the applied contact tractions. Thereby, the actual clinical behavior of an EAB that has freedom to move transversely, but has limited axial movement, was approximated.

Due to the complexity and size of the considered patient-specific aortic discretization, the cross-clamping simulations could not be completed to a state of self-contact. The furthest common simulation point reached for the cross-clamp simulations were a normalized clamped luminal area of $|A_{\mathrm{cl}}^{\mathrm{lumen}}| = 0.25$. However, all the EABO simulations were completed, i.e. a normalized balloon pressure of $|P_{\mathrm{EAB}}| = 1.0$ was reached for each simulation, cf. Section 7.5. This also implied that, occlusion potential could only be evaluated for the EABO simulations.

Definitions of all parameters presented in this section, as well as postprocessing steps performed to extract these, have already been defined in Section 7. Any deviation from these definitions or postprocessing steps are fully elucidated below as needed. Every property evaluated here was also compared with the results obtained pertaining to the respective aorta where calcifications were excluded.

9.1.2. Comparative impact

9.1.2.1. Boundary effects

Occlusion of the patient-specific aorta was not completely void of the influences of the fixed truncated aorta surfaces, cf. Section 6.2.1, as was the case for the idealized aorta, cf. Section 7.6.2.3. Similar to the method of evaluating these boundary effects employed in the referred to section, four axial slices along the centerline near the proximal and distal boundaries were taken in 1.5 mm increments. The resulting first principal strain distributions from each slice, depicted visually in Figure 9.1, are plotted in Figure 9.2. The results showing the second and third principal strains are attached in Appendix C.1.

While cross-clamping the idealized aorta under the considered loading, cf. Figure 7.15, the first principal strains at these boundary slices were indicative of the influence of the fixed boundaries. In that case, the first principal directions were changed during cross-clamp progression due to the large vessel deformation, but magnitudes remained practically unchanged. This configuration was much more complicated for the patient-specific case. Other aspects that influenced the effect of the fixed boundaries are briefly expanded upon below.

Firstly, as can be seen in Figure 6.8, the proximal end of the vessel was severely calcified, meaning that an overall stiffer (and more sensitive) response will be experienced in these regions. Secondly, the truncation of patient-specific geometry inadvertently resulted in a relatively shorter inner curvature. Therefore, an equal displacement of the wall on the inner and outer curvature will yield different responses at the boundaries. Furthermore, combined with the different cross-clamp configurations considered, the actual length and volume of the vessel structural domain were not equal on both sides of the cross-clamps, as was the case for the idealized aorta. No further analyses were made of these boundary phenomena, but are taken into consideration when interpreting the results.

Finally, once again, as for the idealized example, deformation of the vessel due to EABO was small enough to yield a negligible influence of the fixed boundaries. Furthermore, the other complexities, mentioned above, clearly did not further influence the results in these simulations.

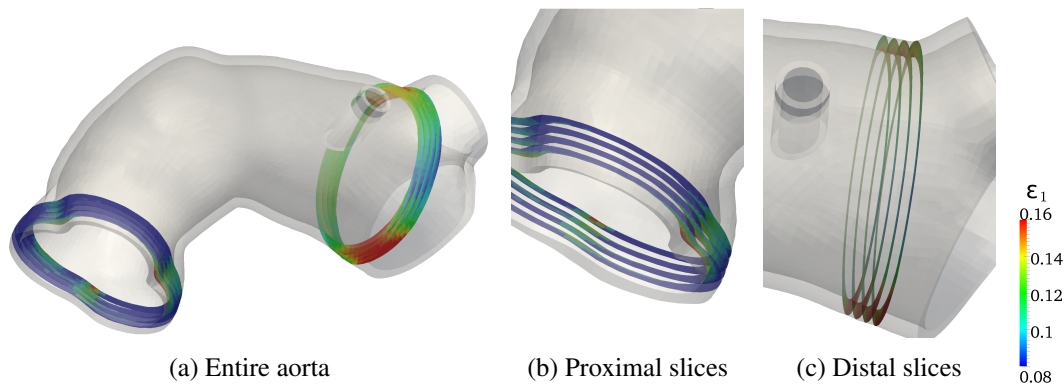(a) Entire aorta   (b) Proximal slices   (c) Distal slices

Figure 9.1.: The influence of fixing the truncated surfaces of the aorta were evaluated by considering the strain distribution in four equi-spaced slices through the structural domain at intervals of 1.5 mm, taken from the proximal and distal ends of the vessel, as indicated here. This example shows two views of the first principal strains evaluated at the different slices for $CC_{0°}^{\mathrm{Calc},1}$ at the maximum occluder progression evaluated, but shown here in the reference configuration.

9.1.2.2. Local progression of strain during occlusion

As in Section 7.5.1, the progression of local strain during occlusion was once again evaluated, but extended to capture the effects of additional local *regions of interest* (ROIs). Data from each such local ROIs were extracted by using the same types of regions previously used, but positioned at specific ROIs, as listed in Table 9.1 and depicted in Figure 9.3.

The ROIs intended to capture a specific calcified region, i.e. *calcification ROIs*, were naturally always kept at the same position, because it is specific to the vessel. The location of the calcification ROIs were distinguished by visual inspection, as shown in Figure 9.3a, but also in size, as listed in Table 9.1. These sizes illustrate not only the physical size of the calcification volume that was extracted from the patient-specific data and included in the model, but also the severity of the lesion. The calcified volume of aortic wall was evaluated by considering the *discretized calcification volume*, V_h^{aCalc}, and the *discretized purely calcification volume*, V_h^{pCalc}, both measured in the reference configuration and defined as,

$$V_h^{\mathrm{aCalc}} = \sum_{j=1}^{n_{\mathrm{ele}}^{\mathrm{ROI}}} V_h^j \left(\mathrm{HU} > \mathrm{HU}_{\mathrm{min}} \right) \tag{9.1}$$

$$V_h^{\mathrm{pCalc}} = \sum_{j=1}^{n_{\mathrm{ele}}^{\mathrm{ROI}}} V_h^j \left(\mathrm{HU} > \mathrm{HU}_{\mathrm{max}} \right) \tag{9.2}$$

with the discretization element volume V_h^j summed over the elements in the extracted ROI $n_{\mathrm{ele}}^{\mathrm{ROI}}$, and the thresholds defined in Eq. (6.96) that always result in $V_h^{\mathrm{aCalc}} \geq V_h^{\mathrm{pCalc}}$.

As can be seen in Figure 9.3, the ROIs influenced by the occluder configuration, or *configurations ROIs*, were positioned accordingly, e.g. the ROI intended to capture the strain progression of the proximal pinching site was positioned according to each specific cross-clamp configuration. Since the EABO does not cause pinching, the ROI locations of the $CC_{0°}^{\mathrm{Calc},i}$ were used, at the corresponding position $i = 1, 2$.

The maximum strain value extracted for each ROI, as plotted in this figure, was the maximum value extracted from the entire region. This meant that the specific element that yielded the maximum value for
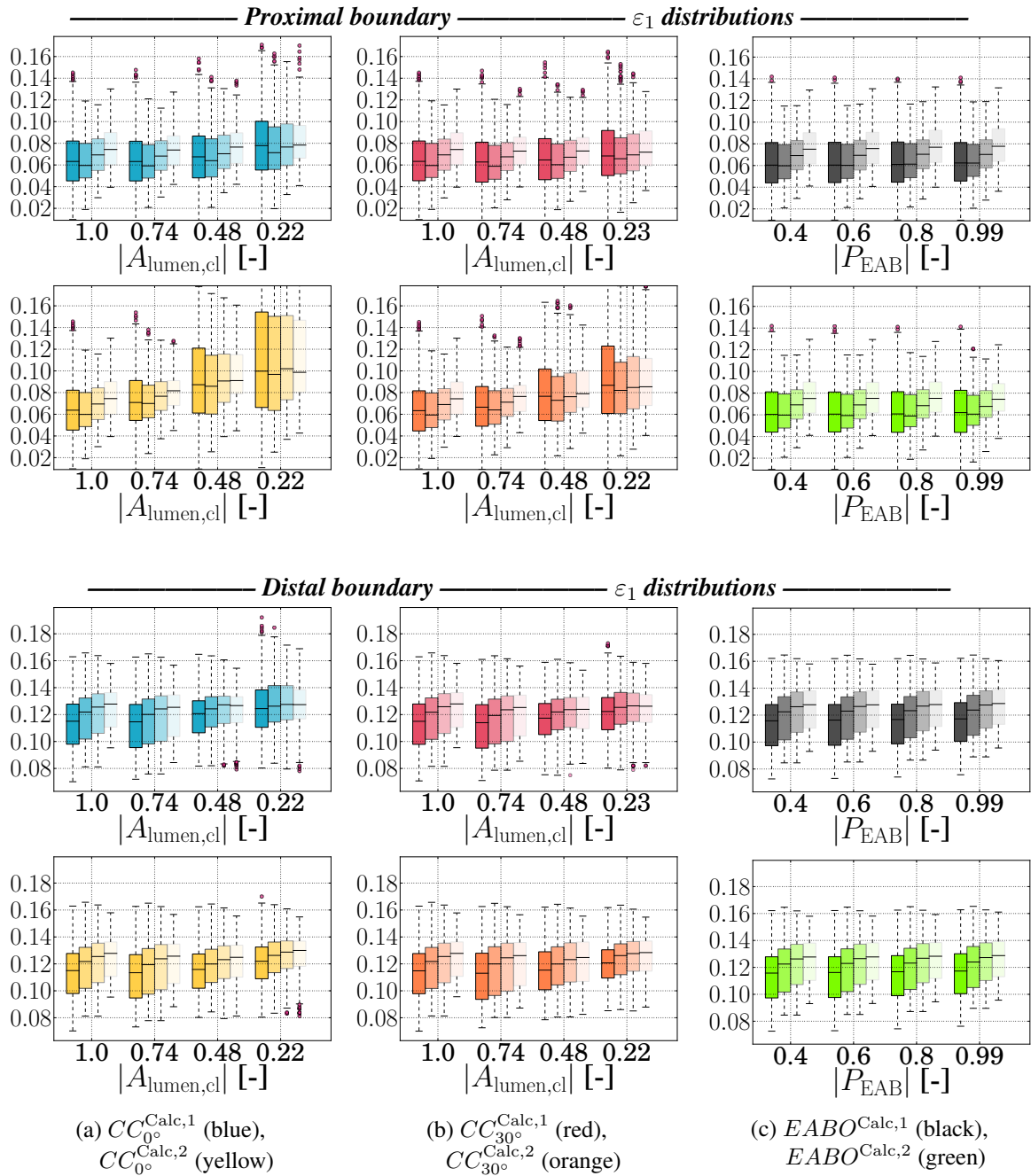
Figure 9.2.: The resulting first principal strain (ε_1 [-]) distributions extracted at the four different axially spaced slices near the proximal and distal ends of the vessel, as depicted in Figure 9.1. Each increasing degree of transparency indicates a slice located further away from the boundary, i.e. the fixed truncated surfaces.

Table 9.1.: Specifications about the regions of interest (ROI) of the aortic vessel wall indicated in Figure 9.3. These were used to evaluate certain local effects occurring during the application of occluder. All spherical ROIs considered were $R = 5$ mm, centered at the intimal surface, except for the *Cann* ROI ($R = 7$ mm). Units of volume in mm^3.

Region of interest (ROI)	Description
Occl-ROI	20 mm tubular segment, centered at corresponding occlusion site, truncated at both ends using plane orthogonal to centerline at occlusion site
Calc1	Spherical region surrounding calcification, $V_{aCalc}^h = 24.9$, $V_{pCalc}^h = 0.9$
Calc2	Spherical region surrounding calcification, $V_{aCalc}^h = 13.4$, $V_{pCalc}^h = 0.0$
Calc3	Spherical region surrounding calcification, $V_{aCalc}^h = 1.8$, $V_{pCalc}^h = 0.0$
Cann	Spherical region surrounding cannula
Dist-pinch	Spherical region at the distal pinching site
Prox-pinch	Spherical region at the proximal pinching site
Superior	Spherical region at the superior site
Inferior	Spherical region at the inferior site

one strain measure did not necessarily correspond with the same element from which the maximum value for a different strain measure was extracted.

Owing to the large volume of data extracted, only the maximum first principal and maximum shear strains values obtained in each each ROI are considered here, as shown in Figures 9.4 and 9.5. Note how the colors from these graphs correspond to the ROIs indicated in Figure 9.3. The third principal and von Mises strain results are attached in Appendix C.2.

From the large amount of data given in these figures, two main observations were evident: firstly, it can clearly be seen whether or not a maximum value from a particular ROI was the most extreme value in the entire occlusion region (*Occl-ROI*), i.e. did the strain response in that particular ROI dominate the strain response at the given point of occluder progression compared to the strain response of the occlusion region, or not? Secondly, the different degrees of transparency help to indicated how much the maximum strain state in each ROI changed from the unoccluded to the nearly occluded state. Some brief observations about cross-clamping, EABO and the cannulation site are expanded upon in the following.

Cross-clamping Compared with the findings from Figure 7.7 of the idealized aorta, it was clear that the first principal strain in the wall at the inferior region would dominate in cross-clamping prior to pinching, as was indeed the case for the patient-specific case considered here, cf. Figure 9.4a and d. However, since *Calc1* and *Inferior* ROIs are in such close proximity for $CC_{0°}^{\text{Calc},1}$ and $CC_{0°}^{\text{Calc},2}$, the high first principal strain were experienced by this calcification, yielding a dominating strain response at the occlusion region, but not for the other clamp configurations, cf. Figure 9.3c and f. Similarly, while the first principal strain in *Calc2* was barely affected by the cross-clamps in *position* 1, it was clearly significantly increased in *position* 2, placing the *Calc2* ROI almost directly adjacent to the a clamp surface, cf. Figure 9.3f–h. The comparatively sharper increase at *Calc2* of $CC_{0°}^{\text{Calc},2}$ towards the final clamp progression can be ascribed to it located near the *Proximal* ROI. Therefore, although the first principal strain dominating effect at the pinching region was not yet observed (due to limited cross-clamp progression), the calcification in *Calc2* clearly accentuated this effect.

Furthermore, the *Inferior* ROI yielded higher first principal strains than the *Superior* ROI, except for $CC_{60°}^{\text{Calc},1}$. This effect can be ascribed the fact that the *Inferior* ROI was mostly located on the inner curvature of the vessel, resulting in increased strains originating either from the geometry or the influence

(a) Thresholded HU values (left, zoomed) contained in *Calc1*, *Calc2*, *Calc3*, cf. Figure 6.8 (right)

(b) *Occl-ROI*: position 1 (top), position 2 (bottom)

(c) $CC_{0°}^{\text{Calc},1}$

(d) $CC_{30°}^{\text{Calc},1}$

(e) $CC_{60°}^{\text{Calc},1}$

(f) $CC_{0°}^{\text{Calc},2}$

(g) $CC_{30°}^{\text{Calc},2}$

(h) $CC_{60°}^{\text{Calc},2}$

(i) $EABO^{\text{Calc},1}$

(j) $EABO^{\text{Calc},2}$

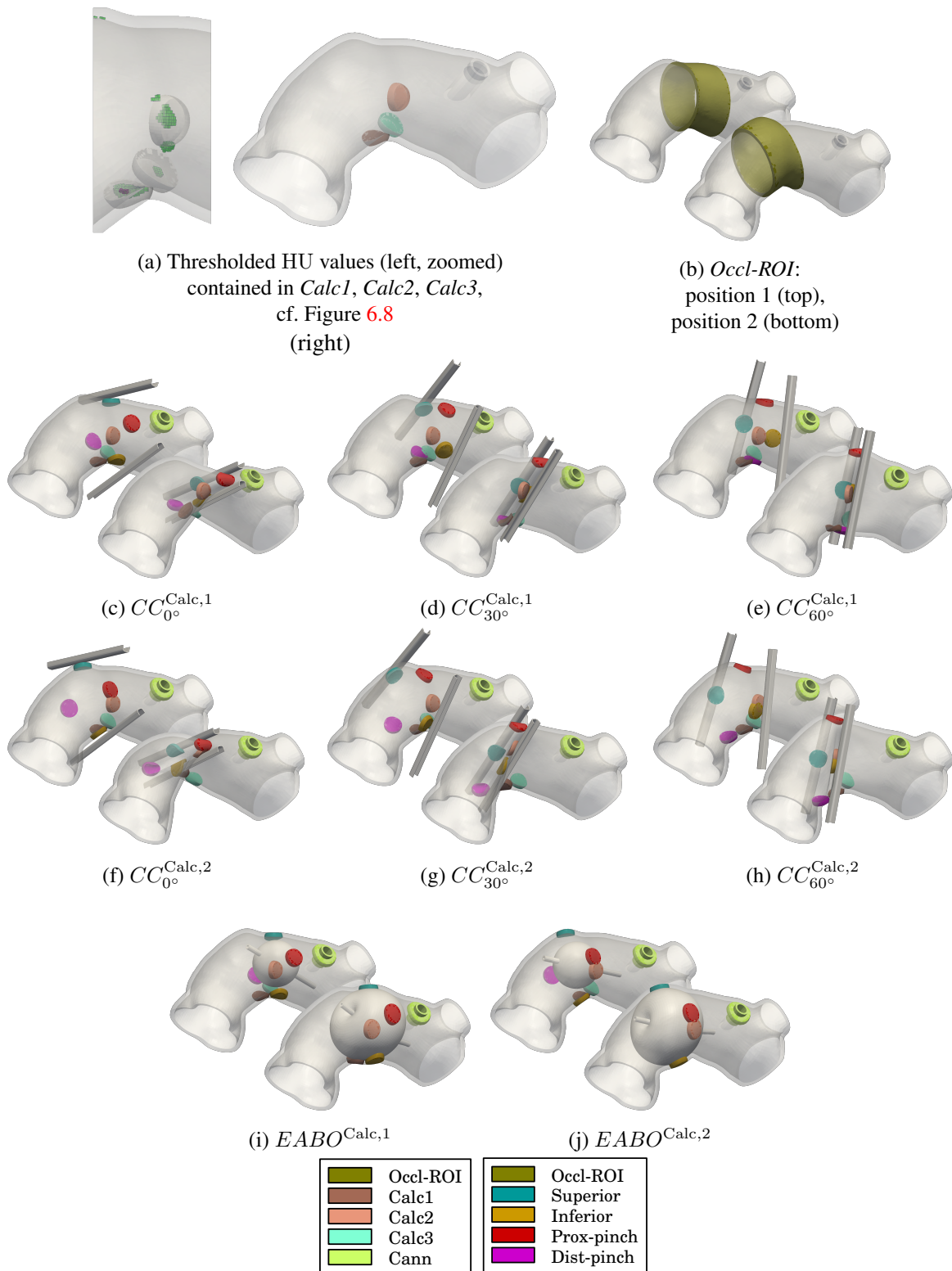|			
Occl-ROI		Occl-ROI	
Calc1		Superior	
Calc2		Inferior	
Calc3		Prox-pinch	
Cann		Dist-pinch	

Figure 9.3.: Localized regions of interest (ROIs) were extracted to evaluate the progression of strain during occlusion, as plotted in Figures 9.4 and 9.5. The representative examples shown here indicate the different ROIs considered, namely the *Occl-ROI*, *Calc1*, *Calc2*, *Calc3*, *Dist-pinch*, *Prox-pinch*, *Superior*, *Inferior* – see Table 9.1 for details.
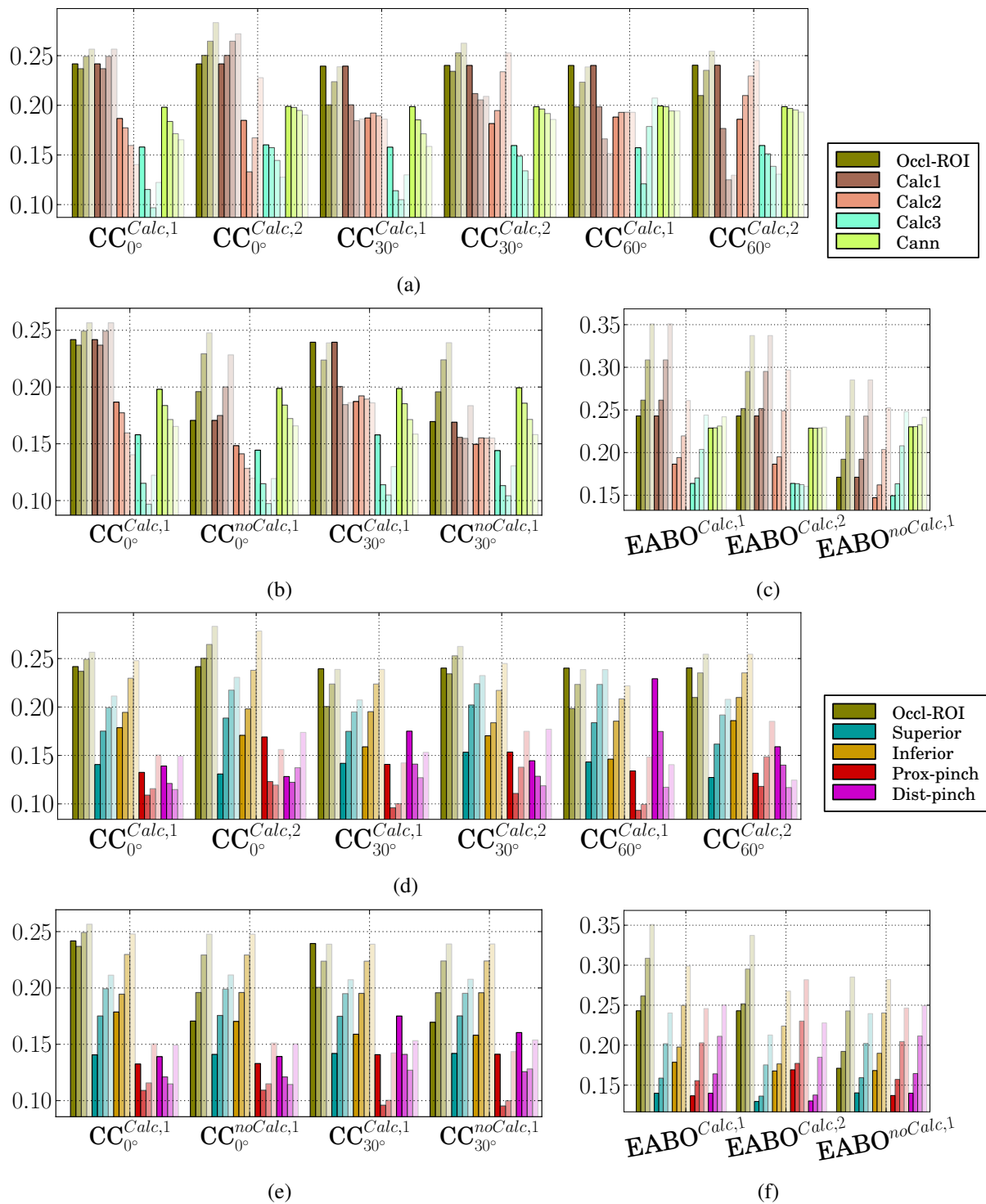
Figure 9.4.: The progression of the maximum first principal strain ($\max(\varepsilon_1)$ [-]) during occlusion, as extracted from the different ROIs indicated in Figure 9.3 – note the corresponding colors. Each increasing degree of transparency corresponds to $|A_{\text{cl}}^{\text{lumen}}| = 1.0, 0.74, 0.48, 0.22$ and $|P_{\text{EAB}}| = 0.4, 0.6, 0.8, 1.0$ for the cross-clamps and EABO, respectively, i.e. from least to most occluded.
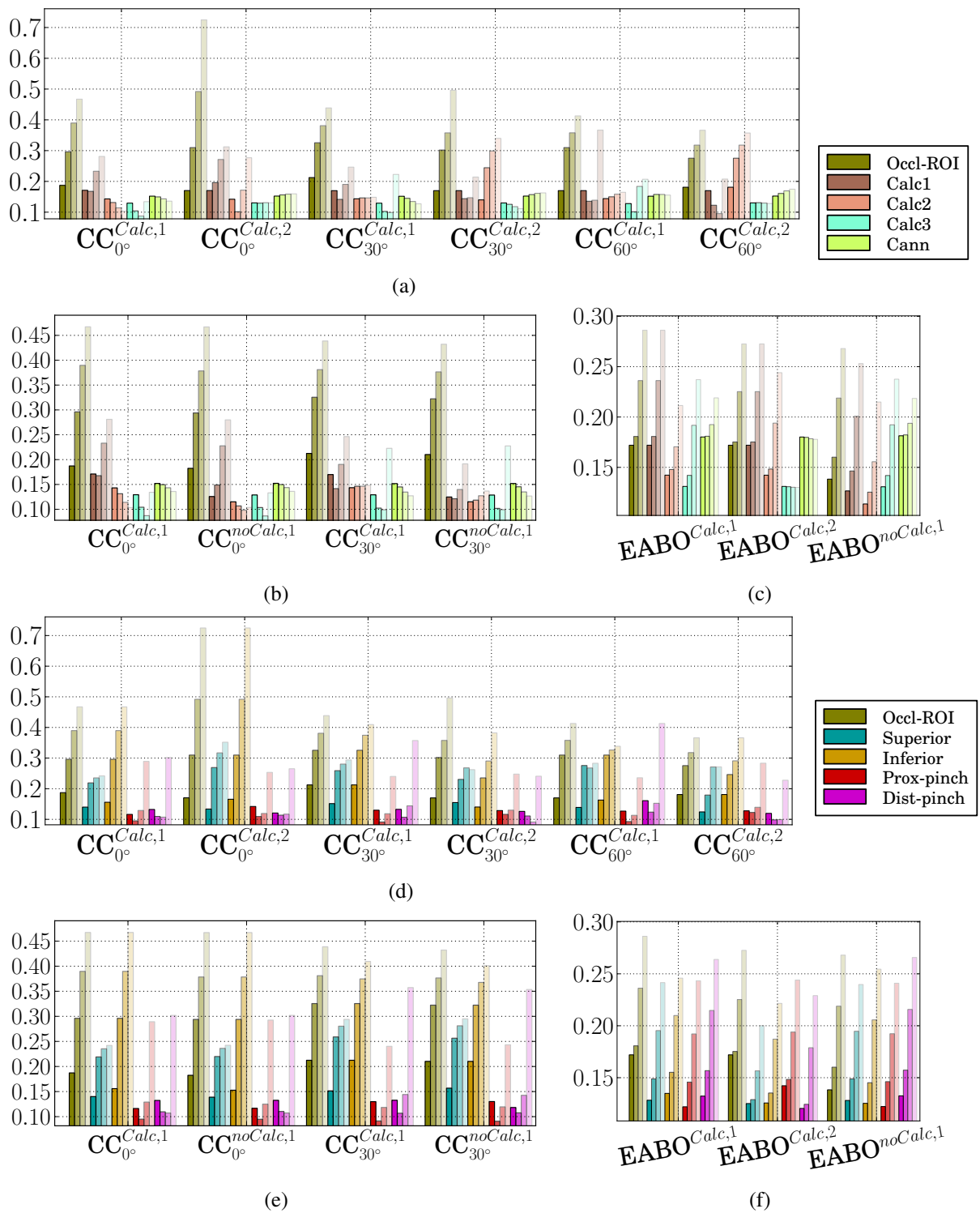
Figure 9.5.: The progression of the maximum value of the maximum shear strain $(\max(\varepsilon_{\tau,\max})$ [-]) during occlusion, as extracted from the different ROIs indicated in Figure 9.3 – note the corresponding colors. Each increasing degree of transparency corresponds to $|A_{\mathrm{cl}}^{\mathrm{lumen}}| = 1.0, 0.74, 0.48, 0.222$ and $|P_{\mathrm{EAB}}| = 0.4, 0.6, 0.8, 1.0$ for the cross-clamps and EABO, respectively, i.e. from least to most occluded.

of the boundary, or both, as seen in Figure 9.3e. Interestingly, in many of the first principal strain responses considered, the maximum first principal strain actually decreased from the initial prestressed state.

Although the maximum shear strains yielded very much the same trends as the first principal strains, it never reached a dominating effect, as shown in Figure 9.5a and d. The only exception was for *Calc2* of $CC_{60°}^{\text{Calc},2}$. Additionally, the same notable increase for *Calc2* of $CC_{30°}^{\text{Calc},2}$ was also observed, due to the same locality reasons described above for the first principal strain trends. The only other clear distinction were the comparatively much higher values of maximum shear strain at the final point of cross-clamp progression measured for *Calc2* (close to the proximal pinching site) of $CC_{0°}^{\text{Calc},2}$ and *Calc1* (close to the distal pinching site) of $CC_{60°}^{\text{Calc},1}$. The proximity to the respective pinching sites would therefore not only be subjected to increased tensile strains, but also compressive strains, hence, emphasizing some trends not clearly visible in the first principal strains.

Comparing the exclusion to the inclusion of calcifications, shown in Figure 9.4b and Figure 9.5b, clearly indicated the lower overall strains in each calcification region considered. Furthermore, comparing $CC_{0°}^{\text{Calc},1}$ to $CC_{0°}^{\text{noCalc},1}$ showed that the presence of calcifications actually determined whether or not the strain in the *Calc1* region would dominate the first principal strain of the entire occlusion region. Interestingly, including/excluding the calcifications had a comparatively small effect on the maximum shear strains between $CC_{0°}^{\text{Calc},1}$ to $CC_{0°}^{\text{noCalc},1}$.

EABO As shown in Figure 9.4c, the first principal strains measured in the calcification regions during EABO, indicated the dominance of first principal strain in the *Calc1* region for both EAB positions, as well as a steep increase in the two other calcification regions, especially at the two final values of $|P_{\text{EAB}}|$. First principal strains in the other regions were less than in the calcification regions, yet also displayed a marked increase, shown in Figure 9.4f. The same dominance was also observed when considering the max shear strains, shown in Figures 9.5c and 9.5f, which was not observed for cross-clamping.

This dominance of maximum strain values for EABO can be ascribed to the large intimal surface area that came into contact with the EAB – and therefore also the size of the vessel wall region affected, as is evident from Figure 9.3. Accordingly, the calcifications ROIs were much more directly influenced by the EAB – for both $EABO^{\text{Calc},1}$ and $EABO^{\text{Calc},2}$ – as opposed to relatively thin cross-clamp arms affecting a smaller region of the aorta. Whereas the strain exerted in some ROIs decreased in certain cases of cross-clamp configuration, it always increased for EABO. This finding further emphasizes the difference in the loading configuration between EABO and cross-clamping.

As with cross-clamping, excluding the calcifications from the vessel wall lowered the overall strains extracted. Interestingly, the fact that the first principal strain in the *Calc1* region of $EABO^{\text{noCalc},1}$ dominated regardless if calcifications were included or not, further emphasizes the above-mentioned explanation of the direct influence of the expanding EAB affecting a large region of the vessel.

Cannulation site The influence of the cannula fixed to the aortic wall (by sharing communal nodes) for the most part did not display any significant increase, as shown in Figure 9.4a,b and c, and Figure 9.5a,b and c. As a matter of fact, for many cross-clamp configurations, the maximum strain values considered actually decreased during cross-clamping. The only exception was the maximum shear strains considered for $EABO^{\text{Calc},1}$ and $EABO^{\text{noCalc},1}$. Geometrically, these peaks occurred at the intimal side of the cannula fixed to the vessel, as the wall was being pushed outwardly by the expanding EAB.

9.1.2.3. Contact area and force-related effects

As mentioned in Section 6.2.1, the axial position and the orientation (axial rotation) of the cross-clamps were prescribed, although the orthogonality of the clamp arms-direction relative to the vessel was determined by visual inspection. For EABO, while the axial position was also prescribed, the orientation of the catheter was not. Only the proximal end (the end attached to the soft boundary material) of the catheter was fixed, implying that the EAB would indeed have a limited range of movement relative to its

fixed boundary. Combined with the local variations in patient-specific geometry, i.e. it is not a straight, constant diameter pipe, the total surface area coming into contact with different configurations of both the cross-clamps and EABO varied, as plotted in Figure 9.6a and b.

Although these differences appear small, it is interesting to note that the combination of the patient-specific geometry and an attempt at visually placing the cross-clamps orthogonal to the vessel yielded a clamp contact area that varied by $\sim 15\%$ for the different clamp configurations at the furthest clamp progression considered. For EABO, although the full EAB-pressure only yielded a variation of approximately $\sim 3\%$, it varied substantially (by up to 60%) progressing up to the full EAB-pressure. These are important findings when considering that other load-related parameters evaluated are dependent on the area of occluder surfaces making contact with the vessel.

The load-related properties considered here were the migration resistance force, the applied clamp force and the normalized EAB volume, shown in Figure 9.6c–f. It can clearly be seen in these figures that for the cross-clamps, the variation in adventitial contact area resulted in a corresponding variation both the migration resistance and applied clamp force. The differences in contact area for the EABO configurations clearly did not show the same dependency, and remained largely unaffected by the induced intimal contact area. These differences effectively demonstrated the differences between prescribed displacement and prescribed load-driven occlusion techniques.

Although not clearly visible from these plots, closer inspection revealed that the effect of including/excluding the calcifications on the these load-parameters were negligible.

9.1.2.4. Contact traction distribution and occlusion potential

Further insight into the cause of the variations shown in the previous section were found by considering the distribution of normal contact traction, as shown in Figure 9.7.

As is evident from these plots, not only the occluder configuration affected the contact traction distribution, but also the inclusion/exclusion of calcifications. These effects are clearly seen in the differences between the median, maximum and interquartile ranges (the box-lengths) between all the different occluder configurations considered. Inclusion/exclusion of calcifications were more prominent for the cross-clamping simulations than for EABO, which can be attributed also to the higher occlusive load delivered by the cross-clamps. Although not explicitly shown, the frictional contact traction showed a similar trend as the normal contact traction (contact pressure) presented here. The difference in peak tangential contact traction at $|P_{\text{EAB}} = 1|$ was 2.85 and 0.86 kPa for $EABO^{\text{Calc},1}$ and $EABO^{\text{noCalc},1}$, respectively. Furthermore, in the Figure 9.7 it can be seen that the contact traction induced depended not only on calcifications, but also on the local geometry. It is interesting to note the substantial difference in the contact tractions due to the presence of calcifications, e.g. for $EABO^{\text{Calc},1}$, the high peak corresponds to the calcification in the *Calc1* ROI indicated in Figure 9.3a.

Since the cross-clamps did not bring the intimal surfaces into self-contact, the occlusion potential, as defined in Section 7.4.1, could only be evaluated for EABO, shown here in Figure 9.8. Furthermore, since the patient-specific geometry did not allow for straight-forward adaptation of the automatic postprocessing strategy described in Section 7.4.1, the presented values were extracted manually, following the same described principals and tolerances used in the automated process.

Despite the demonstrated variations in contact traction, the presence of calcifications did not appear to cause a significant influence to the occlusion potential, indicated in Figure 9.8d, and also seen when comparing Figure 9.8a with 9.8b. Although the clear peak in contact traction at the *Calc1* ROI (cf. Figure 9.3) was absent when not considering calcifications, the similarities in occlusion potential can be explained by considering the definition of the occlusion potential: Since the identification of occlusion potential depends on a finite level of contact pressure along the *entire* luminal surface, an isolated peak, as seen here, was not expected to dramatically influence the occlusion potential. Rather, the different
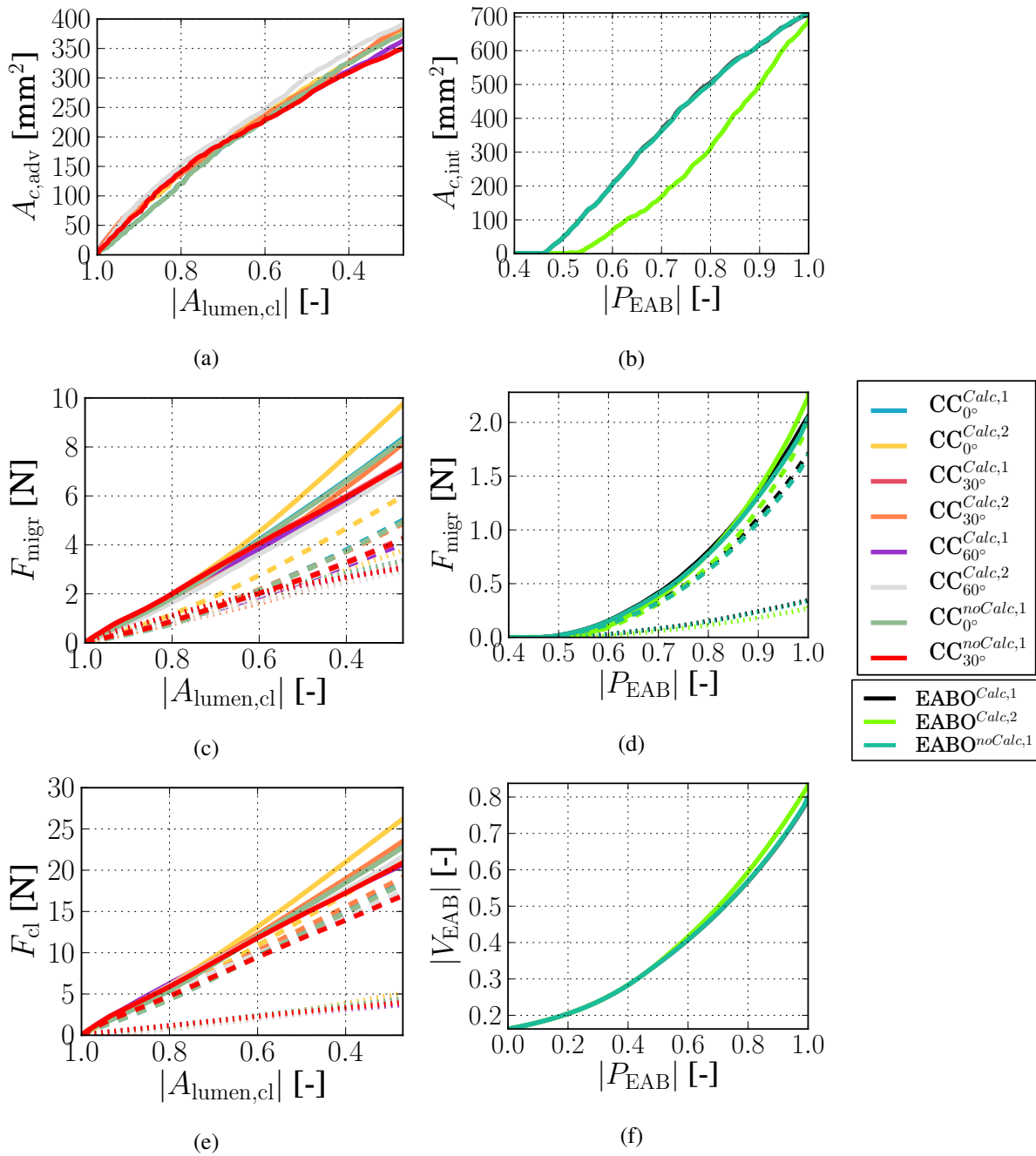
(a)

(b)

(c)

(d)

(e)

(f)

Figure 9.6.: The occluder-vessel contact area and subsequent loads exerted for the different occluder configurations tested, showing the a) adventitial contact area A_c^{adv} for the cross-clamps and (b) intimal contact area A_c^{int} for EABO; the migration resistance force F^{migr} for (c) cross-clamps and (d) EABO; and the applied occluder load, represented by the (e) the applied clamp force F^{cl} for the cross-clamps and (f) the EAB pressure-volume relationship for EABO, i.e. $|P_{\mathrm{EAB}}|$ vs. $|V_{\mathrm{EAB}}|$. Solid lines represent totals, whereas dashed and dotted lines represent the normal and tangential components of the total, respectively, where applicable.
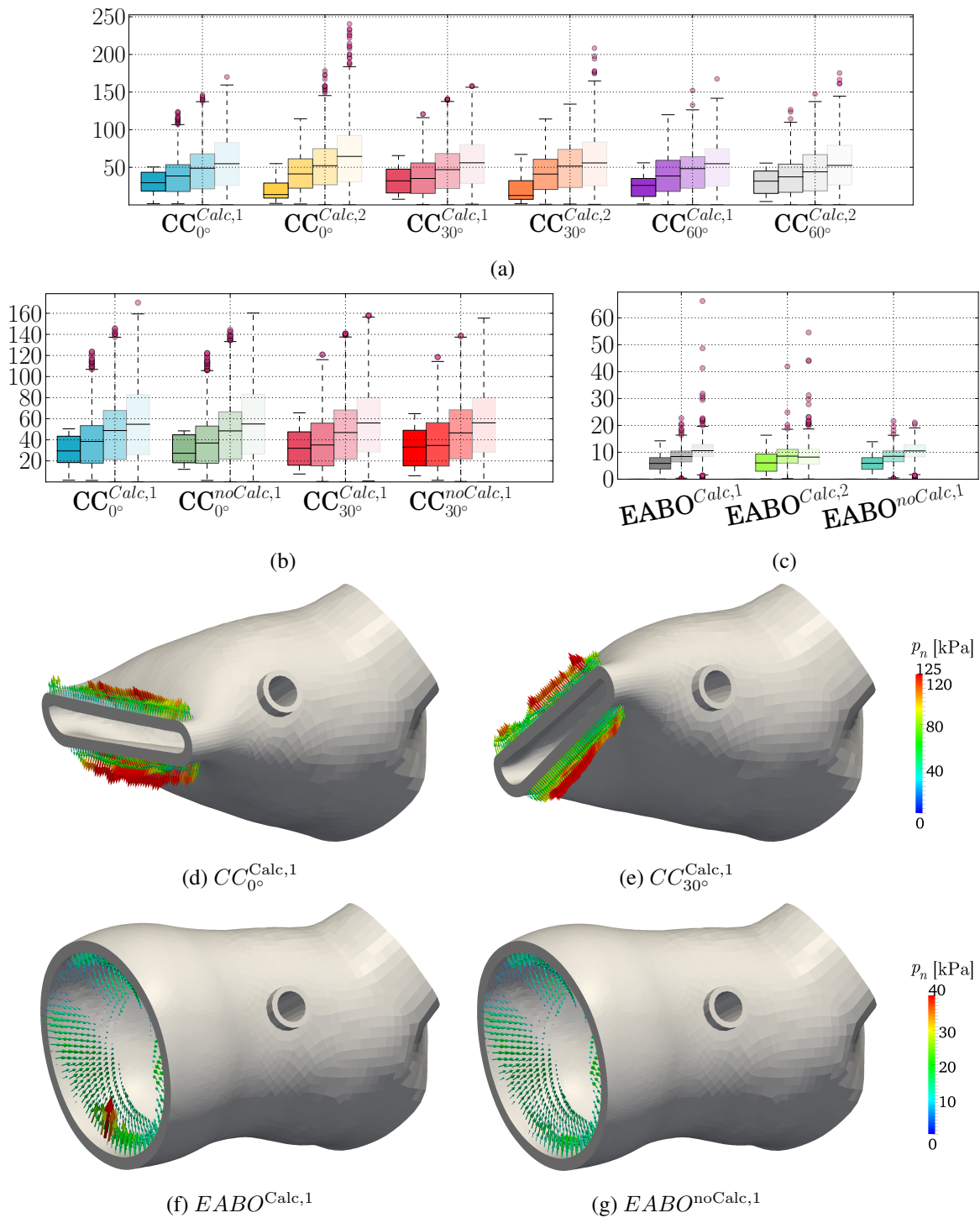
(a)

(b)

(c)

(d) $CC_{0°}^{\mathrm{Calc,1}}$

(e) $CC_{30°}^{\mathrm{Calc,1}}$

(f) $EABO^{\mathrm{Calc,1}}$

(g) $EABO^{\mathrm{noCalc,1}}$

Figure 9.7.: The influence of occluder configuration on the contact pressure (p_n [kPa]) distribution between the vessel and the occluder (a)–(c). Each increasing degree of transparency corresponds to $|A_{\mathrm{cl}}^{\mathrm{lumen}}| = 1.0, 0.74, 0.48, 0.22$ and $|P_{\mathrm{EAB}}| = 0.4, 0.6, 0.8, 1.0$ for the cross-clamps and EABO, respectively, i.e. from least to most occluded. Visualizations of the normal contact traction distribution for four representative examples are given in (d)–(g).

(a) $EABO^{\mathrm{Calc},1}$

(b) $EABO^{\mathrm{noCalc},1}$
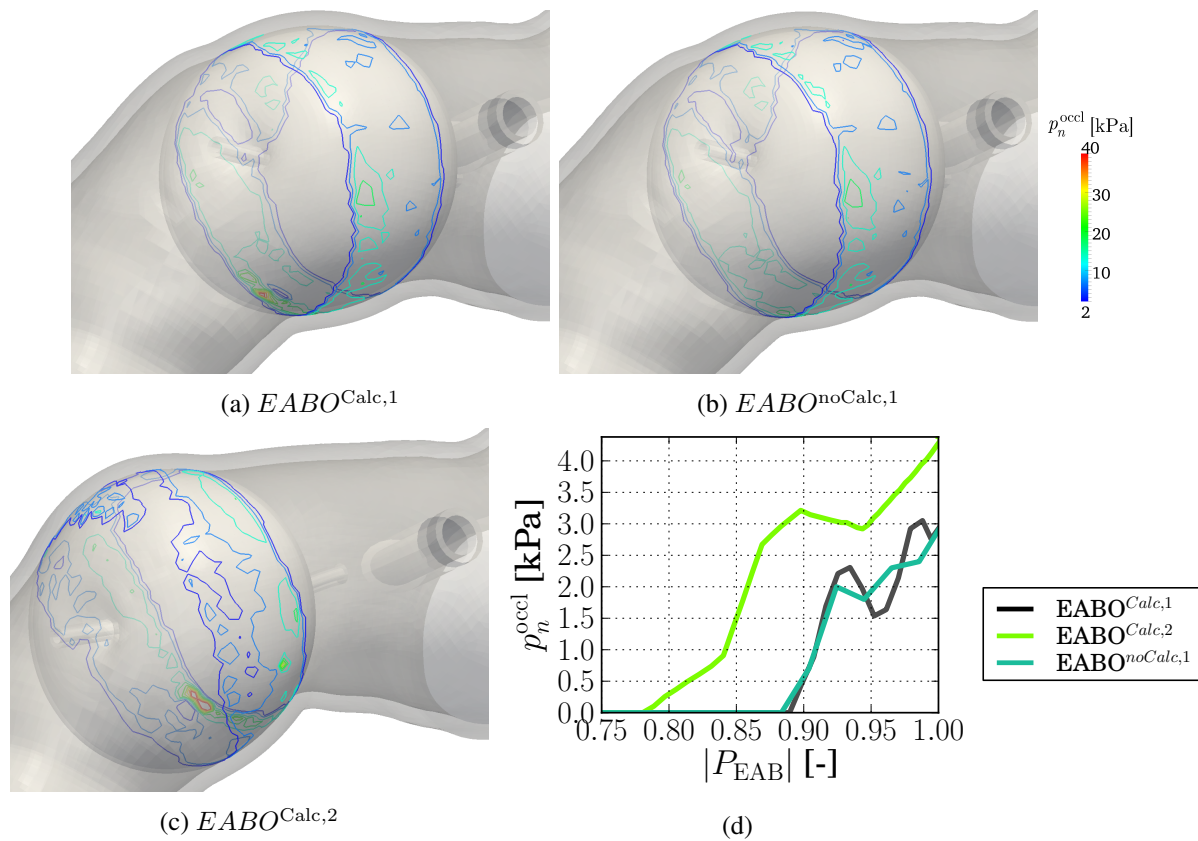
(c) $EABO^{\mathrm{Calc},2}$

(d)

Figure 9.8.: Occlusion potential for EABO of the patient-specific geometry, showing (a) a representative example of the normal contact traction contour lines evaluated to obtain occlusion potential and (b) the resulting occlusion potential for each EABO simulation considered.

geometry irregularities that the EAB was faced with appeared to have a greater influence on the final occlusion potential value.

9.1.3. Discussion

The presented computational study considering occlusion of a mildly calcified patient-specific aorta, not only built upon, but also revealed a number of additional effects not evident from occlusion of the idealized aorta considered in Chapter 7. These effects presented mainly as variations in outcome due to the different occluders used, the occluder configuration (axial position and/or orientation) as well as the material inhomogeneities, i.e. the calcifications. Clearly, these variations in outcome pose significant consequences to the amount of iatrogenic damage potentially inflicted during occlusion, but also underlines the uncertain extent of these effects in a clinical setting. These aspects, as well as relevant limitations to this study, are considered in further detail below.

9.1.3.1. General findings

Both cross-clamping and EABO in the considered configurations yielded distinctly different patterns in which it induced strains in the calcified vessel wall. These patterns were clearly dependent not only on the different fundamental loading configurations of the occluders, cf. Figure 7.2, but also on the variation in

geometric and material properties. Although the cross-clamping could not be brought to a state of intimal self-contact, the strain response showed high sensitivity to a calcified lesion appearing in regions of high strain identified Chapter 7, i.e. the superior and pinching regions. The spherically expanding EAB was responsible for an overall increase in stretch surrounding a relatively large vessel area it came into contact with. Generally, a combination of the calcification size (and conceivably also its morphology), its proximity to the immediate region of the vessel wall that came into contact with the occluder (about the size of the ROIs considered, cf. Figure 9.3, and the occluder loading configuration, was shown to be determinant of the critical strain magnitudes, as well as the strain mode, i.e. tension, shear or compression. The only significant finding from considering the strains induced in the vicinity of the cannula (*Cann* ROI), was significantly increased strain when inflating an EAB very close to it, which can produce leaking around the cannulation site. This confirmed the precautions for a previously proposed solution of performing EABO directly next to the cannulation site [6], cf. Section 2.2.3.

The contact tractions and occluder related loads induced were also clearly related to the occluder loading configuration, and in the case of the displacement-driven cross-clamps, it also implied noticeable variability in the applied load on the vessel, which depended on the total surface area of the vessel that came into contact with the clamps arms. Such variability in load experienced at a comparable state of occluder progression further emphasizes the perils associated of trying to create a system of load-controlled cross-clamping, cf. Section 7.6.2.2. The load-controlled EAB naturally did not display this phenomena. However, concerning was the comparably much lower resistance to migration and also how it varied between the relatively smaller vessel considered in Chapter 7. The peak contact traction caused by occluding at/near to a pronounced calcification was also a cause for concern, cf. contact pressures visualized at the bottom intimal surface in Figure 9.7f. Although this peak was not found to substantially influence the occlusion potential, it was responsible for a dangerously elevated tangential contact traction. Such shearing against the intimal wall is of course extremely hazardous to the endothelial layer of the intima, cf. Section 3.1.2.1. Furthermore, the variations of the surrounding aortic geometry also had a profound effect on the contact traction distribution, as seen in the clearly discernible region low contact traction on the furthest visualized intimal wall shown in Figure 9.7f,g and Figure 9.8a,b.

9.1.3.2. Unknown local damage mechanisms during occluder progression

Although repeated referral was made to the dominance of a strain measure in a particular ROI, it must be emphasized that its dominance is not necessarily indicative of the most critical strains achieved in terms of potential damage. For example, significantly high, yet non-dominating strain in the calcification site might imply damage, whereas the dominating strain in the non-calcification region does not necessarily imply damage.

More accurate insight into this "dominating-strain" phenomenon can only be provided once more experimental information is known with regards to the exact failure mechanisms and corresponding failure thresholds of aortic tissue under different modes of strain, i.e. shear and compressive strains, since damage has predominantly only been considered in tension, cf. Section 7.5.1. Furthermore, more information is needed about the progression of failure of soft tissue with such extreme inhomogeneous properties, i.e. specifically regarding relatively stiff calcifications surrounded by softer aortic wall material and the resulting abrupt changes in stress response.

Despite not knowing the exact mechanism and consequences of failure, it was clear that the calcifications had a profound mechanical significance when considering cases where it was responsible for the dominating strain in the vessel. The significance of its influence, as already discussed in the previous section, was further emphasized by the fact that for some occluder configurations, some regions of calcifications not in the immediate vicinity of the occluder contact region, experienced higher strains than in those regions that were.

9.1.3.3. Limitations

Apart from the limitations discussed in Section 7.6.3, attention needs to be brought to additional aspects included in this chapter.

Probably the most distinct limitation of this investigation was that the simulations of cross-clamping could not bring the aorta to a state of intimal self-contact, as repeatedly referred to above, i.e. $|A_{\mathrm{cl}}^{\mathrm{lumen}}| = 0.22$ was the furthest state reached. Comparing the resulting strains obtained here with those from Chapter 7, clearly indicated that the strain response found to dominate at the pinching sites at an advanced stage of cross-clamp progression was not reached – for the most part, strain in the *Superior* or *Inferior* ROIs dominated. However, exceptions occurred, as shown in Figures 9.4 and 9.5. These exceptions were due to the proximity of the *Calc* ROI to the pinching site. Therefore, it is apparent that increased local stiffness at a pinching site will emphasize the strain response. In other words, it will be particularly dangerous to pinch a calcific lesion.

The influence of the fixed boundaries applied to the truncated surfaces of the ascending aorta modeled, also played an unavoidable role in the strain response of the cross-clamp simulations, as shown in Figure 9.2, especially the results of the occluders applied at *position* 2. However, the actual clinical case of aortic clamping resulting in such large deformations is not devoid of stiff boundaries, i.e. clinically, the aorta is not just an infinitely long tube absent of boundary effects. The ascending aorta itself is connected to a number of relatively stiffer structures, including significantly stiffer material properties of the adjacent aortic root [17], the common occurrence of calcifications in the aortic root (as seen in the considered patient, cf. Figure 6.8), as well as its proximity to the anatomically normal pulmonary trunk and other overlying vascular structures [67]. Additionally, connective tissue surrounding the aorta that is not dissected away during surgery will also limit the deformation of the aorta during occlusion. However, it would be worth to further consider using specialized boundary conditions to model the influence of the surrounding structures, e.g. [248].

Results from a preliminary study [306] showed that the patient-specific calcifications, similar to those investigated here, were sufficiently resolved when discretizing the aortic wall with four elements of a similar aspect ratio. However, this study could also not reach a state of self-contact. Especially for calcifications in the transitional zone, cf. Eq. 6.96. As previously pointed out, physiologically inaccurate modeling of abrupt changes in local stiffness, i.e. from normal to calcific aortic wall, can lead to an overestimation of stress peaks, cf. Section 6.2.3.2. Notwithstanding, a mesh resolution of six elements were used to discretize the wall, which includes the calcifications. However, no further detailed consideration was given to how well these strains were resolved, nor its variability due to changes in the isotropic stiffness used to model the pure calcifications. Also for the strains in the cannulation region, no further consideration of the proficiency by which it was able to resolve strains were performed. Additionally, the cardioplegic cannulation site was also not considered, but owing from the small mechanical influence seen at the arterial cannulation site, its omission is justified.

Prestressing the calcified (inhomogeneous) aorta naturally yielded a non-homogeneous stress/strain distribution prior to occlusion. As in modeling considerations of calcified lesions in abdominal aortic aneurysms (AAA), the same issue of the mechanical role of calcifications within the ascending aorta should be considered here. In other words, how accurately does the unoccluded, prestressed, calcified aorta model represent the actual stress/strain-state of the aorta, especially with the variations due to material inhomogeneities? Previous computational studies of calcifications in AAAs seemed to indicate that it has a homogenizing effect on the stresses and the strains [224]. However, despite potential inaccuracies in the estimation of the unoccluded stress-strain state, the overriding impact of the strains induced by the occluders was clearly noticeable.

Apart from the discrepancies in the resulting strain state of the occluded obtained when considering the influence of local material stiffening and geometric variations, additional sources of variation were

not considered. These include differences in aortic material properties between patients, cf. Section 6.2.2, but also other pathological aspects that can significantly influence the mechanical strength of arteries, such as connective tissue disorders, e.g. Marfan's syndrome or Ehlers-Danlos syndrome (type IV), cf. Section 2.4.2.

In the next section, it is shown how these clinically relevant, largely deformed aortic geometries were used to evaluate proximal arterial cannular flow effects.

9.2. Proximal arterial cannular flow

9.2.1. Simulation specifics

To investigate the proximal effects of arterial cannular flow in a clinically relevant, aortic manipulated patient-specific geometry, the deformed geometry resulting from the structural computational investigation of the previous section was used. Geometries from three different cross-clamp orientations applied at *position* 1 were used, as introduced in Section 6.4.1.1 (cf. Figure 6.9f) and listed in Table A.4. These deformed lumens were discretized and given analogous boundary conditions to the idealized aorta considered in Chapter 8, yielding the following simulations: $Endh_{\mathrm{CC},0^\circ}$, $Endh_{\mathrm{CC},30^\circ}$ and $Endh_{\mathrm{CC},60^\circ}$. The angles given in the subscripts relate to the respective cross-clamp orientation by which the vessel clamped.

Definitions of all parameters presented in this section, as well as postprocessing steps performed to extract these, have already been defined in Chapter 8. Any deviation from these definitions or postprocessing steps are fully elucidated below where applicable.

9.2.2. Comparative impact

9.2.2.1. General flow characteristics

Similar to the results shown in Chapter 8, it was also helpful to first examine the general flow characteristics by considering the thresholded velocity magnitude shown in Figure 9.9.

The most evident observation was probably the extent by which this region of the ascending aorta was deformed, as well as the relative cannula orientation. Cross-clamping of the vessel inherently changed the insertion depth from 21.7 mm, prior to cross-clamping, to 16.2, 15.0 and 7.7 mm for $Endh_{\mathrm{CC},0^\circ}$, $Endh_{\mathrm{CC},30^\circ}$ and $Endh_{\mathrm{CC},60^\circ}$, respectively. Clearly, the incidence angle by which the jet hit the surface was also changed and the jet direction relative to the opposite aortic wall was not near-orthogonal as prior to cross-clamping. Moreover, the cannula was also subjected to transverse rotation, i.e. compare $Endh_{30^\circ,30^\circ}$ (Figure 8.2k) and $Endh_{\mathrm{CC},60^\circ}$ (Figure 9.9c).

9.2.2.2. Extent of jet dissipation

The extent of jet dissipation was evaluated in two different ways, namely by considering the pressure drop, cf. Section 8.6.2, and the vessel outflow exit velocity distribution, cf. Section 8.6.6. The former was measured between the cannula inflow and the vessel outflow, as shown in Figure 9.10a. The latter was also extracted by considering the forward/outward flowing velocity magnitude at four consecutive, planar, equi-spaced slices positioned at the vessel outflow, also at intervals of 3.75 mm, as plotted in Figure 9.10b, with the final slice practically positioned at the outflow, as shown in Figure 9.10c-e.

Once again, as for the idealized aorta, the insertion depth of the same straight end-hole cannula did not have a large effect on the pressure drop. However, it is worth nothing that the cross-clamping related change in cannula rotation did in fact effectively change the insertion depth and the orientation, thereby also influencing the pressure drop, but especially the vessel outflow exit velocity distribution, as can be seen in these figures. The backward-facing change in orientation seen in $Endh_{\mathrm{CC},30^\circ}$ evidently caused

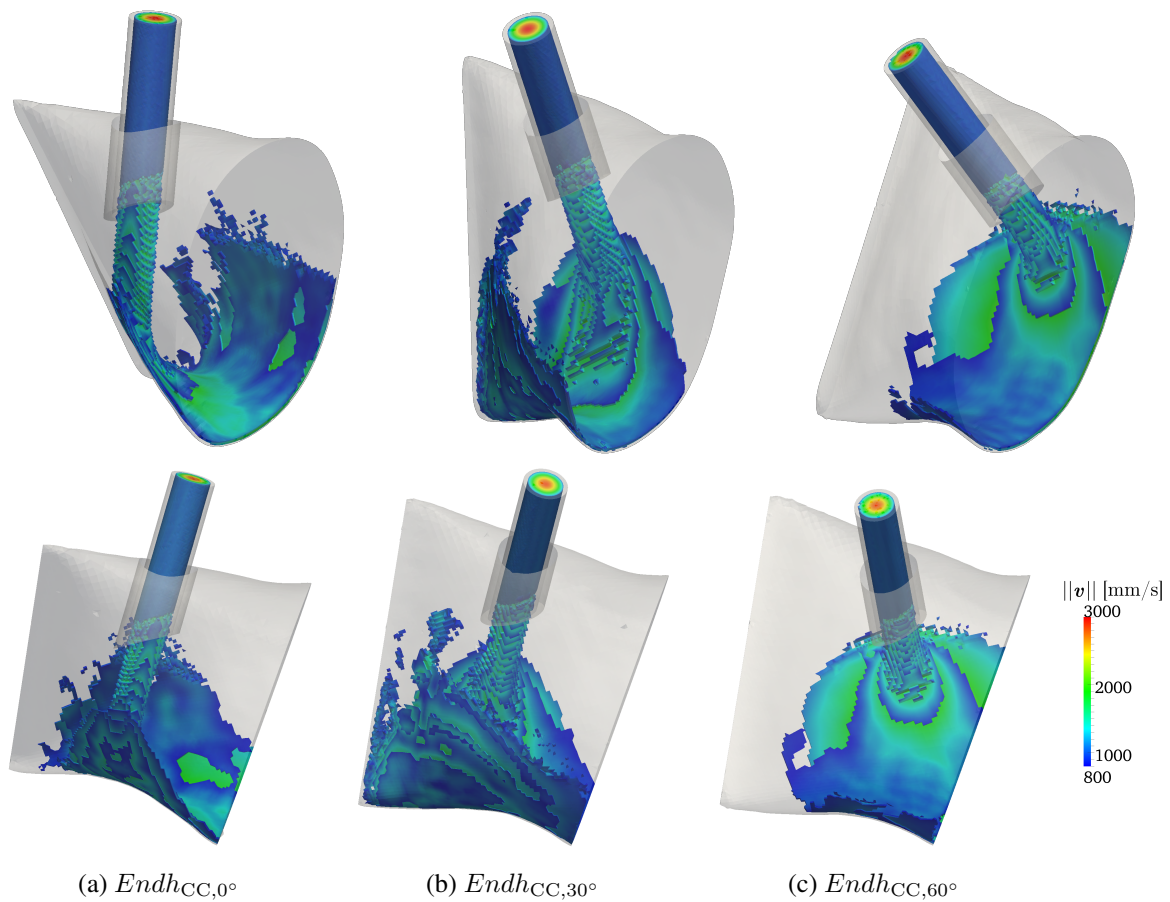(a) $Endh_{CC,0°}$ (b) $Endh_{CC,30°}$ (c) $Endh_{CC,60°}$

Figure 9.9.: Velocity magnitude, thresholded above 800 mm/s of its maximum, showing two arbitrary angles (top and bottom) of each geometry considered for the straight end-hole cannula.

better mixing and a dramatically better (more than halved) outflow distribution, whereas the other two simulations pointing towards the aortic arch resulting in similar distributions.

9.2.2.3. Jet impact on landing-site

The impact that the jet had on the corresponding landing site was evaluated by considering maximum wall shear stress (WSS) and the resulting danger-zone area, shown in Figure 9.11.

Apart from the similarities of these findings to those presented in Sections 8.6.4 and 8.6.5, showing comparable danger-zone area sizes and peak WSS values, was the case of $Endh_{CC,60°}$. Here, it appears that the insertion depth combined with the incidence angle of the jet resulted in a substantially larger peak WSS, yet the danger-zone area remained comparable, despite slight truncation of the evaluated area, as seen in Figure 9.11e.

9.2.3. Discussion

By simply extracting the combined luminal geometry of the vessel and the cannula from the current configuration of the cross-clamped patient-specific model of the ascending aorta, it was possible to evaluate the proximal cannular flow effects in a clinically realistic ascending aorta geometry. This was performed

(a)

(b)

(c) $Endh_{\text{CC},0°}$

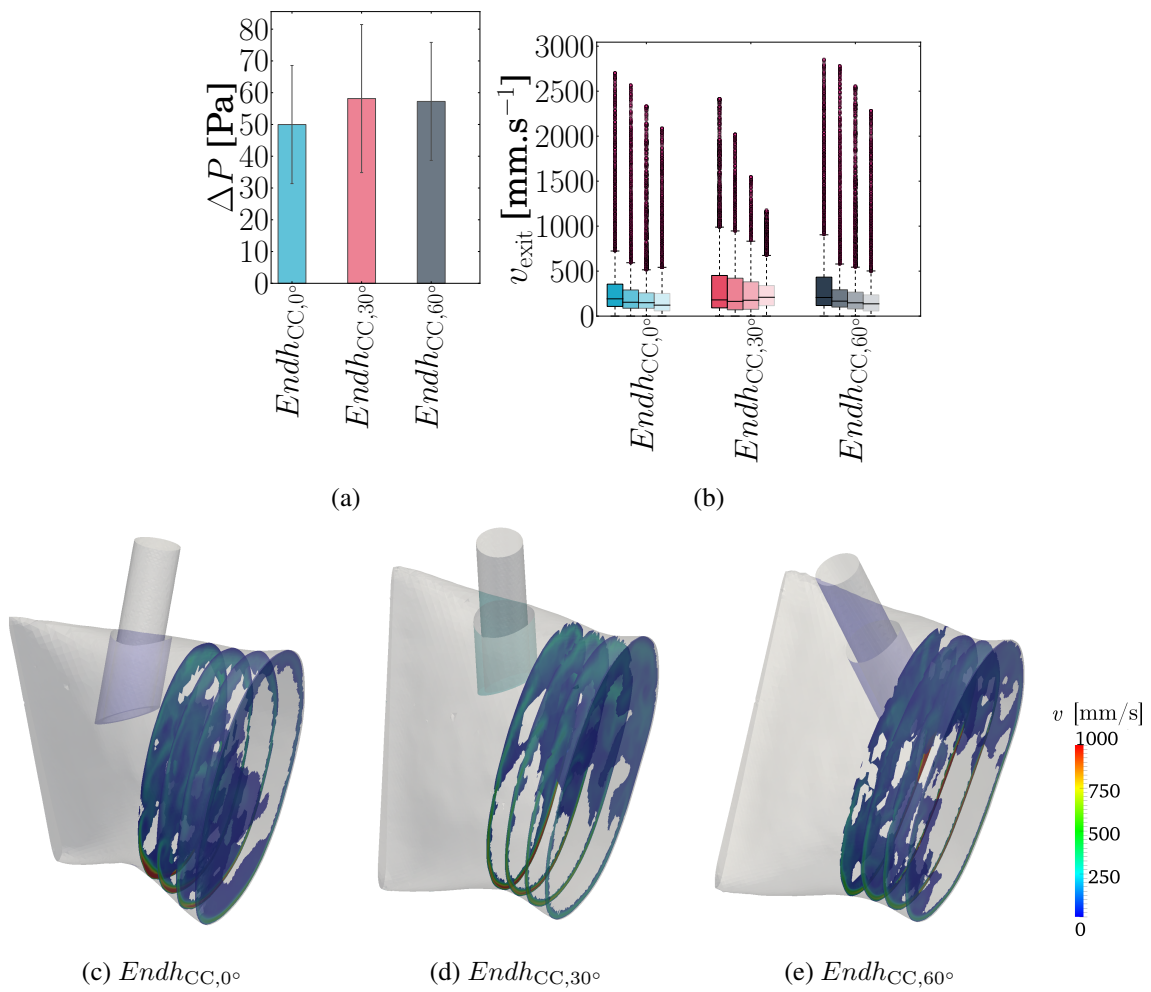(d) $Endh_{\text{CC},30°}$

(e) $Endh_{\text{CC},60°}$

Figure 9.10.: Extent of jet dissipation evaluated by considering (a) the pressure drop from the cannula inflow to the vessel outflow and (b) the vessel outflow exit velocity distribution. Each degree of increasing transparency indicates a slice closer to the outflow surface, as shown for each simulation considered (c)-(e).

(a)

(b)

(c) $Endh_{CC,0°}$ (d) $Endh_{CC,30°}$ (e) $Endh_{CC,60°}$

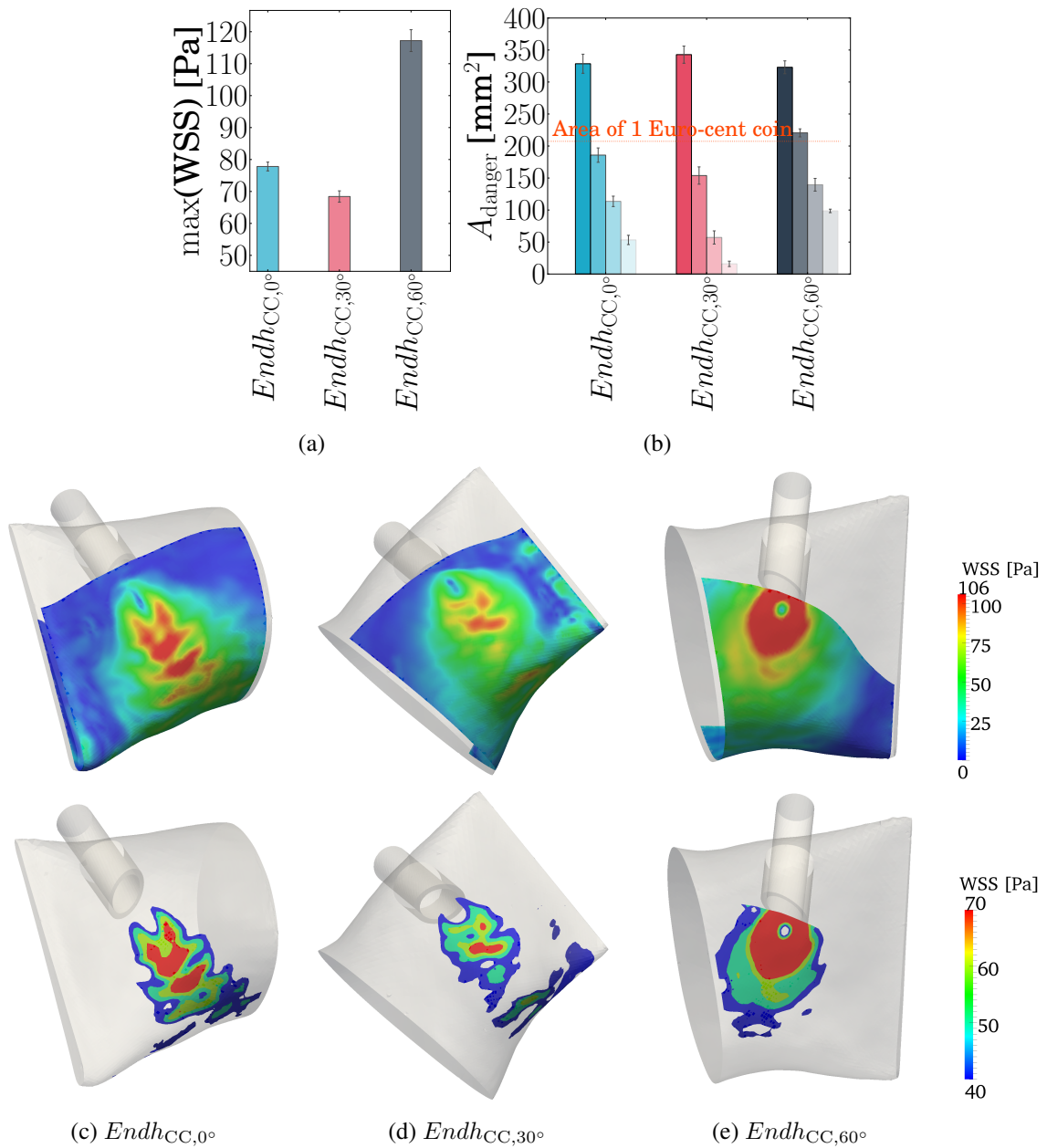Figure 9.11.: The impact of the cannular jet at its landing site, showing (a) the inflicted WSS and (b) danger-zone areas. For the latter, each degree of increasing transparency indicates an increasing endothelial damage threshold, i.e. $40, 50, 60, 70$ Pa. Visualizations of these measures are shown for each simulation from a suitable angle in (c)-(e) showing the WSS (top) and danger-zone area (bottom).

for three different orientations of the cross-clamps. Despite the complicated geometry of the flow domain, it revealed many comparable, but also dissimilar features with respect to the corresponding results for the idealized aorta, presented in Chapter 8 and expanded upon in the following.

9.2.3.1. General findings

A number of previous studies have indicated the consideration of a clamped aortic geometry in their consideration of patient-specific arterial cannular flow, cf. [15, 238, 277] in Section 8.1.2. However, no further mention of the clamped geometry nor its influence was reported, presumably because no significant effect was observed. Furthermore, no indication of how the clamped geometry was obtained was ever given, nor of how far the cannulation site was from the occlusion site. Therefore, the physiologically realistic geometry at the clamp-site of these studies simply cannot be assumed or assessed. Notwithstanding, these studies always either pointed the jet away from the occlusion site (insertion angle or tip design), were not interested in proximal effects of arterial cannular flow, or did not possess sufficient mesh resolution to evaluate such effects. Therefore, the influence of any type of clamped geometry on proximal cannular flow has effectively not been previously evaluated, as considered here.

In this presented investigation, instead of explicitly changing the orientation angle or insertion depth of the straight end-hole cannula, as done in Chapter 8, these parameters were implicitly varied by the large deformation induced due to the cross-clamping. This consequently led to the jet hitting an arbitrarily shaped, non-flat surface. The basic findings the previous chapter were essentially reproduced, namely that the insertion depth and incidence angle of the jet had a non-trivial impact on the pressure drop, a more or less expected impact on the outflow velocity and the WSS and very little difference in the danger-zone area inflicted. However, two exceptions are worth mentioning. Firstly, not seen in the idealized aorta, was the seemingly combined,

Consequently, this study basically illustrates an increase in variability of a complex set of cannula performance parameters that will be confronted in the clinical setting. From the results considering different cannula tip design in Chapter 8, it seems clear that the consideration of additional tip designs will simply add another level of complexity to these results, which clearly does not make it easy to predict or assess the cannula performance in a patient-specific case.

9.2.3.2. Limitations

Apart from the limitations regarding these computational simulations of proximal arterial cannular jet flow, as discussed in Section 8.7.3, the main limitation of this patient-specific study was the accuracy of the simulated cannula position. In other words, not allowing nodes to be shared on the interface between the cannula and the vessel accurately represent the interaction of the cannula fixed with purse-string sutures to the vessel wall? Be that as it may, whether the cannula orientation was changed manually, due to cross-clamping, or remained fixed, the surrounding geometry changed and thus also the resulting flow effects. This study simply reflects the substantial differences obtained in cannula flow performance obtained from subtle changes to the orientation and insertion depth of the *same* cannula inserted into a patient-specific artery.

9.3. Conclusions and future perspectives

9.3.1. Clinically dealing with problems of occlusion and occluder safety

Clinically, if occlusion is lost or incomplete during cross-clamping, the externally applied cross-clamp can be repositioned, tightened and locked into place by its ratchet-system – at some arbitrary high level of

occlusion. Blood pressure will need to overcome the force applied by the locked clamp arms in order for occlusion to be lost. With the internally applied EAB, however, blood pressure only needs to overcome the in-plane stiffness of the artery stretched over the EAB in order for occlusion to be lost. Although the local current in-plane stiffness will increase for the hyperelastic aortic wall subjected to EAB-application, it will have the capacity to increase even more under a sufficient increase of blood pressure. Thereby, EABO will be much more sensitive to lose occlusion due to peaks in the systemic blood pressure or pressure differences on opposite sides of the EAB. This sensitivity will be increased when a geometrically varying or non-uniformly stiff aorta is occluded, as seen in this investigation. Interestingly, exactly this phenomenon might be the reason why case studies exist that describe the successful occlusion of a porcelain aorta (severely calcified) with EABO, cf. Section 2.3.2. Such a severely calcified aorta is expected to offer more uniformly distributed material properties at the occlusion site, albeit stiffer – although it has also been described as causative of incomplete occlusion [113].

Apart from all the clinical considerations of the dangers of aortic occlusion reviewed in Chapter 2, such as to avoid repeated clamping, avoiding it altogether, etc., one recent statements require further comment in hindsight of the performed computational investigation. Nishi et al. [271] essentially concluded that the axial rotation of the cross-clamp to avoid pinching the calcification site in an artery with less than 75% of its circumference having calcified lesions will be a safer strategy than pinching it. No mechanical analysis was employed to make this conclusion. Rather, it was based on the absence of neurological complications in the 11 patients treated with a strategy that incorporated this conclusion. Rightfully so, two *eComments* followed the publication of this article to warn about the danger of this conclusion – even without performing any detailed mechanical analysis. Zingone [368] emphasized the danger of embolic release even when clamping a non-calcified aorta and also referred to alternative clinical strategies to safely manage a severely calcified ascending aorta. Furthermore, [185] questioned how these authors classified a region of the severely calcified aorta that is safe to manipulate and challenged generalizations made with regards to these classifications. From the computational investigation presented, it was also clear that a calcified lesion should not be pinched. But, it was also clearly shown that the impact that the occluder on a calcified lesion was non-trivial, and did not only depend on a two-dimensional adjustment of the clamps (axial rotation) as these authors suggested. It depended on the exact location of specific regions of the cross-clamps relative to the calcific lesion. Furthermore, the size of the lesion also influenced occluder-related impact, and presumably also its morphology and specifics of its composition not considered here. All of these aspects resulted in a highly sensitive response that cannot be generalized as recommended by these authors.

9.3.2. What type of occlusion will be less risky?

Overall, the change in occluder and orientation did change the strain response. However, to what extent such a modification may reduce the risk of damage and, therefore, the subsequent release of emboli is not entirely clear. The aim of this investigation was not to find the safest occluder configuration, but rather to observe the disparities in mechanical response due to subtle changes in surgical technique in the context of patient-specific variability. Clearly, these disparities are large and will be difficult to accommodate for in the patient-specific case.

However, regardless of these disparities, this investigation underlines the need for a more comprehensive understanding and classification of the potential damaging impact that occlusion of the aorta will have. Especially with regards to calcifications, it would be very helpful for clinicians (and safer for patients) if further analysis could provide concrete guidelines for clamping a large artery in general, including, but not limited to aspects regarding the influence of the proximity of a calcified lesion to the occlusion site, as well as the influence of the type of occluder. Alternative strategies available to avoid aortic occlusion have its own trade-offs, and not only severely calcified aortas present potential dangers,

but as shown here, so does a mildly calcified aorta – a single disrupted lesion theoretically has the same detrimental consequences whether surrounded by multiple lesions or by none.

The findings presented here led to two further questions that will have to be elucidated upon in future investigations. Firstly, in what mode of strain does local damage occur in highly strained regions in such an inhomogeneous vessel wall, i.e. tension, compression, shear or maybe some combination of these? Secondly, what are the direct effects of this damage? For example, would it be acceptable to have damage to the aortic wall that remains contained, i.e. does not cause the release of embolic material? If so, how can damage responsible for embolic release be prevented and what are the consequences of contained damage to the aortic wall?

9.3.3. Safer occlusion

Formulating guidelines of more comprehensive, patient-specific considerations for safe aortic occlusion will be of benefit, but only to a limited extent. Attempting to classify, characterize and accurately execute the application of occluders on an aorta with multiple distributed lesion could result in unfeasible complexity, even with robotic type accuracy – kind of like walking through a mine field. Therefore, it will be beneficial for future investigations to focus on improved occluder designs that are capable of robustly delivering safe aortic occlusion.

Without detailing all of its desirable features again, CEABO, as introduced for the first time in this investigation, cf. Section 7.3, yields a very promising solution, do to its ability to the overall limit strain in the vessel wall and superior stability when compared to EABO. Future work will need to elucidate on details of design, including its material requirements, ease of intra-operative application and removal, and also aspects of optimizing the profile and EAB designs.

Ultimately, the extensively reviewed literature and the computational investigation presented, which considered both occluder design and related influences of patient-specific variability, are expected to act as the foundation from which clinicians will acquire a better comprehension about the aortic manipulation challenges that they are faced with, and will consequently one day also lead to improved patient care. Finally, the presented work is expected to be used as valuable input into improving existing occluder designs.

9.3.4. Underestimated influence of the clamped geometry on proximal flow effects

Interestingly, this simple, yet clinically relevant consideration of arterial cannular flow in a patient-specific context, reflected many similarities that to the findings from corresponding simulations done in the idealized aorta. The relatively simple flow domain considered, i.e. with a single inflow and single outflow, allowed the resulting variation to be limited to the cannula tip design, its configuration and the local geometry of the proximal region. Thereby, these results further support the value of the paradigm shift for a new clinical reference of arterial cannular flow performance, as suggested in Section 8.8.3.

Furthermore, these results show a second important, yet subtle interaction effect between two different aortic manipulation maneuvers. The first was the potential of the incompletely cross-clamped geometry from funneling jet flow past the injured distal pinching site upon cross-clamp release. This mechanism of injury has not been previously described, although the release of the cross-clamps has been described as one of the single most dangerous aortic manipulation maneuvers in terms of embolic release, cf. Section 2. The second interaction effect, witnessed in these results, are the altering of proximal flow patterns due to the cross-clamped induced change in aortic geometry. Its a subtle change, but was demonstrated to have a substantial impact on the cannular flow performance, never before described.

Overall summary and outlook

Overall summary and outlook

Objectivity must be operationally defined as fair treatment of data, not absence of preference.

— Stephen J. Gould

Clinical comprehension and the path towards increased safety

Aortic manipulation maneuvers can significantly deteriorate the outcome of cardiac surgery due to its potential for causing cerebral vascular accidents (CVAs). CVAs remain a persistent problem in cardiac surgery that has to cater to an increasingly aging and sicker patient-population. Arguably, the two most prominent etiologies implicated in such manipulation-related CVAs are related to emboli and/or disrupted cerebral perfusion. From this perspective, an in-depth review was made of experimental, clinical and computational studies related to aortic manipulation in general – never before attempted in literature. This evaluation yielded a comprehensive overview that effectively demonstrated the general lack of understanding of the consequences aortic manipulation and how it relates to patient-outcome. The lack of understanding is readily explained by the immense complexities involved.

Furthermore, as was also outlines, remedies aimed at the prevention or cure of manipulation-related consequences (or the complete avoidance thereof) have frequently been marred by inconclusive outcomes, because of two main, interdependent reasons. Firstly, it has become increasingly difficult to demonstrate significant improvement of outcome in a large patient-population in a highly sophisticated cardiac surgical setting. Secondly, many of the proposed remedies presumably do not rigorously consider sufficiently many other manipulation-related consequences, i.e. the danger presented by one maneuver could potentially render the remedy of another useless.

Consequently, many open questions remain unaddressed, because current clinical and experimental methods do not allow for its detailed assessment. Due to the inherent mechanical nature of many such maneuvers, computational mechanics offer a suitable means of investigating some of these questions. Accordingly, a computational evaluation was performed of two of the arguably most dangerous aortic manipulation maneuvers, which comprised the largest part of this investigation. These maneuvers included aortic occlusion, considering the structural effects of occluding the ascending aorta, and arterial cannular flow, considering proximal flow effects, i.e. effects observed prior to entering the aortic arch. Findings revealed detail, and the comparison of new and existing equipment, that have not been described before in literature – for both aortic occlusion and proximal cannular flow effects, as further expanded upon below.

Computational analysis of aortic occlusion

The configuration by which an occluder applies a load on the aorta is of critical importance, and fundamentally different for the two main clinically-used occlusion techniques.

Cross-clamps achieve occlusion by the external application of two thin, rigid, near-parallel plates, that are displacement-driven, to the aorta. In the process, it not only causes regions of critically high strains at

the pinching sites, but also in the regions in between. Whereas standard, clinically-used, Debakey cross-clamps can be simply and accurately applied, they yield an extremely inefficient load to occlude the aorta, considering the high strains that had to be inflicted. This effect is partially accentuated by a deviation from parallel orientated clamp-arms, like Cosgrove/Chitwood clamps used in minimally invasive procedures. Improvement possibilities appear to be limited due to its inherent loading configuration, even when using inaccurately named "atraumatic" inserts (padded surface for the clamp surfaces). Furthermore, strategies of load-driven clamping are marked with difficulties, due to the high load sensitivity that will be required to handle clinical variation and the unknown state of occlusion.

Endo-aortic balloon occlusion (EABO) achieves occlusion by a spherically expanding, load-driven endo-aortic balloon (EAB), internal to the aorta. It yields a comparatively lower strain in the vessel than cross-clamps, but relies primarily on the stiffness resulting from the stretched aorta to provide occlusion. Although it offers a more distributed load, the loading configuration dictates that, compared with cross-clamps, an overall lower load is yielded. This also results in a lack of positional stability and an increased potential to suffer from a loss of occlusion. Improvements to EABO appear to have been discontinued, presumably due to many groups abandoning its use due to its poor performance, despite possessing additional functionalities not offered by cross-clamping.

The inclusion of patient-specific variations to the vessel geometry and material properties, as well as changing the orientation and/or position of the occluder, was shown to considerably complicate the strain response in the aorta. Especially critical was the response found in regions of atherosclerotic-related calcific lesions. A pressing need exists for further evaluation that also considers aortic occlusion under other clinically relevant manifestations of calcific lesions.

A major disadvantage shared by the available occluders is the lack of information pertaining to the state of occlusion. Consequently, the vessel will practically always be over-occluded – i.e. more load will be applied than necessary, implying a higher risk of iatrogenic injury to the vessel and a potential embologenesis. A new measure of determining the potential of occlusion, which was *independent* of the occluder loading configuration, was presented and proved extremely effective in these evaluations.

To address many of these insufficiencies of existing occluders, a novel method of occluding the aorta was proposed in this dissertation, named constrained EABO (CEABO). EABO is basically extended by applying an additional, bendable, but inextensible band, with a convex profile, externally around the vessel at the occlusion site. Thereby, positional stability of EAB was substantially increased and, by restricting the stretching of the vessel by the spherically expanding balloon, allowed for a proportional increase of the potential of vessel occlusion relative to the applied load. This feature also yields the potential of a clinically predictable state of occlusion. Overall, CEABO yielded generally superior performance compared to all the other occlusion techniques investigated, as evaluated by considering a comprehensive list of functional requirements for safe, efficient and reliable aortic occlusion. Importantly, it prevented the dangerous pinching loading configuration of cross-clamps, limited the increase of tensile strain to 30% of the physiological strain (approximately half of the increase yielded by clamps), while efficiently increasing the compressive strain needed to increase achieve occlusion. Furthermore, its inherent design also lends it functionalities of superior stability and positioning accuracy. Detailed design considerations and experimental investigations are needed to further elucidate on these claimed benefits.

Despite using some of the most advanced computational modeling features available, the extremeness of the loading considered, especially where the clamp pinches the aorta, yielded challenging computational modeling aspects that require further consideration in future studies. Nonetheless, despite extreme difficulties in validation, experimental findings in literature existed that indicated broad quantitative correspondence to the results presented here. Although not considered here, additional invaluable insights will be obtainable should adequate damage models be incorporated into these performed simulations. However, models that reliably describe arterial damage, especially in the context of such material inhomogeneities considered here, have seldomly been attempted in literature and require further investigation.

Computational analysis of (proximal) arterial cannular flow

Arterial cannular flow significantly disrupts physiological hemodynamics. Considering an average-sized adult receiving cardiopulmonary bypass (CPB), a typical flow rate of 5 l/min of blood has to be perfused through a conduit with a luminal area roughly six times less than the physiological lumen, i.e. ascending aorta. Furthermore, the flow character employed clinically is mainly continuous (as opposed to physiological pulsatile flow) and delivered as a high speed jet orientated at an angle near orthogonal to the vessel axis.

Clinicians can choose from a broad range of cannula tip designs, but have to base their choice primarily manufacturer information of the pressure-flow rate relationship, i.e. the pressure drop over the cannula corresponding to the flow rate. Such information is obtained from water flowing through the cannula exiting into an open tank at room temperature. Such information provides but one measure of cannula performance, is usually only presented relative to results from other cannulas of the same manufacturer and ultimately supplies an insufficient comparison of the overall cannula performance that will be achieved in-vivo.

Even prior to computational evaluation, certain aspects influencing cannula performance remain largely unaddressed in literature. The fact that all cannulas are sized based on their outer diameter at the tip, means that the inner diameter is basically unknown, which when measured, varies enough between different cannulas to cause a significant difference in the pressure-flow rate performance, not to even mentions aspects of variation in temperature or hematocrit. Moreover, this performance is also significantly influenced by the length and tapering geometry of the cannula tubing the precedes the tip, which is not even standard between cannulas from the same manufacturer.

In the computational study performed, the performance of a range of six fundamentally different, clinically available tip designs was evaluated in an idealized aorta, using a comprehensive list of functional requirements. Aspects of cannula configuration (cannulation-site orientation and insertion depth) of a straight end-hole cannula was also investigated. Results showed certain substantial inefficiencies of current cannnula designs: even the best performing clinically available cannulas relied primarily on the vessel wall for the dissipation of the high velocity jet. Furthermore, this landing-site of these jets were responsible for an area, where endothelial erosion will occur due to increased wall shear stresses (WSS), of at least 100 mm^2 – approximately half of the surface area of a 1-Euro-cent coin. All of this while still yielding flow that will enter the aortic arch that has a maximum velocity in the range of physiological flow at its systolic peak and at a much poorer distributed profile. Evidently, the vessel was found to play a substantial, yet complex role in determining cannula performance, especially in the trade-off of aiding in the jet dispersion at the cost of increased WSS. The strength of the jet at a given flow rate, combined with the incidence angle by which the jet hits the aortic wall and the distance that the jet travels prior to hitting the aortic wall, will additionally influence the cannula performance in a complicated manner. These effects are further accentuated in when including patient-specific variations in the aortic geometry.

The performance of a new shielded cannula tip, introduced elsewhere, was also evaluated due to its expected potential of yielding better cannula performance. It is not clinically available, nor has it been evaluated in literature. Although it did outperform the other cannula tip designs in most measures, its good performance came at the cost of poor pressure-flow rate performance. However, investigations are needed to determine whether this design can be further optimized, due to its clear potential of delivering robust performance despite changes in the cannula configuration.

These findings show that future evaluation of cannula performance is in need of a paradigm shift. This entails the additional consideration of the influence of the vessel on the cannula performance, and considering the distribution of flow entering the aortic arch, as it deviates from the physiological flow profile, as an additional performance parameter. Not only are such additions expected to be experimentally

feasible to determine, but they will aid clinicians to make better decisions and yield the potential of being able to sooner incorporate computational findings into daily clinical practice.

One of the main challenges of modeling these flow effects was to use a sufficiently fine mesh resolution to capture all the desired effects, as evaluated here in detail. Although not directly validated, the results yielded qualitative trends corresponding to a comparable experimental investigation. For all cannula tip designs and configurations (orientation and insertion depths) considered, only 50% of CPB flow was simulated to avoid the onset of significant turbulent effects. The effect of full flow rates used clinically will be a very important aspect to consider in future studies, as well as measures such as the expected hemolysis due to correspondingly increased shear rates.

Final remarks

The findings presented in this dissertation should facilitate a better grasp and appreciation of the complexities, but also consequences, associated with aortic manipulation. Given the large scale of this problem and its broad applicability not only to cardiac surgery, but also to interventional cardiology, this investigation will hopefully stimulate much further research on this topic. Conceivably, future improvements to the safety of aortic manipulation will depend on the increased understanding of the origins and extents of these etiologies. Furthermore, comprehensive and robust approaches will have to be pursued by both clinicians and medical device designers in order to minimize the overall invasiveness or disruption caused by these frequently unavoidable aortic manipulation maneuvers. Only once such approaches have been implemented, are safer aortic manipulation strategies expected to yield improved patient outcomes. Towards this aim, the presented investigation has arguably served a valuable purpose.

A. Detailed geometry and computational mesh information

A.1. Structural simulations

Table A.1.: Geometrical and mesh information pertaining to all structural simulations

For all simulations	Measurement source	Characteristic geometry	Mesh edge lengths	
			Radial/ thickness	Avg. lateral
Idealized artery	[216]	$L_a = 150, D_i = 29.7,$ $T_w = 2.3$	0.38	(varied[b] / 1.26/2.57)[a]
Patspec artery	CT-data	$L_a = 60, D_i^* = 32,$ $T_w = 2.3$	0.38	(0.62/ 1.68/1.84)[a]
Cannula structure	$Str_{0°,0°}$ (Table A.4), without tip chamfer	$L_a = 30, D_i = 6.6,$ $T_w = 2$	0.55	1.14

a *Occlusion site/intermediate/furthest, incl. boundary*
b *Finer resolved pinching edge length of 0.65mm (2×30deg) and rest of 1.12mm (2×150)*

Table A.2.: Structural simulation-specific information about the geometry and meshes used.

Single simulation specifics	Simulation abbr.	Model; manufacturer	Measurement source	Characteristic geometry	Clamp mesh edge lengths	
					Thickness	Avg. lateral
Cross-clamps, parallel	$CC_\parallel$	na	clamp-surfaces: DeBakey	$L_a = 40,\, L_w = 4,$ $T_w = 0.3,\, L_{rot} = \infty,$ $\alpha_{rot} = 0$		
Cross-clamps, crab-pincher type (often used in MIS)	CC_{crab}	CV1061, Cosgrove clamps; CareFusion Waukegan, IL, USA	clamp-surfaces: DeBakey, rotation axis: adapted from [56]	$L_a = 40,\, L_w = 4,$ $T_w = 0.3,\, L_{rot} = 20,$ $\alpha_{rot} = 0°,\, T_{pg} = 3,$ $L_w = 3$		
Cross-clamps, std. clinically used	CC_{std}		own measurements	$L_a = 40,\, L_w = 4,$ $T_w = 0.3,\, L_{rot} = 32,$ $\alpha_{rot} = 68°,\, T_{pg} = 3$	0.35	0.75
Cross-clamps (std.), patient-specific, axial position 1[d] (different axial rotations)	$CC_{0°}^{Calc,1}$	FB 512, DeBakey angled clamps; Aesculap,Inc., Center Valley, PA, USA	Patient geometry: CT-data Occluder: standard (DeBakey) Application site: surgically realistic	$L_a^{occl/cann} = 15,$ $\theta_{CC} = 0°$		
	$CC_{30°}^{Calc,1}$			$L_a^{occl/cann} = 15,$ $\theta_{CC} = 30°$		
	$CC_{60°}^{Calc,1}$			$L_a^{occl/cann} = 15,$ $\theta_{CC} = 60°$		
Cross-clamps (std.), patient-specific, axial position 2[d] (different axial rotations)	$CC_{0°}^{Calc,2}$			$L_a^{occl/cann} = 30,$ $\theta_{CC} = 0°$		
	$CC_{30°}^{Calc,2}$			$L_a^{occl/cann} = 30,$ $\theta_{CC} = 30°$		
	$CC_{60°}^{Calc,2}$			$L_a^{occl/cann} = 30,$ $\theta_{CC} = 60°$		
Cross-clamps (std.), patient-specific, axial position 1[d] (different axial rotations, no calcs)	$CC_{0°}^{noCalc,1}$			$L_a^{occl/cann} = 15,$ $\theta_{CC} = 0°$		
	$CC_{30°}^{noCalc,1}$			$L_a^{occl/cann} = 15,$ $\theta_{CC} = 30°$		

[c] *Profile geometry formulation, cf. Eq.* (6.81)
[d] *Position 1 and Position 2 are 15mm apart on centerline (for balloon, it's 12mm apart)*

Table A.2.: *(continued)* Structural simulation-specific information about the geometry and meshes used.

Single simulation specifics	Simulation abbr.	Model; manufacturer	Measurement source	Characteristic geometry	Mesh edge lengths	
					Radial/thickness edge length	Avg. lateral edge length
EAB		EndoClamp Aortic Catheter (EC1001); Edwards Lifesciences, Irvine, CA, USA	Brochure [97]	$D_i = 24, T_w = 1.73$	0.87	0.82
EAB catheter (real)	$EABO_{pure}$		Brochure [97]	$L_a = 50, D_i = 3, T_w = 1$	0.70	1.00
EAB catheter (artif. soft)		na	assumed	$L_a = 20, D_i = 3, T_w = 1$	0.70	0.94
EABO, patient-specific, position 1^d	$EABO^{Calc,1}$	Same as above (EndoClamp)	Patient geometry: CT-data Occluder: EABO Application site: surgically realistic	$L_a^{occl/cann} = 15$	Same EAB, EAB catheter throughout	
EABO, patient-specific, position 2^d	$EABO^{Calc,2}$			$L_a^{occl/cann} = 30$		
EABO, patient-specific, position 1^d	$EABO^{noCalc,1}$			$L_a^{occl/cann} = 15$		
Constrainer (narrow), EAB offset 0mm	$CEABO_{n,0}$	EABO: Same as above (EndoClamp) Constrainer: own design	own design	$L_a^{constr/EABO} = (0, 2, 4), L_a = 4, D_i = 34.4, T_w = 1$	1.00	1.07
Constrainer (narrow), EAB offset 2mm	$CEABO_{n,2}$				1.00	1.07
Constrainer (narrow), EAB offset 4mm	$CEABO_{n,4}$				1.00	1.07
Constrainer (wide)	$CEABO_w$		own design	$L_a^{constr/EABO} = 0, L_a = 12.85, D_i = 34.4, T_w = 1$	1.00	1.07
Constrainer (profiled), EAB offset 0mm	$CEABO_{p,0}$		own design	$L_a^{constr/EABO} = (0, 2, 4), L_a = 12.85, D_i = 34.4, T_w = 1, R_f = 1$, profiled^c	1.00	0.83
Constrainer (profiled), EAB offset 2mm	$CEABO_{p,2}$				1.00	0.83
Constrainer (profiled), EAB offset 4mm	$CEABO_{p,4}$				1.00	0.83

^{c} Profile geometry formulation, cf. Eq. (6.81)
^{d} Position 1 and Position 2 are 15mm apart on centerline *(for balloon, it's 12mm apart)*

A.2. Fluid simulations

Table A.3.: Geometrical and mesh information pertaining to all fluid simulations

For all simulations	Measurement source	Geometry	Average element edge length (base level)
Vessel (aorta) lumen	[216]	$D_i^v = 29.7$, $L_a^v = 50$, unless otherwise specified	Boundary layer: 0.02 / 7 / 1.7[b]; jet: 0.55[c]; specific surfaces: 0.55[d]; rest: 1.1
Cannulation site to vessel outflow	assumed based on dimensions reported in [216]	$L_a^{\mathrm{cann/out}} = 35$, except patient-specific simulations: $L_a^{\mathrm{cann/out}} = \sim\!21$	na
Cannulation site to occlusion site	assumed based on dimensions reported in [216]	$L_a^{\mathrm{occl/cann}} = 15$, except for patient-specific simulations: $L_a^{\mathrm{occl/cann}} = \sim\!15$	na
Tip conduit length[a]	based on shortest, reasonable length for all cannulas	$L_a^c = 25$	Boundary layer: 0.02 / 6 / 1.7[b]; specific surfaces: 0.55[d]; rest: 1.1

a From cannula inflow to cannula outflow, along centerline
b First element thickness/number of layers/first element thickness expansion factor
c Mesh resolving the jet prior to hitting the vessel wall for the first time
d Specific surfaces which received a higher average lateral mesh edge length: bottom half of the aortic wall, cannular inflow, cannular inner surface, vessel outflow

Table A.4.: Fluid simulation-specific information about the geometry and meshes used.

Single simulation specifics	Simulation abbr.	Model; manufacturer	Measurement source	Geometry
End-hole, straight (different orientations)	$Endh_{0°,0°}$ [h]	ASR 2185 Z 21Fr, adapted to 24Fr, no insertion depth flange; Jostra AG, Hirrlingen/Hechingen, BW, DE	own measurements	$D_i^c = 6.6$, $\theta_{trans} = 0°$, $\theta_{long} = 0°$
	$Endh_{0°,-30°}$		own measurements	$D_i^c = 6.6$, $\theta_{trans} = 0°$, $\theta_{long} = -30°$
	$Endh_{30°,-30°}$		own measurements	$D_i^c = 6.6$, $\theta_{trans} = 30°$, $\theta_{long} = -30°$
	$Endh_{30°,0°}$		own measurements	$D_i^c = 6.6$, $\theta_{trans} = 30°$, $\theta_{long} = 0°$
	$Endh_{30°,30°}$		own measurements	$D_i^c = 6.6$, $\theta_{trans} = 30°$, $\theta_{long} = 30°$
	$Endh_{0°,30°}$		own measurements	$D_i^c = 6.6$, $\theta_{trans} = 0°$, $\theta_{long} = 30°$
End-hole, straight (different insertion depths)	$Endh_{d,-5}$		own measurements	$D_i^c = 6.6$, $\theta_{trans} = 0°$, $\theta_{long} = 0°$, $L_{depth} = -5$
	$Endh_{d,0}$ [h]		own measurements	$D_i^c = 6.6$, $\theta_{trans} = 0°$, $\theta_{long} = 0°$, $L_{depth} = 0$
	$Endh_{d,+5}$		own measurements	$D_i^c = 6.6$, $\theta_{trans} = 0°$, $\theta_{long} = 0°$, $L_{depth} = +5$
	$Endh_{d,+10}$		own measurements	$D_i^c = 6.6$, $\theta_{trans} = 0°$, $\theta_{long} = 0°$, $L_{depth} = +10$
End-hole, straight, incompletely clamped, ideal artery [f]	$Endh_{ic}$		own measurements	$L_a^v = 70$, $D_i^c = 6.6$, $\theta_{trans} = 0$, $\theta_{long} = 0$, $|A_{cl}^{lumen}| = 0.4$
End-hole, straight, only physiological inflow	$Phys_{hb}$ [h]		v_{in} [196]	physiological vessel inflow
End-hole, straight, incompletely clamped patient specific artery [g] (different clamp orientations)	$Endh_{CC,0°}$	Same as above (ASR 2185 Z 21Fr, adapted to 24Fr)	$CC_{0°}^{Calc,1}$ (Table A.2)	$D_i^c = 6.6$, $D_i^{v*} = 37.07$ [i], $|A_{cl}^{lumen}| = 0.088$
	$Endh_{CC,30°}$		$CC_{30°}^{Calc,1}$ (Table A.2)	$D_i^c = 6.6$, $D_i^{v*} = 36.88$ [i], $|A_{cl}^{lumen}| = 0.084$
	$Endh_{CC,60°}$		$CC_{60°}^{Calc,1}$ (Table A.2)	$D_i^c = 6.6$, $D_i^{v*} = 36.86$ [i], $|A_{cl}^{lumen}| = 0.085$

[e] For shield, Softflow and Stöckert geometries, see Figure 6.9
[f] Incompletely clamped prestressed pressurized artery with parallel clamps up to the given $|A_{cl}^{lumen}|$
[g] Incompletely clamped prestressed pressurized artery with standard (DeBakey) clamps up to the given $|A_{cl}^{lumen}|$
[h] Is the same mesh as $Endh_{str}$
[i] At the clamp-site

Table A.4.: (continued) Fluid simulation-specific information about the geometry and meshes used.

Single simulation specifics	Simulation abbreviation	Model, Manufacturer	Measurement source	Geometry
End-hole, curved	$Endh_{curv}$	A24-2107 24Fr, no insertion depth flange, forward-facing (i.e. Downstream); Maquet GmbH, Rastatt, BW, DE	own measurements	$D_i^c = 7.1$, $R_{center} = 12.1$, $\beta_{tip} = 90°$
End-hole, curved, shielded	$Endh_{curv}^{sh}$	Same as above (A24-2107 24Fr, no insertion depth flange), backward-facing (i.e. Upstream), shielded	own measurements, custom designed shield	$L_a^v = 60$, $D_i^c = 7.1$, $R_{center} = 12.1$, $\beta_{tip} = 90°$, shield[e]
Side-hole, curved	$Side_{curv}$	Sarns 5762 8.0mm (24Fr, Softflow); Terumo Medical Corporation, Shibuya, Tokyo, JP	own measurements	$D_i^{c*} = 6.3$, $R_{center} = 6.5$, $\beta_{tip} = 40°$, Softflow[e]
Side-hole, straight	$Side_{str}$	Same as above (Sarns 5762 8.0mm), adapted to a straight configuration	own measurements	$D_i^{c*} = 6.3$, Softflow[e]
Hybrid, curved	$Hybr_{curv}$	Stöckert 8.0mm curved (24Fr), Sorin Group, Milan, Italy	own measurements	$D_i^{c*} = 6.3$, $R_{center} = 4.65$, $\beta_{tip} = 30°$, Stöckert[e]
Hybrid, straight	$Hybr_{str}$	Same as above (Stöckert 8.0mm curved), adapted to a straight configuration	own measurements	$D_i^{c*} = 6.3$, Stöckert[e]

[e] For shield, Softflow and Stöckert geometries, see Section 6.4.1.2 and Figure 6.9
[f] Incompletely clamped prestressed pressurized artery with parallel clamps up to the given $|A_{cl}^{lumen}|$
[g] Incompletely clamped prestressed pressurized artery with standard (DeBakey) clamps up to the given $|A_{cl}^{lumen}|$
[h] Is the same mesh as $Endh_{str}$
[i] At the clamp-site

B. Guideline for rating/scoring relative functional performance

Following a basic mechanical design process of concept evaluation for rating dissimilar concepts performing the same final task,a simple scoring system was employed to determine the relative performance of each concept (and existing designs) considered, i.e. occlusion technique or cannula. In order to consistently score or rate this relative performance of each functional performance parameter considered, the following scoring convention was followed:

- Assign a "5" to the best and a "1" to the worst performing concept. Concepts yielding results inbetween these two extremes were rated proportionally on this scale;

- Allowing a score to be skipped and repeated, respectively, e.g. $(5, 4, 2, 2, 1)$ is valid. In this example, such a scoring will be given to results that show a gradual difference in performance with a large difference between the second and third values, followed by a similar result and with the final result clearly the worst;

- Relative performance *not* quantifiable by computational results presented, but rather by a conservative estimate based on results from a given source, were assigned a "3" to the best and a "1" to the worst performing concept. Hence, its influence on the totals, i.e. overall performance, is limited.

Such a convention was needed since the acquired results did not present a simple linearity in performance outcome of each concept. However, this scoring process essentially remains subjective and the results thereof should be interpreted accordingly. Furthermore, future studies should include a more rigorous scoring convention, as well as a system that includes weighting of importance, i.e. how important is the fulfillment of one functional requirement over the other, and exclusion criteria, i.e. when does insufficient fulfillment of a requirement justify its exclusion.

C. Additional results

C.1. Boundary effects of occluding the patient-specific aorta

Continued from Section 9.1.2.1, the second and third principal strains at the proximal and distal boundaries are plotted below in Figures C.1 and C.2, respectively.

C.2. Local progression of strain

Continued from Section 9.1.2.2, the progression of strain in the various different local regions of interest (ROIs) are plotted below for the third principal and von Mises strain in Figures C.3 and C.4, respectively.
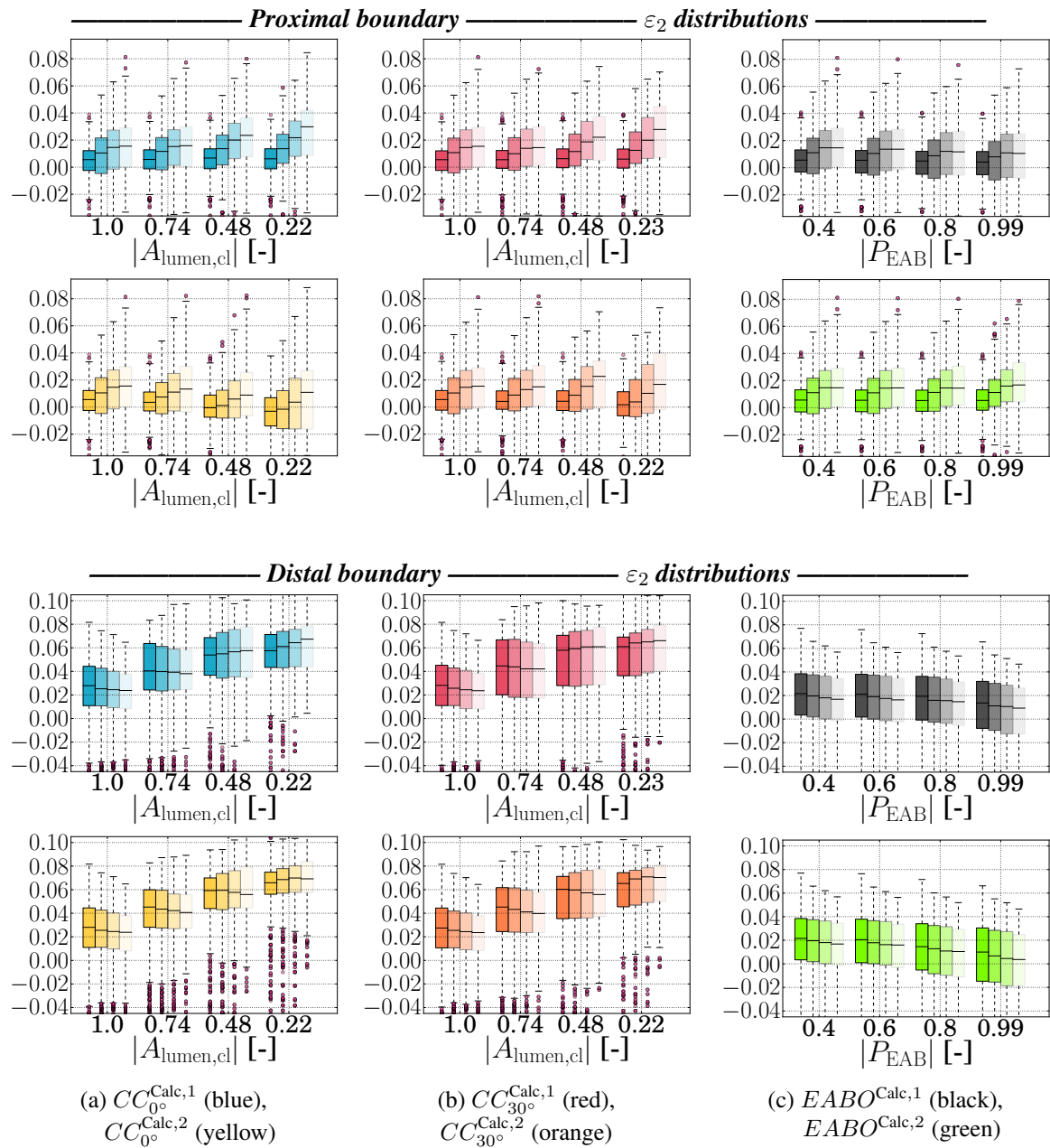
Figure C.1.: The resulting second principal strain (ε_2 [-]) distributions extracted at the four different axially spaced slices near the proximal and distal ends of the vessel, as depicted in Figure 9.1. Each increasing degree of transparency indicates a slice located further away from the boundary, i.e. the fixed truncated surfaces.

(a) $CC_{0°}^{\text{Calc},1}$ (blue),
$CC_{0°}^{\text{Calc},2}$ (yellow)

(b) $CC_{30°}^{\text{Calc},1}$ (red),
$CC_{30°}^{\text{Calc},2}$ (orange)

(c) $EABO^{\text{Calc},1}$ (black),
$EABO^{\text{Calc},2}$ (green)

Figure C.2.: The resulting third principal strain (ε_3 [-]) distributions extracted at the four different axially spaced slices near the proximal and distal ends of the vessel, as depicted in Figure 9.1. Each increasing degree of transparency indicates a slice located further away from the boundary, i.e. the fixed truncated surfaces.
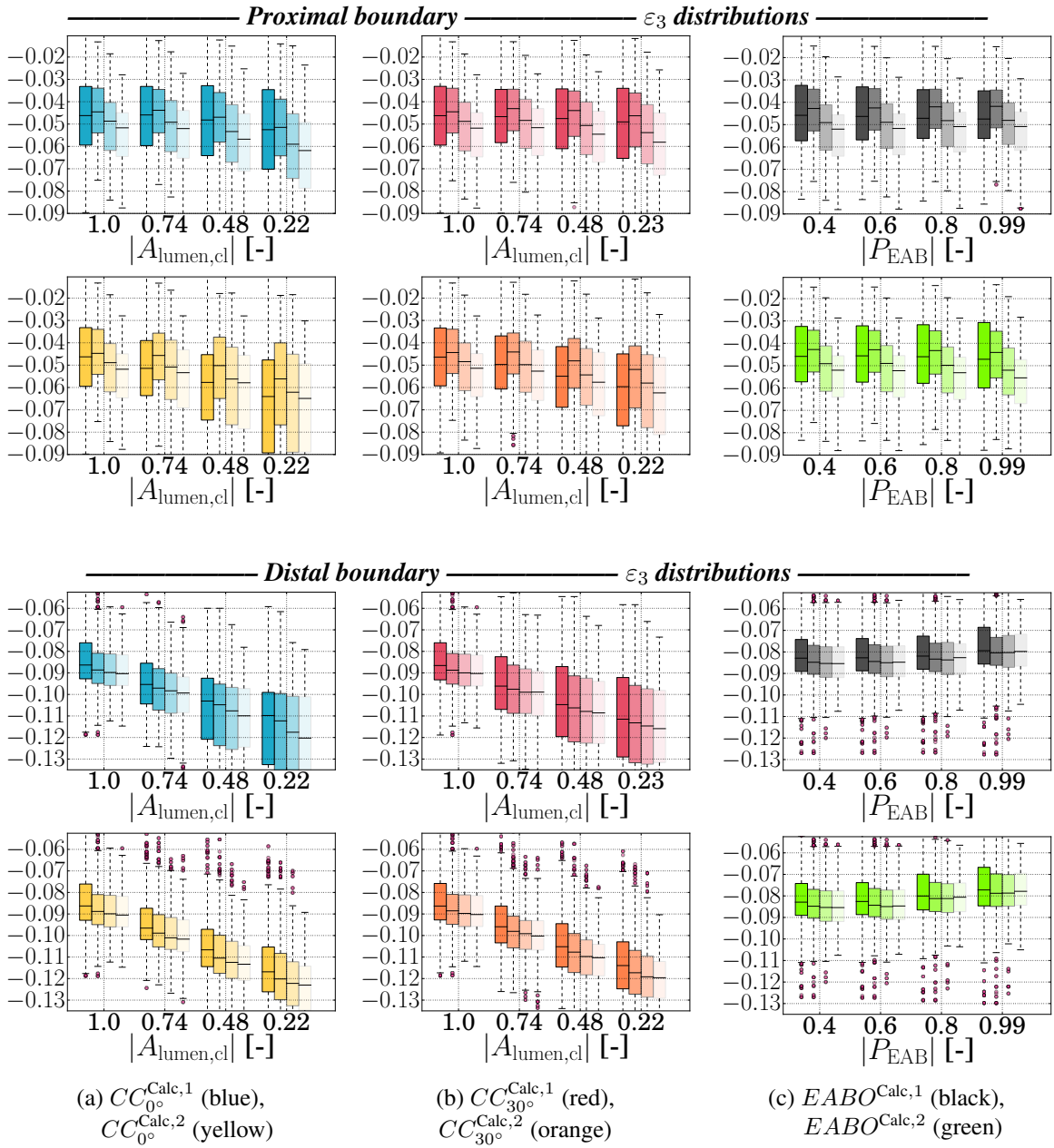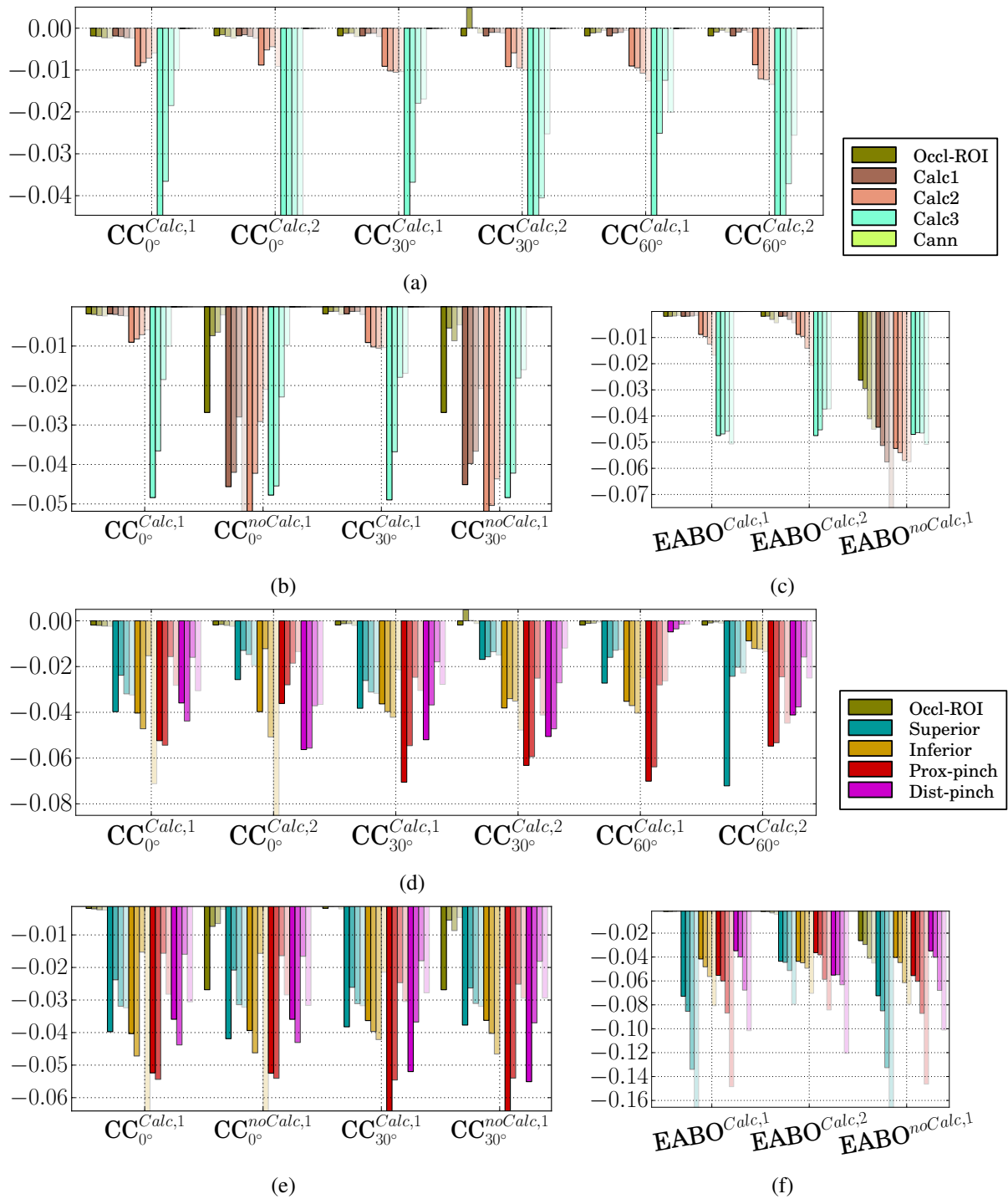
Figure C.3.: The progression of the third principal strain (ε_3, [-]) during occlusion of the patient-specific aorta, as extracted from the different regions of interest indicated in Figure 9.3 – note the corresponding colors. Each increasing degree of transparency corresponds to $|A_{lumen,cl}| = 1.0, 0.74, 0.48, 0.22$ and $|P_{EAB}| = 0.4, 0.6, 0.8, 1.0$ for the cross-clamps and EABO, respectively, i.e. from least to most occluded.

Figure C.4.: The progression of the von Mises strain (ε_{VM}, [-]) during occlusion of the patient-specific aorta, as extracted from the different regions of interest indicated in Figure 9.3 – note the corresponding colors. Each increasing degree of transparency corresponds to $|A_{lumen,cl}| = 1.0, 0.74, 0.48, 0.22$ and $|P_{EAB}| = 0.4, 0.6, 0.8, 1.0$ for the cross-clamps and EABO, respectively, i.e. from least to most occluded.
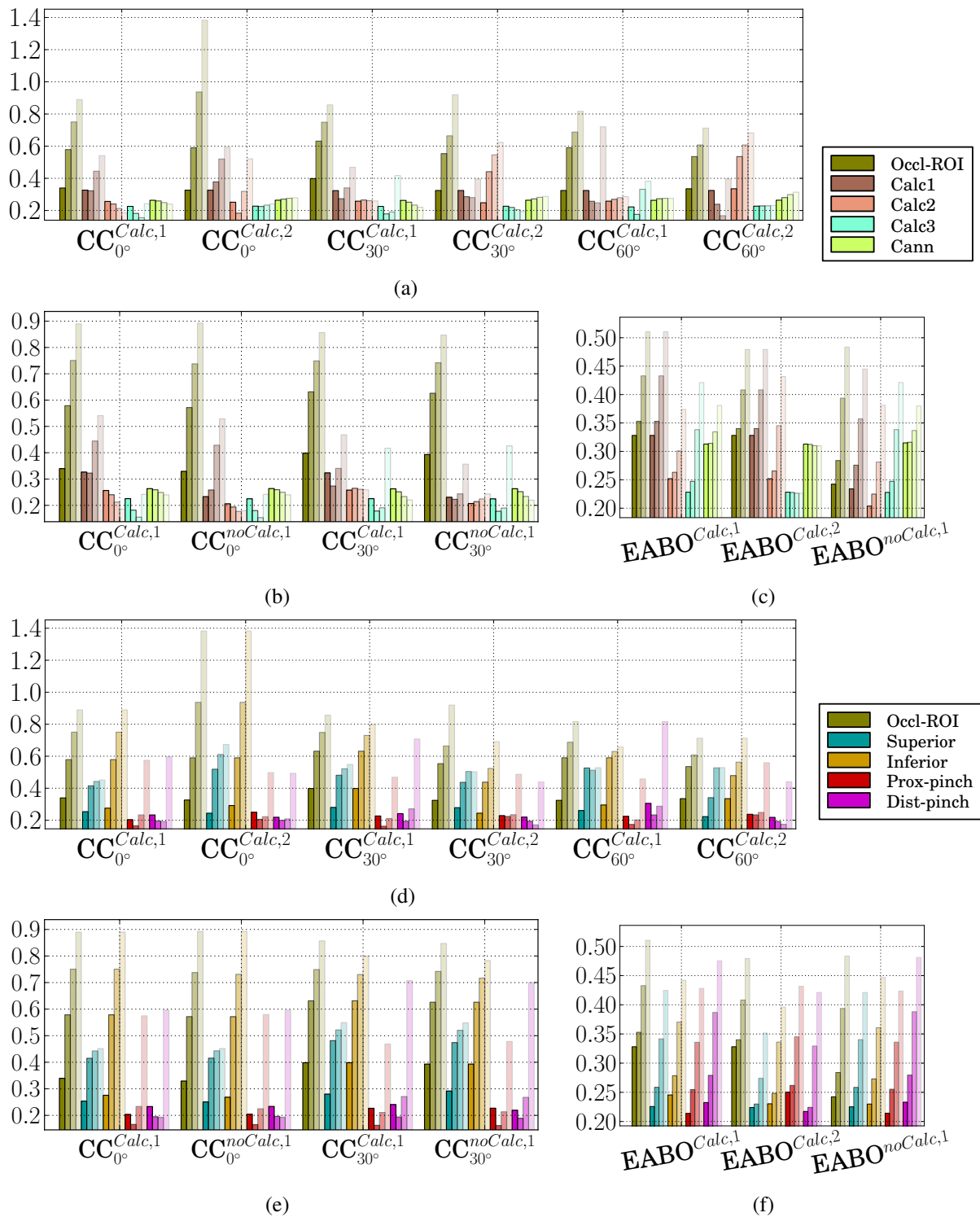
Bibliography

[1] A. L. Abbott, M. A. Adelman, A. V. Alexandrov, P. A. Barber, H. J. Barnett, J. Beard, P. Bell, M. Bjrck, D. Blacker, L. H. Bonati, M. M. Brown, C. J. Buckley, R. P. Cambria, J. E. Castaldo, A. J. Comerota, E. S. Connolly, R. L. Dalman, A. H. Davies, H.-H. Eckstein, R. Faruqi, T. E. Feasby, G. Fraedrich, P. Gloviczki, G. J. Hankey, R. E. Harbaugh, E. Heldenberg, M. G. Hennerici, M. D. Hill, T. J. Kleinig, D. P. Mikhailidis, W. S. Moore, R. Naylor, A. Nicolaides, K. I. Paraskevas, D. M. Pelz, J. W. Prichard, G. Purdie, J.-B. Ricco, P. A. Ringleb, T. Riles, P. M. Rothwell, P. Sandercock, H. Sillesen, J. D. Spence, F. Spinelli, J. Sturm, A. Tan, A. Thapar, F. J. Veith, T. Wijeratne, and W. Zhou, Why calls for more routine carotid stenting are currently inappropriate: An international, multispecialty, expert review and position statement, *Stroke* **44**, 1186–1190, 2013.

[2] Y. Abu-Omar and D. P. Taggart, The present status of off-pump coronary artery bypass grafting, *Eur. J. Cardiothorac. Surg.* **36**, 312–321, 2009.

[3] N. Alexopoulos and P. Raggi, Calcification in atherosclerosis, *Nat Rev Cardiol* **6**, 681–688, 2009.

[4] A. A. Alghamdi and D. A. Latter, Pulsatile versus nonpulsatile cardiopulmonary bypass flow: An evidence-based approach, *J. Card. Surg.* **21**, 347–354, 2006.

[5] R. P. Alston, 16, pages 191–205, *Off-Pump and On-Pump Coronary Artery Surgery and the Brain: Brain Protection in Cardiac Surgery*, R. S. Bonser, D. Pagano, and A. Haverich (eds.), Springer London, 2011.

[6] J. R. Alvarez and J. S. Quiroga, An alternative method for endoaortic clamping in atherosclerotic aorta, *Asian Cardiovasc. Thorac. Ann.* **20**, 493–494, 2012.

[7] M. N. Andersen, S. Ringgaard, J. M. Hasenkam, and H. Nygaard, Quantitative haemodynamic evaluation of aortic cannulas, *Perfusion* **19**, 323–330, 2004.

[8] T. Anzai, Y. Iino, T. Kumeno, and R. Yozu, Feasibility study of a direct endo-aortic clamp balloon, *ASAIO J.* **53**, 136–139, 2007.

[9] S. F. Aranki, R. J. Rizzo, D. H. Adams, G. S. Couper, N. M. Kinchla, J. S. Gildea, and L. H. Cohn, Single-clamp technique: An important adjunct to myocardial and cerebral protection in coronary operations, *Ann. Thorac. Surg.* **58**, 296–303, 1994.

[10] S. F. Aranki, M. Nathan, P. Shekar, G. Couper, R. Rizzo, and L. H. Cohn, Hypothermic circulatory arrest enables aortic valve replacement in patients with unclampable aorta, *Ann. Thorac. Surg.* **80**, 1679–1687, 2005.

[11] J. E. Arrowsmith and M. S. Ganugapenta, pages 83–111, *Intraoperative Brain Monitoring in Cardiac Surgery*, R. S. Bonser, D. Pagano, and A. Haverich (eds.), Springer London, 2011.

[12] M. Ates, M. Yangel, A. U. Gullu, Y. Sensoz, M. Kizilay, and M. Akcar, Is single or double aortic clamping safer in terms of cerebral outcome during coronary bypass surgery?, *Int. Heart. J.* **47**, 185–192, 2006.

[13] G. A. Ateshian, Anisotropy of fibrous tissues in relation to the distribution of tensed and buckled fibers, *J. Biomech. Eng.* **129**, 240–249, 2007.

[14] I. Avrahami, B. Dilmoney, A. Azuri, M. Brand, O. Cohen, L. Shani, R.-R. Nir, and G. Bolotin, Investigation of risks for cerebral embolism associated with the hemodynamics of cardiopulmonary bypass cannula: A numerical model, *Artif. Organs* **37**, 857–865, 2013.

[15] I. Avrahami, B. Dilmoney, O. Hirshorn, M. Brand, O. Cohen, L. Shani, R.-R. Nir, and G. Bolotin, Numerical investigation of a novel aortic cannula aimed at reducing cerebral embolism during cardiovascular bypass surgery, *J. Biomech.* **46**, 354–361, 2013.

[16] T. Aybek, S. Dogan, G. Wimmer-Greinecker, K. Westphal, and A. Mortiz, The micro-mitral operation comparing the port-access technique and the transthoracic clamp technique, *J. Card. Surg.* **15**, 76–81, 2000.

[17] A. N. Azadani, S. Chitsaz, P. B. Matthews, N. Jaussaud, J. Leung, T. Tsinman, L. Ge, and E. E. Tseng, Comparison of mechanical properties of human ascending aorta and aortic sinuses, *Ann. Thorac. Surg.* **93**, 87–94, 2012.

[18] J. Babin-Ebell, K. Gimpel-Henning, H.-H. Sievers, and M. Scharfschwerdt, Influence of clamp duration and pressure on endothelial damage in aortic cross-clamping, *Interact. CardioVasc. Thorac. Surg.* **10**, 168–171, 2010.

[19] H. Baek, M. V. Jayaraman, P. D. Richardson, and G. E. Karniadakis, Flow instability and wall shear stress variation in intracranial aneurysms, *Journal of The Royal Society Interface* **7**, 967–988, 2010.

[20] S. Baek, R. Gleason, K. Rajagopal, and J. Humphrey, Theory of small on large: Potential utility in computations of fluidsolid interactions in arteries, *Computer Methods in Applied Mechanics and Engineering* **196**, 3070–3078, 2007.

[21] C. Bailey, A. May, and W. Lemmon, Survival after coronary endarterectomy in man, *JAMA* **164**, 641–646, 1957.

[22] D. S. Baim, D. Wahr, B. George, M. B. Leon, J. Greenberg, D. E. Cutlip, U. Kaya, J. J. Popma, K. K. Ho, R. E. Kuntz, and on behalf of the Saphenous vein graft Angioplasty Free of Emboli Randomized (SAFER) Trial Investigators, Randomized trial of a distal embolic protection device during percutaneous intervention of saphenous vein aorto-coronary bypass grafts, *Circulation* **105**, 1285–1290, 2002.

[23] J. C. Baldwin, J. A. Elefteriades, and G. S. Kopf, 25, pages 313–329, *Heart surgery*, B. L. Zaret, M. M. D. Moser, and L. S. Cohen (eds.), Yale University, School of Medicine, 1992.

[24] D. Balzani, *Polyconvex anisotropic energies and modeling of damage applied to arterial walls*, PhD thesis, Universität Duisburg-Essen Ingenieurswissenschaften, 2006.

[25] M. K. Banbury, N. T. Kouchoukos, K. B. Allen, M. S. Slaughter, N. J. Weissman, G. J. Berry, and K. A. Horvath, Emboli capture using the embol-x intraaortic filter in cardiac surgery: Amulticentered randomized trial of 1,289 patients, *Ann. Thorac. Surg.* **76**, 508–515, 2003.

[26] D. Barbut, R. Hinton, T. Szatrowski, G. Hartman, M. Bruefach, P. Williams-Russo, M. Charlson, and J. Gold, Cerebral emboli detected during bypass surgery are associated with clamp removal, *Stroke* **25**, 2398–2402, 1994.

[27] D. Barbut, F.-S. F. Yao, Y.-W. Lo, R. Silverman, D. N. Hager, R. R. Trifiletti, and J. P. Gold, Determination of size of aortic emboli and embolic load during coronary artery bypass grafting, *Ann. Thorac. Surg.* **63**, 1262–1265, 1997.

[28] O. K. Baskurt and H. J. Meiselman, Blood rheology and hemodynamics, *Semin. Thromb. Hemost.* **29**, 435–450, 2003.

[29] J. R. Beck, D. Y. Park, and L. B. Mongero, 8, pages 171–191, *Cannulation and Clinical Concerns for Cardiopulmonary Bypass Access: On Bypass: Advanced Perfusion Techniques*, J. R. B. Linda B. Mongero (ed.), Humana Press, 2008. Meer explanatory as nommers.

[30] C. Beckman, F. Hurley, R. Mammana, and S. Levitsky, Risk factors for air embolization during cannulation of the ascending aorta, *J. Thorac. Cardiovasc. Surg.* **80**, 302–307, 1980.

[31] P. Bergman and J. van der Linden, Atherosclerosis of the ascending aorta as a major determinant of the outcome of cardiac surgery, *Nat. Clin. Pract. Cardiovasc. Med.* **2**, 246–251, 2005.

[32] S. K. Bhudia, D. A. Stump, and T. J. Jones, 9, pages 73–81, *Current Techniques of Emboli Detection and Their Utility in Brain Protection Studies: Brain Protection in Cardiac Surgery*, R. S. Bonser, D. Pagano, and A. Haverich (eds.), Springer London, 2011.

[33] J. B. Bijker and A. W. Gelb, Review article: The role of hypotension in perioperative stroke **60**, 159–167, 2013.

[34] K. Bijuklic, A. Wandler, F. Hazizi, and J. Schofer, The profi study (prevention of cerebral embolization by proximal balloon occlusion compared to filter protection during carotid artery stenting)a prospective randomized trial, *J. Am. Coll. Cardiol.* **59**, 1383–1389, 2012.

[35] J. Bismuth, Z. Garami, J. E. Anaya-Ayala, J. J. Naoum, H. F. El Sayed, E. K. Peden, A. B. Lumsden, and M. G. Davies, Transcranial doppler findings during thoracic endovascular aortic repair, *J. Vasc. Surg.* **54**, 364–369, 2011.

[36] C. I. Blauth, Macroemboli and microemboli during cardiopulmonary bypass, *Ann. Thorac. Surg.* **59**, 1300–1303, 1995.

[37] J. A. Blumenthal, E. P. Mahanna, D. J. Madden, W. D. White, N. D. Croughwell, and M. F. Newman, Methodological issues in the assessment of neuropsychologic function after cardiac surgery, *Ann. Thorac. Surg.* **59**, 1345–1350, 1995.

[38] P. Boivie, C. Edstrom, and K. G. Engstrom, Side differences in cerebrovascular accidents after cardiac surgery: A statistical analysis of neurologic symptoms and possible implications for anatomic mechanisms of aortic particle embolization, *J. Thorac. Cardiovasc. Surg.* **129**, 591–598, 2005.

[39] P. Boivie, M. Hansson, and K. Engström, Embolic material generated by multiple aortic cross-clamping: A perfusion model with human cadaveric aorta, *J. Thorac. Cardiovasc. Surg.* **125**, 1451–1460, 2003.

[40] P. Boivie, M. Hansson, and K. G. Engström, Intraluminal aortic manipulation by means of intra-aortic filter, cannulation, and external clamp maneuvers evaluated versus dislodged embolic material, *J. Thorac. Cardiovasc. Surg.* **131**, 283–289, 2006.

[41] P. Boivie, M. Hansson, and K. Gunnar Engström, Aortic plaque distribution in relation to cross clamp and cannulation procedures during cardiac surgery, *Scand. Cardiovasc. J.* **41**, 120–125, 2007.

[42] P. Boivie, M. Hedberg, and K. G. Engström, Size distribution of embolic material produced at aortic cross-clamp manipulation, *Scand. Cardiovasc. J.* **44**, 367–372, 2010.

[43] M. Bonacchi, E. Prifti, G. Giunti, A. Salica, G. Frati, and G. Sani, Respiratory dysfunction after coronary artery bypass grafting employing bilateral internal mammary arteries: The influence of intact pleura, *Eur. J. Cardiothorac. Surg.* **19**, 827–833, 2001.

[44] J. Bonatti, W. J. van Boven, G. Nagele, G. Shahin, T. Schachner, G. Laufer, P. Bergman, J. van der Linden, and The Assessment Of the Risk of Emboli Transmission In Coronary Surgery Study Group, Do particulate emboli from the ascending aorta in coronary bypass grafting correlate with aortic wall thickness?, *Interact. CardioVasc. Thorac. Surg.* **5**, 716–720, 2006.

[45] M. A. Borger, R. L. Taylor, R. D. Weisel, G. Kulkarni, M. Benaroia, V. Rao, G. Cohen, L. Fedorko, and C. M. Feindel, Decreased cerebral emboli during distal aortic arch cannulation: A randomized clinical trial, *J. Thorac. Cardiovasc. Surg.* **118**, 740–745, 1999.

[46] M. A. Borger, J. Ivanov, R. D. Weisel, V. Rao, and C. M. Peniston, Stroke during coronary bypass surgery: Principal role of cerebral macroemboli, *Eur. J. Cardiothorac. Surg.* **19**, 627–632, 2001.

[47] D. M. Bravata, A. L. Gienger, K. M. McDonald, V. Sundaram, M. V. Perez, R. Varghese, J. R. Kapoor, R. Ardehali, D. K. Owens, and M. A. Hlatky, Systematic review: The comparative effectiveness of percutaneous coronary interventions and coronary artery bypass graft surgery, *Ann. Intern. Med.* **147**, 703–716, 2007.

[48] K. Brechtel, G. Kalender, U. Stock, and S. Wildhirt, Hybrid debranching and tevar of the aortic arch off-pump, in re-do patients with complicated chronic type-a aortic dissections: a critical report, *Journal of Cardiothoracic Surgery* **8**, 188, 2013.

[49] S. Brinkhues, *Modeling and simulation of arterial walls with focus on damage and residual stresses*, PhD thesis, Universitt Duisburg-Essen, 2012.

[50] R. Brodman, H. Siegel, M. Lesser, and R. Frater, A comparison of flow gradients across disposable arterial perfusion cannulas, *Ann. Thorac. Surg.* **39**, 225–233, 1985.

[51] W. R. Brown, D. M. Moody, V. R. Challa, D. A. Stump, and J. W. Hammon, Longer duration of cardiopulmonary bypass is associated with greater numbers of cerebral microemboli, *Stroke* **31**, 707–713, 2000.

[52] A. M. Calafiore, M. Di Mauro, G. Teodori, G. Di Giammarco, S. Cirmeni, M. Contini, A. L. Iacò, and M. Pano, Impact of aortic manipulation on incidence of cerebrovascular accidents after surgical myocardial revascularization, *Ann. Thorac. Surg.* **73**, 1387–1393, 2002.

[53] R. A. Caldwell, J. E. Woodell, S. P. Ho, S. W. Shalaby, T. Boland, E. M. Langan, and M. Laberge, In vitro evaluation of phosphonylated low-density polyethylene for vascular applications, *J. Biomed. Mater. Res.* **62**, 514–524, 2002.

[54] B. Calvo, E. Peña, M. A. Martinez, and M. Doblaré, An uncoupled directional damage model for fibred biological soft tissues. formulation and computational aspects, *Int. J. Numer. Meth. Engng.* **69**, 2036–2057, 2007.

[55] L. Cardamone, A. Valent, J. F. Eberth, and J. D. Humphrey, Origin of axial prestretch and residual stress in arteries, *Biomech. Model. Mechanobiol.* **8**, 431–446, 2009.

[56] *V. Mueller instruments: Cosgrove flex clamps*. CareFusion Corporation, Waukegan, IL, USA, 2010.

[57] C. G. Caro, D. J. Doorly, M. Tarnawski, K. T. Scott, Q. Long, and C. L. Dumoulin, Non-planar curvature and branching of arteries and non-planar-type flow, *Proc. R. Soc. A* **452**, 185–197, 1996.

[58] J. P. Carpenter, J. T. Carpenter, A. Tellez, J. G. Webb, G. H. Yi, and J. F. Granada, A percutaneous aortic device for cerebral embolic protection during cardiovascular intervention, *J. Vasc. Surg.* **54**, 174–181.e1, 2011.

[59] F. P. Casselman, S. Van Slycke, F. Wellens, R. De Geest, I. Degrieck, F. Van Praet, Y. Vermeulen, and H. Vanermen, Mitral valve surgery can now routinely be performed endoscopically, *Circulation* **108**, II–48–II–54, 2003.

[60] P. Chassot, P. van der Linden, M. Zaugg, X. M. Mueller, and D. R. Spahn, Off-pump coronary artery bypass surgery: physiology and anaesthetic management, *Br. J. Anaesth.* **92**, 400–413, 2004.

[61] O. Chavanon, M. Carrier, R. Cartier, Y. Hébert, M. Pellerin, P. Pagé, and L. P. Perrault, Increased incidence of acute ascending aortic dissection with off-pump aortocoronary bypass surgery?, *Ann. Thorac. Surg.* **71**, 117–121, 2001.

[62] H. Chen, J. Navia, and G. Kassab, A simulation of vessel-clamp interaction: Transient closure dynamics, *Ann. Biomed. Eng.* **37**, 1772–1780, 2009.

[63] H. Y. Chen, J. A. Navia, S. Shafique, and G. S. Kassab, Fluid-structure interaction in aortic cross-clamping: Implications for vessel injury, *J. Biomech.* **43**, 221–227, 2010.

[64] R.-L. Chen, J. S. Balami, M. M. Esiri, L.-K. Chen, and A. M. Buchan, Ischemic stroke in the elderly: An overview of evidence, *Nat. Rev. Neurol.* **6**, 256–265, 2010.

[65] D. C. H. Cheng, J. Martin, A. Lal, A. Diegeler, T. A. Folliguet, L. W. Nifong, P. Perier, E. Raanani, J. M. Smith, J. Seeburger, and V. Falk, Minimally invasive versus conventional open mitral valve surgery: A meta-analysis and systematic review, *Innovations* **6**, 84–103, 2011.

[66] W. R. Chitwood Jr, J. R. Elbeery, and J. F. Moran, Minimally invasive mitral valve repair using transthoracic aortic occlusion, *Ann. Thorac. Surg.* **63**, 1477–1479, 1997.

[67] N. Choudhury, O. Bouchot, L. Rouleau, D. Tremblay, R. Cartier, J. Butany, R. Mongrain, and R. L. Leask, Local mechanical and structural properties of healthy and diseased human ascending aorta tissue, *Cardiovascular Pathology* **18**, 83–91, 2009.

[68] C. Chuong and Y. Fung, Compressibility and constitutive equation of arterial wall in radial compression experiments, *J. Biomech.* **17**, 35–40, 1984.

[69] D. Cikrit, J. Miles, and D. Silver, Spontaneous arterial perforation: the ehlers-danlos specter, *J. Vasc. Surg.* **5**, 248–255, 1987.

[70] R. E. Clark, J. Brillman, D. A. Davis, M. R. Lovell, T. R. Price, and G. J. Magovern, Microemboli during coronary artery bypass grafting: Genesis and effect on outcome, *J. Thorac. Cardiovasc. Surg.* **109**, 249–258, 1995.

[71] J. C. Coelho, B. Sigel, D. P. Flanigan, J. J. Schuler, J. Justin, and J. Machi, Arteriographic and ultrasonic evaluation of vascular clamp injuries using an in vitro human experimental model, *Surg. Gynecol. Obstet.* **155**, 506–512, 1982.

[72] L. H. Cohn, Fifty years of open-heart surgery, *Circulation* **107**, 2168–2170, 2003.

[73] D. J. Cook, T. A. Orszulak, K. J. Zehr, N. A. Nussmeier, J. J. Livesay, J. W. Hammon, and X. Chen, Effectiveness of the Cobra aortic catheter for dual-temperature management during adult cardiac surgery, *J. Thorac. Cardiovasc. Surg.* **125**, 378–384, 2003.

[74] C. J. Crnich, J. A. Halfmann, W. C. Crone, and D. G. Maki, The effects of prolonged ethanol exposure on the mechanical properties of polyurethane and silicone catheters used for intravascular access, *Infect. Control Hosp. Epidemiol.* **26**, 708–714, 2005.

[75] I. Danaila, J. Dusek, and F. Anselmet, Coherent structures in a round, spatially evolving, unforced, homogeneous jet at low reynolds numbers, *Physics of Fluids* **9**, 3323–3342, 1997.

[76] O. Darcin, Pressure-controlled vascular clamp: A novel device for atraumatic vessel occlusion, *Ann. Vasc. Surg.* **18**, 254–256, 2004.

[77] S. Das and J. Dunning, Can epiaortic ultrasound reduce the incidence of intraoperative stroke during cardiac surgery?, *Interact. CardioVasc. Thorac. Surg.* **3**, 71–75, 2004.

[78] D. de Cannière, M. Dindar, C. Stefanidis, O. Jegaden, and J.-L. Jansens, Early experience with a new aortic clamping system designed for port access cardiac surgery, *The Heart Surgery Forum* **7**, E240–E244, 2004.

[79] S. de Putter, F. N. van de Vosse, M. Breeuwer, and F. A. Gerritsen, Local influence of calcifications on the wall mechanics of abdominal aortic aneurysm, Volume 6143, pages 61432E–61432E–11, 2006.

[80] E. de Souza Neto, D. Perić, M. Dutko, and D. Owen, Design of simple low order finite elements for large strain analysis of nearly incompressible solids, *International Journal of Solids and Structures* **33**, 3277–3296, 1996.

[81] M. H. de Vaal, S. M. Wildhirt, M. W. Gee, U. A. Stock, and W. A. Wall, Current state of large deformation aortic manipulation during cardiac surgery, *In preparation*, 2014.

[82] G. R. DeFoe, C. S. Ross, E. M. Olmstead, S. D. Surgenor, M. P. Fillinger, R. C. Groom, R. J. Forest, J. W. Pieroni, C. S. Warren, M. E. Bogosian, C. F. Krumholz, C. Clark, R. A. Clough, P. W. Weldner, S. J. Lahey, B. J. Leavitt, C. A. Marrin, D. C. Charlesworth, P. Marshall, and G. T. O'Connor, Lowest hematocrit on bypass and adverse outcomes associated with coronary artery bypass grafting, *Ann. Thorac. Surg.* **71**, 769–776, 2001.

[83] R. E. Delius, J. Montoya, S. I. Merz, J. McKenzie, S. Snedecor, E. L. Bove, and R. H. Bartlett, New method for describing the performance of cardiac surgery cannulas, *Ann. Thorac. Surg.* **53**, 278–281, 1992.

[84] J. W. Demmel, J. R. Gilbert, and X. S. Li, An asynchronous parallel supernodal algorithm, for sparse gaussian elimination, *SIAM J. Matrix Analysis and Applications* **20**, 915–952, 1999.

[85] G. Dhondt, *The Finite Element Method for Three-Dimensional Thermomechanical Applications*, Wiley, 2004.

[86] J. C. Diephuis, K. G. M. Moons, A. N. Nierich, M. Bruens, D. van Dijk, and C. J. Kalkman, Jugular bulb desaturation during coronary artery surgery: a comparison of off-pump and on-pump procedures, *Br. J. Anaesth.* **94**, 715–720, 2005.

[87] P. Dimotikas, The mixing transition in turbulent flows, *Journal of Fluid Mechanics* **409**, 69–98, 2000.

[88] R. Dittrich and E. B. Ringelstein, Occurrence and clinical impact of microembolic signals during or after cardiosurgical procedures, *Stroke* **39**, 503–511, 2008.

[89] G. N. Djaiani, Aortic arch atheroma: stroke reduction in cardiac curgical catients, *Semin. Cardiothorac. Vasc. Anesth.* **10**, 143–157, 2006.

[90] P. B. Dobrin, J. F. McGurrin, and J. A. McNulty, Chronic histologic changes after vascular clamping are not associated with altered vascular mechanics, *Ann. Vasc. Surg.* **6**, 153–159, 1992.

[91] T. Doenst, M. A. Borger, R. D. Weisel, T. M. Yau, M. Maganti, and V. Rao, Relation between aortic cross-clamp time and mortality – not as straightforward as expected, *Eur. J. Cardiothorac. Surg.* **33**, 660–665, 2008.

[92] S. Dogan, T. Aybek, P. S. Risteski, F. Detho, A. Rapp, G. Wimmer-Greinecker, and A. Moritz, Minimally invasive port access versus conventional mitral valve surgery: prospective randomized study, *Ann. Thorac. Surg.* **79**, 492–498, 2005.

[93] J. Donea and A. Huerta, *Finite Element Methods for Flow Problems*, Wiley, 2003.

[94] M. Dujovny, N. Wakenhut, N. Kossovsky, C. W. Gomes, R. K. Laha, L. Leff, and D. Nelson, Minimum vascular occlusive force, *J. Neurosurg.* **51**, 662–668, 1979.

[95] K. A. Eagle, R. A. Guyton, R. Davidoff, G. A. Ewy, J. Fonger, T. J. Gardner, J. P. Gott, H. C. Herrmann, R. A. Marlow, W. Nugent, G. T. OConnor, T. A. Orszulak, R. E. Rieselbach, W. L. Winters, S. Yusuf, T. F. Members, R. J. Gibbons, J. S. Alpert, K. A. Eagle, T. J. Gardner, A. Garson, G. Gregoratos, R. O. Russell, T. J. Ryan, S. C. Smith, and C. Members, ACC/AHA guidelines for coronary artery bypass graft surgery: Executive summary and recommendations, *Circulation* **100**, 1464–1480, 1999.

[96] D. M. Eckmann, S. Bowers, M. Stecker, and A. T. Cheung, Hematocrit, volume expander, temperature, and shear rate effects on blood viscosity, *Anesthesia & Analgesia* **91**, 539–545, 2000.

[97] *Port access systems: The complete system for minimally invasive valve surgery.* Edwards Life-sciences LCC, One Edwards Way, Irvine, CA 92614 USA, 2009.

[98] T. Eitz, M. Kawohl, D. Fritzsche, K. Minami, U. Raute-Kreinsen, and R. Körfer, Aortic dissection after previous coronary artery bypass grafting, *J. Card. Surg.* **18**, 519–523, 2003.

[99] M. Y. Emmert, S. P. Salzberg, B. Seifert, J. Scherman, A. Plass, C. T. Starck, O. Theusinger, S. P. Hoerstrup, J. Grünenfelder, S. Jacobs, and V. Falk, Clampless off-pump surgery reduces stroke in patients with left main disease, *Int. J. Cardiol.* **167**, 2097–2101, 2012.

[100] J. Erath, Harold G. and J. Stoney, William S., Balloon catheter occlusion of the ascending aorta, *Ann. Thorac. Surg.* **35**, 560–561, 1983.

[101] D. A. Etzioni and V. A. Starnes, The epidemiology and economics of cardiothoracic surgery in the elderly, In M. R. Katlic (ed.), *Cardiothoracic Surgery in the Elderly*, pages 5–24, Springer New York, 2011.

[102] N. Famaey, E. Verbeken, S. Vinckier, B. Willaert, P. Herijgers, and J. V. Sloten, In vivo soft tissue damage assessment for applications in surgery, *Med. Eng. Phys.* **32**, 437–443, 2010.

[103] N. Famaey, G. Sommer, J. Vander Sloten, and G. A. Holzapfel, Arterial clamping: Finite element simulation and in vivo validation, *Journal of the Mechanical Behavior of Biomedical Materials* **12**, 107–118, 2012.

[104] N. Famaey, J. Vander Sloten, and E. Kuhl, A three-constituent damage model for arterial clamping in computer-assisted surgery, *Biomech. Model. Mechanobiol.*, 1–14, 2012.

[105] N. Famaey, E. Kuhl, G. A. Holzapfel, and J. Van der Sloten, Cardiovascular tissue damage: An experimental and computational framework, In G. A. Holzapfel and E. Kuhl (eds.), *Computer Models in Biomechanics*, pages 129—148, Springer Netherlands, 2013.

[106] F. Farhat, O. Metton, F. Thivolet, and O. Jegaden, Comparison between 3 aortic clamps for video-assisted cardiac surgery: A histological study in a pig model, *The Heart Surgery Forum* **9**, E657–E660, 2006.

[107] T. B. Ferguson, B. G. Hammill, E. D. Peterson, E. R. DeLong, and F. L. Grover, A decade of change–risk profiles and outcomes for isolated coronary artery bypass grafting procedures, 1990-1999: A report from the STS National Database Committee and the Duke Clinical Research institute, *Ann. Thorac. Surg.* **73**, 480–489, 2002.

[108] J. Ferruzzi, D. A. Vorp, and J. D. Humphrey, On constitutive descriptors of the biaxial mechanical behaviour of human abdominal aorta and aneurysms, *Journal of The Royal Society Interface* **8**, 435–450, 2011.

[109] A. C. Fiore, K. S. Naunheim, P. Dean, G. C. Kaiser, D. Pennington, V. L. Willman, L. R. McBride, and H. B. Barner, Results of internal thoracic artery grafting over 15 years: Single versus double grafts, *Ann. Thorac. Surg.* **49**, 202–209, 1990.

[110] P. J. Flory, Thermodynamic relations for high elastic materials, *Trans. Faraday Soc.* **57**, 829–838, 1961.

[111] D. L. Fry, Responses of the arterial wall to certain physical factors, In *Ciba Foundation Symposium 12 - Atherogenesis: Initiating Factors*, pages 93–125, John Wiley & Sons, Ltd, 2008.

[112] I. Fukuda, S. Fujimori, K. Daitoku, H. Yanaoka, and T. Inamura, Flow velocity and turbulence in the transverse aorta of a proximally directed aortic cannula: Hydrodynamic study in a transparent model, *Ann. Thorac. Surg.* **87**, 1866–1871, 2009.

[113] I. Fukuda, K. Daitoku, M. Minakawa, and W. Fukuda, Shaggy and calcified aorta: surgical implications., *Gen. Thorac. Cardiovasc. Surg.* **61**, 301–313, 2013.

[114] I. Fukuda, M. Minakawa, K. Fukui, S. Taniguchi, K. Daitoku, Y. Suzuki, and H. Hashimoto, Breakdown of atheromatous plaque due to shear force from arterial perfusion cannula, *Ann. Thorac. Surg.* **84**, e17–e18, 2007.

[115] Y. Fung, Elasticity of soft tissue in simple elongation, *Am. J. Physiol.* **213**, 1532–44, 1967.

[116] H. Furtado, T. Stüdeli, M. Sette, E. Samset, and B. Gersak, A system for visualization and automatic placement of the endoclamp balloon catheter, *Proceedings of SPIE* **7625**, 76250C–1–8, 2010.

[117] A. C. Galloway, R. J. Shemin, D. D. Glower, J. Boyer, Joseph H., M. A. Groh, R. E. Kuntz, T. A. Burdon, G. H. Ribakove, B. A. Reitz, and S. B. Colvin, First report of the port access international registry, *Ann. Thorac. Surg.* **67**, 51–58, 1999.

[118] J. S. Gammie, Y. Zhao, E. D. Peterson, S. M. O'Brien, J. S. Rankin, and B. P. Griffith, Less-invasive mitral valve operations: Trends and outcomes from the Society of Thoracic Surgeons Adult Cardiac Surgery Database, *Ann. Thorac. Surg.* **90**, 1401–1410, 2010.

[119] P. Gamnitzer, *Residual-based variational multiscale methods for turbulent flows and fluid-structure interaction*, PhD thesis, Technische Universität München, 2010.

[120] D. Garcia, P. Pibarot, J. G. Dumesnil, F. Sakr, and L.-G. Durand, Assessment of aortic valve stenosis severity: A new index based on the energy loss concept, *Circulation* **101**, 765–771, 2000.

[121] J. Garcia, V. Venkataramana, and J. Gold, 8, pages 74–82, *Prevention of neurological injury during cardiac and great vessel surgery: Advanced therapy of Cardiac Surgery*, K. Franco and E. Verrier (eds.), BC Decker Inc., Ontario, 2003.

[122] R. Garcia-Rinaldi, G. Vaughan, J. Revuelta, J. Goiti, and C. Gomez-Durán, Simplified aortic cannulation, *Ann. Thorac. Surg.* **36**, 226–227, 1983.

[123] T. Gasser and G. Holzapfel, Finite element modeling of balloon angioplasty by considering overstretch of remnant non-diseased tissues in lesions, *Comput. Mech.* **40**, 47–60, 2007.

[124] T. C. Gasser, C. A. J. Schulze-Bauer, and G. A. Holzapfel, A three-dimensional finite element model for arterial clamping, *J. Biomech. Eng.* **124**, 355–363, 2002.

[125] T. C. Gasser, R. W. Ogden, and G. A. Holzapfel, Hyperelastic modelling of arterial layers with distributed collagen fibre orientations, *J. R. Soc. Interface* **3**, 15–35, 2006.

[126] *Balloon Catheter Inspection.* GDO bv, Albert Thijsstraat 67, 6471 WX Eygelshoven NL, 2013. URL http://www.gdo-bv.com/v2/products-services/lifescience-examples.

[127] M. W. Gee, C. Förster, and W. A. Wall, A computational strategy for prestressing patient-specific biomechanical problems under finite deformation, *Int. J. Numer. Meth. Biomed. Engng.* **26**, 52–72, 2010.

[128] M. Gee, C. Reeps, H. Eckstein, and W. Wall, Prestressing in finite deformation abdominal aortic aneurysm simulation, *Journal of Biomechanics* **42**, 1732–1739, 2009.

[129] S. Gelman, The pathophysiology of aortic cross-clamping and unclamping, *Anesthesiology* **82**, 1026–1057, 1995.

[130] A. Gerdes, T. Hanke, and H.-H. Sievers, In vitro hydrodynamics of the Embol-X cannula, *Perfusion* **17**, 153–156, 2002.

[131] F. Gijsen, E. Allanic, F. van de Vosse, and J. Janssen, The influence of the non-newtonian properties of blood on the flow in large arteries: unsteady flow in a 90 curved tube, *Journal of Biomechanics* **32**, 705–713, 1999.

[132] L. N. Girardi, K. H. Krieger, C. A. Mack, and O. W. Isom, No-clamp technique for valve repair or replacement in patients with a porcelain aorta, *Ann. Thorac. Surg.* **80**, 1688–1692, 2005.

[133] M. Gitterle, *A dual mortar formulation for finite deformation frictional contact problems including wear and thermal coupling*, PhD thesis, TUM, 2012.

[134] D. D. Glower and B. Desai, Transaortic endoclamp for mitral valve operation through right minithoracotomy in 369 patients, *Innovations* **5**, 394–399, 2010.

[135] D. D. Glower, F. M. Clements, N. P. Debruijn, M. Stafford-Smith, R. Davis, K. P. Landolfo, and P. K. Smith, Comparison of direct aortic and femoral cannulation for port-access cardiac operations, *Ann. Thorac. Surg.* **68**, 1529–1531, 1999.

[136] D. D. Glower, L. C. Siegel, K. J. Frischmeyer, A. C. Galloway, G. H. Ribakove, E. A. Grossi, N. B. Robinson, W. H. Ryan, and S. B. Colvin, Predictors of outcome in a multicenter port-access valve registry, *Ann. Thorac. Surg.* **70**, 1054–1059, 2000.

[137] J. P. Gold, K. E. Torres, W. Maldarelli, I. Zhuravlev, D. Condit, and J. Wasnick, Improving outcomes in coronary surgery: The impact of echo-directed aortic cannulation and perioperative hemodynamic management in 500 patients, *Ann. Thorac. Surg.* **78**, 1579–1585, 2004.

[138] V. Gravemeier, A. Comerford, L. Yoshihara, M. Ismail, and W. A. Wall, A novel formulation for neumann inflow boundary conditions in biomechanics, *Int. J. Numer. Meth. Biomed. Engng.* **28**, 560–573, 2012.

[139] H. P. Grocott and K. Yoshitani, Neuroprotection during cardiac surgery, *J. Anesth.* **21**, 367–377, 2007.

[140] H. Grocott, 22, pages 311–334, *Protecting the Nervous System during Cardiac Surgery: Perioperative Medicine: Managing for Outcome*, M. F. Newman, L. A. Fleisher, and M. P. Fink (eds.), Saunders, Elsevier, 2008.

[141] R. C. Groom, A. G. Hill, B. Kuban, W. Oneill, B. F. Akl, A. M. Speir, J. Koningsberg, G. T. Sprissler, M. Shakoor, P. S. Massimiano, N. A. Burton, R. A. Albus, Q. Macmanus, and E. A. Lefrak, Aortic cannula velocimetry, *Perfusion* **10**, 183–188, 1995.

[142] R. K. Grooters, K. C. Thieman, R. F. Schneider, and M. G. Nelson, Assessment of perfusion toward the aortic valve using the new dispersion aortic cannula during coronary artery bypass surgery, *Tex. Heart Inst. J.* **27**, 361, 2000.

[143] R. K. Grooters, D. A. Ver Steeg, M. J. Stewart, K. C. Thieman, and R. F. Schneider, Echocardiographic comparison of the standard end-hole cannula, the soft-flow cannula, and the dispersion cannula during perfusion into the aortic arch, *Ann. Thorac. Surg.* **75**, 1919–1923, 2003.

[144] E. A. Grossi, A. C. Galloway, A. LaPietra, G. H. Ribakove, P. Ursomanno, J. Delianides, A. T. Culliford, C. Bizekis, R. A. Esposito, F. G. Baumann, M. S. Kanchuger, and S. B. Colvin, Minimally invasive mitral valve surgery: A 6-year experience with 714 patients, *Ann. Thorac. Surg.* **74**, 660–664, 2002.

[145] E. Grossi, R. Esposito, L. Harris, G. Crooke, A. Galloway, S. Colvin, A. Culliford, F. Baumann, K. Yao, and F. Spencer, Sternal wound infections and use of internal mammary artery grafts, *J. Thorac. Cardiovasc. Surg.* **102**, 342–6; discussion 346–7, 1991.

[146] E. A. Grossi, M. S. Kanchuger, D. S. Schwartz, D. E. McLoughlin, M. LeBoutillier III, G. H. Ribakove, K. E. Marschall, A. C. Galloway, and S. B. Colvin, Effect of cannula length on aortic arch flow: Protection of the atheromatous aortic arch, *Ann. Thorac. Surg.* **59**, 710–712, 1995.

[147] E. A. Grossi, A. C. Galloway, G. H. Ribakove, P. K. Zakow, C. C. Derivaux, F. G. Baumann, D. Schwesinger, and S. B. Colvin, Impact of minimally invasive valvular heart surgery: A case-control study, *Ann. Thorac. Surg.* **71**, 807–810, 2001.

[148] J. Gummert, U. Opfermann, S. Jacobs, T. Walther, J. Kempfert, F. Mohr, and V. Falk, Anastomotic devices for coronary artery bypass grafting: Technological options and potential pitfalls, *Comput. Biol. Med.* **37**, 1384–1393, 2007.

[149] C. Hagl, M. A. Ergin, J. D. Galla, D. Spielvogel, S. Lansman, R. P. Squitieri, and R. B. Griepp, Delayed chronic type A dissection following CABG: Implications for evolving techniques of revascularization, *J. Card. Surg.* **15**, 362–367, 2000.

[150] J. W. Hammon, D. A. Stump, J. F. Butterworth, D. M. Moody, K. Rorie, D. D. Deal, E. H. Kincaid, T. E. Oaks, and N. D. Kon, Coronary artery bypass grafting with single cross-clamp results in fewer persistent neuropsychological deficits than multiple clamp or off-pump coronary artery bypass grafting, *Ann. Thorac. Surg.* **84**, 1174–1179, 2007.

[151] J. W. Hammon and D. A. Stump, 4, pages 29–36, *Neurocognitive Decline Following Cardiac Surgery: Incidence, Risk Factors, Prevention, and Outcomes*, R. S. Bonser, D. Pagano, and A. Haverich (eds.), Springer London, 2011.

[152] M. Hamon, J.-C. Baron, F. Viader, and M. Hamon, Periprocedural stroke and cardiac catheterization, *Circulation* **118**, 678–683, 2008.

[153] W. Harringer, Capture of particulate emboli during cardiac procedures in which aortic cross-clamp is used, *Ann. Thorac. Surg.* **70**, 1119–1123, 2000.

[154] D. Harrington, V. Dronavalli, and R. Bonser, 15, pages 177–189, *Pharmacological Studies to Reduce Brain Injury in Cardiac Surgery*, R. S. Bonser, D. Pagano, and A. Haverich (eds.), Springer London, 2011.

[155] G. S. Hartman, F.-s. F. Yao, M. Bruefach, D. Barbut, J. C. Peterson, M. E. Charlson, J. P. Gold, S. J. Thomas, and T. P. Szatrowski, Severity of aortic atheromatous disease diagnosed by transesophageal echocardiography predicts stroke and other outcomes associated with coronary artery surgery: A prospective study, *Anesth. Analg.* **83**, 701–708, 1996.

[156] S. Hartmann, *Kontaktanalyse dünnwandiger Strukturen bei grossen Deformationen*, PhD thesis, Universität Stuttgart, 2007.

[157] J. G. Harvey and M. H. Gough, A comparison of the traumatic effects of vascular clamps, *Br. J. Surg.* **68**, 267–272, 1981.

[158] D. Haskett, G. Johnson, A. Zhou, U. Utzinger, and J. Vande Geest, Microstructural and biomechanical alterations of the human aorta as a function of age and location, *Biomech. Model. Mechanobiol.* **9**, 725–736, 2010.

[159] S. Hazelrigg, J. Wellons, HA, J. Schneider, and P. Kolm, Wound complications after median sternotomy. Relationship to internal mammary grafting, *J. Thorac. Cardiovasc. Surg.* **98**, 1096–1099, 1989.

[160] D. Heistad, M. Marcus, and S. Mueller, Measurement of cerebral blood flow with microspheres, *Arch. Neurol.* **34**, 657–659, 1977.

[161] M. A. Heroux, R. A. Bartlett, V. E. Howle, R. J. Hoekstra, J. J. Hu, T. G. Kolda, R. B. Lehoucq, K. R. Long, R. P. Pawlowski, E. T. Phipps, A. G. Salinger, H. K. Thornquist, R. S. Tuminaro, J. M. Willenbring, A. Williams, and K. S. Stanley, An overview of the trilinos project, *ACM Trans. Math. Softw.* **31**, 397–423, 2005.

[162] K. Hindler and N. A. Nussmeier, 8, pages 69–88, *Central Nervous System Risk Assessment: Perioperative Medicine: Managing for Outcome*, M. F. Newman, L. A. Fleisher, and M. P. Fink (eds.), Saunders, Elsevier, 2008.

[163] M. Hirschvogel. Computational solid mechanics evaluation of the efficiency and safety of aortic occlusion during cardiopulmonary bypass surgery – Cross-clamping vs. Endoclamping, 2012.

[164] A. Ho, C. Hong, M. Yang, P. Lu, and P. Lin, Stroke after intraaortic balloon counterpulsation associated with mobile atheroma in thoracic aorta diagnosed using transesophageal echocardiography, *Chang Gung Med. J.* **25**, 612–616, 2002.

[165] C. W. Hogue, R. F. Gottesman, and J. Stearns, Mechanisms of cerebral injury from cardiac surgery, *Crit. Care Clin.* **24**, 83–98, 2008.

[166] G. Holzapfel, *Nonlinear solid mechanics*, Wiley, 2000.

[167] G. A. Holzapfel, T. C. Gasser, and R. W. Ogden, A new constitutive framework for arterial wall mechanics and a comparative study of material models, *Journal of Elasticity* **61**, 1–48, 2000.

[168] G. A. Holzapfel, G. Sommer, C. T. Gasser, and P. Regitnig, Determination of layer-specific mechanical properties of human coronary arteries with nonatherosclerotic intimal thickening and related constitutive modeling, *American Journal of Physiology - Heart and Circulatory Physiology* **289**, H2048–H2058, 2005.

[169] J. Humphrey, *Cardiovascular Solid Mechanics: Cells, Tissues, and Organs*, Springer, 2002.

[170] A. Hurt, J. Michael Smith, and A. M. Engel, Predictors and outcomes associated with intraoperative aortic dissection in cardiac surgery, *J. Card. Surg.* **23**, 422–425, 2008.

[171] N. H. Hwang, S. Borik, G. P. Noon, and J. H. Kennedy, Hydraulic studies of aortic cannulation return nozzles, *Trans. Am. Soc. Artif. Intern. Organs* **21**, 237–41, 1975.

[172] J. A. J. Hyde and R. A. Delius, 3, pages 23–56, *Physiology and pathophysiology of extracorporeal circulation: Techniques in Extracorporeal Circulation*, P. H. Kay and C. M. Munsch (eds.), Arnold, London, 2004.

[173] M. Ismail, W. A. Wall, and M. W. Gee, Adjoint-based inverse analysis of windkessel parameters for patient-specific vascular models, *Journal of Computational Physics* **244**, 113–130, 2013.

[174] F. Ius, E. Mazzaro, V. Tursi, G. Guzzi, E. Spagna, L. Vetrugno, F. Bassi, and U. Livi, Clinical results of minimally invasive mitral valve surgery: Endoaortic clamp versus external aortic clamp techniques, *Innovations* **4**, 311–318, 2009.

[175] A. Jacobs, M. Neveling, M. Horst, M. Ghaemi, J. Kessler, H. Eichstaedt, J. Rudolf, P. Model, H. Bönner, E. R. de Vivie, and W.-D. Heiss, Alterations of neuropsychological function and cerebral glucose metabolism after cardiac surgery are not related only to intraoperative microembolic events, *Stroke* **29**, 660–667, 1998.

[176] O. Jazaeri, R. Gupta, P. J. Rochon, and T. B. Reece, Endovascular approaches and perioperative considerations in acute aortic dissection, *Semin. Cardiothorac. Vasc. Anesth.* **15**, 141–162, 2011.

[177] H. Jeanmart, F. P. Casselman, Y. De Grieck, I. Bakir, J. Coddens, L. Foubert, G. Van Vaerenbergh, Y. Vermeulen, and H. Vanermen, Avoiding vascular complications during minimally invasive, totally endoscopic intracardiac surgery, *J. Thorac. Cardiovasc. Surg.* **133**, 1066–1070, 2007.

[178] B. M. Johnston, P. R. Johnston, S. Corney, and D. Kilpatrick, Non-newtonian blood flow in human right coronary arteries: steady state simulations, *Journal of Biomechanics* **37**, 709–720, 2004.

[179] E. Jones, O. Lattouf, and W. Weintraub, Catastrophic consequences of internal mammary artery hypoperfusion, *J. Thorac. Cardiovasc. Surg.* **98**, 902–907, 1989.

[180] E. Joubert-Huebner, A. Gerdes, and H.-H. Sievers, An in vitro evaluation of a new cannula tip design compared with two clinically established cannula-tip designs regarding aortic arch vessel perfusion characteristics, *Perfusion* **15**, 69–76, 2000.

[181] M. V. Kameneva, G. W. Burgreen, K. Kono, B. Repko, J. F. Antaki, and M. Umezu, Effects of Turbulent Stresses upon Mechanical Hemolysis: Experimental and Computational Analysis, *ASAIO J.* **50**, 418–423, 2004.

[182] V. Kanyanta and A. Ivankovic, Mechanical characterisation of polyurethane elastomer for biomedical applications, *Journal of the Mechanical Behavior of Biomedical Materials* **3**, 51–62, 2010.

[183] E. I. Kapetanakis, S. C. Stamou, M. K. C. Dullum, P. C. Hill, E. Haile, S. W. Boyce, A. S. Bafi, K. R. Petro, and P. J. Corso, The impact of aortic manipulation on neurologic outcomes after coronary artery bypass surgery: A risk-adjusted study, *Ann. Thorac. Surg.* **78**, 1564–1571, 2004.

[184] D. G. Karalis, V. Quinn, M. F. Victor, J. J. Ross, M. Polansky, K. A. Spratt, and K. Chandrasekaran, Risk of catheter-related emboli in patients with atherosclerotic debris in the thoracic aorta, *Am. Heart J.* **131**, 1149–1155, 1996.

[185] J. H. Karimov, K. Latsuzbaia, and M. Glauber, eComment: Cross-clamping the heavily calcified ascending aorta after a preoperative computed tomography evaluation, *Interact. CardioVasc. Thorac. Surg.* **10**, 20, 2010.

[186] E. S. Katz, P. A. Tunick, H. Rusinek, G. Ribakove, F. C. Spencer, and I. Kronzon, Protruding aortic atheromas predict stroke in elderly patients undergoing cardiopulmonary bypass: Experience with intraoperative transesophageal echocardiography, *J. Am. Coll. Cardiol.* **20**, 70–77, 1992.

[187] T. A. S. Kaufmann, M. Hormes, M. Laumen, D. L. Timms, T. Linde, T. Schmitz-Rode, A. Moritz, O. Dzemali, and U. Steinseifer, The Impact of Aortic/Subclavian Outflow Cannulation for Cardiopulmonary Bypass and Cardiac Support: A Computational Fluid Dynamics Study, *Artif. Organs* **33**, 727–732, 2009.

[188] T. A. S. Kaufmann, M. Hormes, M. Laumen, D. L. Timms, T. Schmitz-Rode, A. Moritz, O. Dzemali, and U. Steinseifer, Flow Distribution During Cardiopulmonary Bypass in Dependency on the Outflow Cannula Positioning, *Artif. Organs* **33**, 988–992, 2009.

[189] T. A. Kaufmann, T. Schmitz-Rode, and U. Steinseifer, Implementation of cerebral autoregulation into computational fluid dynamics studies of cardiopulmonary bypass, *Artificial Organs* **36**, 754–758, 2012.

[190] T. A. Kaufmann, K. C. Wong, T. Schmitz-Rode, and U. Steinseifer, Mimicking of cerebral autoregulation by flow-dependent cerebrovascular resistance: A feasibility study, *Artificial Organs* **36**, E97–E101, 2012.

[191] H. Kaukuntla, A. Walker, D. Harrington, T. Jones, R. S. Bonser, and O. behalf of the Study Group, Differential brain and body temperature during cardiopulmonary bypass – a randomised clinical study, *Eur. J. Cardiothorac. Surg.* **26**, 571–579, 2004.

[192] K. Kellermann and B. Jungwirth, Avoiding stroke during cardiac surgery, *Semin. Cardiothorac. Vasc. Anesth.* **14**, 95–101, 2010.

[193] A. Khoynezhad and K. Plestis, Cannulation in the diseased aorta: A safe approach using the seldinger technique, *Tex. Heart Inst. J.* **33**, 353–355, 2006.

[194] P. J. Kilner, G. Z. Yang, R. H. Mohiaddin, D. N. Firmin, and D. B. Longmore, Helical and retrograde secondary flow patterns in the aortic arch studied by three-directional magnetic resonance velocity mapping, *Circulation* **88**, 2235–2247, 1993.

[195] H. Kim, K. Jansen, and C. Taylor, Incorporating autoregulatory mechanisms of the cardiovascular system in three-dimensional finite element models of arterial blood flow, *Ann. Biomed. Eng.* **38**, 2314–2330, 2010.

[196] H. Kim, C. Figueroa, T. Hughes, K. Jansen, and C. Taylor, Augmented lagrangian method for constraining the shape of velocity profiles at outlet boundaries for three-dimensional finite element simulations of blood flow, *Computer Methods in Applied Mechanics and Engineering* **198**, 3551–3566, 2009.

[197] W. G. Kim and S.-S. Park, Clinical application of the m-numbers of aortic cannulas during hypothermic cardiopulmonary bypass in pediatric patients, *Artif. Organs* **23**, 369–372, 1999.

[198] R. C. King, I. L. Kron, R. C. Kanithanon, K. S. Shockey, W. D. Spotnitz, and C. G. Tribble, Hypothermic circulatory arrest does not increase the risk of ascending thoracic aortic aneurysm resection, *Ann. Surg.* **227**, 702–707, 1998.

[199] J. Kirkup, *The evolution of surgical instruments: An illustrated history from ancient times to the twentieth century*, Norman Publishing, 2006.

[200] T. W. Koh, K. H. Parker, M. Kon, and J. R. Pepper, Changes in aortic rotational flow during cardiopulmonary bypass studied by transesophageal echocardiography and magnetic resonance velocity imaging: A potential mechanism for atheroembolism during cardiopulmonary bypass, *Heart Vessels* **16**, 1–8, 2001.

[201] K. Kohler, K. Valchanov, G. Nias, and A. Vuylsteke, Ecmo cannula review, *Perfusion* **28**, 114–124, 2013.

[202] R. Kornowski, M. K. Hong, F. O. Tio, O. Bramwell, H. Wu, and M. B. Leon, In-stent restenosis: Contributions of inflammatory responses and arterial injury to neointimal hyperplasia, *J. Am. Coll. Cardiol.* **31**, 224–230, 1998.

[203] F. Koschnick, *Geometrische Locking-Effekte bei Finiten Elementen und ein allgemeines Konzept zu ihrer Vermeidung*, PhD thesis, Technische Universität München, 2004.

[204] D. Kotelis, M. S. Bischoff, B. Jobst, H. Tengg-Kobligk, U. Hinz, P. Geisbüsch, and D. Böckler, Morphological risk factors of stroke during thoracic endovascular aortic repair, *Langenbecks Arch. Surg.* **397**, 1267–1273, 2012.

[205] C. Krapf, P. Wohlrab, S. Häuß inger, T. Schachner, H. Hangler, M. Grimm, L. Müller, J. Bonatti, and N. Bonaros, Remote access perfusion for minimally invasive cardiac surgery: to clamp or to inflate?, *Eur. J. Cardiothorac. Surg.* **44**, 898–904, 2013.

[206] F. Lange, G. B. Mackensen, and M. Swaminathan, 18, pages 395–416, *Atherosclerosis of the Aorta and Prevention of Neurological Dysfunction After Cardiac Surgery: Anesthesia and Perioperative Care for Aortic Surgery*, K. Subramaniam, K. W. Park, and B. Subramaniam (eds.), Springer New York, 2011.

[207] E. W. Larson and W. D. Edwards, Risk factors for aortic dissection: A necropsy study of 161 cases, *The American Journal of Cardiology* **53**, 849–855, 1984.

[208] H. L. Lazar, Should off-pump coronary artery bypass grafting be abandoned?, *Circulation* **128**, 406–413, 2013.

[209] J. D. Lee, M. Srivastava, and J. Bonatti, History and current status of robotic totally endoscopic coronary artery bypass, *Circ. J.* **76**, 2058–2065, 2012.

[210] J.-F. Legare, A. Hassan, K. Buth, and J. Sullivan, The effect of total arterial grafting on medium-term outcomes following coronary artery bypass grafting, *Journal of Cardiothoracic Surgery* **2**, 44, 2007.

[211] J. E. Liddicoat, S. M. Bekassy, J. M. Duncan, and M. E. DeBakey, Safe cannulation of the ascending aorta, *Ann. Thorac. Surg.* **21**, 70–71, 1976.

[212] J. R. Liddicoat, J. R. Doty, and R. S. Stuart, Management of the atherosclerotic ascending aorta with endoaortic occlusion, *Ann. Thorac. Surg.* **65**, 1133–1135, 1998.

[213] Y.-H. Liu, D.-X. Wang, L.-H. Li, X.-M. Wu, G.-J. Shan, Y. Su, J. Li, Q.-J. Yu, C.-X. Shi, Y.-N. Huang, and W. Sun, The effects of cardiopulmonary bypass on the number of cerebral microemboli and the incidence of cognitive dysfunction after coronary artery bypass graft surgery, *Anesth. Analg.* **109**, 1013–1022, 2009.

[214] A. Loforte, G. Luzi, A. Montalto, F. Ranocchi, V. Polizzi, F. Sbaraglia, P. Lilla Della Monica, A. Menichetti, and F. Musumeci, Video-assisted minimally invasive mitral valve surgery: External aortic clamp versus endoclamp techniques, *Innovations* **5**, 413–418, 2010.

[215] F. Loop, T. Higgins, R. Panda, G. Pearce, and F. Estafanous, Myocardial protection during cardiac operations. decreased morbidity and lower cost with blood cardioplegia and coronary sinus perfusion, *J. Thorac. Cardiovasc. Surg.* **104**, 608–618, 1992.

[216] T.-L. Lu, C. Huber, E. Rizzo, J. Dehmeshki, L. von Segesser, and S. Qanadli, Ascending aorta measurements as assessed by ECG-gated multi-detector computed tomography: A pilot study to establish normative values for transcatheter therapies, *Eur. Radiol.* **19**, 664–669, 2009.

[217] A. Luk, S. Leong, G. Soor, M. Borger, and J. Butany, Histological analysis of aortic dissections following previous cardiovascular surgery, *Cardiovascular Pathology* **17**, 199–205, 2008.

[218] Y. Luo, K. Shingo, Z. Ye, and T. Toshiyuki, The application of superelastic SMAs in less invasive haemostatic forceps, *Smart Mater. Struct.* **16**, 1061–1065, 2007.

[219] M. J. Mack, Introduction, *Semin. Thorac. Cardiovasc. Surg.* **15**, 44, 2003.

[220] G. B. Mackensen, L. K. Ti, B. G. Phillips-Bute, J. P. Mathew, M. F. Newman, H. P. Grocott, and the Neurologic Outcome Research Group, Cerebral embolization during cardiac surgery: Impact of aortic atheroma burden, *Br. J. Anaesth.* **91**, 656–661, 2003.

[221] G. Mackensen, H. Grocott, and M. Newman, 10, pages 148–176, *Cardiopulmonary bypass and the brain: Techniques in Extracorporeal Circulation*, 4th Edition, P. H. Kay and C. M. Munsch (eds.), Arnold, London, 2004. Here I got: equipment, procedural, patient sources of emboli.

[222] A. Maier, *Computational Modeling of Rupture Risk in Abdominal Aortic Aneurysms*, PhD thesis, TUM, 2012.

[223] A. Maier, M. Gee, C. Reeps, J. Pongratz, H.-H. Eckstein, and W. Wall, A comparison of diameter, wall stress, and rupture potential index for abdominal aortic aneurysm rupture risk prediction, *Ann. Biomed. Eng.* **38**, 3124–3134, 2010.

[224] A. Maier, M. Gee, C. Reeps, H.-H. Eckstein, and W. Wall, Impact of calcifications on patient-specific wall stress analysis of abdominal aortic aneurysms, *Biomech. Model. Mechanobiol.* **9**, 511–521, 2010.

[225] A. I. Margovsky, R. S. A. Lord, A. C. Meek, and Y. V. Bobryshev, Artery wall damage and platelet uptake from so-called atraumatic arterial clamps: an experimental study, *Cardiovasc. Surg.* **5**, 42–47, 1997.

[226] A. I. Margovsky, A. J. Chambers, and R. S. A. Lord, The effect of increasing clamping forces on endothelial and arterial wall damage: an experimental study in the sheep, *Cardiovasc. Surg.* **7**, 457–463, 1999.

[227] M. A. Mariani, A. D'Alfonso, and J. G. Grandjean, Total arterial off-pump coronary surgery: Time to change our habits?, *Ann. Thorac. Surg.* **78**, 1591–1597, 2004.

[228] G. Marini, A. Maier, C. Reeps, H.-H. Eckstein, W. A. Wall, and M. W. Gee, A continuum description of the damage process in the arterial wall of abdominal aortic aneurysms, *Int. J. Numer. Meth. Biomed. Engng.* **28**, 87–99, 2011.

[229] D. Maselli, G. Santise, A. Montalto, and F. Musumeci, Endovascular aortic clamping for pseudo-neurysms of the aortic root with aortic regurgitation, *Ann. Thorac. Surg.* **80**, 1303–1308, 2005.

[230] D. Maselli, R. Pizio, G. Borelli, and F. Musumeci, Endovascular balloon versus transthoracic aortic clamping for minimally invasive mitral valve surgery: Impact on cerebral microemboli, *Interact. CardioVasc. Thorac. Surg.* **5**, 183–186, 2006.

[231] J. Masuda, C. Yutani, J. Ogata, Y. Kuriyama, and T. Yamaguchi, Atheromatous embolism in the brain, *Neurology* **44**, 1231, 1994.

[232] K. D. May-Newman, B. K. Hillen, C. S. Sironda, and W. Dembitsky, Effect of LVAD outflow conduit insertion angle on flow through the native aorta, *J. Med. Eng. Technol.* **28**, 105–109, 2004.

[233] K. May-Newman, B. Hillen, and W. Dembitsky, Effect of Left Ventricular Assist Device Outflow Conduit Anastomosis Location on Flow Patterns in the Native Aorta, *ASAIO J.* **52**, 132–139, 2006.

[234] A. Mazine, M. Pellerin, J.-S. Lebon, P.-O. Dionne, H. Jeanmart, and D. Bouchard, Minimally invasive mitral valve surgery: Influence of aortic clamping technique on early outcomes, *Ann. Thorac. Surg.* **96**, 2116–2122, 2013.

[235] G. McKhann, R. Gottesman, M. Grega, W. Baumgartner, and O. Selnes, 3, pages 19–28, *Neurological and Cognitive Sequelae of Cardiac Surgery*, R. S. Bonser, D. Pagano, and A. Haverich (eds.), Springer London, 2011.

[236] MedtronicInc., 2, pages 7–22, *Design and principles of the extracorporeal circuit*, P. H. Kay and C. M. Munsch (eds.), Arnold, London, 2004. See Mulpur2004 for pdf.

[237] G. Melissano, Y. Tshomba, L. Bertoglio, E. Rinaldi, and R. Chiesa, Analysis of stroke after tevar involving the aortic arch, *Eur. J. Vasc. Endovasc. Surg.* **43**, 269–275, 2012.

[238] P. Menon, J. Antaki, A. Undar, and K. Pekkan, Aortic outflow cannula tip design and orientation impacts cerebral perfusion during pediatric cardiopulmonary bypass procedures, *Ann Biomed Eng.* **41**, 2588–602, 2013.

[239] P. G. Menon, N. Teslovich, C.-Y. Chen, A. Undar, and K. Pekkan, Characterization of neonatal aortic cannula jet flow regimes for improved cardiopulmonary bypass, *J. Biomech.* **46**, 362–372, 2013.

[240] T. Mihaljevic, C. M. Jarrett, A. M. Gillinov, S. J. Williams, P. A. DeVilliers, W. J. Stewart, L. G. Svensson, J. F. Sabik III, and E. H. Blackstone, Robotic repair of posterior mitral valve prolapse versus conventional approaches: Potential realized, *J. Thorac. Cardiovasc. Surg.* **141**, 72–80.e4, 2011.

[241] N. Mills and C. Everson, Atherosclerosis of the ascending aorta and coronary artery bypass. Pathology, clinical correlates, and operative management, *J. Thorac. Cardiovasc. Surg.* **102**, 546–553, 1991.

[242] M. Minakawa, I. Fukuda, J. Yamazaki, K. Fukui, H. Yanaoka, and T. Inamura, Effect of Cannula Shape on Aortic Wall and Flow Turbulence: Hydrodynamic Study During Extracorporeal Circulation in Mock Thoracic Aorta, *Artif. Organs* **31**, 880–886, 2007.

[243] M. Minakawa, I. Fukuda, T. Inamura, H. Yanaoka, K. Fukui, K. Daitoku, Y. Suzuki, and H. Hashimoto, Hydrodynamic evaluation of axillary artery perfusion for normal and diseased aorta, *Gen. Thorac. Cardiovasc. Surg.* **56**, 215–221, 2008.

[244] M. Minakawa, I. Fukuda, T. Igarashi, K. Fukui, H. Yanaoka, and T. Inamura, Hydrodynamics of Aortic Cannulae During Extracorporeal Circulation in a Mock Aortic Arch Aneurysm Model, *Artif. Organs* **34**, 105–112, 2010.

[245] P. Modi, A. Hassan, and W. R. Chitwood Jr., Minimally invasive mitral valve surgery: A systematic review and meta-analysis, *Eur. J. Cardiothorac. Surg.* **34**, 943–952, 2008.

[246] F. Mohr, V. Falk, A. Diegeler, T. Walther, J. van Son, R. Autschbach, and H. G. Borst, Minimally invasive port-access mitral valve surgery, *J. Thorac. Cardiovasc. Surg.* **115**, 567–576, 1998.

[247] F. Mohr, J. Onnasch, V. Falk, T. Walther, A. Diegeler, R. Krakor, F. Schneider, and R. Autschbach, The evolution of minimally invasive mitral valve surgery – 2 year experience, *Eur. J. Cardiothorac. Surg.* **15**, 233–239, 1999.

[248] P. Moireau, N. Xiao, M. Astorino, C. Figueroa, D. Chapelle, C. Taylor, and J.-F. Gerbeau, External tissue support and fluid-structure simulation in blood flows, *Biomech. Model. Mechanobiol.* **11**, 1–18, 2012.

[249] I. Momjian-Mayor and J.-C. Baron, The pathophysiology of watershed infarction in internal carotid artery disease: Review of cerebral perfusion studies, *Stroke* **36**, 567–577, 2005.

[250] J. P. Montoya, S. I. Merz, and R. H. Bartlett, A standardized system for describing flow/pressure relationships in vascular access devices, *ASAIO J.* **37**, 4–8, 1991.

[251] D. M. Moody, M. A. Bell, V. R. Challa, W. E. Johnston, and D. S. Prough, Brain microemboli during cardiac surgery or aortography, *Ann Neurol.* **28**, 477–486, 1990.

[252] U. Morbiducci, R. Ponzini, G. Rizzo, M. Cadioli, A. Esposito, F. Cobelli, A. Maschio, F. Montevecchi, and A. Redaelli, In vivo quantification of helical blood flow in human aorta by time-resolved three-dimensional cine phase contrast magnetic resonance imaging, *Ann. Biomed. Eng.* **37**, 516–531, 2009.

[253] U. Morbiducci, R. Ponzini, G. Rizzo, M. Cadioli, A. Esposito, F. Montevecchi, and A. Redaelli, Mechanistic insight into the physiological relevance of helical blood flow in the human aorta: An in vivo study, *Biomech. Model. Mechanobiol.*, 1–17, 2010.

[254] L. Morris, P. Delassus, A. Callanan, M. Walsh, F. Wallis, P. Grace, and T. McGloughlin, 3-D numerical simulation of blood flow through models of the human aorta, *J. Biomech. Eng.* **127**, 767–775, 2005.

[255] R. Motallebzadeh, J. M. Bland, H. S. Markus, J. C. Kaski, and M. Jahangiri, Neurocognitive function and cerebral emboli: Randomized study of on-pump versus off-pump coronary artery bypass surgery, *Ann. Thorac. Surg.* **83**, 475–482, 2007.

[256] P. Mott, J. Dorgan, and C. Roland, The bulk modulus and poisson's ratio of "incompressible" materials, *Journal of Sound and Vibration* **312**, 572–575, 2008.

[257] S. Muehlschlegel, L. Davies, and C. N. Scubert, 24, pages 337–350, *Perioperative stroke: Complications in Anesthesiology*, E. Lobato, N. Gravenstein, and K. R.R. (eds.), Lippincott Williams & Wilkins, 2008.

[258] D. D. Muehrcke, J. F. Cornhill, J. D. Thomas, and D. M. Cosgrove, Flow characteristics of aortic cannulae, *J. Card. Surg.* **10**, 514–519, 1995.

[259] W. Müllges, D. Franke, W. Reents, and J. Babin-Ebell, Brain microembolic counts during extracorporeal circulation depend on aortic cannula position, *Ultrasound Med. Biol.* **27**, 933–936, 2001.

[260] A. K. Mulpur and C. M. Munsch, 1, pages 1–6, *A brief history of bypass: Techniques in Extracorporeal Circulation*, P. H. Kay and C. M. Munsch (eds.), Arnold, London, 2004.

[261] J. M. Murkin, Pulsatile versus nonpulsatile perfusion revisited, *J. Card. Surg.* **21**, 355–356, 2006.

[262] D. Murphy, J. Craver, E. Jones, D. Bone, R. Guyton, and C. Hatcher, Recognition and management of ascending aortic dissection complicating cardiac surgical operations., *J. Thorac. Cardiovasc. Surg.* **85**, 247–256, 1983.

[263] D. A. Murphy, J. S. Miller, D. A. Langford, and A. B. Snyder, Endoscopic robotic mitral valve surgery, *J. Thorac. Cardiovasc. Surg.* **132**, 776–781, 2006.

[264] R. Murphy and R. Lilly. Cannula with flow diversion mechanism, 2009.

[265] G. Ndrepepa and A. Kastrati, Need for critical reappraisal of intra-aortic balloon counterpulsation, *JAMA* **306**, 1376–1377, 2011.

[266] J. W. Newburger, R. A. Jonas, G. Wernovsky, D. Wypij, P. R. Hickey, K. Kuban, D. M. Farrell, G. L. Holmes, S. L. Helmers, J. Constantinou, E. Carrazana, J. K. Barlow, A. Z. Walsh, K. C. Lucius, J. C. Share, D. L. Wessel, F. L. Hanley, J. E. Mayer, A. R. Castaneda, and J. H. Ware, A comparison of the perioperative neurologic effects of hypothermic circulatory arrest versus low-flow cardiopulmonary bypass in infant heart surgery, *N. Engl. J. Med.* **329**, 1057–1064, 1993.

[267] M. F. Newman, T. O. Stanley, and H. P. Grocott, Strategies to protect the brain during cardiac surgery, *Semin. Cardiothorac. Vasc. Anesth.* **4**, 53–64, 2000.

[268] A. Ni Annaidh, M. Destrade, M. D. Gilchrist, and J. G. Murphy, Deficiencies in numerical models of anisotropic nonlinearly elastic materials, *Biomech. Model. Mechanobiol.* **12**, 781–791, 2013.

[269] W. W. Nichols and M. F. O'Rourke, *McDonald's Blood Flow in Arteries*, Hodder Arnold, 5th Edition, 2005.

[270] F. Nietlispach, N. Wijesinghe, R. Gurvitch, E. Tay, J. P. Carpenter, C. Burns, D. A. Wood, and J. G. Webb, An embolic deflection device for aortic valve interventions, *JACC: Cardiovascular Interventions* **3**, 1133–1138, 2010.

[271] H. Nishi, M. Mitsuno, M. Ryomoto, and Y. Miyamoto, Comprehensive approach for clamping severely calcified ascending aorta using computed tomography, *Interact. CardioVasc. Thorac. Surg.* **10**, 18–20, 2010.

[272] J. Nissinen, F. Biancari, J.-O. Wistbacka, T. Peltola, P. Loponen, P. Tarkiainen, M. Virkkila, and M. Tarkka, Safe time limits of aortic cross-clamping and cardiopulmonary bypass in adult cardiac surgery, *Perfusion* **24**, 297–305, 2009.

[273] R. Ogden, Large deformation isotropic elasticity: on the correlation of theory and experiment for compressible rubberlike solids, *Proceedings of the Royal Society of London* **A328**, 567–583, 1972.

[274] K. Okada, T. Sueda, K. Orihashi, and K. Imai, Early type a dissection with the aortic connector device, *Eur. J. Cardiothorac. Surg.* **25**, 902–904, 2004.

[275] J. Onnasch, F. Schneider, V. Falk, M. Mierzwa, J. Bucerius, and F. Mohr, Five years of less invasive mitral valve surgery: from experimental to routine approach, *Heart Surg. Forum* **5**, 132–5, 2002.

[276] M. Parish, T. Asai, E. Grossi, R. Esposito, A. Galloway, S. Colvin, and F. Spencer, The effects of different techniques of internal mammary artery harvesting on sternal blood flow, *J. Thorac. Cardiovasc. Surg.* **104**, 1303–1307, 1992.

[277] K. Pekkan, O. Dur, K. Sundareswaran, K. Kanter, M. Fogel, A. Yoganathan, and A. Undar, Neonatal aortic arch hemodynamics and perfusion during cardiopulmonary bypass, *J. Biomech. Eng.* **130**, 061012–13, 2008.

[278] K. Perktold, M. Resch, and H. Florian, Pulsatile non-newtonian flow characteristics in a three-dimensional human carotid bifurcation model, *Journal of Biomechanical Engineering* **113**, 464–475, 1991.

[279] A. T. Pezzella, Global aspects of cardiothoracic surgery with focus on developing countries, *Asian Cardiovasc. Thorac. Ann.* **18**, 299–310, 2010.

[280] L. M. Pfaender, Hemodynamics in the extra corporeal aortic cannula: review of factors affecting choice of the appropriate size, *J. Extra-Corp. Technol.* **13**, 224, 1981.

[281] P. Pibarot, D. Garcia, and J. G. Dumesnil, Energy loss index in aortic stenosis: From fluid mechanics concept to clinical application, *Circulation* **127**, 1101–1104, 2013.

[282] M. A. Pichlmaier, O. E. Teebken, H. Baraki, and A. Haverich, The frozen elephant trunk technique, *MMCTS*, 2007.

[283] A. Popp, *Mortar Methods for Computational Contact Mechanics and General Interface Problems*, PhD thesis, Technische Universität München, 2012.

[284] A. Popp, A. Seitz, M. W. Gee, and W. A. Wall, Improved robustness and consistency of 3d contact algorithms based on a dual mortar approach, *Computer Methods in Applied Mechanics and Engineering* **264**, 67–80, 2013.

[285] S. Prakash and C. R. Ethier, Requirements for Mesh Resolution in 3D Computational Hemodynamics, *J. Biomech. Eng.* **123**, 134–144, 2001.

[286] O. Preventza, M. Aftab, and J. Coselli, Hybrid techniques for complex aortic arch surgery, *Tex. Heart Inst. J.* **40**, 568–571, 2013.

[287] W. Pugsley, L. Klinger, C. Paschalis, T. Treasure, M. Harrison, and S. Newman, The impact of microemboli during cardiopulmonary bypass on neuropsychological functioning, *Stroke* **25**, 1393–9, 1994.

[288] D. A. Pybus, Aortic atheromatous plaque instability associated with rotational aortic flow during cardiopulmonary bypass, *Anesth. Analg.* **103**, 303–304, 2006.

[289] A. Quarteroni, R. Sacco, and F. Saleri, *Numerical mathematics*, Springer, 2007.

[290] M. Raghavan and D. A. Vorp, Toward a biomechanical tool to evaluate rupture potential of abdominal aortic aneurysm: Identification of a finite strain constitutive model and evaluation of its applicability, *J. Biomech.* **33**, 475–482, 2000.

[291] A. M. Ranasinghe and T. J. Jones, 14, pages 159–175, *Studies of Nonpharmacological Interventions to Reduce Brain Injury: Brain Protection in Cardiac Surgery*, R. S. Bonser, D. Pagano, and A. Haverich (eds.), Springer London, 2011.

[292] J. H. Rapp, X. M. Pan, B. Yu, R. A. Swanson, R. T. Higashida, P. Simpson, and D. Saloner, Cerebral ischemia and infarction from atheroemboli <100 μm in size, *Stroke* **34**, 1976–1980, 2003.

[293] D. M. Razi, The challenge of calcific aortitis, *J. Card. Surg.* **8**, 102–107, 1993.

[294] H. Reichenspurner, C. Detter, T. Deuse, D. H. Boehm, H. Treede, and B. Reichart, Video and robotic-assisted minimally invasive mitral valve surgery: A comparison of the port-access and transthoracic clamp techniques, *Ann. Thorac. Surg.* **79**, 485–490, 2005.

[295] R. Reneman, T. Arts, and A. Hoeks, Wall shear stress – an important determinant of endothelial cell function and structure in the arterial system in vivo, *J. Vasc. Res.* **43**, 251–269, 2006.

[296] G. W. Roach, M. Kanchuger, C. M. Mangano, M. Newman, N. Nussmeier, R. Wolman, A. Aggarwal, K. Marschall, S. H. Graham, C. Ley, G. Ozanne, D. T. Mangano, A. Herskowitz, V. Katseva, and R. Sears, Adverse cerebral outcomes after coronary bypass surgery, *N. Engl. J. Med.* **335**, 1857–1864, 1996.

[297] S. Roccabianca, C. Figueroa, G. Tellides, and J. Humphrey, Quantification of regional differences in aortic stiffness in the aging human, *Journal of the Mechanical Behavior of Biomedical Materials* **29**, 618–634, 2014.

[298] E. B. Rosero, R. M. Peshock, A. Khera, G. P. Clagett, H. Lo, and C. Timaran, Agreement between methods of measurement of mean aortic wall thickness by MRI, *J. Magn. Reson. Imaging* **29**, 576–82, 2009.

[299] J. L. Rudolf, K. A. Schreiber, D. J. Culley, R. E. McGlinchey, G. Crosby, S. Levitsky, and E. R. Marcantonio, Measurement of post-operative cognitive dysfunction after cardiac surgery: a systematic review, *Acta Anaesthesiol. Scand.* **54**, 663–677, 2010.

[300] W. Ryan, W. Brinkman, T. Dewey, M. Mack, S. Prince, and M. Herbert, Mitral valve surgery: comparison of outcomes in matched sternotomy and port access groups, *J. Heart Valve Dis.* **19**, 51–58, 2010.

[301] A. P. Sage, Y. Tintut, and L. L. Demer, Regulatory mechanisms in vascular calcification, *Nat Rev Cardiol* **7**, 528–536, 2010.

[302] L. Santos, M. Carmona, S. Kim, R. Dias, and J. Auler, Uncommon causes of hemodynamic instability during myocardial revascularization without cardiopulmonary bypass, *Rev. Bras. Anestesiol.* **60**, 84–89, 2010.

[303] Y. Sari, T. Minematsu, L. Huang, H. Noguchi, T. Mori, G. Nakagami, T. Nagase, M. Oe, J. Sugama, K. Yoshimura, and H. Sanada, Establishment of a novel rat model for deep tissue injury deterioration, *Int Wound J* **12**, 202–209, 2013.

[304] L. D. Sauren, M. la Meir, G. Bolotin, F. H. van der Veen, J. H. Heijmans, W. H. Mess, and J. G. Maessen, The emblocker: Efficiency of a new ultrasonic embolic protection device adjunctive to heart valve surgery, *Ann. Thorac. Surg.* **88**, 253–257, 2009.

[305] M. Scharfschwerdt, A. Richter, K. Boehmer, D. Repenning, and H.-H. Sievers, Improved hydrodynamics of a new aortic cannula with a novel tip design, *Perfusion* **19**, 193–197, 2004.

[306] C. Schlenk. Could aortic cross-clamp orientation and position relative to vessel calcifications influence the risk of stroke during cardiopulmonary bypass surgery?, 2012.

[307] F. Schneider, J.-F. Onnasch, V. Falk, T. Walther, R. Autschbach, and F. W. Mohr, Cerebral microemboli during minimally invasive and conventional mitral valve operations, *Ann. Thorac. Surg.* **70**, 1094–1097, 2000.

[308] F. Schneider MD, V. Falk MD, T. Walther MD, and F. W. Mohr MD, PhD, Control of endoaortic clamp position during port-access mitral valve operations using transcranial doppler echography, *Ann. Thorac. Surg.* **65**, 1481–1482, 1998.

[309] A. J. Schriefl, G. Zeindlinger, D. M. Pierce, P. Regitnig, and G. A. Holzapfel, Determination of the layer-specific distributed collagen fibre orientations in human thoracic and abdominal aortas and common iliac arteries, *J. R. Soc. Interface* **9**, 1275–1286, 2011.

[310] J. M. Schultz, T. Karamlou, J. Swanson, I. Shen, and R. M. Ungerleider, Hypothermic low-flow cardiopulmonary bypass impairs pulmonary and right ventricular function more than circulatory arrest, *Ann. Thorac. Surg.* **81**, 474–480, 2006.

[311] O. A. Selnes, R. F. Gottesman, M. A. Grega, W. A. Baumgartner, S. L. Zeger, and G. M. McKhann, Cognitive and neurologic outcomes after coronary-artery bypass surgery, *N. Engl. J. Med.* **366**, 250–257, 2012.

[312] L. Shani, O. Cohen, Z. Beckerman, R.-R. Nir, and G. Bolotin, Novel emboli protection cannula during cardiac surgery: first animal study, *Asian Cardiovasc. Thorac. Ann.* **22**, 25–30, 2014.

[313] T. Shimokawa, N. Minato, N. Yamada, Y. Takeda, Y. Hisamatsu, and M. Itoh, Assessment of ascending aorta using epiaortic ultrasonography during off-pump coronary artery bypass grafting, *Ann. Thorac. Surg.* **74**, 2097–2100, 2002.

[314] U. Sigwart, J. Puel, V. Mirkovitch, F. Joffre, and L. Kappenberger, Intravascular stents to prevent occlusion and re-stenosis after transluminal angioplasty, *N. Engl. J. Med.* **316**, 701–706, 1987.

[315] I. Sipahi, M. Akay, S. Dagdelen, A. Blitz, and C. Alhan, Coronary artery bypass grafting vs percutaneous coronary intervention and long-term mortality and morbidity in multivessel disease: Meta-analysis of randomized clinical trials of the arterial grafting and stenting era, *JAMA Intern. Med.* **174**, 223–230, 2013.

[316] K. D. Sjauw, A. E. Engström, M. M. Vis, R. J. van der Schaaf, J. Baan, K. T. Koch, R. J. de Winter, J. J. Piek, J. G. Tijssen, and J. P. Henriques, A systematic review and meta-analysis of intra aortic balloon pump therapy in st-elevation myocardial infarction: should we change the guidelines?, *Eur. Heart J.* **30**, 459–468, 2009.

[317] J. M. Slater, T. A. Orszulak, K. J. Zehr, and D. J. Cook, Use of the cobra catheter for targeted temperature management during cardiopulmonary bypass in swine, *J. Thorac. Cardiovasc. Surg.* **123**, 936–942, 2002.

[318] M. S. Slaughter, M. A. Sobieski, A. J. Tatooles, and P. S. Pappas, Reducing emboli in cardiac surgery: does it make a difference?, *Artif. Organs* **32**, 880–884, 2008.

[319] L. Soltero and S. Greenberg. Surgical clamp. US Patent no. 2,842,132, 1958.

[320] L. Speelman, A. Bohra, E. M. H. Bosboom, G. W. H. Schurink, F. N. van de Vosse, M. S. Makaroun, and D. A. Vorp, Effects of wall calcifications in patient-specific wall stress analyses of abdominal aortic aneurysms, *J. Biomech. Eng.* **129**, 105–109, 2007.

[321] A. Stalder, M. Russe, A. Frydrychowicz, J. Bock, J. Hennig, and M. Markl, Quantitative 2D and 3D phase contrast MRI: Optimized analysis of blood flow and vessel wall parameters, *Magn. Reson. Med.* **60**, 1218–1231, 2008.

[322] A. Stekelenburg, *Mechanisms associated with deep tissue injury induced by sustained compressive loading*, PhD thesis, Technische Universiteit Eindhoven, 2005.

[323] A. Stern, P. A. Tunick, A. T. Culliford, J. Lachmann, F. Baumann, M. S. Kanchuger, K. Marschall, A. Shah, E. Grossi, and I. Kronzon, Protruding aortic arch atheromas: Risk of stroke during heart surgery with and without aortic arch endarterectomy, *Am. Heart J.* **138**, 746–752, 1999.

[324] R. J. Still, A. D. Hilgenberg, C. W. Akins, W. M. Daggett, and M. J. Buckley, Intraoperative aortic dissection, *Ann. Thorac. Surg.* **53**, 374–380, 1992.

[325] P. A. Stonebridge, P. R. Hoskins, P. L. Allan, and J. F. Belch, Spiral laminar flow in vivo, *Clin. Sci.* **91**, 17–21, 1996.

[326] D. A. Stump, A. T. Rogers, J. W. Hammon, and S. P. Newman, Cerebral emboli and cognitive outcome after cardiac surgery, *J. Cardiothorac. Vasc. Anesth.* **10**, 113–119, 1996.

[327] D. A. Stump, T. J. J. Jones, and K. D. Rorie, Neurophysiologic monitoring and outcomes in cardiovascular surgery, *J. Cardiothorac. Vasc. Anesth.* **13**, 600–613, 1999.

[328] M. Swaminathan, H. P. Grocott, G. B. Mackensen, M. V. Podgoreanu, D. D. Glower, and J. P. Mathew, The "sandblasting" effect of aortic cannula on arch atheroma during cardiopulmonary bypass, *Anesth. Analg.* **104**, 1350–1351, 2007.

[329] S. Sylivris, C. Levi, G. Matalanis, A. Rosalion, B. F. Buxton, A. Mitchell, G. Fitt, D. B. Harberts, M. M. Saling, and A. M. Tonkin, Pattern and significance of cerebral microemboli during coronary artery bypass grafting, *Ann. Thorac. Surg.* **66**, 1674–1678, 1998.

[330] I. F. Tabry and E. M. Costantini, Acute aortic dissection early after off-pump coronary surgery, *Tex. Heart Inst. J.* **36**, 462–467, 2009.

[331] Y. Takami, K. Tajima, S. Terazawa, N. Okada, K. Fujii, and Y. Sakai, Safer aortic crossclamping during short-term moderate hypothermic circulatory arrest for cardiac surgery in patients with a bad ascending aorta, *J. Thorac. Cardiovasc. Surg.* **137**, 875–880, 2009.

[332] R. L. Taylor, M. A. Borger, R. D. Weisel, L. Fedorko, and C. M. Feindel, Cerebral microemboli during cardiopulmonary bypass: Increased emboli during perfusionist interventions, *Ann. Thorac. Surg.* **68**, 89–93, 1999.

[333] T. Teitelbaum and P. D. Mininni, Effect of helicity and rotation on the free decay of turbulent flows, *Phys. Rev. Lett.* **103**, 014501–014504, 2009.

[334] M. M. Thompson, J. Smith, A. Naylor, A. Nasim, R. D. Sayers, J. R. Boyle, J. Thompson, K. Tinkler, D. Evans, G. Smith, and P. R. Bell, Microembolization during endovascular and conventional aneurysm repair, *J. Vasc. Surg.* **25**, 179–186, 1997.

[335] M. Thubrikar, *Vascular Mechanics and Pathology*, Springer, 2007.

[336] Y. Tokuda, M.-H. Song, Y. Ueda, A. Usui, T. Akita, S. Yoneyama, and S. Maruyama, Three-dimensional numerical simulation of blood flow in the aortic arch during cardiopulmonary bypass, *Eur. J. Cardiothorac. Surg.* **33**, 164–167, 2008.

[337] R. Trobec and B. Gersak, Direct measurement of clamping forces in cardiovascular surgery, *Med. Biol. Eng. Comput.* **35**, 17–20, 1997.

[338] J. C. Tsang, J.-F. Morin, C. I. Tchervenkov, R. W. Platt, J. Sampalis, and D. Shum-Tim, Single aortic clamp versus partial occluding clamp technique for cerebral protection during coronary artery bypass: A randomized prospective trial, *J. Card. Surg.* **18**, 158–163, 2003.

[339] K. Tuman, R. McCarthy, H. Najafi, and A. Ivankovich, Differential effects of advanced age on neurologic and cardiac risks of coronary artery operations, *J. Thorac. Cardiovasc. Surg.* **104**, 1510–1517, 1992.

[340] M. Ünal, C. Konuralp, M. diz, A. Ekinci, and M. Akcar, Novel approach to aortic cannulation suturing: Tangential suture technique, *ANZ J. Surg.* **75**, 897–900, 2005.

[341] M. Ura, R. Sakata, Y. Nakayama, and T. Goto, Ultrasonographic demonstration of manipulation-related aortic injuries after cardiac surgery, *J. Am. Coll. Cardiol.* **35**, 1303–1310, 2000.

[342] J. van der Linden and H. Casimir-Ahn, When do cerebral emboli appear during open heart operations? A transcranial doppler study, *Ann. Thorac. Surg.* **51**, 237–241, 1991.

[343] J. van der Linden, L. Hadjinikolaou, P. Bergman, and D. Lindblom, Postoperative stroke in cardiac surgery is related to the location and extent of atherosclerotic disease in the ascending aorta, *J. Am. Coll. Cardiol.* **38**, 131–135, 2001.

[344] J. van der Linden, P. Bergman, and L. Hadjinikolaou, The topography of aortic atherosclerosis enhances its precision as a predictor of stroke, *Ann. Thorac. Surg.* **83**, 2087–2092, 2007.

[345] S. S. Varghese, S. H. Frankel, and P. F. Fischer, Direct numerical simulation of stenotic flows. Part 2. Pulsatile flow, *J. Fluid Mech.* **582**, 281–318, 2007.

[346] P. Verbrugghe and P. Herijgers, The influences of pressure changes on endoclamp balloon stability, In *Proceedings of the 2011 SCATh Joint Workshop on New Technologies for Computer/Robot Assisted Surgery, July 11-13, 2011, Graz, Austria.*, pages 1–4, 2011.

[347] P. Verdonck, U. Siller, D. de Wachter, and G. de Somer, F. van Nooten, Hydrodynamical comparison of aortic arch cannulae, *Int. J. Artif. Organs* **21**, 705–713, 1998.

[348] L. Vergori, M. Destrade, P. McGarry, and R. W. Ogden, On anisotropic elasticity and questions concerning its finite element implementation, *Comput. Mech.* **52**, 1185–1197, 2013.

[349] R. P. Vito and S. A. Dixon, Blood vessel constitutive models – 1995-2002, *Annual Review of Biomedical Engineering* **5**, 413–439, 2003.

[350] T. Walther, V. Falk, and F. W. Mohr, Minimally invasive surgery for valve disease, *Curr. Probl. Cardiol.* **31**, 399–437, 2006.

[351] P. A. Walts, R. Lee, and A. M. Gillinov, Balloon occlusion of calcified aortic aneurysm with aortic insufficiency, *J. Card. Surg.* **19**, 279–280, 2004.

[352] C. Weber and H. Noels, Atherosclerosis: current pathogenesis and therapeutic options, *Nat Med* **17**, 1410–1422, 2011.

[353] G. S. Weinstein, Left hemispheric strokes in coronary surgery: Implications for end-hole aortic cannulas, *Ann. Thorac. Surg.* **71**, 128–132, 2001.

[354] H. Weisbecker, D. M. Pierce, P. Regitnig, and G. A. Holzapfel, Layer-specific damage experiments and modeling of human thoracic and abdominal aortas with non-atherosclerotic intimal thickening, *Journal of the Mechanical Behavior of Biomedical Materials* **12**, 93–106, 2012.

[355] E. Weiss and W. Baumgartner, 1, pages 1–10, *Molecular and Biochemical Basis of Brain Injury Following Heart Surgery Interventions for the Future*, R. S. Bonser, D. Pagano, and A. Haverich (eds.), Springer London, 2011.

[356] C.-Y. Wen, C.-Y. Lee, H.-Y. Yu, and H.-T. Chang, A novel inflatable belt-type clamp in open heart surgery, *Journal of Mechanics* **27**, 57–62, 2011.

[357] J. K. White, A. Jagannath, J. Titus, R. Yoneyama, J. Madsen, and A. K. Agnihotri, Funnel-Tipped Aortic Cannula for Reduction of Atheroemboli, *Ann. Thorac. Surg.* **88**, 551–557, 2009.

[358] B. Wicker, H. Hutchens, Q. Wu, A. Yeh, and J. Humphrey, Normal basilar artery structure and biaxial mechanical behaviour, *Computer Methods in Biomechanics and Biomedical Engineering* **11**, 539–551, 2008.

[359] M. L. Williams, S. Sheng, J. S. Gammie, J. S. Rankin, P. K. Smith, and G. C. Hughes, Aortic dissection as a complication of cardiac surgery: Report from the society of thoracic surgeons database, *Ann. Thorac. Surg.* **90**, 1812–1817, 2010.

[360] World Health Organization. Fact sheet 310: The top ten causes of death, 2008.

[361] P. Wriggers, *Nonlinear Finite Element Methods*, Springer-Verlag Berlin Heidelberg, 2008.

[362] L. J. Wurzinger and H. Schmid-Schönbein, The interaction of fluid-dynamic, physicochemical and cell biological reactions in thrombus formation, *Ann. N. Y. Acad. Sci.* **516**, 316–332, 1987.

[363] K. Yamana, T. Ito, A. Maekawa, T. Yoshizumi, M. Sunada, and S. Hoshino, Atherosclerotic arch aneurysm operations with perfusion toward the aortic valve, *Ann. Thorac. Surg.* **89**, 435–439, 2010.

[364] N. Yang, S. Deutsch, E. G. Paterson, and K. B. Manning, Numerical study of blood flow at the end-to-side anastomosis of a left ventricular assist device for adult patients, *J. Biomech. Eng.* **131**, 111005–9, 2009.

[365] N. Yang, S. Deutsch, E. Paterson, and K. Manning, Comparative study of continuous and pulsatile left ventricular assist devices on hemodynamics of a pediatric end-to-side anastomotic graft, *Cardiovascular Engineering and Technology* **1**, 88–103, 2010.

[366] N. Yang, S. Deutsch, E. G. Paterson, and K. B. Manning, Hemodynamics of an end-to-side anastomotic graft for a pulsatile pediatric ventricular assist device, *J. Biomech. Eng.* **132**, 031009–13, 2010.

[367] O. Zienkiewicz and R. Taylor, *The Finite Element Method*, Volume 1,2, Butterworth-Heinemann, 5th Edition, 2000.

[368] B. Zingone, ecomment: Clamping a calcified aorta: note of caution, *Interactive CardioVascular and Thoracic Surgery* **10**, 20–21, 2010.

[369] B. Zingone, G. Gatti, E. Rauber, A. Pappalardo, B. Benussi, and L. Dreas, Surgical management of the atherosclerotic ascending aorta: Is endoaortic balloon occlusion safe?, *Ann. Thorac. Surg.* **82**, 1709–1714, 2006.